



# Durham E-Theses

---

## *Indium phosphide - langmuir film mis devices*

Sykes, R. W.

### How to cite:

---

Sykes, R. W. (1980) *Indium phosphide - langmuir film mis devices*, Durham theses, Durham University. Available at Durham E-Theses Online: <http://etheses.dur.ac.uk/7563/>

### Use policy

---

The full-text may be used and/or reproduced, and given to third parties in any format or medium, without prior permission or charge, for personal research or study, educational, or not-for-profit purposes provided that:

- a full bibliographic reference is made to the original source
- a [link](#) is made to the metadata record in Durham E-Theses
- the full-text is not changed in any way

The full-text must not be sold in any format or medium without the formal permission of the copyright holders.

Please consult the [full Durham E-Theses policy](#) for further details.

INDIUM PHOSPHIDE - LANGMUIR FILM

MIS DEVICES

by

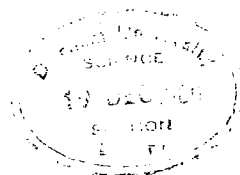
R.W.Sykes, B.Sc.

A thesis submitted for the degree

of Doctor of Philosophy in the

University of Durham

NOVEMBER 1980



The copyright of this thesis rests with the author.  
No quotation from it should be published without  
his prior written consent and information derived  
from it should be acknowledged.

*To my wife*

*For her endless encouragement*

*help, and sacrifice.*

ABSTRACT

Langmuir-Blodgett films are an interesting example of two dimensional ordered structure. Their fabrication involves the building-up of a multilayer film by repeated deposition of single monomolecular layers upon the substrate material. The resultant structure is of defined thickness and excellent uniformity. Because of these qualities, Langmuir films enjoy potential applications in many areas of modern science. In particular, their excellent insulating properties have led to the proposition of their use within the semiconductor device industry.

Indium phosphide, although a relatively new semiconductor, is already becoming an important device material, particularly in areas where its high mobility gives rapid device response and good high frequency operation. This thesis combines these two materials, and looks at the electrical behaviour of InP/Langmuir film metal-insulator-semiconductor (MIS) devices and their associated structures.

The Langmuir-Blodgett process is a low temperature deposition technique, and thus induces little or no surface damage to its recipient substrate. Because of this, it is likely that the chemical surface of the InP, prior to deposition, will be of critical importance in defining the device characteristics. This has in fact been found to be the case, and a detailed study of the correlation between ESCA surface chemical information and device electrical data has been undertaken. In addition, the device results obtained have been found to be rather different to those produced by the use of a conventional high temperature deposition process.

In order to capitalise upon the use of these organic insulating films, and the sensitive nature of the InP surface, the effect of various gases upon these device structures have been investigated. This study has revealed the existence of many interesting bulk and interface effects, and is likely to form the basis of a more detailed programme aiming to develop a range of solid state sensors.



ACKNOWLEDGEMENTS

I would like to gratefully acknowledge the help given to me by numerous members of the Department of Applied Physics and Electronics at the University of Durham. In particular, I would like to thank my supervisor, Professor G. G. Roberts, for his guidance, encouragement and time spent directing me. I am indebted to Dr. M. C. Petty, Mr. P. J. Martin and all other members of the group for their help and stimulating discussion. For their unlimited patience, skill and advice, I wish to thank all the workshop staff, particularly Messrs. F.Spence, B.Blackburn and P.Friend, and for her expertise in typing this thesis, I am grateful to Mrs. S. Mellanby.

I am indebted to I.C.I.Limited for financial support, and to the members of the research group at the Corporate Lab., particularly Dr.W.A.Barlow, for their advice and useful discussion. I am also grateful to Professor D.T.Clark and Dr. T. Fok for their help with ESCA analysis, and to members of R.S.R.E.(Malvern) and Plessey (Caswell) Ltd., for supplying various samples.

Finally, I am eternally indebted to my wife, my father and late mother, and my wife's parents for all the help, encouragement and support given to me over the past years.

## CONTENTS

	<u>Pages</u>
ABSTRACT	i
ACKNOWLEDGEMENTS	ii
<u>CHAPTER 1</u> INTRODUCTION	1
<u>CHAPTER 2</u> ELECTRICAL BEHAVIOUR OF SEMICONDUCTOR AND THIN FILM STRUCTURES	3
2.1 Introduction to Semiconductor Physics	3
2.1.1 Band Structure	3
2.1.2 Electronic Conduction in Semiconductors	7
2.2 Metal-Semiconductor Contacts	9
2.3 DC Conduction Mechanisms in Thin Films	14
2.3.1 Schottky and Poole-Frenkel Conduction	15
2.3.2 Tunnelling Conduction	18
2.3.3 Conduction in Low Mobility Solids	19
2.4 AC Conduction in Thin Films	20
2.5 Metal-Insulator-Semiconductor Structures (MIS)	27
2.5.1 The Ideal MIS Structure	27
2.5.2 Modelling Real Devices (1): Surface State Effects	30
2.5.3 Modelling Real Devices (2): Other Effects	40
<u>CHAPTER 3</u> EXPERIMENTAL TECHNIQUES	45
3.1 Surface Analysis	46
3.1.1 Introduction to Surface Analysis Techniques	46
3.1.2 Detailed Consideration of ESCA (1): Theoretical Background	49
3.1.3 Detailed Consideration of ESCA (2): Data Interpretation	51
3.1.4 Detailed Consideration of ESCA (3): Instrumentation	52

	<u>Pages</u>
3.2 Device Fabrication Technology	53
3.2.1 Surface Preparation (1): Pre-cleaning	54
3.2.2 Surface Preparation (2): Wet Etching	55
3.2.3 Surface Preparation (3): Dry Etching	56
3.2.4 Electrode Deposition (1): Semiconductors	58
3.2.5 Electrode Deposition (2): Langmuir films	60
3.2.6 General Device Handling	62
3.3 Electrical Measurement Equipment	64
3.3.1 DC Measurement	65
3.3.2 AC Measurement	66
3.4 Environmental Control	73
<u>CHAPTER 4</u> LANGMUIR FILM TECHNOLOGY	75
4.1 Some Basic Concepts	75
4.2 Historical Review	77
4.3 Review of Previous Electrical Characterisation	83
4.3.1 DC Conduction : Tunnelling	84
4.3.2 DC Conduction : Multilayer Structures	84
4.3.3 AC Properties : Conductance	86
4.3.4 AC Properties : Capacitance	86
4.3.5 Other Properties and Structures	88
4.4 General Consideration of Potential Applications	90
<u>CHAPTER 5</u> DEPOSITION EQUIPMENT AND INSTRUMENTATION	94
5.1 Details of the Langmuir Trough	94
5.1.1 Trough and Barrier Construction	95
5.1.2 Compression Ratio	97
5.1.3 Dipping Mechanism	98
5.1.4 Surface Pressure Measurement	98
5.1.5 Instrumentation	101

		<u>Pages</u>
<u>CHAPTER 6</u>	LANGMUIR FILM DEPOSITION	104
	6.1 Subphase Cleanliness	104
	6.2 Monolayer Spreading	105
	6.3 Monolayer Compression	107
	6.4 Film Deposition	111
<u>CHAPTER 7</u>	QUALITY ASSESSMENT AND ELECTRICAL PROPERTIES OF LANGMUIR-BLODGETT FILMS	117
	7.1 Insulator Film Quality and Assessment	117
	7.2 Electrical Characterisation	120
	7.2.1 Reciprocal Capacitance Plots	121
	7.2.2 DC Conduction Properties	123
	7.2.3 Frequency Dependence of AC Characteristics	129
	7.2.4 Summary of Results	131
<u>CHAPTER 8</u>	INTRODUCTION TO InP MIS DEVICES	133
	8.1 Introduction to Indium Phosphide	133
	8.1.1 Band Structure and Electrical Properties	133
	8.1.2 Material Growth	134
	8.1.3 InP Devices	135
	8.2 Review of Current Ideas about the InP Surface	137
	8.3 Review of InP MIS Work	143
<u>CHAPTER 9</u>	THE CHARACTERISATION OF InP-LANGMUIR FILM MIS DEVICES	149
	9.1 Chemical Analysis of the InP Surface	149
	9.1.1 As Received Samples	150
	9.1.2 The Effect of Wet Etching	152
	9.1.3 The Effect of Dry Etching	155
	9.2 Metal-Semiconductor Contacts	157
	9.2.1 Ohmic Contacts	157
	9.2.2 Schottky Barriers	158

	<u>Pages</u>
9.3 N-Type InP : MIS Characterisation	160
9.3.1 Wet Etchants	160
9.3.2 Dry Etchants	164
9.4 P-Type InP : MIS Characterisation	165
9.4.1 Wet Etchant	165
9.4.2 Dry Etchant	167
9.5 Additional Effects on InP MIS Devices	168
9.5.1 Series Resistance	168
9.5.2 Electrode Material	169
9.5.3 Insulator Effects	169
9.5.4 Discussion of Additional Effects	171
9.6 Discussion of Fermi Level Pinning	174
9.6.1 N-Type Material	175
9.6.2 P-Type Material	176
9.6.3 Unified Band Gap Model : Summary	177
<u>CHAPTER 10</u> GAS EFFECTS ON MIS DEVICES	179
10.1 Introduction to Gas Detection	179
10.2 Top Electrode Effects	181
10.3 Insulator Effects	183
10.4 Interface Effects	184
10.5 Summary of Effects	185
10.6 Suggestions for Further Development	186
10.6.1 Polymeric Insulators	186
10.6.2 Other Semiconductor Substrates	187
10.6.3 Long Term Developments	188
<u>CHAPTER 11</u> SUMMARY AND CONCLUSIONS	191
REFERENCES	193
LIST OF LEGENDS	207

CHAPTER 1

INTRODUCTION

Because of its near ideal behaviour, the silicon/silicon dioxide system has virtually dominated the semiconductor industry for at least the last decade. This system combines a substrate which is relatively easy to grow, with a native oxide which has excellent uniformity and good insulating properties. More recently however, the insatiable demand for faster device response and lower power consumption has begun to uncover some of the fundamental limitations of the silicon system. This has generated increased interest in other substrate materials in the hope of their fulfilling these new demands. Of the various compounds available, indium phosphide with its high mobility shows good promise for fast devices. However, like other III-V materials its native oxide is far from ideal and it is therefore necessary to use a separate insulator when fabricating field effect devices. At present, considerable difficulty is being encountered in finding a material suitable for this purpose which does not interfere with the properties of the resultant device.

This thesis deals with the investigation of one possible group of materials, collectively known as Langmuir-Blodgett or Langmuir films, and looks at the behaviour of InP/Langmuir film metal-insulator-semiconductor (MIS) devices. These films are produced from compressed organic monolayers, by repeatedly passing the substrate, in this case InP, through the monolayer, and building up a multilayer structure. Because of the deposition process, not only is the substrate totally unaffected (by comparison with say sputtering or evaporation) but the molecular length and the number of layers precisely define the final thickness of the film. Moreover, the relatively porous nature



of these multilayers allows molecular diffusion through the film structure ; a property which is capitalised upon in the later part of the thesis with an investigation of gas effects upon these MIS structures.

The background theory required to understand the characterisation and operation of the MIS system is presented in Chapter 2. This covers basic semiconductor physics, metal-semiconductor junctions, conduction in thin films, and finally the behaviour of an ideal MIS device. Also given is a discussion of the many effects that lead to non-ideal behaviour, together with various methods of identifying them. The experimental measurement details of processes applied during this investigation : chemical surface analysis, D.C. and A.C. electrical characterisation, together with basic fabrication techniques (excluding insulator deposition) are given in Chapter 3. This is followed by a detailed study of the Langmuir-Blodgett process in Chapters 4,5,6 and 7, giving an historical review, a discussion of the specialised deposition equipment required and the methods employed to ensure the production of good quality films. The final Langmuir film chapter presents characterisation results for these films considered in isolation as MIM structures and discusses the origin of the various mechanisms observed. Consideration of the substrate material, InP, begins in Chapter 8 with a brief review of its preparation and general properties. This is followed by a discussion of previous surface characterisation and associated MIS work. Discussion of the results obtained from ESCA and Schottky barrier work, as well as detailed MIS investigations are presented in Chapter 9, together with some proposed explanation for the origin of the effects observed.

The results obtained from the exploratory study of the effect of gases upon these devices are given in Chapter 10.

## CHAPTER 2

### ELECTRICAL BEHAVIOUR OF SEMICONDUCTOR AND

#### THIN FILM STRUCTURES

This thesis investigates, in some detail, relatively new types of metal-insulator-semiconductor (MIS) structures. As a preliminary, it was considered necessary to characterise the constituent parts before looking at the device as a whole. This process involved the fabrication of metal-insulator-metal (MIM) structures to help study the insulator, and metal-semiconductor (MS) barriers to investigate the bulk and surface behaviour of the substrate. In consequence, in addition to MIS theory, thin film conduction and metal-semiconductor junction physics must also be discussed.

This chapter aims to describe the necessary background theories and models required to enable the characterization of these independent systems, and subsequently the composite device. It is divided into five sections, broadly covering each type of structure configuration. Initially, some background semiconductor physics is presented, which serves as an introduction to various basic concepts. This is followed by sections dealing with semiconductor contacts, DC and AC conduction in thin insulating films, and finally a detailed description of MIS physics and device interpretation. In most cases the volume of material precludes any detailed derivation, but where appropriate, the resultant expressions are presented for use later in the thesis.

### 2.1 INTRODUCTION TO SEMICONDUCTOR PHYSICS

#### 2.1.1 Band Structure

When individual atoms are brought together to form a covalent solid, the overlapping of electron orbitals causes the broadening of the outer levels



into bands of allowed electron energy. The extent of occupancy of these bands is governed by the Fermi level ; this may occur within a band or between bands in the forbidden gap (see later). It is the position of this level, and the width of the associated conduction and valence bands along with the gap between them that defines many of the electrical properties of a particular material. The precise position of the Fermi level is a function of temperature and is defined by the Fermi-Dirac function :

$$F = \frac{1}{1 + \exp\left(\frac{\epsilon - E_F}{kT}\right)} \quad (2.1)$$

where  $F$  is the probability of occupancy at an energy level  $\epsilon$ , at a temperature  $T$  and  $E_F$  is the Fermi level energy. Thus at  $\epsilon = E_F$ ,  $F = \frac{1}{2}$  and the level is equally likely to be occupied or unoccupied. At room temperature the sharpness of this transition from occupancy to non-occupancy is less defined and so a few electrons exist at levels above the Fermi energy.

When a material has a wide band gap (several electron volts), it is relatively hard to excite carriers into the conduction band ; in consequence it will usually exhibit insulating properties. Where the bands overlap, electron excitation is easy and the material is metallic. Between these two extremes, band gaps of a few electron volts usually lead to semiconducting behaviour, although a great many other properties influence the final characteristics. With indium phosphide, the chief substrate material used in this investigation, the band gap of 1.35 eV gives good semiconductor behaviour.

In practice, a pure (intrinsic) semiconductor with the Fermi level midway between bands is not very useful as its conductivity is still quite low. To overcome this situation it is normal to add small amounts of dopant material which produces new levels within the band gap. With silicon for example, group  $\bar{V}$  materials have an extra easily removed electron, and when included in the lattice generate an electron donor level just below the

conduction band. If we assume that at room temperature the number of intrinsic carriers is negligible, then the ionisation of these donors will dominate and the Fermi level will reside midway between the conduction band and the donor level. This effect results in the conductivity being of a much more useful value. The material is now referred to as being extrinsic, and in this case is doped n-type, as shown in Fig 2.1b. If group III materials are used, electron acceptor centres are produced and holes are generated in the valence band. In this situation the additional levels are just above the valence band and the material is p-type (Fig 2.1c). Holes are now the majority carrier of the doped semiconductor.

In many cases these additional levels are completely exhausted at room temperature and the position of the Fermi level is given by :

$$E_F' = kT \log_e \frac{N_C}{N_D} \quad (2.2)$$

where  $E_F'$  is the position (in an n-type material) measured down from the conduction band,  $N_C$  is the density of states in the conduction band, and  $N_D$  is the concentration of added donor centres. A similar expression can be derived for p-type doping. It is of course possible to have both types of dopant present at one time, but in this situation carriers produced by donors tend to be absorbed by acceptors, and the effects cancel. This compensation process is normally more useful in adding levels to remove the effects of unwanted impurities, included during the growth process. For example in GaAs, chromium is added in controlled amounts and the additional levels near the mid-gap region absorb many free carriers from the dominant unwanted donor levels. This considerably reduces the conductivity enabling semi-insulating properties to be produced. It is also possible for impurities to give more than one level in the band gap, for example sulphur produces two levels just above the mid gap in silicon, and copper generates three in the lower gap region

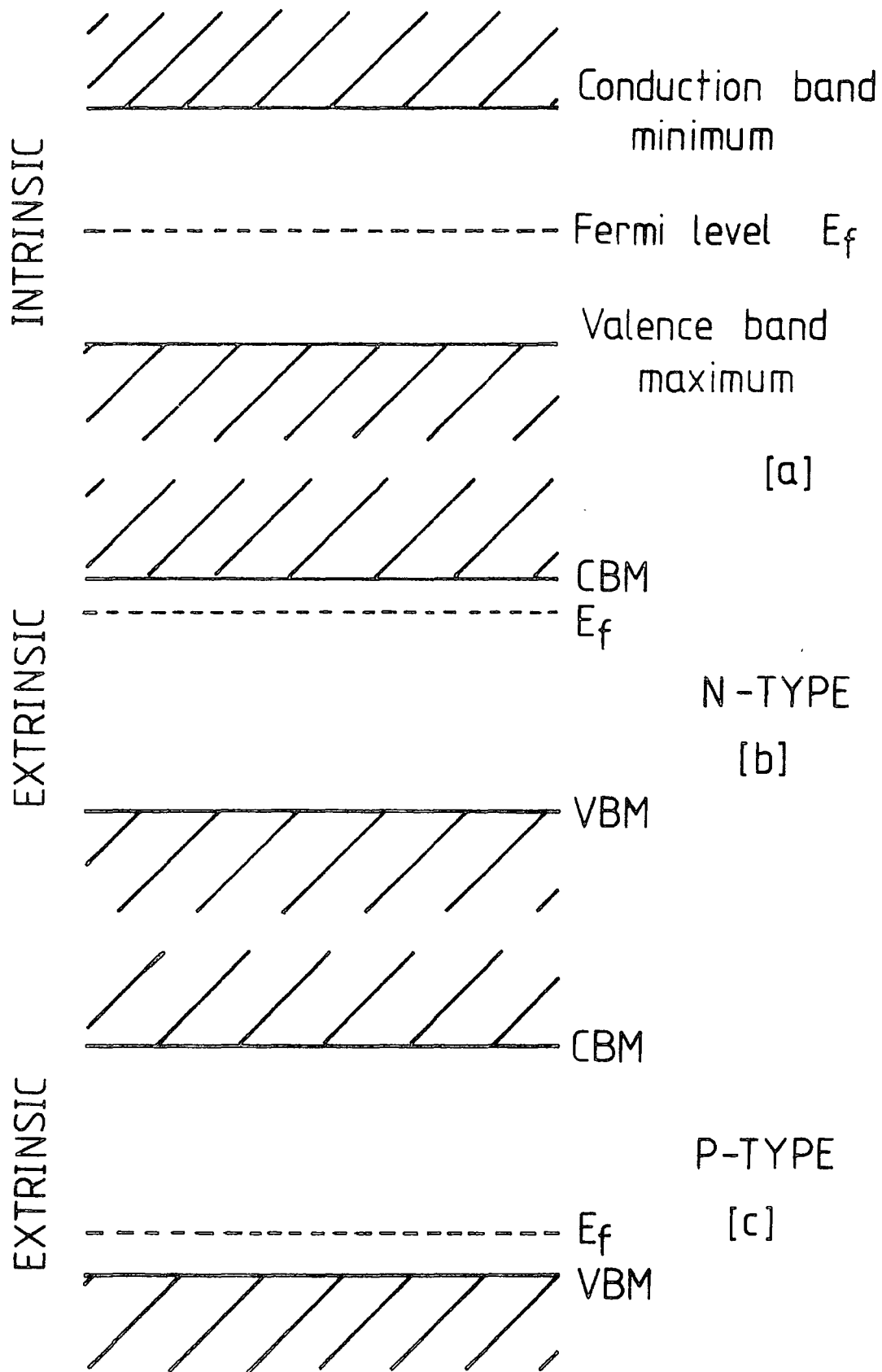


Figure 2.1 : Simplified semiconductor band structure, showing (a) intrinsic, (b) n-type, (c) p-type.

For these multi-level systems each one has its own density, and activation energy, and so the displacement of the Fermi level and its variation with temperature become much more difficult to predict.

For compound semiconductors, growth and purification is normally considerably more difficult than for silicon, and the problems caused by additional levels in the gap is more serious. In addition the production of controlled doping is less well understood. With InP for example, group IV materials appear to produce high conductivity n-type properties, whereas Zn and Cd (group II elements) produce p-type properties. The use of group VI elements also appears to give n-type material.

Although valid for many materials, the assumption of a relatively wide continuous band structure is not always true. In amorphous materials for example, only short range order is present, and although some form of band structure is apparent, the band edges extend considerable distances into the gap. At these edges there is a gradual transition from the continuous states of the band, in which carriers can move freely, to strictly localised states or traps in which the carriers are relatively immobile. Thus in this type of material electrical conduction is dominated by this high ( $\sim 10^{19} \text{ cm}^{-3}$ ) density of additional levels, and carrier hopping between them.

As well as being able to produce a crystalline lattice from single atoms, it is possible to assemble an ordered structure using molecules; this is termed a molecular crystal. In these materials the bonding between the component units is relatively weak and so the electronic orbital overlap is less than normal. As a consequence the energy bands are very narrow, normally considerably less than one electron volt, but have quite large gaps between them. Thus in a pure material there are very few thermally excited carriers. In these materials normal band theory must be adapted to account for the narrowness of the bands, and electrical transport is again somewhat different to that in normal semiconductors.

### 2.1.2 Electronic Conduction in Semiconductors

For any charge transport to occur within a semiconductor, electrons must be present in the conduction band and/or holes in the valence bands. In most structures, these carriers are injected from Ohmic (see section 2.2) contacts on the semiconductor surface, although promotion from donor/acceptor levels or across the band gap is often an important process. Once in the conduction band, the movement of the carriers through the lattice is controlled by the mobility of the material  $\mu$ , given by

$$v = \mu E \quad \text{m/sec} \quad (2.3)$$

where  $E$  is the applied electric field, and  $v$  is the average drift velocity of the carriers. The value of  $\mu$  is normally considerably larger for electrons than for holes. In group IV (non polar) semiconductors, there are two scattering mechanisms which significantly affect the carrier motion through the lattice, and thus the mobility. Both are temperature dependent effects. The presence of ionised impurities (often dopants) generates a  $T^{3/2}$  dependence, and scattering due to phonon (quantized lattice vibration) interactions leads to a  $T^{-3/2}$  variation. These two effects are often present together but normally one is dominant at low values of  $T$  (ionised impurity), and the other at high  $T$  (phonon). In III-V and other polar materials, additional effects due to optical phonon scattering are also important.

#### (a) Ohmic conduction

Under low field conditions the motion of the carriers through the material will show simple Ohmic behaviour, where the conductivity of the sample is given by ;

$$\sigma = ne\mu \quad (2.4)$$

where  $n$  is the density of carriers. This expression applies equally well for holes or electrons. In addition to Ohmic (drift) conduction, it is possible

for carriers to move through the material by diffusion. This process relies upon a non-uniform concentration of carriers (for example near an injecting contact) causing a net motion away from this area to even out the distribution. It is quite normal for both drift and diffusion mechanisms to be present at the same time ; although the former type is dominant under most conditions.

(b) Space-charge-limited conduction

When higher fields ( $\sim 10^4$  V/cm) are applied to an Ohmic contact an excess of electrons (or holes) are injected into the surface region of the semiconductor. This leads to the formation of a space charge region in the vicinity of the contact, and mutual repulsion between the carriers, which tends to limit the amount of charge reaching the bulk. Under these conditions, the current flow is space charge limited. In addition, rather than the carriers being under constant acceleration, as in a space charge limited thermionic diode, continuous interaction with the lattice results in a constant velocity. Accordingly, the currents in a solid are several orders of magnitude lower than in the diode. The process of space charge limitation, although very complex, is now well understood but is very hard to model in an easy way. The simplest expression gives ;

$$J \propto V^2/d^3 \tag{2.5}$$

where d is the thickness. In more general terms the currents can be represented by a scaling law which gives ;

$$J \propto d \left( \frac{V}{d} \right)^m \tag{2.6}$$

where m is a constant, not necessarily an integer. For example, a trap free material gives  $m = 2$ , whereas double injection (of both holes and electrons) gives  $m = 3$ .

## 2.2 METAL-SEMICONDUCTOR CONTACTS

When a metal is deposited onto a semiconductor<sup>(1,2,3)</sup>, one of three types of contact will be produced ; Ohmic, rectifying or neutral. These possibilities are caused by the different relative positions of the two Fermi levels, which may aid or inhibit carrier exchange. It can be seen from Fig 2.2, that when an n-type semiconductor and a metal are brought together under zero bias conditions, charge flow must occur between the two materials in order to level the Fermi energies. The direction of this flow is defined by the relative magnitudes of the two work functions (the work function is defined as the energy required to enable an electron with energy corresponding to the Fermi level, to escape from the material). If  $\phi_m$  is less than  $\phi_s$ , then the metal Fermi level is higher than the semiconductor, and so carriers will flow into the latter. The resultant space charge region acts as a reservoir of carriers ready to flow into the semiconductor upon the application of an electric field. This type of contact is known as Ohmic or injecting. In fact the former definition is rather a misnomer and merely signifies the lack of a barrier, whereas the use of the term injecting is more accurate due to the resultant surface reservoir produced by this type of electrode. For a p-type semiconductor  $\phi_m$  must be greater than  $\phi_s$  in order to produce an Ohmic contact (Fig.2.2). In this case the contact potential  $\phi_{ms} = \phi_m - \phi_s$  is positive, and the surface reservoir of holes causes the semiconductor bands to bend upwards.

If these situations are reversed, and for example the contact potential is positive for an n-type substrate, then a blocking or barrier contact is produced. In this situation, electrons flow into the electrode material to produce levelling of the Fermi energies, and so a region depleted of majority carriers is produced within the semiconductor. This depletion region represents a high resistance, and so limits the flow of carriers into the semiconductor. Similarly, for a p-type material a negative contact

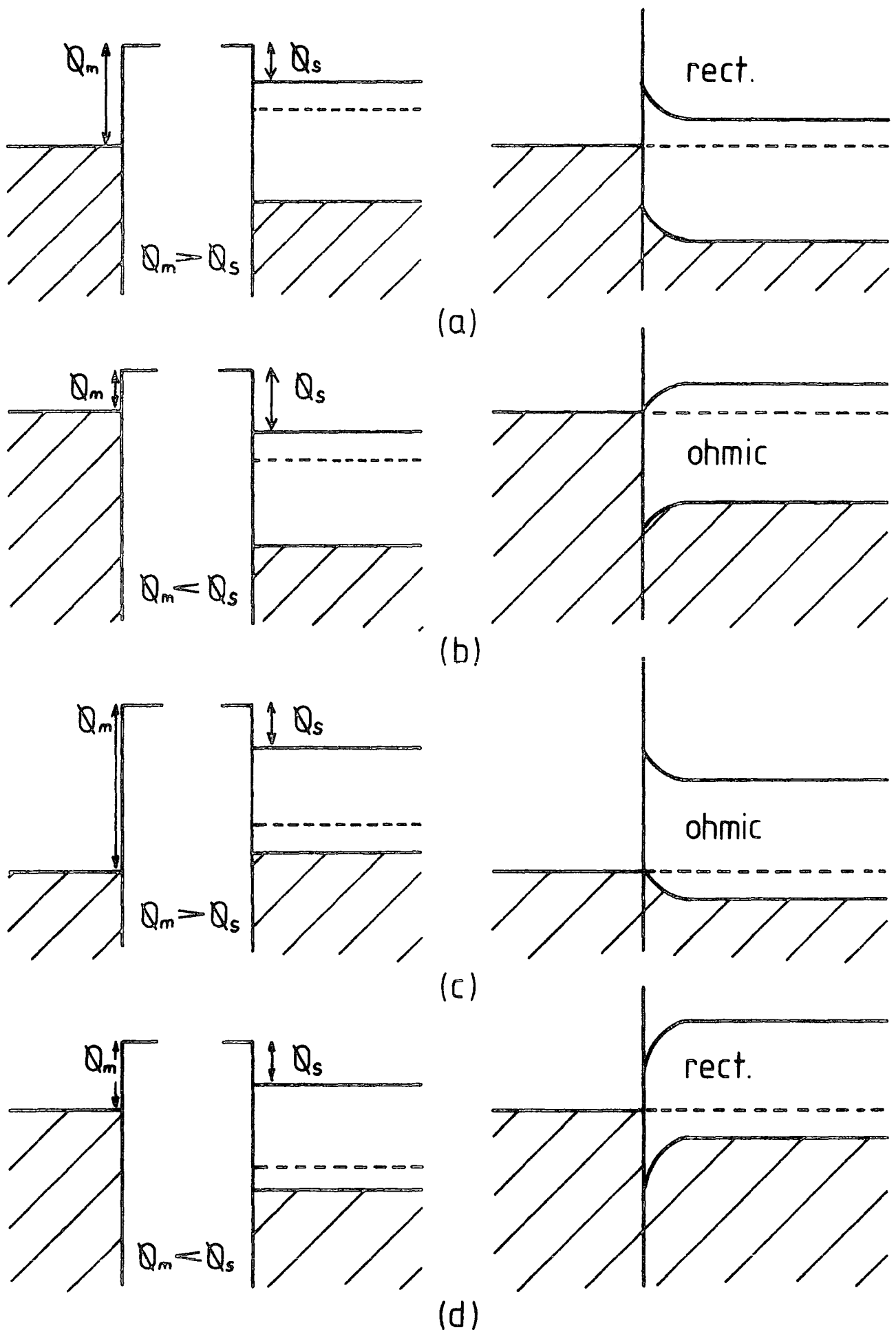


Figure 2.2 : Energy band diagrams for Ohmic and rectifying semiconductor contacts, (a,b) n-type, (c,d) p-type.



potential will result in a barrier region and the production of a rectifying contact.

The third situation is where the Fermi levels are equal to begin with, and so the contact potential is zero. In this case, known as a neutral contact, no transfer of charge takes place, but the characteristics tend to be similar to those for an Ohmic contact under low applied field conditions. The occurrence of this type of contact is very rare, and its usefulness extremely limited ; in consequence it will be considered no further.

For an ideal barrier contact \*\*, the application of an external field can be used to vary the barrier height, and so this type of contact produces asymmetrical current-voltage characteristics. Under forward bias (positive applied voltage) conditions the gradual reduction of the barrier produces an exponential curve ;

$$J_F = A^* T^2 \exp\left(\frac{-e\phi_b}{kT}\right) \exp\left(\frac{eV}{kT}\right) A/m^2 \tag{2.7}$$

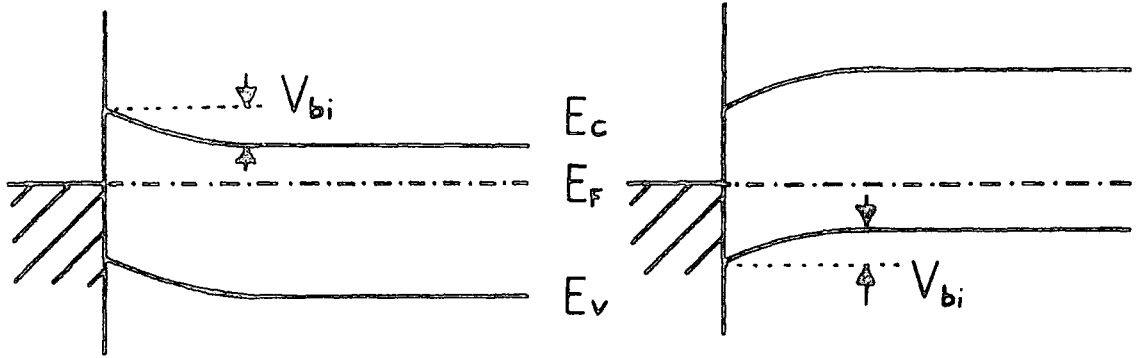
where  $\phi_b$  is the barrier height (normally equal to the contact potential), V is the applied voltage, and  $A^*$  is the compensated Richardson constant (equal to  $9.4 A cm^{-2} K^{-2}$  for InP). This latter term is similar to the value used in the vacuum diode model except now the mass of the carriers must be modified due to their motion through a solid lattice. The new constant thus becomes  $A^* = \frac{m^*}{m} A$  where  $m^*$  is the effective mass of the carriers in the semiconductor, and m their mass in free space.

In reverse bias (negative applied electrode voltage), the additional potential causes a widening of the depletion region as more free carriers are removed from the semiconductor (Fig. 2.3). Under these conditions the current through the junction is very much less than in forward bias, and hence its

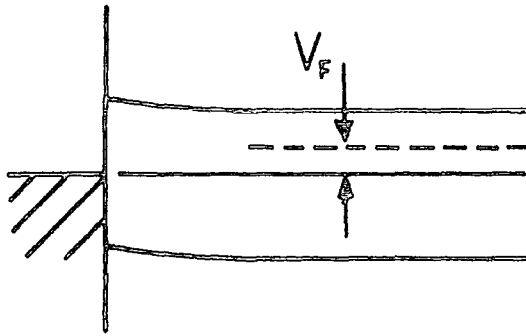
\*\* The ensuing detailed consideration of barrier contacts deals primarily with n-type semiconductors . Similar arguments can be applied to p-type materials, but the relative barrier considerations must be reversed.

n-type semiconductor

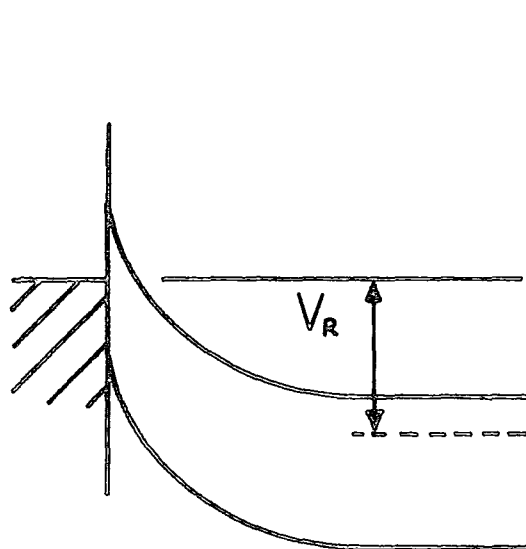
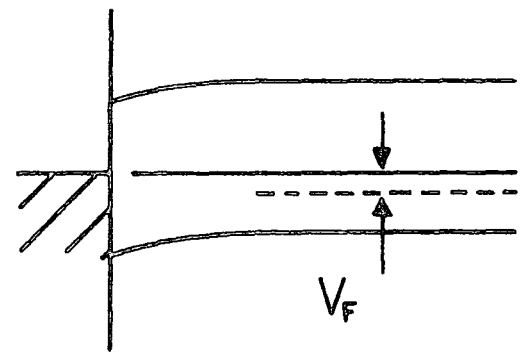
p-type semiconductor



(a) thermal equilibrium



(b) forward bias



(c) reverse bias

Figure 2.3 : Schottky barrier contacts under various bias conditions.

use as a rectifying electrode. The reverse bias current is given by :

$$J_R = A^* T^2 \exp\left(\frac{-e\phi_B}{kT}\right) \text{ A/m}^2 \quad (2.8)$$

and is effectively the forward bias curve with the voltage dependence removed. From this simplified expression it can be seen that the reverse bias current is in practice a constant leakage value, independent of applied bias, and determined largely by the zero bias barrier height. In addition, the production of this region depleted of mobile carriers gives rise to a capacitance associated with the junction. The value of this capacitance is defined by the width of the depletion region ( $W$ ), and is thus a voltage dependent parameter, whereby ;

$$C = \frac{\epsilon_0 \epsilon_r e N_d}{2(V_{bi} - V - kT/e)} = \frac{\epsilon_0 \epsilon_r}{W} \text{ Farad/m}^2 \quad (2.9)$$

where  $V_{bi}$  is the zero bias bending of the semiconductor bands, normally called the built-in voltage. The effect of various applied biases on the metal and semiconductor bands are shown in Fig 2.3.

From these three basic equations it is possible to obtain the majority of the important parameters which define the junction behaviour. A plot of  $1/C^2 - V$  for example from equation 2.9 will give a straight line whose gradient is proportional to the semiconductor doping density ( $N_D$ ), and whose intercept with the voltage axis gives the built-in voltage ( $V_{bi}$ ). This latter parameter is related to the barrier height  $\phi_b$  by the expression :

$$\phi_b = V_{bi} + \frac{kT}{e} \left( \ln \frac{N_c}{N_d} \right) - \Delta\phi \quad (2.10)$$

where  $\Delta\phi$  is a relatively small term arising from image force lowering of the barrier, and  $N_c$  is the density of states in the semiconductor conduction

band, given by

$$N_c = 2 \left( 2\pi m_e^* \frac{kT}{h^2} \right)^{3/2} \quad (2.11)$$

where  $m_e^*$  is the electron effective mass.

It is also possible to obtain a value of barrier height from the reverse bias curve, where the current is largely independent of voltage, and of magnitude related to the barrier height. In practice, the behaviour of a real device does not always show total flattening of the curve as predicted by the simple theory, and it may well exhibit a slight positive gradient. There are many more detailed theories which attempt to explain this effect, amongst which are those considering carrier generation in the depletion region, and edge leakage currents around the electrode. It is likely however that the dominant effect is due to image force (Schottky) lowering of the barrier, which although also present in forward bias only becomes significant in reverse bias. This model gives rise to an extra term ;

$$\exp \left[ - \frac{e \sqrt{E/4\pi\epsilon_0\epsilon_r}}{kT} \right] \quad (2.12)$$

$$\text{where } E = \sqrt{\frac{2eN_D}{\epsilon_0\epsilon_r} \left( V + V_{bi} - \frac{kT}{e} \right)}$$

which becomes another multiplying factor in the simple reverse bias expression, giving an additional  $\exp(V^{1/4})$  dependence (this effect is discussed again in section (2.3) in more general terms. In this situation the recovery of the barrier height now utilizes the intercept with the current axis.

With real devices it is normal to add an extra term to the forward bias expression to allow for non-ideal behaviour of the junction. This is

termed the ideality factor  $n$ , and resides in the denominator of the exponent. If the remaining terms in the equation are combined into a constant  $J_s$  then the new expression becomes ;

$$J_F = J_s \exp \left( \frac{e (\Delta\phi + V)}{nkT} \right) \quad (2.13)$$

where  $J_s = A^* T^2 \exp \left( -\frac{e\phi_b}{nkT} \right)$ , and  $\Delta\phi$  is added to account for image lowering.

Thus, from a  $\ln J$ - $V$  plot it is possible to directly obtain a value for this ideality factor for any given device. It is normally slightly larger than unity, but can be considerably more if an interfacial layer is present. In addition, from the expression for  $J_s$  it can be seen that the intercept value with the current axis will yield a value for the barrier height  $\phi_b$ .

More recent investigations have shown that there are a number of additional influences which can have quite significant effects on the characteristics of normal Schottky barriers. The presence of a thin oxide or contamination layer between the metal and the semiconductor has been discussed by Card and Rhoderick<sup>(4)</sup>, who proposed an additional multiplying term for the normal bias expressions of  $\exp(-\chi^{\frac{1}{2}} \sigma)$ ; where  $\chi$  is the mean barrier height in eV, and  $\sigma$  is the interfacial oxide thickness in  $\text{\AA}$ . The resulting equation thus becomes ;

$$J_F = J_s \exp(-\chi^{\frac{1}{2}} \sigma) \exp \frac{eV}{nkT} \quad (2.14)$$

where  $J_s$  represents the same constant as that used in eqn.(2.13). There has also been considerable interest in recent years in the effect of surface states on the barrier height of a device. In consequence, it is now thought by many workers<sup>(5,6,7,8,9)</sup> that the measured value of  $\phi_b$  is defined more by the presence of surface states than by the top electrode. This is particularly

obvious where the resultant value is independent of metal type. These effects are not pronounced on silicon where current manufacturing technology can reduce the surface state density to a value where their influence becomes insignificant. For  $\overline{\text{III}}:\overline{\text{V}}$  materials however problems of Fermi level pinning by surface states are more predominant<sup>(10)</sup>, and so their effect on barrier height may be greater. Indeed, a great deal of work is currently underway to investigate these effects, and it is now thought that even a fraction of 1% of a monolayer of oxygen or various metals can lead to significant pinning effects. These ideas will be discussed in more detail in Chapter 8.

### 2.3 DC CONDUCTION MECHANISMS IN THIN FILMS

The Langmuir-Blodgett insulating films used for the majority of the work in the thesis were normally looked at in relatively thin structures. In consequence even small applied voltages produced very large electric fields and resulted in the possible occurrence of a variety of different conduction mechanisms. In order to aid data interpretation at a later stage of this thesis, a number of the more popular conduction processes occurring in insulating films will now be discussed :

Although Ohmic and space charge limited conduction have been considered primarily in connection with semiconductors, it is quite possible to observe these mechanisms in insulators. With this type of material, however, the conductivity is considerably lower due to a lack of carriers in the conduction band (rather than a small mobility) and the usual current limiting process is the promotion of an electron (or hole) into the conduction (or valence)band. Once there, the carriers are normally assumed to be rapidly swept out of the material. The chief method of achieving this promotion into the conduction band is by high field lowering of the normal barrier . This will produce either Schottky, Poole-Frenkel, or certain assisted tunnelling processes depending upon the situation.

### 2.3.1 Schottky and Poole-Frenkel Conduction

These two conduction mechanisms can be considered together as they both rely upon the emission of carriers over a barrier. In the former case this barrier is at the surface of the material and carriers are obtained from the plentiful reservoir of the metal contact. With the latter process the electrons are lifted out of trapping centres (localised states) in the bulk of the material into the conduction band. The resultant expressions for both types of mechanism are very similar. First we consider the Schottky effect. At the surface of a material, in the presence of an applied electric field, the metal-insulator junction can be represented as in Fig 2.4. The energy  $\phi(x)$  required to move an electron from the metal Fermi level into the insulator conduction band is given by :

$$\phi(x) = \phi_{MI} - \frac{e^2}{4\pi\epsilon_0\epsilon_r(4x + e^2/\phi_{MI})} - Eex \quad (2.15)$$

where  $\phi_{MI}$  is the initial work function difference in the absence of a field,  $Eex$  is lowering of the barrier by the external field, and the remaining term is due to the potential energy acquired by the electron leaving the metal. The distance into the insulator is represented by the variable  $x$ . The maximum height of this barrier can be found by differentiation of the above expression ; which gives

$$\phi_{max} = \phi_{MI} - \sqrt{\frac{Ee^3}{4\pi\epsilon_0\epsilon_r}} \quad (2.16)$$

The resulting current density from this mechanism will thus be proportional to the number of carriers that have this amount of energy.

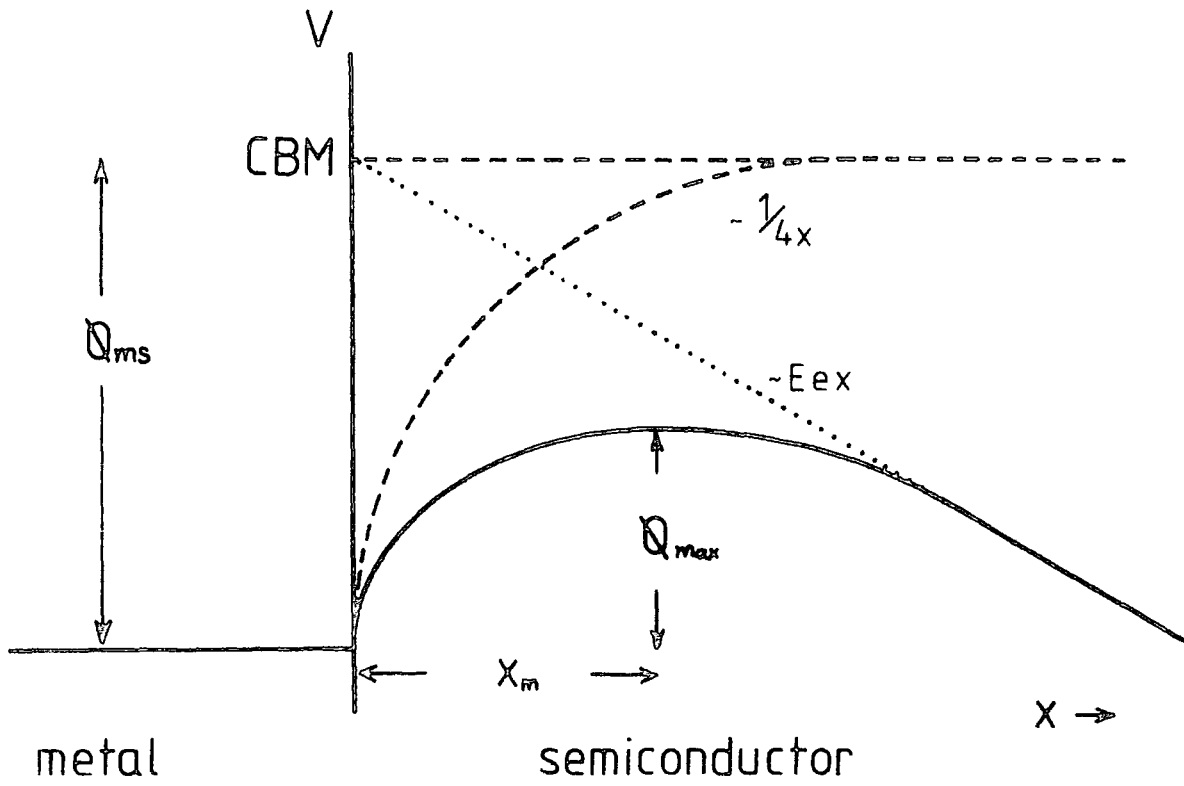


Figure 2.4 : Schematic representation of Schottky emission process.

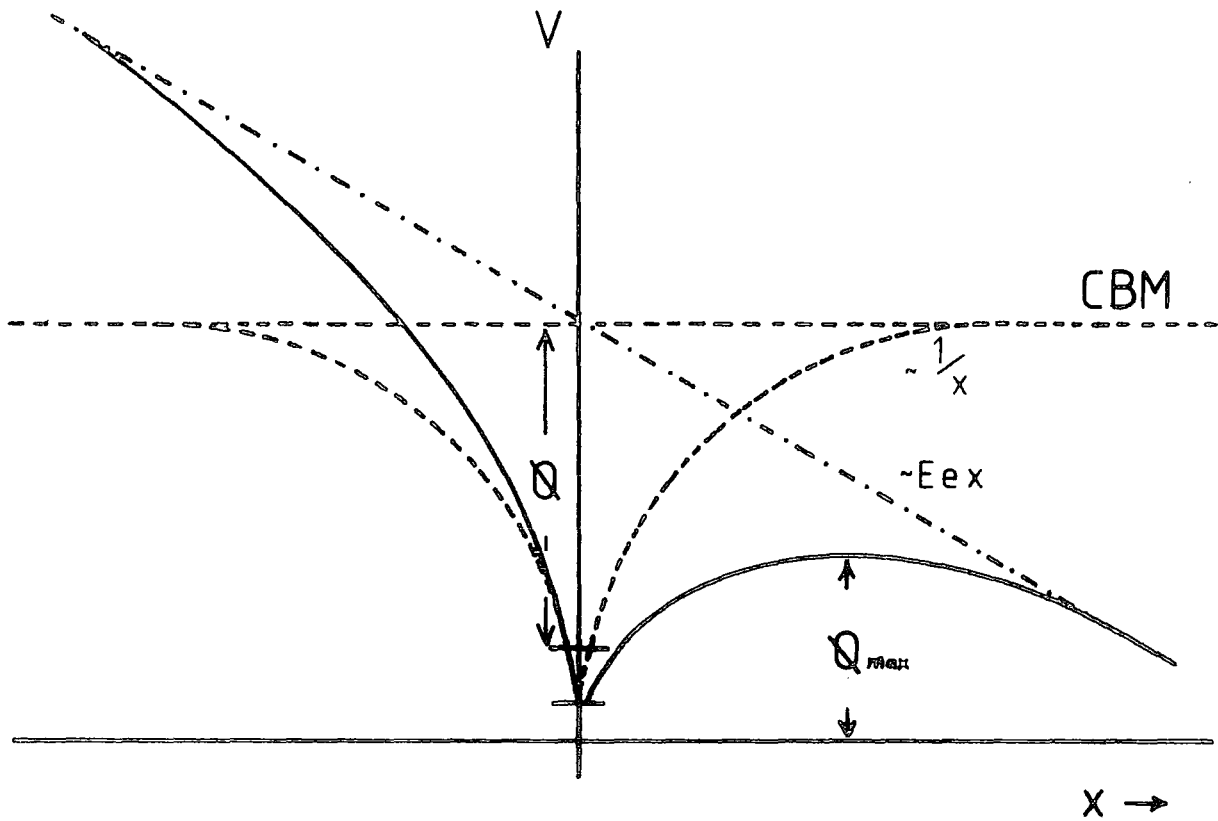


Figure 2.5 : Schematic representation of Poole-Frenkel emission process.



Therefore :

$$n \sim \exp\left(-\frac{\phi_{\max}}{kT}\right) \quad (2.17)$$

$$= \exp\left(-\frac{\phi_{MI}}{kT}\right) \cdot \exp\left[-\sqrt{\frac{Ee^3}{4\pi\epsilon_0\epsilon_r}}\right] \cdot \frac{1}{kT} \quad (2.18)$$

Or more simply :

$$J \sim \exp\left(-\frac{c}{T}\right) \cdot \exp\left(-\frac{b\sqrt{V}}{T}\right) \quad (2.19)$$

where c and b are constant.

For the Poole-Frenkel effect, the arguments are very similar, but now the carrier is emitted from a positively charged trap (as shown in Fig2.5), and the required energy is given by :

$$\phi(x) = \phi - \frac{e^2}{4\pi\epsilon_0\epsilon_r x} - Eex \quad (2.20)$$

where  $\phi$  is now the difference between the trap level and the conduction band, and the Coulombic potential is due to a fixed charge, and therefore only varies as  $1/x$ . In this case the maximum barrier height is :

$$\phi_{\max} = \phi - 2\sqrt{\frac{Ee^3}{4\pi\epsilon_0\epsilon_r}} \quad (2.21)$$

which shows twice the lowering exhibited by the Schottky process. The final current density expression is almost the same as before, but with important differences in constants ;

$$J \sim \exp\left(-\frac{c'}{T}\right) \cdot \exp\left(-\frac{2b\sqrt{V}}{T}\right) \quad (2.22)$$

The full expressions for each process are given in Table 2.1.

This consideration of Poole-Frenkel conduction is not general as it deals with only one specific situation. In practice, therefore, there are a number of other cases which lead to slightly different expressions. A particular case of interest is where the trapping sites lie beneath the Fermi level, and can thus be regarded as neutral traps, or deep donors (low down in the band gap). With this situation the final expression (2.22) is altered to have an extra factor of two in the denominator and so becomes virtually identical to the Schottky conduction equation (2.19). The existence of this latter case makes Schottky and Poole-Frenkel conduction mechanisms very difficult to distinguish experimentally.

In fact these two situations along with image force lowering in a Schottky barrier can be considered as merely specific examples of a more general scaling law for barrier limited conduction. For this situation, if the potential varies as  $1/r^n$ , then the current is given by  $\log J \propto V^{n/n+1}$ . Thus for normal Poole-Frenkel, Schottky etc.,  $n = 1$ , whereas for a reverse biased barrier (Eqn.2.12)  $n = 1/3$ . Moreover, any mechanism that obeys this general law can be considered to be barrier limited.

From the full expressions for Schottky and Poole-Frenkel conduction given in Table 2.1 it can be seen that experimental data plotted on  $\log J - V^{1/2}$  axes will yield a straight line, from which the gradient and intercept points can be used to determine various constants. In the basic situation the two mechanisms will vary by a factor of two in the gradient, and so can easily be separated; if however neutral traps are present, this distinction disappears. It is also possible to use the variation of temperature to classify these mechanisms, as a plot of  $\log J/T^2 - 1/T$  will only show a straight line for the Schottky process. The problem here, however, lies in the slow variation of this parameter which leads to the need for a very wide range of temperature variation to be considered. This is normally rather inconvenient, and in some cases damaging to the insulator.

Because of these problems, the only practical way of separating these effects is by sample and electrode dependence. The Poole-Frenkel mechanism is essentially a bulk property and will scale with film thickness, whereas the Schottky process is independent of this but will vary with electrode material. It should be noted, however, that as both effects are field dependent, it is essential to look at variation of currents with thicknesses at a constant field, and not a constant voltage. In the case of the electrode effects the use of different materials will lead to vertical displacements of the  $\log J-V^{1/2}$  line depending upon the particular work function.

### 2.3.2 Tunnelling Conduction

The other type of barrier limited conduction mechanism is quantum mechanical tunnelling. In this situation electrons from either localised states, or from the surface electrodes penetrate thin ( $< 50 \text{ \AA}$ ), field reduced barriers. The rate of these processes depends upon many variables and in spite of a great deal of theoretical modelling, no simplified expression has yet been produced. As with space-charge limited conduction, it is not that the process is badly understood, indeed quite the contrary, it is merely that there exist very many different "limited application" situations. The simplest consideration assumes a rectangular barrier of height  $\phi$  and this gives ;

$$J \sim V^2 \exp\left(\frac{-\phi^{3/2} c}{V}\right) \quad (2.23)$$

where  $c$  is a constant. From this expression it can also be seen that the normal process is largely temperature independent, but highly voltage dependent. When very high voltages are used Fowler-Nordheim tunnelling becomes dominant, in this case a plot of  $\log J/V^2 - 1/V$  will yield a straight line, from which the gradient gives the barrier height. This mechanism is very common in thin insulators and can frequently be observed over many decades of current.

Process	Expression
Ohmic conduction	$J \propto E \exp\left(-\frac{\Delta\epsilon}{kT}\right)$
Space charge limited conduction	$J = \frac{9 \epsilon_0 \epsilon_r \mu V^2}{8d^3}$
Schottky emission	$J = A^* T^2 \exp\left[-\frac{e\left(\phi_{ms} - \sqrt{eE/4\pi\epsilon_0\epsilon_r}\right)}{kT}\right]$
Poole-Frenkel emission	$J \propto E \exp\left[-\frac{e\left(\phi - \sqrt{eE/\pi\epsilon_0\epsilon_r}\right)}{kT}\right]$
Tunnelling emission (simple model)	$J \propto E^2 \exp\left[-\frac{-4\sqrt{2m^*}(e\phi_B)^{3/2}}{3ehE}\right]$

where  $\Delta\epsilon$  = Activation energy of conduction  
 $A^*$  = Effective Richardson constant  
 $m^*$  = Effective mass  
 $E$  = Applied electric field  
 $d$  = Insulator thickness  
 $\phi$  = Barrier height

TABLE 2.1 Summary of DC Conduction Mechanisms in Thin Films.

### 2.3.3 Conduction in Low Mobility Solids

In addition to the processes considered so far, any review of conduction mechanisms must also look at the phenomena peculiar to narrow band and amorphous materials. These will be briefly discussed here .

#### (a) Disordered materials

As previously mentioned, an amorphous material is characterised by only short range order and thus exhibits a high density of localised states within the band gap. In most situations, these states can be represented as long tails on the conduction and valence bands, and are thus of a higher density near the band edges. In certain conditions they can equally produce wide bands distributed around one or two points within the gap. Often both effects are present. These localised states provide an alternative conduction path for electrons, in parallel with band (extended state) conduction. In most conditions the number of electrons present in the conduction band is sufficiently small for this localised mechanism to dominate. Charge can move between these closely packed states in one of three possible ways , thermally over the potential barrier between the states (very rarely), by tunnelling through the barrier, and finally by a combination of these two. This latter process is the most important effect, and is commonly known as hopping. Simple treatment of this mechanism yields a conductivity given by :

$$\sigma \sim \exp - \left( \frac{T_0}{T} \right)^{1/4} \quad (2.24)$$

where  $T_0$  is proportional to  $a^3$ , the inverse radius of the localised state. With thinner films and/or lower temperatures, this variable range mechanism changes to an exponential  $T^{-1/3}$  dependence. In practice more detailed consideration of the process yields many specific situations and it has become obvious that any really general treatment of the effect will be quite involved.

(b) Molecular crystals

In molecular crystals the weakness of the bonding interactions leads to a very narrow band structure. This situation calls into question the applicability of band theory for these types of material, and even where appropriate, significant band population at moderate temperatures must be allowed for. This situation usually also gives quite low values of mobility when compared to an inorganic semiconductor. With molecular crystals the carrier effective mass is significant when compared to the mass of the "fixed" lattice points. Because of this the motion of carriers through the material is normally accompanied by a deformation or polarization of the surrounding lattice. The deformation, together with the carrier is known as a polaron. More specifically, in molecular crystals the extent of this deformation is normally limited to one or two molecules; in consequence in this situation the disturbance is known as a "small" polaron. In all cases the combined carrier and perturbation have a higher effective mass than the bare carrier.

Conduction mechanisms in these materials are as yet not very well understood, mainly because of the great variety of apparently different situations that have been observed. In general, all processes so far proposed show some temperature dependence and the current mechanisms can be divided into narrow band conduction, often phonon assisted, and polaron conduction, normally by some form of hopping motion. Considerably more work needs to be undertaken however before the understanding of molecular crystals begins to approach that available for other materials and conduction mechanisms.

2.4 AC CONDUCTION IN THIN FILMS

The capacitance (C) of a parallel plate capacitor can be represented by <sup>(13)</sup> ;

$$C = \frac{A\epsilon_0\epsilon_r}{d} \quad (2.25)$$

where A is the plate area, d the plate spacing, and  $\epsilon_r$  the relative permittivity of the dielectric. This structure will obey Ohms law for DC applied signals, but will have an impedance Z in all other situations. In the case of a perfect dielectric there is no leakage current, and so;

$$Z = \frac{1}{\omega C} = \frac{1}{2\pi fC} \quad (2.26)$$

where Z is the impedance in ohms. A real dielectric however will pass some current when a DC bias is applied, and a practical capacitor can thus be considered as an ideal one in parallel with a leakage resistance. When an AC field is applied to this real structure the current sinusoid is found to lead the applied voltage signal by an angle ( $\theta$ ) depending upon the degree of leakage. This effect can be represented by a vector diagram, as shown in Fig 2.6 ; where the axes represent the real and imaginary components of the impedance. If the capacitor is ideal, the conductance G (1/R) is zero and  $\theta$  is  $90^\circ$  ; the impedance in this case is purely imaginary. The ratio of the real and imaginary components is normally represented by  $\tan \delta$ , where  $\delta = 90 - \theta$ . Thus for real capacitors,  $\delta$  is quite small and  $\tan \delta$  is often referred to as the loss tangent. Using complex notation, the admittance of a capacitor can be expressed as ;

$$Y = \frac{1}{Z} = \frac{1}{R} + j\omega c \quad (2.27)$$

and thus ;

$$\tan\delta = \frac{1}{\omega CR} \quad (2.28)$$

In addition, it is convenient to relate this expression to the

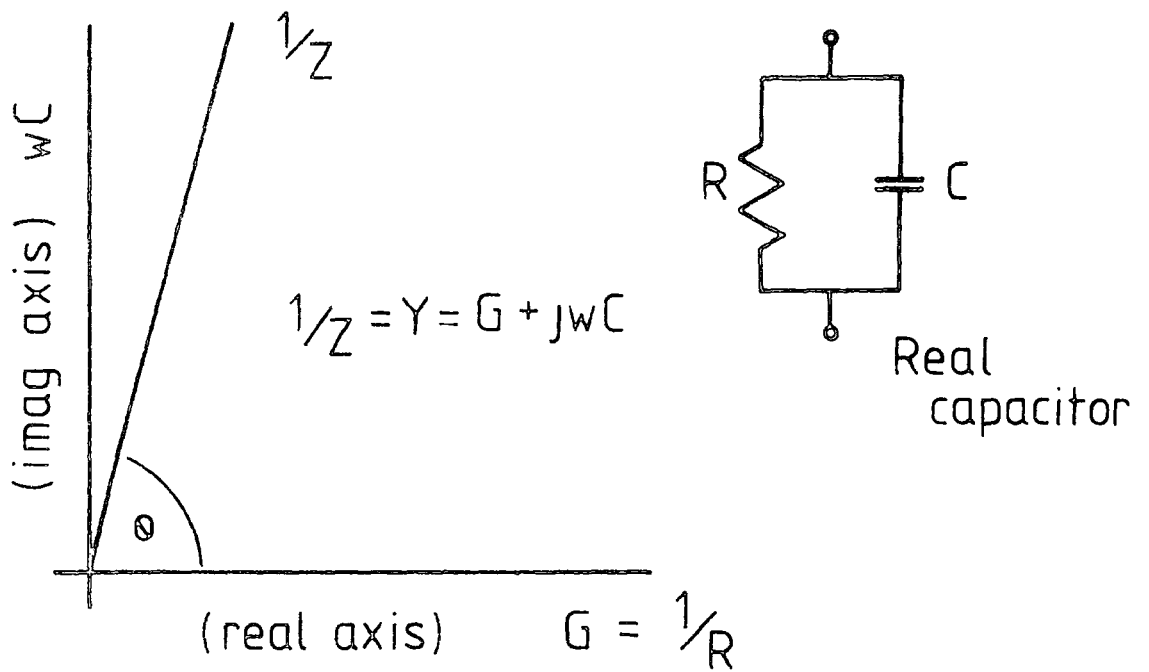


Figure 2.6 : Representation of real capacitor, and accompanying vector diagram.

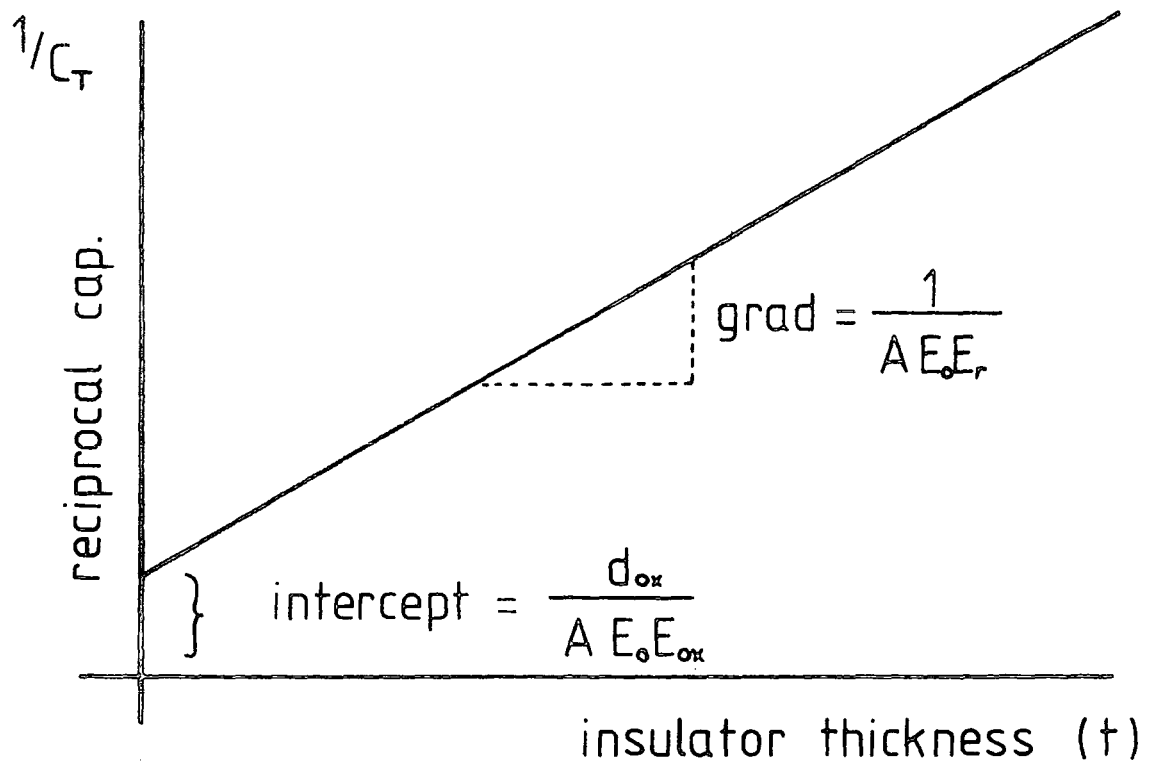


Figure 2.7 : Ideal reciprocal capacitance against thickness plot.



dielectric constant ; hence we can define

$$\tan \delta = \frac{\epsilon''}{\epsilon_r} \tag{2.29}$$

where  $\epsilon_r$  is the relative permittivity of the dielectric and relates to the ideal or imaginary part of the impedance. The other term,  $\epsilon''$  represents the in-phase or loss component of the material. In most cases both  $\epsilon_r$  and  $\epsilon''$  are frequency dependent as various configurations of dipoles within the material pass through absorption peaks. These effects subsequently give rise to local peaks in  $\epsilon''$ , and steps in  $\epsilon_r$  at each relaxation point. It should be noted however that these phenomena are spread over the whole of the frequency spectrum ,  $10^{-6}$  to  $10^{18}$  Hz, and relatively narrow bands of measurement may therefore show little or no variations. This frequency dependence of the dielectric constants also tend to complicate the equivalent circuit, and extra components sometimes have to be added to the simple RC circuit to model the more complex behaviour over specific bands of frequency. For the purposes of this investigation, measurements were restricted to the relatively narrow frequency band of 10 Hz - 100 kHz.

It can be seen from Equation 2.25 that if a structure is prepared with many different values of  $d$ , but a constant electrode area  $A$ , then a plot of  $1/C$  against  $d$  will yield a straight line. This is illustrated in Figure 2.7 ; from which it can be seen that the gradient of this line is inversely proportional to  $\epsilon_r$ , and therefore this type of plot can be used as a simple means of determining the dielectric constant of the insulator. In addition, it can also be seen from Fig 2.7 that this line has a positive value of intercept with the Y axis ; this represents the effect of the interfacial layer : The total capacitance of the structure is given by ;

$$\frac{1}{C_T} = \frac{1}{C_{Ox}} + \frac{1}{C_{ins}} \tag{2.30}$$

where  $C_{ox}$  and  $C_{ins}$  are the capacitance values due to the interfacial oxide and the insulator respectively. This expression can be further reduced to ;

$$\frac{1}{C_T} = \frac{d}{A\epsilon_o \epsilon_{ox}} + \frac{t}{A\epsilon_o \epsilon_r} \quad (2.31)$$

where  $\epsilon_{ox}$  and  $\epsilon_r$  are the relative permittivities of the oxide and the insulator,  $d$  is the oxide thickness, and  $t$  the insulator thickness. Thus at the intercept point,  $t$  is zero and the oxide thickness can be directly obtained.

Although it has been previously mentioned that good dielectric materials show little or no dispersion of dielectric constant (and hence capacitance) within the frequency band used here, it is not unusual for the conductance component to be affected. Experimental evidence for Langmuir-Blodgett films shows the imaginary constituent of the dielectric constant  $\epsilon_r$ , to vary systematically with frequency, such that

$$\epsilon_r(\omega) \propto \omega^{(n-1)} \quad (2.32)$$

where  $n$  is slightly less than or equal to unity. In this situation the dispersion in  $\epsilon_r$  causes the real part of the permittivity to vary as  $\omega^{(n)}$ . The AC conductivity of a structure can be represented as

$$\sigma(\omega) = \sigma_o + \sigma'(\omega) \quad (2.33)$$

where  $\sigma_o$  is the frequency independent DC component, and  $\sigma'(\omega)$  is related to the dielectric loss ;

$$\sigma'(\omega) = \epsilon_o \omega \epsilon''(\omega) \quad (2.34)$$

Thus from Equation 2.32 the frequency dependent component will show a

similar  $\omega^n$  dependence. The value of  $n$  is defined largely by the origin of the effect ; whether it is a lattice (intrinsic) effect, or due to injected carriers (extrinsic). The former processes invariably show  $n$  close to unity, whereas charge transport shows  $n$  in the region between 0.5 and 0.9. It is now generally believed that these lower values of  $n$  in Langmuir films are due to hopping conduction between impurity or dislocation sites<sup>(14)</sup>, as discussed in detail by Mott<sup>(15)</sup>.

Variation of both capacitance and conductance with frequency can also be caused by other influences. In particular, the effect of contact or lead resistance is a dominant possibility<sup>(16)</sup>. If the simple MIM structure is considered as a capacitor in parallel with a resistor, as shown in Figure 2.6, then adding the effect of the electrodes will give the circuit shown in Figure 2.8.

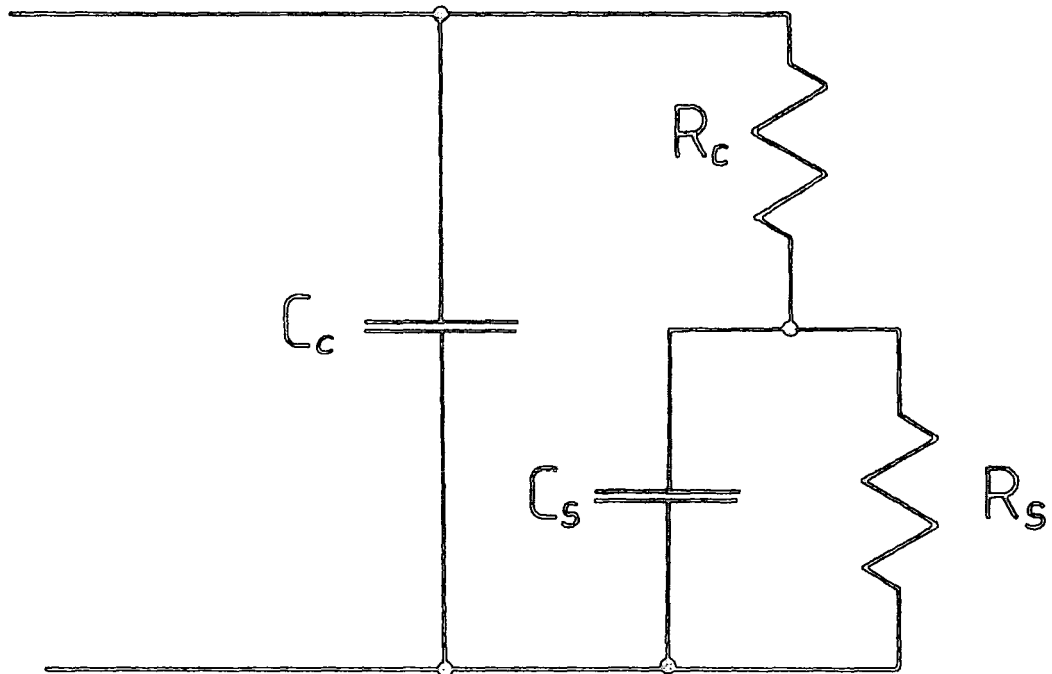


Figure 2.8 : Device equivalent circuit incorporating additional contact and series resistance components.

In this case, the additional components  $R_c$  and  $C_c$  represent the contact components. From this circuit, the equivalent parallel components are ;

$$R_p = R_c + \frac{R_s}{1 + \omega^2 \tau_R^2} \quad (2.35)$$

$$C_p = C_c + \frac{\left[ \frac{R_s}{R_c + R_s} \right]^2 C_s}{1 + \omega^2 \tau_C^2} \quad (2.36)$$

where

$$\tau_R^2 = \frac{C_s^2 R_s^2 R_c}{R_s + R_c} \quad (2.37)$$

$$\tau_C^2 = \frac{C_s^2 R_s^2 R_c^2}{(R_c + R_s)^2} \quad (2.38)$$

Under normal conditions,  $R_s \gg R_c$  (if any sensible results are to be obtained), therefore  $\tau_R$  and  $\tau_C$  can be reduced to

$$\tau_R = C_s (R_s R_c)^{\frac{1}{2}} \quad (2.39)$$

$$\tau_C = C_s R_c \quad (2.40)$$

Using Equations 2.35 and 2.36, it is now possible to look at the frequency behaviour of the overall circuit, in three main regions :

I. Low frequency :

$$\omega^2 < 1/C_s^2 R_s R_c \quad (\omega < 1/\tau_R) \quad (2.41)$$

$$R_p = R_s \quad (2.42)$$

$$C_p = C_c + C_s \quad (2.43)$$

II. Medium frequency :

$$\omega^2 \cdot 1/C_s^2 R_s R_c \ll \omega^2 \ll 1/C_s^2 R_c^2 \quad (2.44)$$

$$1/\tau_R \ll \omega \ll 1/\tau_C$$

$$R_F = 1/\omega^2 C_s^2 R_c \quad (2.45)$$

$$C_p = C_c + C_s \quad (2.46)$$

III. High frequency :

$$\omega^2 \gg 1/C_s^2 R_c^2 \quad (\omega \gg 1/\tau_C) \quad (2.47)$$

$$R_F = R_c \quad (2.48)$$

$$C_p = C_c + C_s/\omega^2 \tau_C^2 \quad (2.49)$$

Thus it can be seen that in the low frequency range, conductance is controlled by the sample ( $1/R_s$ ), and in the absence of any other influence will be frequency independent. For mid-range frequencies, however, the conductance becomes sample independent and shows an  $\omega^2$  relationship. The actual transition point is defined largely by the physical values of the structure, but it must occur somewhere, even if it is outside the normal measurement range. It should be noted from these expressions that only the high frequency band has any direct frequency dependence of the capacitance, and that this is normally outside the applied range of measurement.

## 2.5 METAL-INSULATOR-SEMICONDUCTOR STRUCTURES (MIS)

Initial interest in MIS devices and their characterisation originated from a need to understand the surface properties of silicon. To this end, Grove et al<sup>(17)</sup> were probably the first to provide a reasonable picture of this new type of device ; both theoretically and experimentally. Following this early work, progressively more complex models have been developed to explain the wide variety of observed properties, and the problems caused by impurities, surface states and other non-idealities. More recently, the availability of  $\text{III}\cdot\text{V}$  and  $\text{II}\cdot\text{VI}$  semiconducting materials has led to the expansion of MIS physics, as investigations into these other systems are undertaken. It should be noted, however, that virtually all the techniques and models used for MIS interpretation up to now, have been developed mainly from the Si/SiO<sub>2</sub> system, and as yet no specific models have been produced for these newer structures. In consequence, in spite of the majority of later work being carried out on the novel InP/Langmuir film system , the models used and presented here are better proven on the Si/SiO<sub>2</sub> system.

The first part of this section looks at the ideal behaviour of the MIS system, this is followed by consideration of the various effects which can cause deviation from this ideal behaviour and some of the methods available to characterise them.

### 2.5.1 The Ideal MIS Structure

A schematic representation of an MIS device is given in Figure 2.11, showing the use of a metal electrode on top of the insulating dielectric layer. This layer is normally thicker than 100 Å to avoid any tunnelling effects which tend to complicate the subsequent data interpretation. This type of device is therefore a voltage or field controlled structure, rather than systems like a junction transistor which are current controlled. Under conditions of thermal equilibrium [ Figure 2.9 ] the Fermi levels are aligned, and if the respective work functions of each component are similar then no initial band bending will occur.

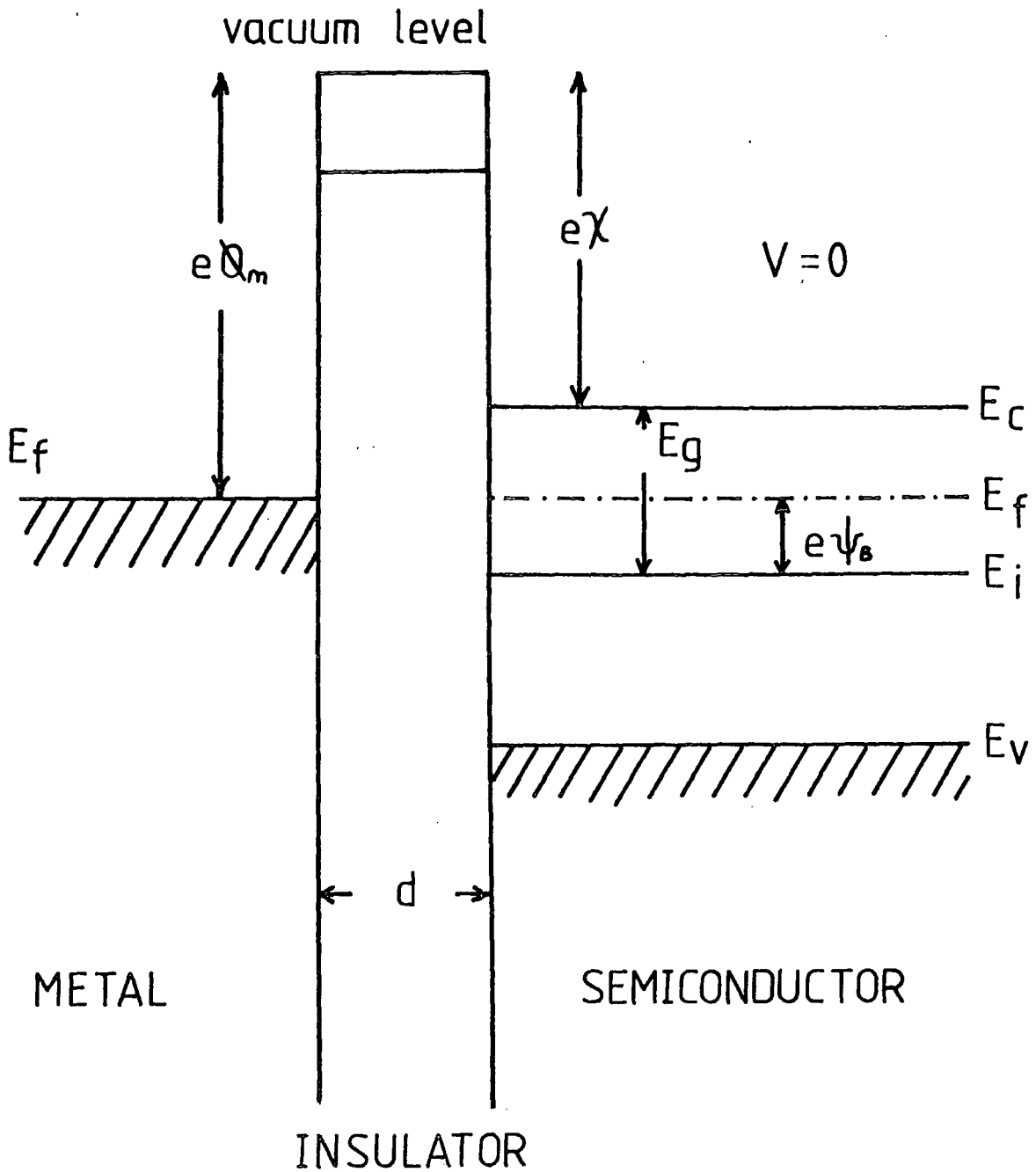


Figure 2.9 : Zero bias energy band diagram for ideal MIS (n-type) device.

Upon the application of positive voltage (on an n-type substrate) to the top electrode, electrons are accumulated at the semiconductor surface, and its bands are bent downwards [ Figure 2.10a ]. The high density of charge on the metal and semiconductor surfaces cause all the applied bias to be dropped across the insulator, and in this condition the device is accumulated. A small negative (or reverse) <sup>\*</sup> bias repels electrons from the semiconductor surface leaving a fixed space charge of ionised donors ; this is known as depletion [ Figure 2.10b ]. In this situation the semiconductor bands are bent upwards and the surface Fermi level approaches the mid-band gap position. A further increase of negative bias causes the onset of inversion (Figure 2.10c), where the Fermi level now moves into the lower half of the band gap. Thus it can be seen that it is the deviation of the extrinsic Fermi level at the surface from the bulk value that defines the state of the device. The difference in the two values is termed the surface potential ( $\psi_s$ ), and although it closely follows the applied bias in the ideal case, a great many influences occur in the real device that break this linearity. By considering the variation of ( $\psi_s$ ) into the bulk of the material, it is possible from Poisson's equation to find the change in charge density through the substrate for various values of bias. This semiconductor charge must be mirrored in the electrode, and so with an insulator separating these two there will be a small signal capacitance associated with each value of ( $\psi_s$ ). Thus a plot of capacitance against applied bias provides an excellent method of directly recording the state of the device. An idealised C-V plot is given in Figure 2.11, clearly showing the capacitance associated with each region of applied bias. In accumulation the capacitance is constant and defined by the insulator thickness, whereas in depletion an additional term is added due to the depletion layer capacitance. This latter term is obviously voltage dependent and so the total capacitance

\* In general accumulation is caused by a forward bias, and depletion/inversion by a reverse bias. Thus, for n-type substrates forward bias is a positive voltage on the top electrode, but for p-type ones it is negative.



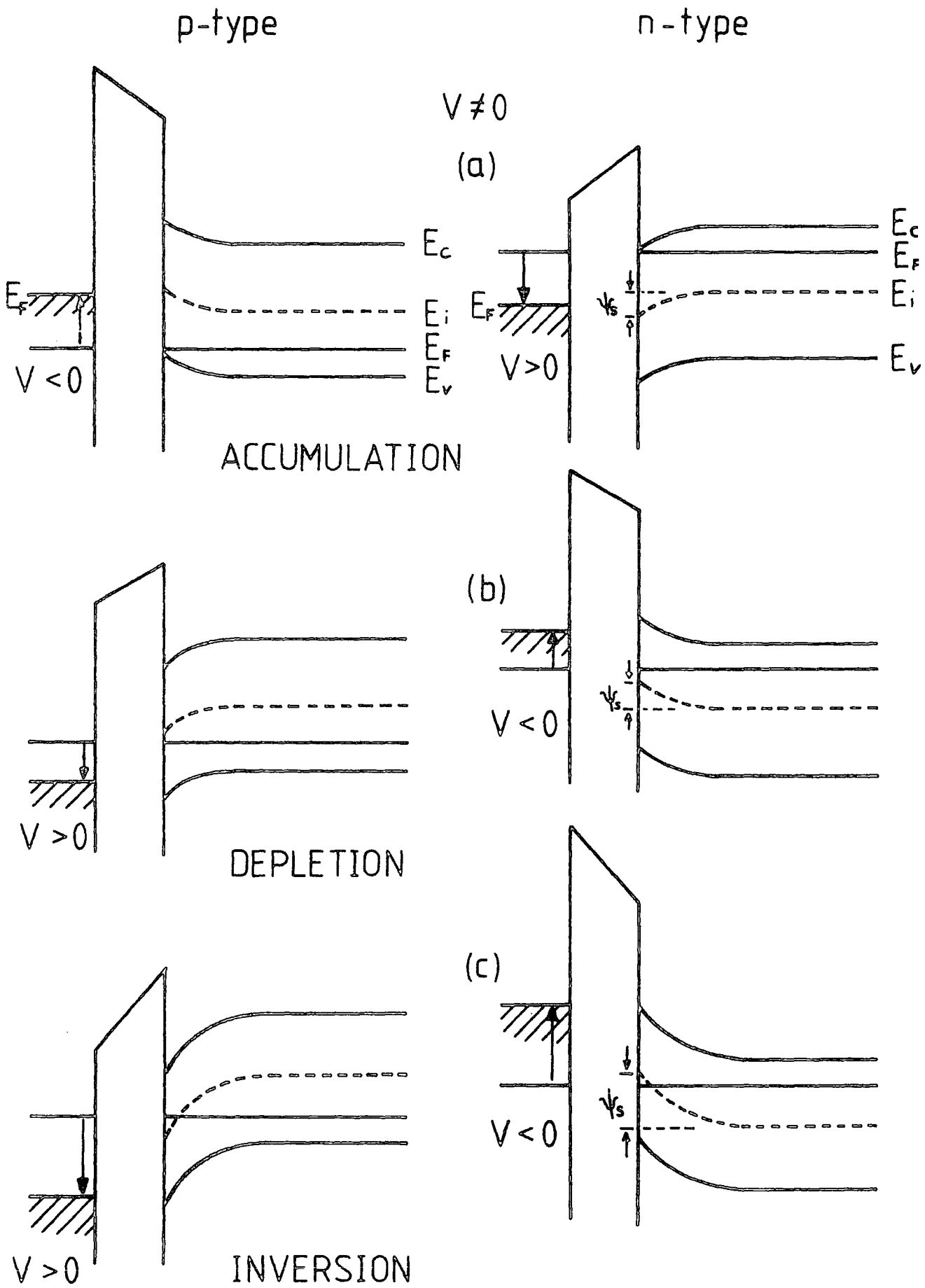


Figure 2.10 : Energy band diagram for ideal MIS device under various bias conditions.

value is seen to decrease with increased reverse bias. For the inversion region it is found that two situations can exist, depending largely upon the bias frequency. The formation of an inversion layer involves not only the bulk generation of holes and their transport to the surface region, but also the removal of electrons further into the bulk to extend the depletion layer. The former of these two processes is by far the slowest, due to the low mobility of holes. In consequence, if the applied bias frequency is too high the holes cannot respond, and no charge exchange between the bulk and the surface inversion layer takes place. In this case the measured capacitance merely shows an eventual levelling off as the depletion region is prevented from widening by the shielding of the inversion layer. At lower frequencies, however, the minority carriers can respond to the applied signal, allowing charge to be pumped into and out of the surface region. The resultant capacitance is now seen to rise back to the accumulation value. It is also possible to avoid the inversion regime altogether. In this case, called deep depletion, the capacitance continues to decrease beyond the normal minimum value due to the applied signal frequency being too high for the inversion layer to form at all. This situation can also be induced if the insulator is leaky and allows charge exchange to remove the inversion region as it forms. From the knowledge of the behaviour of the device, it is possible to produce simple equivalent circuits to model this ideal response, as shown in Figure 2.11.

The ideal C-V characteristics can be shown to have certain critical parameters which closely define the device behaviour: the flat band capacitance, occurs where the surface potential ( $\psi_s$ ) is zero, and the semiconductor bands are therefore flat. In an ideal device, this will occur at zero bias, and is given by ;

$$C_{FB} = \frac{\epsilon_r \epsilon_0}{d + \frac{\epsilon_r}{\epsilon_s} \sqrt{\frac{kT}{e^2 N_D} \epsilon_s \epsilon_0}} \quad (2.50)$$

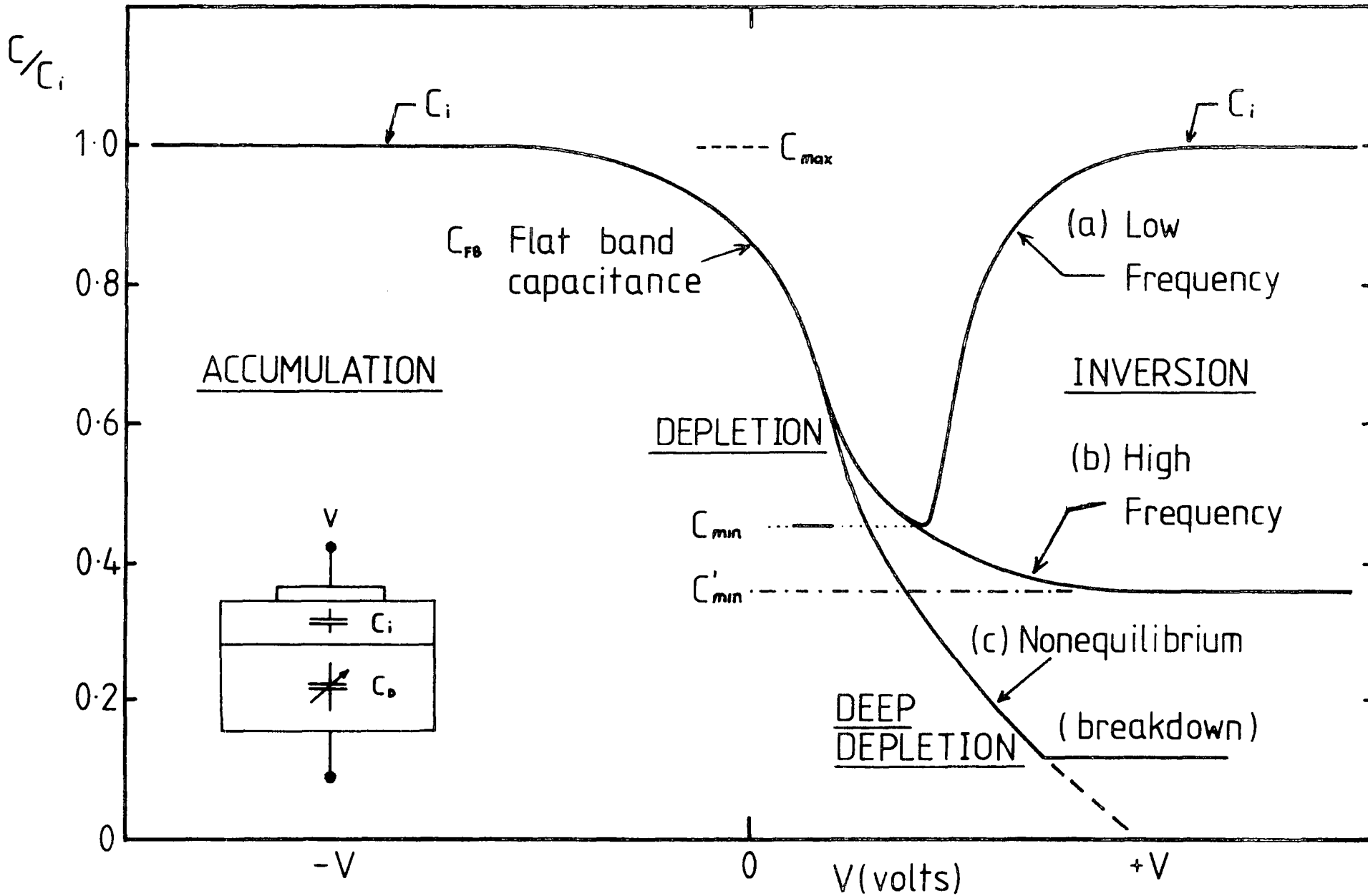


Figure 2.11 : Idealized MIS capacitance-voltage curves (for p-type material).

where  $\epsilon_r$  and  $\epsilon_s$  are the relative permittivities of the insulator and semiconductor respectively, and  $d$  is the insulator thickness. Also important are the maximum and minimum values of capacitance ;

$$C_{\max} = \frac{\epsilon_r \epsilon_0}{d} \quad (2.51)$$

$$C_{\min} = \frac{\epsilon_r \epsilon_0}{d + \frac{\epsilon_r}{\epsilon_s} W_m} \quad (2.52)$$

where  $W_m$ , the depletion layer width is given by ;

$$W_m = \sqrt{\frac{4 \epsilon_0 \epsilon_s kT \ln(N_D/n_i)}{e^2 N_D}} \quad (2.53)$$

and  $n_i$  is the intrinsic carrier density. Thus from these expressions it can be seen that ;

$$\frac{C_{\max}}{C_{\min}} = 1 + \frac{W_m \epsilon_r}{d \epsilon_s} \quad (2.54)$$

It should be noted that so far this discussion has dealt only with device capacitance. Under ideal conditions, the conductance will be zero throughout the bias range. It is only when practical loss mechanisms are included in the model that any significant structure appears in the G-V plot.

### 2.5.2 Modelling Real Devices (1): Surface State Effects

In real devices, there are many effects which lead to deviation from the previously mentioned ideal behaviour. These will be considered in two separate sections ; the first one dealing with the effect of interface states, and the second dealing with the remaining significant effects.

The covalent structure of most semiconductors being considered here, prohibits the formation of a perfectly abrupt junction at the interface with

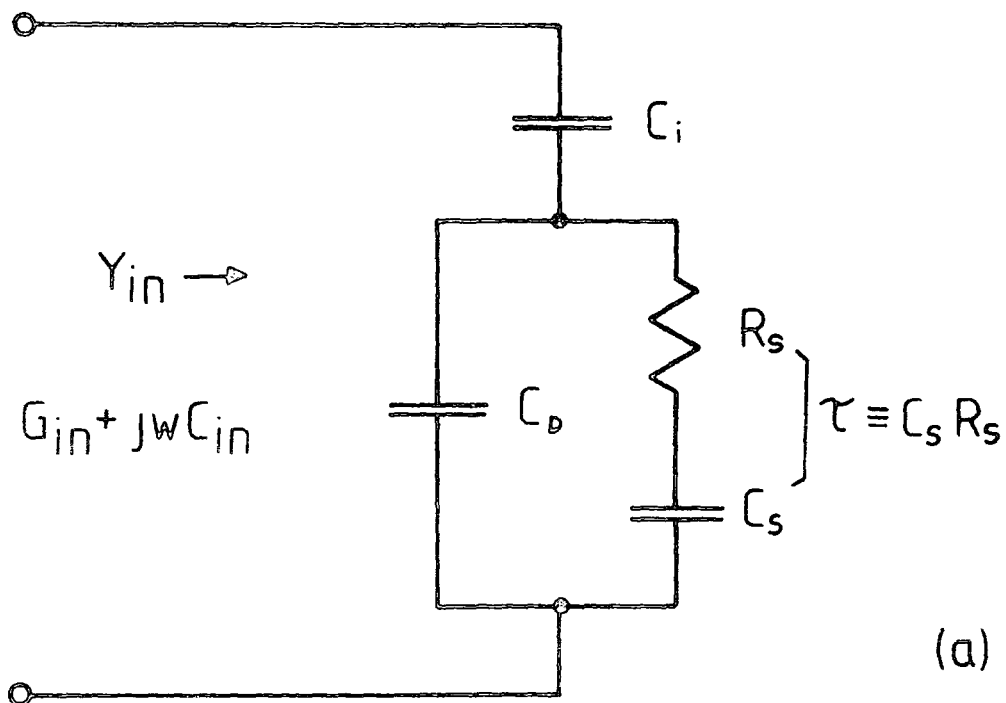
the insulator. The resulting diffuse interruption of the lattice has been proposed<sup>(18-21)</sup> to leave dangling bonds and vacancies which give rise to energy levels within the band gap. The existence of these surface states was first shown experimentally by Shockley and Pearson<sup>(22)</sup> in their surface conductance measurement on Si/SiO<sub>2</sub>. Later work<sup>(23)</sup> on clean surfaces in ultra high vacuum confirmed this inherently high density of states ; of the order of the density of atoms at the semiconductor surface.

Surface states can be either donors or acceptors depending upon their atomic origin . Their condition at any particular bias is defined largely by their location in the band gap, and the relative position of the Fermi level. When this voltage is varied, the Fermi level will effectively sweep up or down the band gap and so change the state of any defect it passes. This exchange of charge with the states contributes to the total MIS capacitance and conductance and so will cause deviations from the ideal behaviour. By modelling this effect with extra components in the equivalent circuit it is possible to obtain useful information about the behaviour of this interface region.

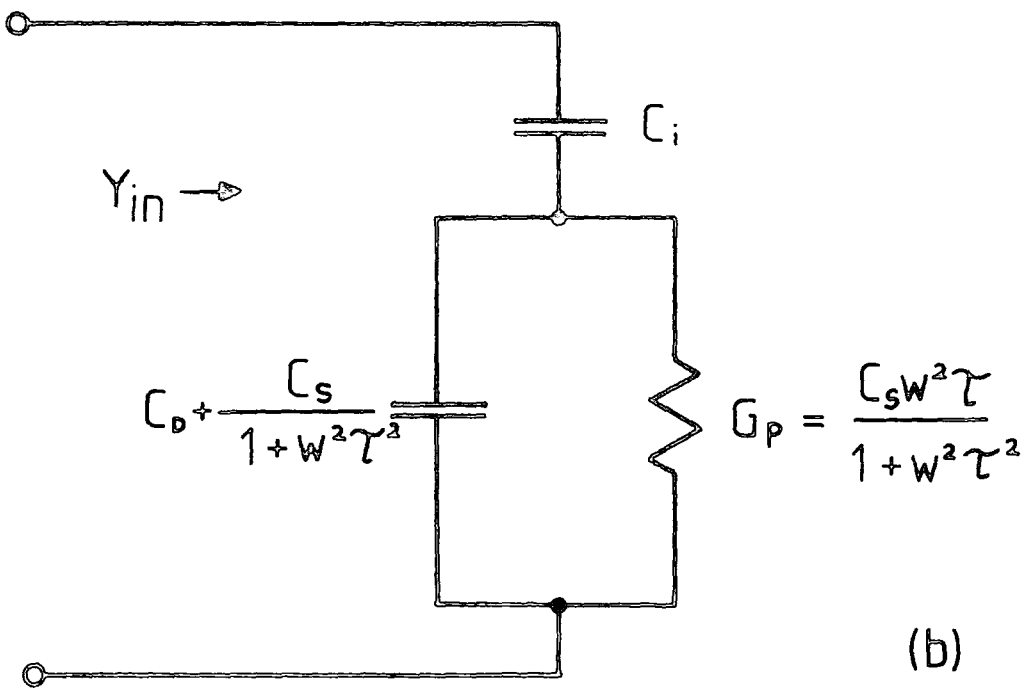
The simplest consideration of surface states involves assuming the effects are due to a single level in the band gap, and can thus be represented by an extra capacitance C<sub>s</sub>, and resistance R<sub>s</sub> in parallel with the original depletion layer capacitance. The resulting circuit is given in Figure 2.12, where the lower model represents an equivalent rearrangement to give a two branch network in series with the insulator capacitance. In this case C<sub>p</sub> and G<sub>p</sub> are the parallel frequency dependent components that can be obtained directly from the measured admittance.

$$C_p = C_D + \frac{C_s}{1 + \omega^2 C_s^2 R_s^2} \quad (2.55)$$

$$\frac{G_p}{\omega} = \frac{C_s^2 R_s \omega}{1 + \omega^2 C_s^2 R_s^2} \quad (2.56)$$



(a)



(b)

Figure 2.12 : Device equivalent circuits incorporating surface state components ( $R_s, C_s$ ).

The measured admittance for both circuits is given by ;

$$Y_{in} = G_{in} + j\omega C_{in} \quad (2.57)$$

where

$$G_{in} = \frac{\omega^2 C_s^2 R_s C_i^2}{(C_i + C_D + C_s)^2 + \omega^2 R_s^2 C_c^2 (C_i + C_D)^2} \quad (2.58)$$

$$C_{in} = \frac{C_i}{C_i + C_D + C_s} \left[ C_D + \frac{C_s (C_i + C_D + C_s)^2 + C_D^2 R_s^2 C_s^2 (C_i + C_D)}{(C_i + C_D + C_s)^2 + R_s^2 C_c^2 (C_i + C_D)^2} \right] \quad (2.59)$$

It can be seen that both these expressions contain surface state information ( $C_s$  and  $R_s$ ), and so it is possible to use either for the purposes of analysis. In practice the capacitance is easier to measure but is the combination of insulator and depletion components as well as  $C_s$ , making the extraction of surface state information relatively inaccurate, as shown in Figure 2.13. By contrast, the conductance data, although being harder to measure, contains only surface state data and so can lead to a more accurate result. The use of  $G_m$  data also involves considerably more processing to obtain a final surface state density plot.

In practice, although this single level model serves as a very good introduction to surface state modelling, it is far from adequate. It was quickly realised by early workers therefore that the real interface region gave rise to a large number of states within the gap, all of different energy, time constant, and capture cross section. In consequence, various additional equivalent circuits were proposed in an attempt to model this behaviour. Of particular significance in this area was the work of Lehovc and Slobodskoy<sup>(24)</sup>, who proposed an extremely complex circuit, representing each different mode

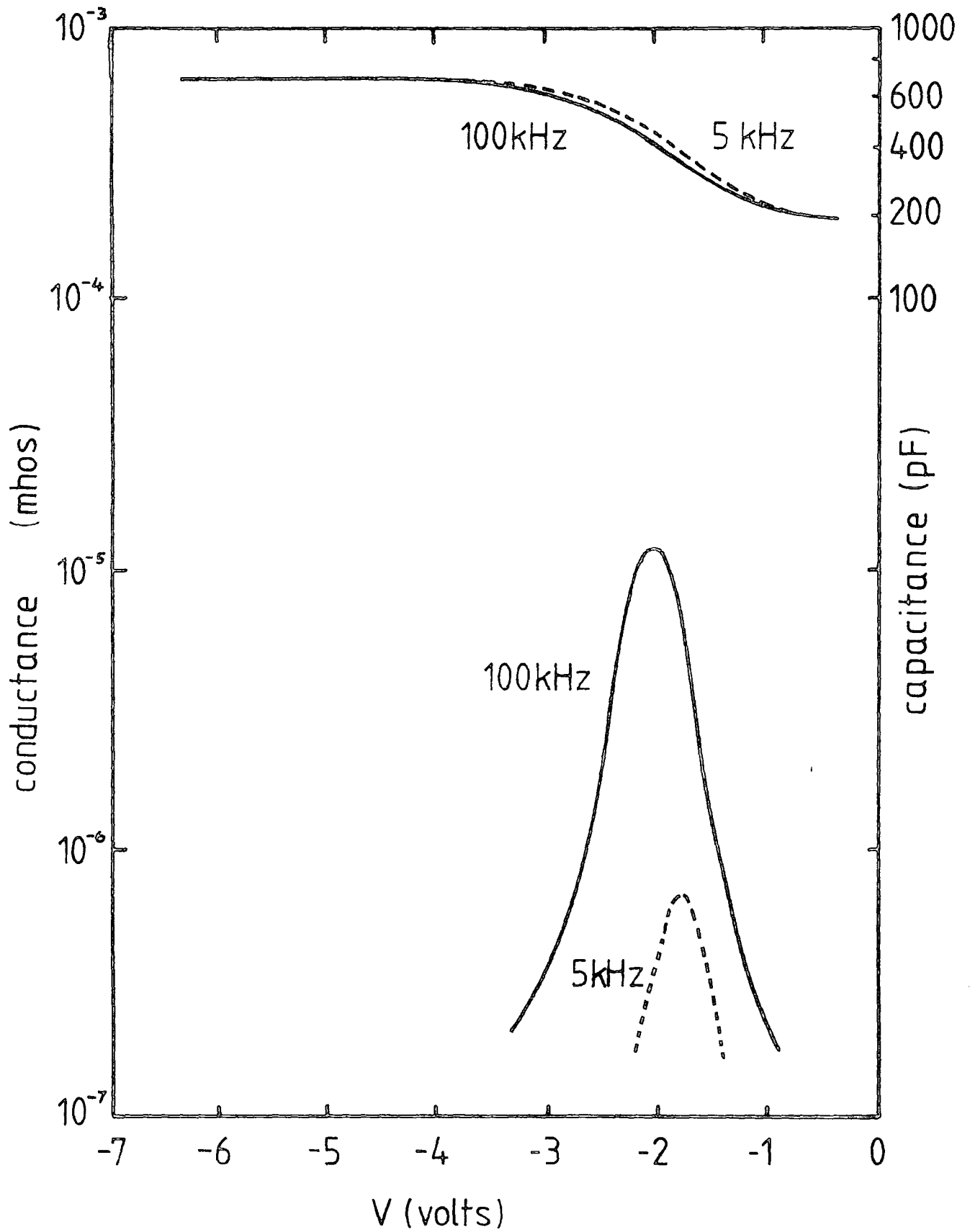


Figure 2.13 : Comparison of surface state effects on capacitance and conductance data (After Nicollian & Goetzberger, Ref.25).



of the device with RC networks. Some time later, together with their proposition of the conductance technique, Nicollian and Goetzberger<sup>(25)</sup> proposed the representation of each level by a single RC network, thus producing a long parallel chain of RC components. Although better, even this approach was not perfect as their resultant equations did not fit the practical results. This model, however, with some modifications to account for time constant dispersion, and variation in surface potential (discussed later), is the one still used by many workers.

(a) Analysis of the Capacitance Curve

The majority of early methods of surface state investigation looked at capacitance data only, and ignored the existence of any device conductance. In consequence the assumed equivalent circuit has only capacitive surface state components, originating from the trapped charge, and it is thus irrelevant whether single or multistate models are proposed. In general, all capacitance methods look at shifts in the ideal curve, and relate this to the existence of surface state charge. From this value of charge at each point on the voltage scale, a value of the number of states per unit area can be obtained. In practice, surface state density ( $N_{ss}$ ) is normally expressed as states/unit area/eV and it is thus often necessary to numerically differentiate the initial plot to obtain the desired values. In addition, it is also conventional to express this spectrum as a function of position in the band gap, rather than against applied bias. This requirement involves rescaling the bias to surface potential ( $\psi_s$ ) and then to band gap energy.

The simplest method to achieve this conversion was developed by Berglund<sup>(26)</sup>, who used numerical integration of the normal capacitance-voltage curve to directly generate  $d\psi/dV$ . This method requires that the surface states are at all times in equilibrium with the applied bias, and thus uses a very

low frequency signal. Berglund showed that ;

$$\frac{d\psi_s}{dV} = 1 - \frac{C(V)}{C_i} \quad (2.60)$$

where  $C(V)$  is the measured capacitance, and thus by integrating this expression we have ;

$$\psi_s(1) - \psi_s(2) = \int_{V_1}^{V_2} \left[ 1 - \frac{C(V)}{C_i} \right] dV \quad (2.61)$$

For this expression,  $\psi_2$  is normally evaluated for a voltage in strong accumulation, and can thus be approximated to zero.

#### Differential Method

The differential procedure of surface state measurement was first developed by Terman<sup>(27)</sup>, and relies upon the simple comparison of high and low frequency capacitance curves, as illustrated in Figure 2.14. The former plot is evaluated at a very high frequency where no surface states can respond ; it is thus taken to be ideal. The latter low frequency curve is then found to be shifted from the ideal, by different amounts along its length, all assumed to be due to interface state charge. From the difference in these two curves a plot of  $\Delta V$  (shift from ideal) against  $V$  (applied bias) can be obtained. The total charge in the states at any particular bias is given by ;

$$Q_{ss} = C_i (\Delta V) \quad (2.62)$$

where  $C_i$  is the insulator capacitance, and thus the surface density of states is ;

$$N_{ss} = \frac{Q_{ss}}{e} = \frac{C_i}{e} (\Delta V) \quad \text{states/unit area} \quad (2.63)$$

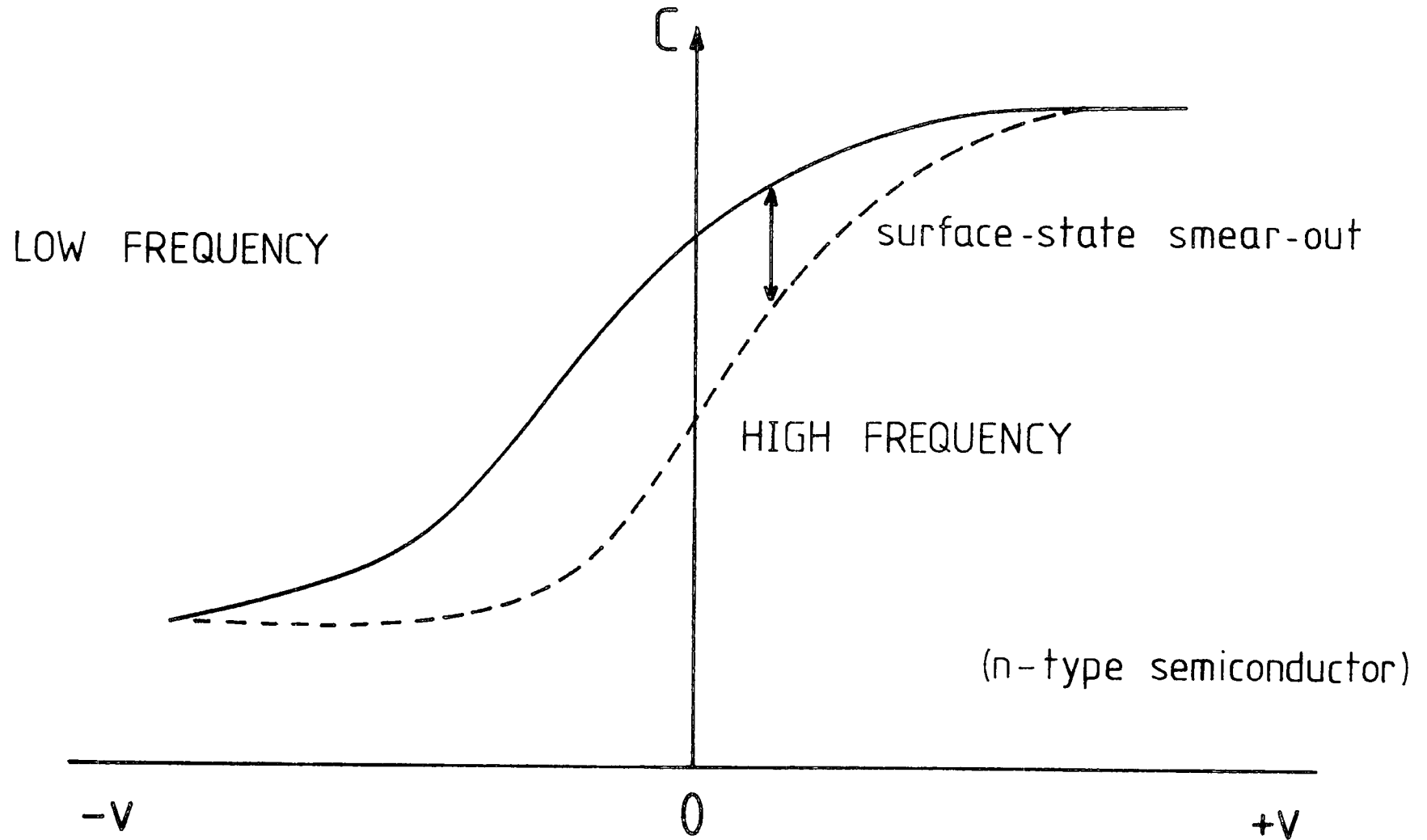


Figure 2.14 : High and low frequency capacitance curves illustrating additional effect of surface states.

or more correctly

$$N_{ss} = \frac{1}{e} \left( \frac{d Q_{ss}}{d \psi_s} \right) \quad \text{states/unit area/eV} \quad (2.64)$$

### Temperature Method

Another method of interpreting capacitance data was proposed by Gray and Brown<sup>(28)</sup>, and uses the variation of the temperature of a device as the means of moving the Fermi level. As the ambient temperature is increased the gradual upward movement of the Fermi level through the band gap leads to a progressive shift of the C-V curve, but no band bending occurs under ideal conditions. Thus the flat band voltage is always zero. In the presence of surface states, the downward motion of the Fermi level uncovers additional charge as the various defects change state. This charge leads to band bending in the semiconductor, and a subsequent shift in the flat band voltage. The experimental procedure thus consists of varying the temperature and noting the voltage required to maintain the flat band condition. To obtain a surface state plot, the temperature is converted to Fermi level position (and thus surface potential), and the voltage shift to corresponding surface state charge. This technique was widely used during the early era of interface characterisation, but has now fallen from favour, as recent work has shown that additional device parameters are temperature dependent, and so lead to errors in result interpretation. In consequence, the peaks in  $N_{ss}$  initially obtained by Gray and Brown at the band edges are merely manifestations of capture cross section variation, and are not real effects. This method therefore gives reliable results only in the mid-gap region, but here the values of shift are very small, and thus extremely difficult to measure.

### Quasi-static Method

The quasi-static technique was developed by Kuhn<sup>(29)</sup> in 1970, and uses a slightly more complex equivalent circuit derived from that presented

by Lehovec and Slobodskoy<sup>(24)</sup>. This technique essentially produces a DC capacitance-voltage plot, obtained by applying a slow ramp to the sample and measuring the subsequent displacement current ; this is given by

$$I = C \frac{dV}{dt} , \tag{2.65}$$

since  $\frac{dV}{dt}$  is constant, the output current will directly follow the variation in capacitance. The resultant output curve is similar to the normal low frequency AC type plot. Under these slow ramp conditions, both the minority carriers and the surface states can stay in thermal equilibrium, and so the device can be represented by a simplified equivalent circuit, as given in Figure 2.15. Where  $C_{SS}$  is the surface state capacitance,

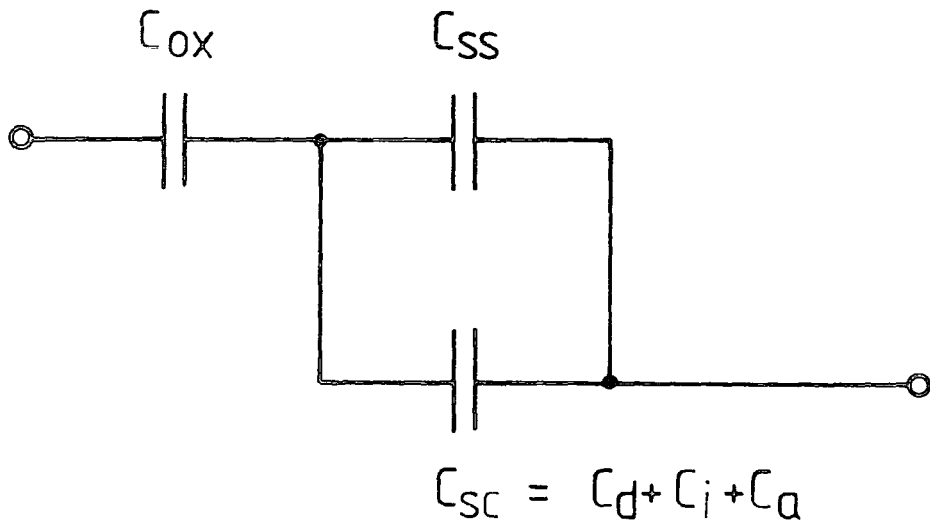


Figure 2.15 : Quasi-static equivalent circuit.

and  $C_{sc}$  represents a parallel combination of depletion, inversion, and accumulation capacitance (some of which may be zero). From this model, it can be seen that the measured capacitance  $C(v)$  is given by ;

$$\frac{1}{C(v)} = \frac{1}{C_i} + \frac{1}{C_{sc} + C_{ss}} \tag{2.66}$$

and thus the surface state density is given by

$$N_{ss}(\psi_s) = \frac{C_{ss}}{e} (\psi_s) = \frac{1}{e} \left[ \frac{C(V)}{1 - \frac{C(V)}{C_i}} - C_{sc}(\psi_s) \right] \quad (2.67)$$

where  $C_{sc}(\psi_s)$  is obtained from ideal MIS curves.

In addition, if the curve is only considered in depletion/accumulation, then the effect of the inversion capacitance can be ignored, and the expression simplified. The approach was first suggested by Castagne<sup>(30)</sup> and generates an expression for surface state density of ;

$$N_{ss} = \frac{C_{ss}}{e} \left[ \frac{C_{LF} C_i}{C_i - C_{LF}} - \frac{C_{HF} C_i}{C_i - C_{HF}} \right] \quad (2.68)$$

where  $C_{LF}$  and  $C_{HF}$  are simply the capacitance values for high and low frequency (i.e. with and without surface states). This method, although even simpler, only gives  $N_{ss}$  values over a relatively small range of the band gap, and so is useful only for certain applications.

These techniques, in general, are relatively easy to implement and as yet have shown none of the drawbacks of the previously mentioned ones. In consequence the initial one in particular is widely used as a simple method of obtaining surface state data.

#### Other Methods

It should perhaps be noted before concluding this section that direct interpretation of MIS capacitance curves is not the only means of obtaining information about surface states. Indeed, there are a whole group of temperature orientated approaches which look at the thermal excitation of carriers from trapping levels. These techniques in general were designed to investigate mainly bulk traps in a material, but can be used for surface traps as well. In particular, deep level transient spectroscopy (DLTS)<sup>(31)</sup> is rapidly becoming

a standard approach to supplement PSD measurement techniques.

Briefly, the Schottky barrier or MIS device is biased into depletion and narrow forward bias spikes are superimposed on this steady voltage. The resultant impulse of majority carriers are initially trapped in the depletion layer states, and are then slowly released during the time between pulses. Thus by monitoring the escape of these carriers as a function of time, temperature, and depletion layer width, a profile of the trapping states can be obtained.

#### (b) Analysis of the Conductance Curve

The conductance technique was first developed and applied to surface state characterisation by Nicollian and Goetzberger<sup>(25)</sup>. Its advantage over the various capacitance methods lies in the direct dependence of the conductance data on interface state density. The observed peak in this component is produced by steady state loss mechanisms originating from surface state carrier exchanges. In consequence, the spectra obtained from the conductance technique are considerably more accurate than from corresponding capacitance data.

#### Single Level Model

If we consider initially the simple single state model for surface defects, then the analysis procedure can be outlined as follows : The sample insulator capacitance is initially evaluated from the accumulation region of the C-V curve, and then subtracted from the equivalent circuit in Figure 2.12a. This is achieved through conversion to an equivalent impedance arrangement. The operation is now repeated for data at many different frequencies, but all at the same bias. From this data plots of  $\frac{G}{\omega}$  and  $C_p$  against  $\omega$  can be obtained, as shown in Figure 2.16.

In this simple model the single level of interface states are characterised by additional resistance and capacitance components  $R_s$  and  $C_s$ . The product of these two values has units of time, and can thus conveniently be

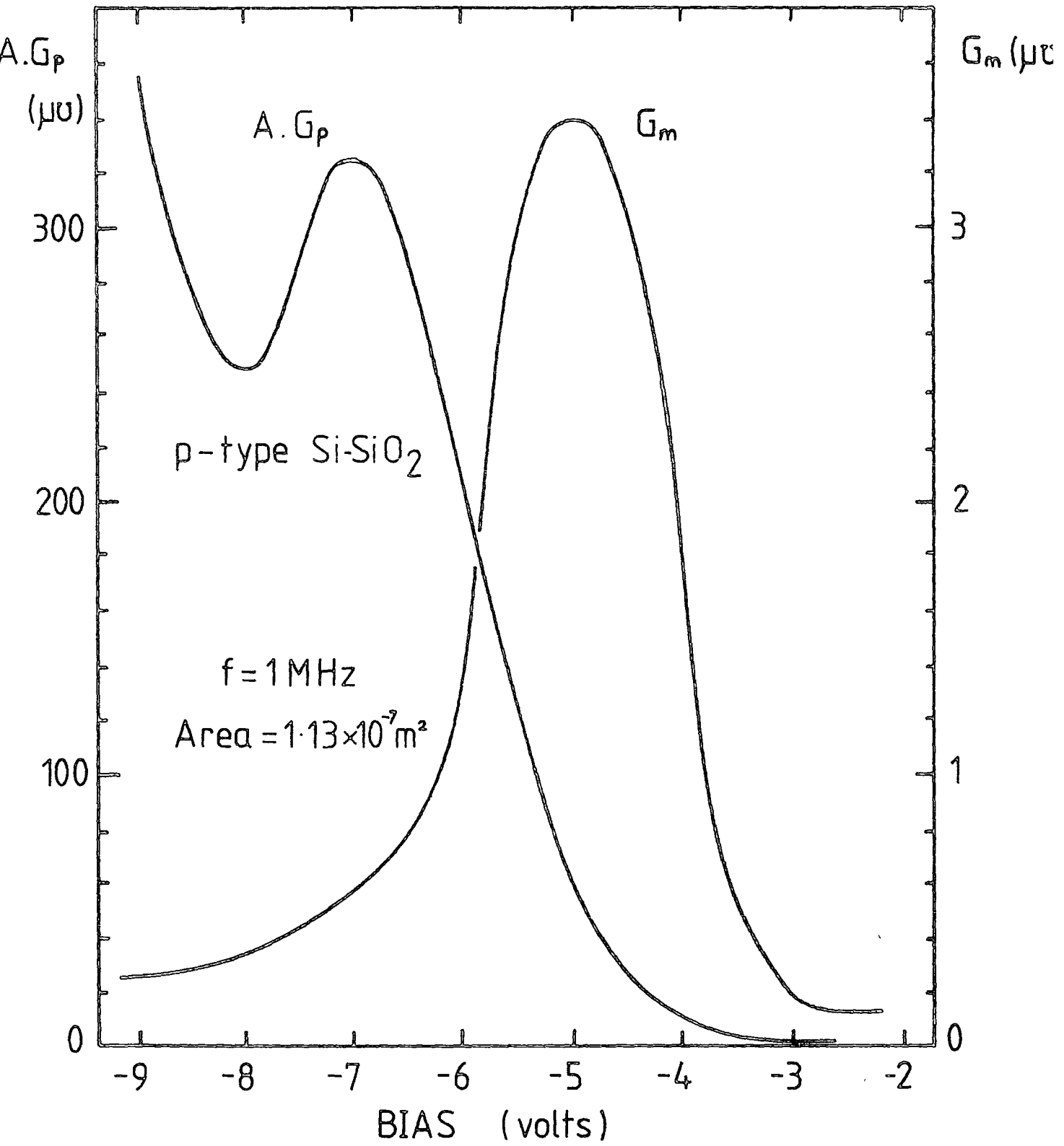


Figure 2.16 : Sample device data showing  $G_m$  and  $G_p$  peaks as a function of applied bias (After Warashina and Ushirokawa, Ref. 35).



defined as the time constant  $\tau$  of this level. The value of this product can be considered as determining the frequency response of these states. With this new term, equations 2.55 and 2.56 can be re-written as ;

$$C_p = C_D + \frac{C_s}{1 + \omega^2 \tau^2} \quad (2.69)$$

$$\frac{G_p}{\omega} = \frac{C_s \omega \tau}{1 + \omega^2 \tau^2} \quad (2.70)$$

which now define the behaviour of the previously obtained plots. It can be seen from simple differentiation of equation 2.70, that the peak in the  $G_p/\omega$  plot occurs at  $\omega\tau = 1$ , and its height is given by  $G_p/\omega = C_s/2$ . Thus from this experimental curve, values at  $\tau$  and  $C_s$  can be measured. From these values,  $R_s$  and  $N_{ss}$  can then be obtained ;

$$R_s = \tau/C_s \quad (2.71)$$

$$N_{ss} = \frac{C_s}{eA} \quad (2.72)$$

where A is the top electrode area. These two curves give only one point on the surface state diagram, however, and so the procedure must be repeated for each different applied bias (surface potential) in order to obtain a satisfactory spectrum.

### Multi-Level Model

In practice, the inadequacy of the single level model is immediately shown by the experimental  $G_p/\omega$  plot being considerably broader than predicted by equation 2.70. This model was therefore adapted by Nicollian and Goetzberger to represent a continuum of states in the band gap, each characterised by a single RC network and an individual time constant ( $\tau$ ) (as previously discussed).

Even in this situation, however, the theoretical curves were found not to match the practical ones, and the model was concluded to be inadequate. After this early work, considerable investigation and modelling was undertaken in order to produce a better fit to the practical data. Among the many explanations suggested was the local variation of surface potential at the interface, [ Goetzberger<sup>(32)</sup> ], or the tunnelling of carriers from the semiconductor, different distances into traps in the interface [ Preier<sup>(33)</sup> ]. These newer models in general appear to represent the real interface better than the original ideas, but the behaviour is by no means fully understood, and detailed investigation is still being carried out.

### 2.5.3 Modelling Real Devices (2) : Other Effects

#### (a) Work function

In the initial section, it was assumed that the top contact metal had the same work function as that of the semiconductor. Normally, this is not the case, and thus some band bending will be produced even at zero bias. This results in the curves being shifted from the ideal (Figure 2.17) by an amount corresponding to the work function difference ;

$$V_{\text{shift}} = \phi_m - \left( \chi + \frac{E_g}{2e} + \psi_B \right) \quad (2.73)$$

where the term in brackets is effectively the semiconductor work function as defined in Figure 2.9.

#### (b) Temperature

The effect of temperature variation has been mentioned previously in connection with surface state analysis, where lateral shifts in the curve were explained by induced movement of the Fermi level. The other notable effect caused by a rise in temperature is an increase in the low frequency inversion capacitance, as shown in Figure 2.18. This is caused by the increase of the inversion charge generation rate, which allows the quicker

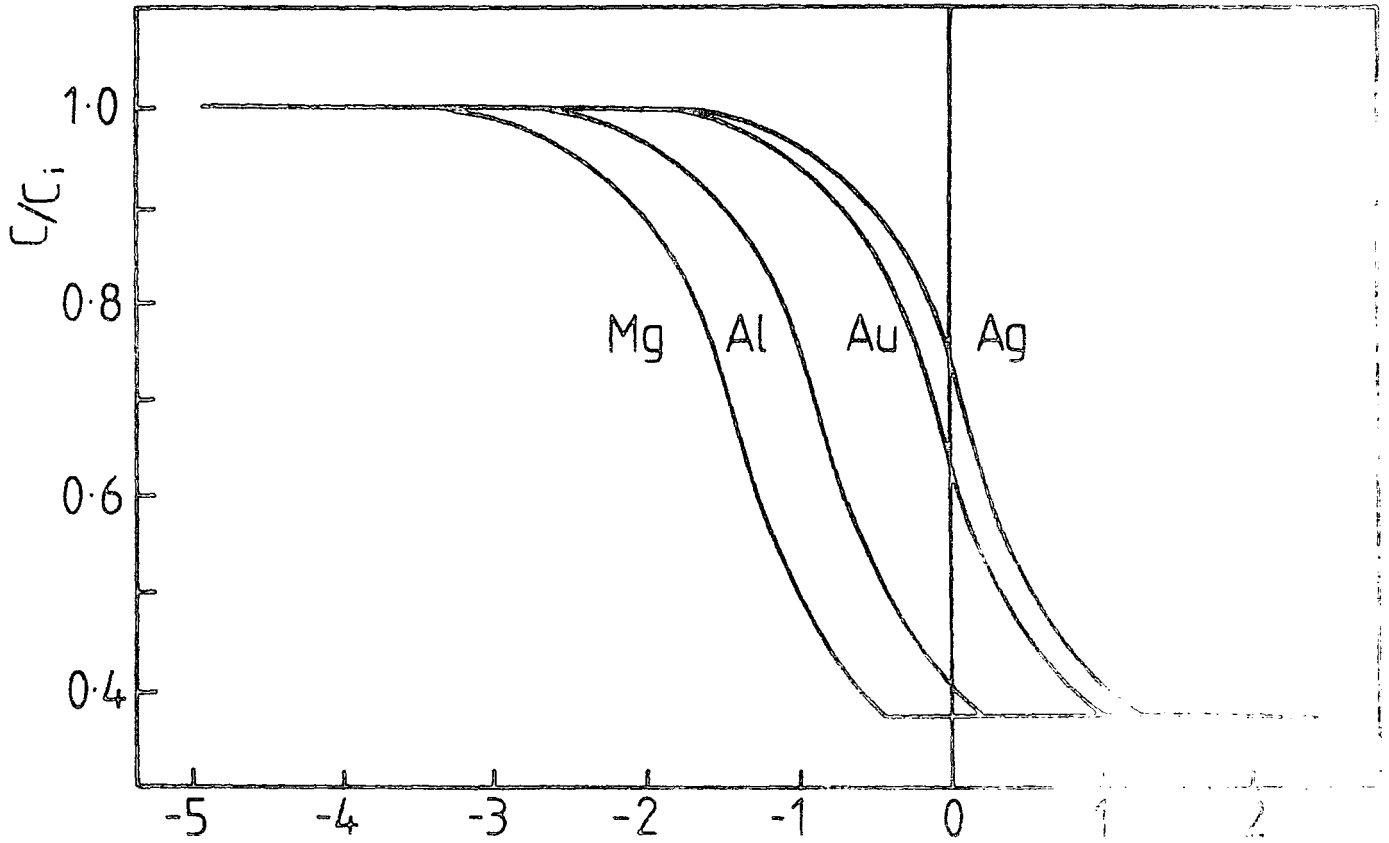


Figure 2.17 : The effect of electrode work function variation.

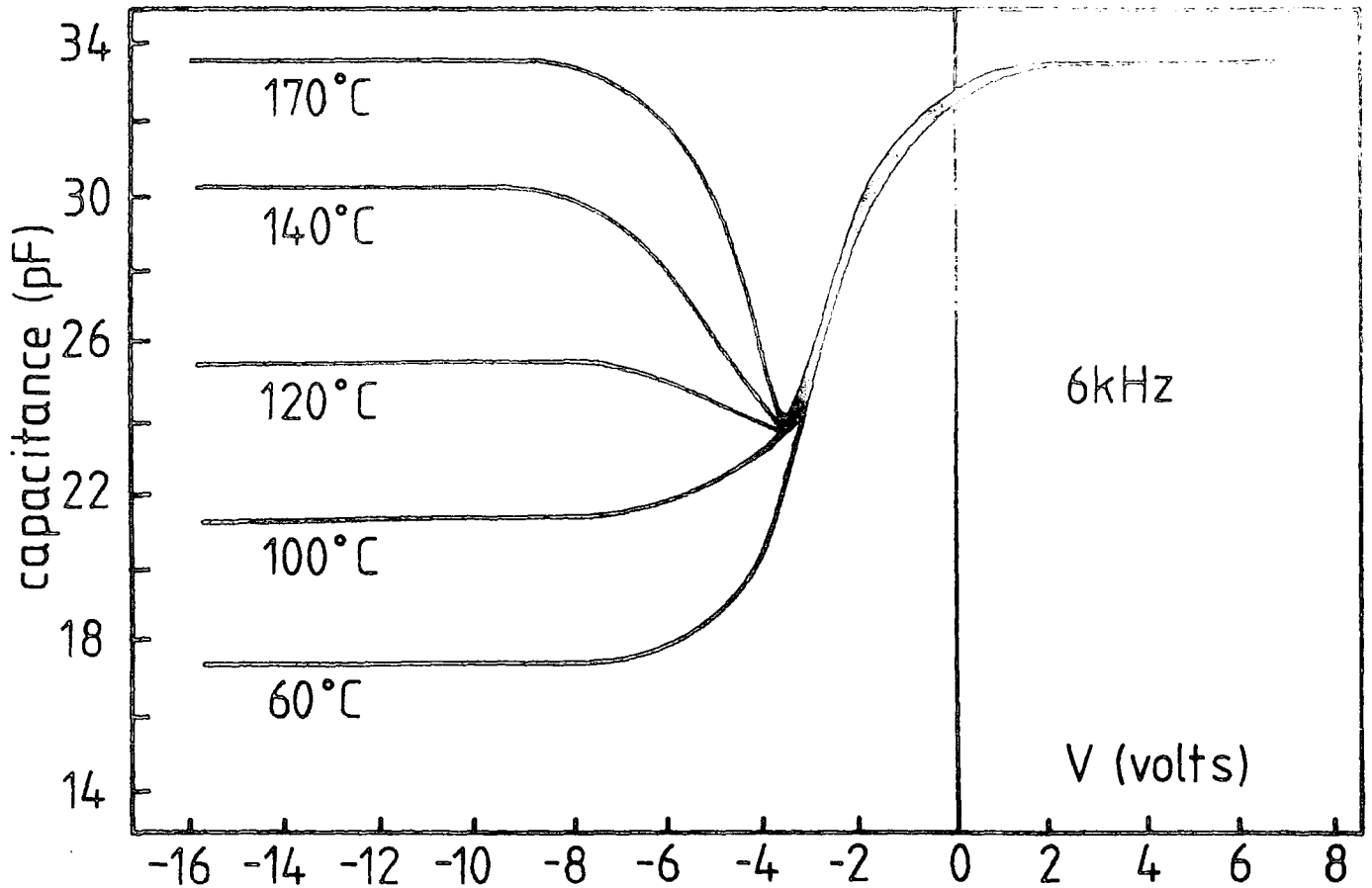


Figure 2.18 : The effect of temperature variation.

formation of an inversion layer. This in turn gives a curve corresponding to a lower frequency. Similarly, reduction of temperature produces a decrease in the inversion capacitance.

(c) Illumination

The main effect of illumination is also upon the inversion region of the curve. It produces similar effects to those noted with a decrease in temperature, by allowing full inversion to be produced at a higher carrier frequency. The effect of light is however a non equilibrium situation, as it influences only the immediate surface region of the device, thus prohibiting the application of normal analysis procedures. The extra energy supplied to the surface decreases the generation time constant of the minority carriers<sup>(17)</sup>, and increases the electron-hole pair generation rate, both of which enhance inversion layer formation. In addition, it has been shown that this latter effect gives rise to a decrease in surface potential ( $\psi_s$ )<sup>(18)</sup>, which causes a reduction in the space charge layer width, and a corresponding increase in capacitance. At relatively high frequencies the effect on the inversion layer is negligible and the surface potential variation dominates. The conductance curve is also influenced by the availability of extra carriers, which cause a considerable increase in the height of the  $G_m$  peak; even for small amounts of illumination. In practice, the use of optical band gap filters in conjunction with incident white light can be used as a simple means of distinguishing optical effects from other influences.

(d) Substrate resistance

The majority of previous considerations have assumed the active interface region to be supported by an ideal substrate. In practice, it is quite probable that the semiconductor will have a finite resistivity, which will give rise to an additional series resistance in the device equivalent circuit. This improved circuit is given in Figure 2.19.

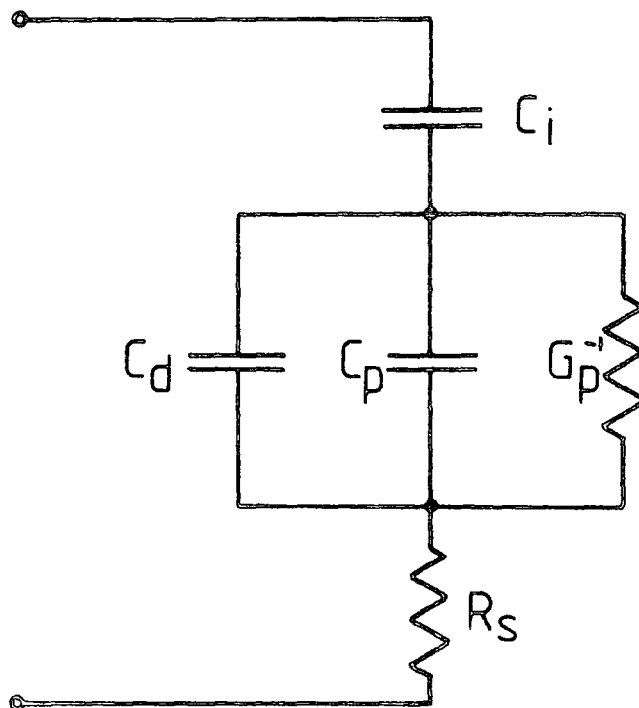


Figure 2.19 : Device equivalent circuit showing additional components for substrate resistance.

The main effect of this parasitic component is to produce an increase in the background conductance ( $G_m$ ) in the measured accumulation region. This in turn also gives a marginal variation in the measured capacitance, changing it from the insulator value ( $C_i$ ). These effects are represented by<sup>(35)</sup> ;

$$R_s = \frac{G}{(G^2 + \omega^2 C^2)} \tag{2.74}$$

$$C_i = C \left[ 1 + \frac{G^2}{\omega^2 C^2} \right] \tag{2.75}$$

where C and G are measured values of capacitance and conductance. When thick bulk grown substrates are used it is quite possible for  $R_s$  to be several tens of Ohms, and in these cases the forward bias increase in conductance will be quite substantial and may totally obscure any surface state loss peak.

Similar effects upon conductance data can be produced by bad Ohmic contacts, whereby the resultant barrier behaves somewhat like an additional series resistance. These effects are however frequency dependent and as such are considerably more difficult to separate out as a single component.

(e) Surface leakage

Under conditions of high reverse bias, and relatively high frequency, the inversion layer in a normal MIS device cannot respond to the applied signal. This causes the measured characteristics to show only the insulator and depletion layer capacitance, as outlined in section 2.41. Under certain conditions, however, a surface layer can act as a lateral conduction channel which significantly alters the device characteristics. This effect was first noted by Nicollian and Goetzberger<sup>(36)</sup> who recorded "low frequency" characteristics, at high frequencies, and a conductance plot with two peaks, as shown in Figure 2.20. These effects were caused by the use of certain oxide growth conditions which induced a layer of positive charge due to surface states at the insulator/semiconductor interface. This charge was modelled by a distributed resistance-capacitance network which could be condensed into two additional lumped components, as shown in Figure 2.20. Subsequent analysis of this circuit produced the observed characteristics, with the additional  $G_m$  peak being merely a manifestation of the component configuration. From this original investigation it can be concluded that any type of surface conduction will give rise to anomalous AC characteristics.

(f) Hysteresis

The presence of mobile charge in the insulator, either as intrinsic contamination (ions), or as injected carriers (electrons or holes), leads to time dependent lateral displacement of the device characteristics. These shifts, normally referred to as hysteresis, are one of the major problem areas of device fabrication, simply because they are so hard to quantify and analyse.

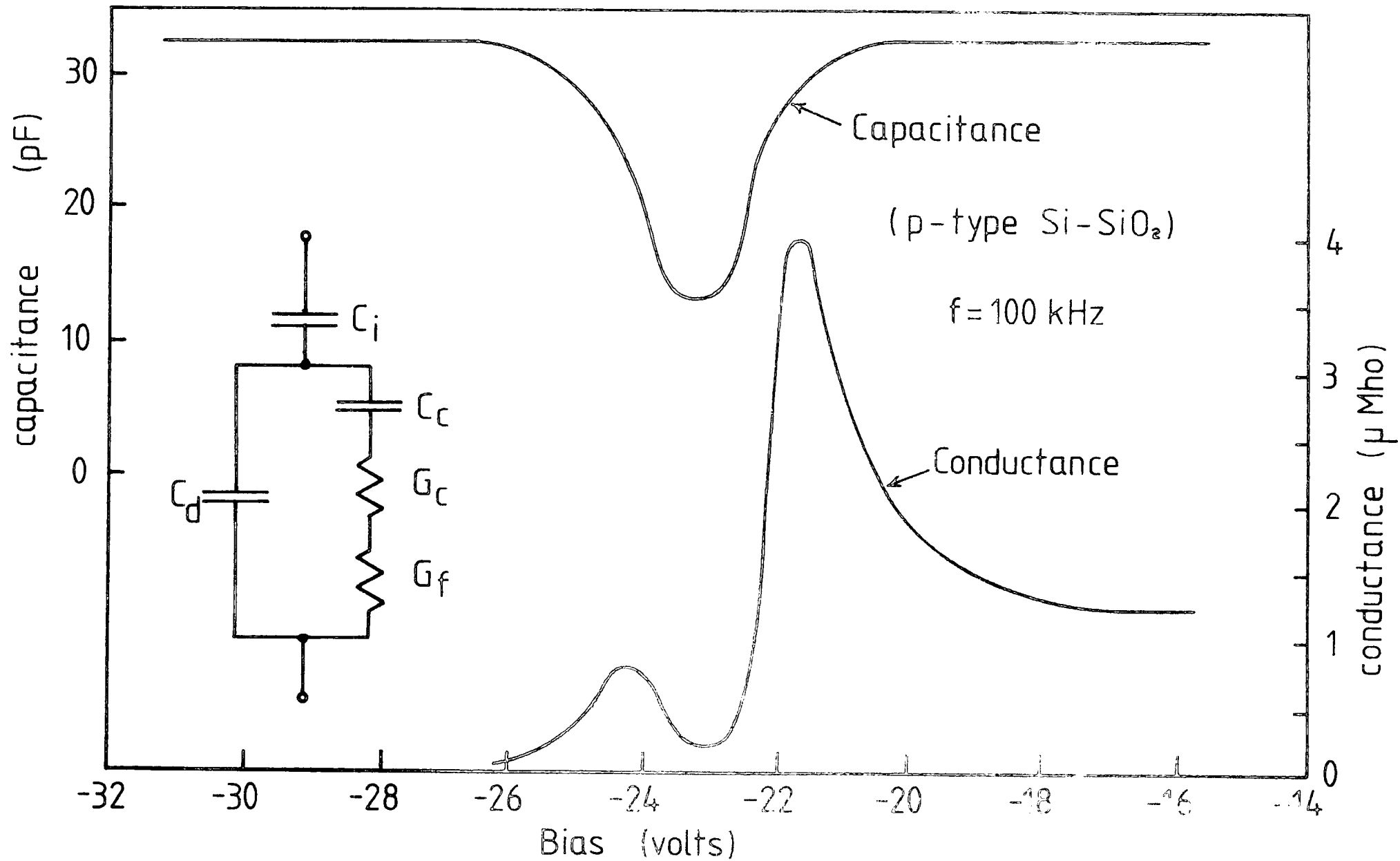


Figure 2.20 : The effect of lateral conduction on capacitance and conductance curves where  $G_f$  represents a bias dependent conductance channel, and  $C_c$ ,  $G_c$  represent lumped component network (After Nicholson and Goetzberger, Ref. 25)

Consider an MIS device with mobile positive charge in the insulator, as illustrated in Figure 2.21. Under an initial positive bias, the charge will reside at the semiconductor interface and cause an effective increase in the applied voltage. As the bias is ramped into depletion and inversion the charge will move through to the electrode interface and thus give an apparent increase in the bias. The final curve shows a net shift to reverse bias as shown in Figure 2.22(a). The return ramp will fall between the initial one and the ideal one, depending upon the mobility of the ions and the duration of the negative bias. In practice, movement of the charge during the ramp will also tend to distort the curve. If the mobile ions are negative, the displacement is to the right of the ideal curve, as shown in Figure 2.22(b), but the sense of the hysteresis is still anticlockwise.

The second source of hysteresis is carrier injection from either electrode ; this is also a complicated problem as both the injection rate and the charge mobility are difficult to measure. For electron injection, positive bias causes the movement of carriers from the accumulation region into the insulator. Some of this charge will reside at the interface, and the remainder will drift inwards, into the bulk of the insulator. The net effect is a shift of the curve to the right, as shown in Figure 2.22(c). Hole injection will give the opposite effect, resulting in a displacement to the left. For both injection situations, however the sense of the hysteresis can be seen to be clockwise, and thus can easily be distinguished from effects due to ion motion.



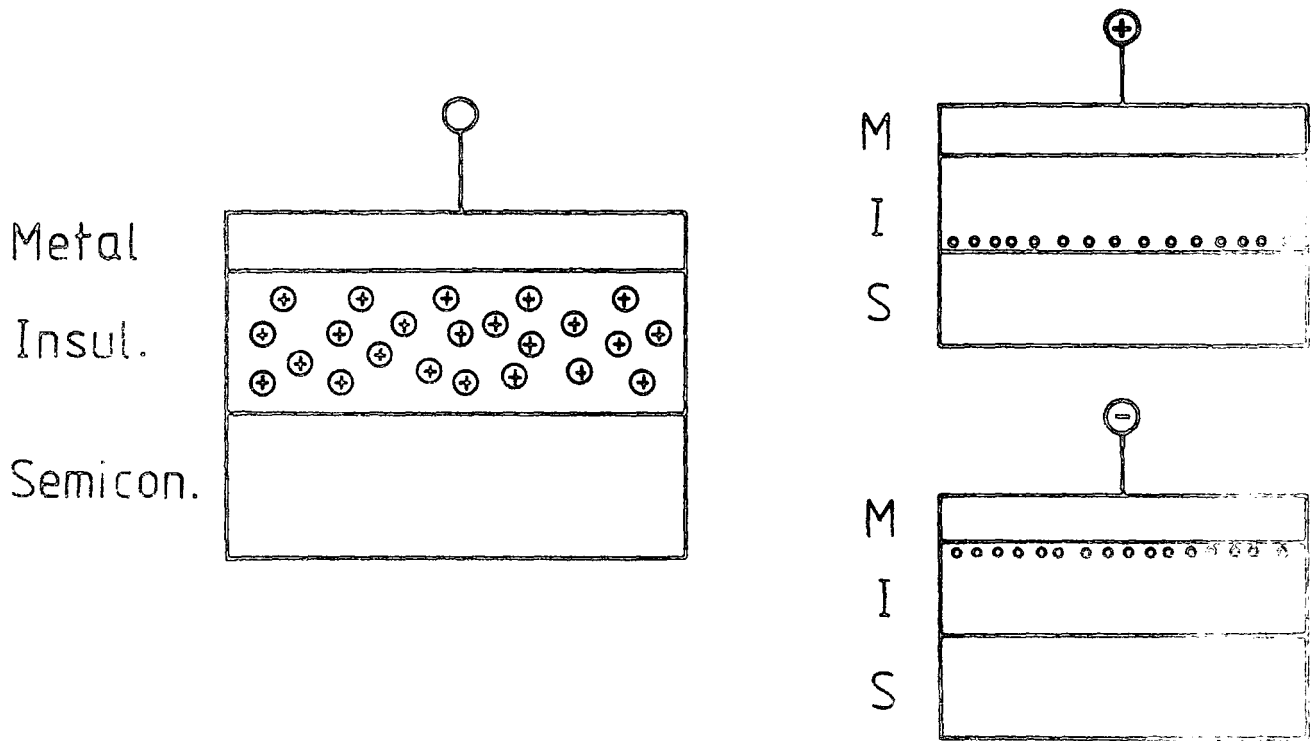


Figure 2.21 : Device with mobile positive charge, under equilibrium, forward, and reverse bias.

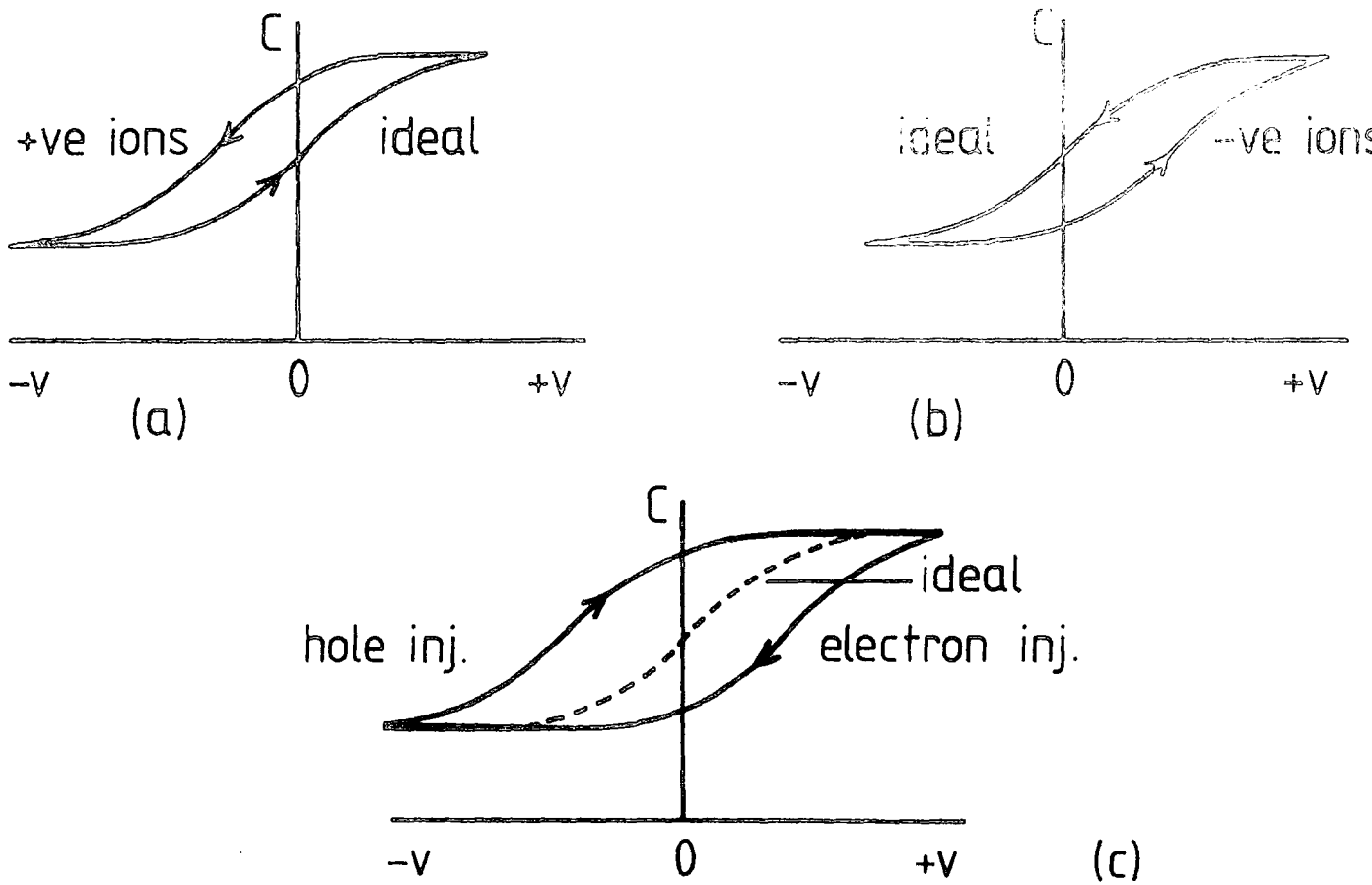


Figure 2.22 : The effect of (a) mobile positive ions, (b) mobile negative ions, and (c) hole and electron injection.

### CHAPTER 3

#### EXPERIMENTAL TECHNIQUES

The fabrication and measurement of devices used in this thesis involved many different stages. Some of these were purely for initial characterisation of device component materials, but the majority were applied in the normal production process. It is the aim of this chapter to consider, in some detail, the more routine parts of the operation as a precursor to descriptions of the more specialised techniques.

Preliminary characterisation of the InP substrate material was undertaken using chemical surface analysis as the primary technique. Section 3.1 therefore considers the general ideas involved in surface characterisation and outlines the various methods available. This is followed by details and chemical background of ESCA ; the main technique used for the characterisation work.

The chemical cleaning and pre-treatment of substrates prior to device fabrication is considered in section 3.2. The operations carried out at this stage were found to influence significantly the quality and performance of subsequent devices, and so followed a careful path of development. In practice a fairly wide range of structures were prepared, but the initial processing was eventually standardised to two approaches, one for InP, and one for Al/Al<sub>2</sub>O<sub>3</sub>. For MIS devices, the deposition of an insulating film was required ; the process used, however, was a non-standard technique and is thus considered in more detail later. In addition this section deals with all the other stages involved in device fabrication, in particular electrode evaporation, and the specialised techniques evolved for use with the organic insulating films.

Device measurement and characterisation were undertaken using both D.C. and A.C. approaches, the lock-in amplifier being a particularly useful piece of equipment. All apparatus and techniques as used throughout the project are thus described in section 3.3.

The final section in this chapter deals with the specialist gas handling apparatus constructed for device environment variation and control. This equipment was used not only to provide inert conditions for characterisation work, but also to enable the devices to be exposed to more toxic materials. These materials, mainly gases and vapours were applied in feasibility studies in the development of solid state gas sensors.

### 3.1 SURFACE ANALYSIS

For the production of an MIS device, it is necessary to deposit an insulating film onto the surface of a semiconductor substrate. The quality of this interface region controls the performance of the resultant device, and is determined as much by the initial treatment of the substrate, as by the type and perfection of the insulating film. Thus by initially characterising the surface it is possible to obtain more understanding of device behaviour and thereby improve the performance and yield during manufacture.

In practice there are many different techniques available to aid this surface characterisation, the following section will therefore begin by briefly comparing some of these methods. It will then go on to discuss in detail the technique of ESCA, the main process applied during the characterisation of the InP.

#### 3.1.1 Introduction to Surface Analysis Techniques

The majority of surface analysis involves the perturbation, of the sample in some way <sup>(1,2,3)</sup>, and the characterisation of the resultant emission. This disturbance is produced by bombarding the surface with photons, electrons or ions, and looking at the resultant secondary species : a summary of useful processes is given in Table (3.1).

Prim. Excitation		Detected Emission		
		X-Ray	Electron	Ions
PHOTONS	UV		Ultra-violet Photoelectron Spectroscopy (UVPS)	
	X-RAY	X-Ray Fluorescence Spectroscopy (XRFS)	X-Ray Photo-elect. spect. (ESCA)	
ELECTRONS		Electron Micro-probe analysis (EPM)	Auger electron spectroscopy (AES) (Scanning auger)	
IONS				Secondary ion mass spectrometry (SIMS) Ion scattering spectrometry

TABLE 3.1 Survey of available methods for surface characterisation.

(a) Photon Interaction

When X-rays enter a solid sample, many interactions occur, of which two are of primary interest : secondary X-rays are produced by the ionisation of inner shell electrons, and the subsequent decay of particles from the upper levels to fill these vacancies. These X-rays originate from depths up to 100  $\mu\text{m}$ , and are characteristic of the source atom. This technique is termed X-ray fluorescence spectroscopy (XRFS), and because of its relatively large depth of penetration, it is useful for avoiding the effects of surface contamination and epitaxial layers. Incident X-rays also give rise to the ejection of core electrons, again characteristic of the source atom. These electrons have only very shallow escape depths of no more than 50  $\text{\AA}$  however, and therefore the technique is essentially for surface characterisation only. This method, ESCA, will be dealt with in greater detail in later sections.

It is also possible to use lower energy photons for material characterisation, in particular ultra-violet radiation. In u.v. photoelectron spectroscopy, outer shell electrons are ejected from the material, and their collection and measurement allow information about their source material to be obtained. Depths of escape are again small, and due to the use of outer bands, the specificity of the resultant information is generally less by comparison with other methods. This technique is also used for looking at surface states directly, by measuring their emission products.

(b) Electron Interaction

With electron/surface interactions there are three processes of special interest ; the generation of X-rays, secondary electrons, and the diffraction of primary electrons. In electron probe micro-analysis, high energy electrons create inner shell vacancies, which are filled by subsequent decays as in XRFS, and the resultant X-rays are characterised to again give in depth structural and atomic information. The primary electron beam is normally a very small spot (1000  $\text{\AA}$ ), and can thus be used for selective area

analysis, giving the technique significant advantage over its X-ray counterpart. The emission of Auger electrons is characterised in Auger electron spectroscopy; here, as in ESCA, the electrons are inner shell particles, but now from slightly higher in the shell. Again, the technique allows relative area measurement, and when coupled with a scanning beam (scanning Auger) becomes a particularly useful approach.

The final techniques considered in this section is low energy electron diffraction, and this is rather a different approach to the previously outlined ones as the interaction with the solid is very weak. The information obtained is largely structural, as the diffracted beam is normally collected photographically, and from the resultant pattern, lattice spacing data can be obtained. This technique looks at only the top one or two monolayers of material and is thus useful in the examination of contaminated species, and adsorbed layers. Once again, the small beam allows relative area analysis, but the process is normally not a real time one, and thus is at a disadvantage when compared to more modern approaches.

(c) Ion Interaction

The use of ions to disturb the surface of the sample is a much less subtle approach, and can result in considerable damage. It does, however, lead to information not obtainable by other methods. Ionic interaction can in general take two paths, depending upon the energies involved. These are elastic collisions, where no damage results, or inelastic collisions, where surface material is removed, this is commonly known as sputtering. The use of low energy rare gas ions, produces elastic scattering off the outermost atomic layer at a surface. This process produces returning ions whose energy spectra are characteristic of the scattering centres, and thus enables composition determination of this outer layer. The technique is known as ion scattering spectroscopy (ISS). When higher energy incident ions are used

this causes expulsion of particles from the surface of the lattice. These can be identified by the use of a mass spectrometer, and a depth profile of the material thereby undertaken. This process is, however, relatively slow as it involves continuously removing material, and also suffers from lack of depth resolution. In addition, secondary ion mass spectrometry (SIMS) data tend to be qualitative rather than quantitative, as it is presently difficult to predict the ratio of charged to uncharged debris. A summary of all these processes is presented in Table (3.2).

### 3.1.2 Detailed Consideration of ESCA (1) : Theoretical Background

In any atom a core electron is subject to a combination of many external forces. The positively charged nucleus provides an attractive force proportional to its atomic number  $Z$ , whilst the surrounding assembly of valence electrons give a complicated repulsive force. The net result of all these external influences is referred to as the binding energy ( $E_b$ ). It can be seen that the removal of an electron from the outer shell (chemical oxidation) will therefore change this binding energy, as will oxidation, or indeed any form of interactive bonding. Binding energies are therefore very sensitive to all changes in chemical environment, and thus the measurement of absolute values, and changes in values, enables chemical identification of surface materials and their bonding environment.

The earliest reported investigations of X-ray induced spectra were by Robinson and Rawlinson<sup>(4)</sup>, who in 1914 looked at the emissions from a variety of metal plates when excited by incident X-radiation. This work was however quite restricted, and due to the lack of equipment, very little detailed analysis was undertaken. The first significant characterisation of a broad variety of surfaces was carried out by Siegbahn et al<sup>(5)</sup> at Uppsala in Sweden. This investigation required the development of very sensitive electron spectrometers, but demonstrated for the first time the

	Probe dia. μm.	Sampling depth atomic layers	Detection sensitivity (ppm atomic)	Lateral Resolution	Features
XRFS	$10^4$	$10^4 - 10^5$	1-100	None	Quantitative Non destructive
EPM	1	$10^2 - 10^3$	100-1000	Exc.	Quantitative Non-destructive
ISS	$10^3$	1	0.1-1%	Poor	Semi-Quantitative
SIMS	$10^3$	3	0.1-100	Fair	Non-Quantitative
AES	~ 100	2-10	0.01-0.1%	Fair	Semi-Quantitative Non-destructive
ESCA	$10^4$	2-10	0.1-1	None	Semi-Quantitative Non-destructive
UVBS	$10^4$	2-10		None	Outer Shell. Surface states.
LEED	$10^4$	1-2	-	None	Lattice Data. Non-destructive.

TABLE 3.2 Summary of capabilities and limitations of various surfaces and thin film analysis techniques



enormous potential that existed in photo-electron spectrometry. Encouraged by these investigations, the commercial production of ESCA equipment began in the 1960's, and since then the application of the technique has spread to virtually every corner of applied science.

In XPS or ESCA, the primary X-ray photon of energy  $h\nu$  is absorbed by the surface of the subject material, and its energy duly imparted to the surrounding area. In most cases the majority of this energy is passed onto a core electron, causing it to be emitted as a photo-electron. In order to escape totally from the material this electron must overcome a number of potential steps, as shown in Fig (3.1) : an initial increment of energy (binding energy  $E_b$ ) is required to excite the electron from its ground state to the Fermi level. To this is added the work function ( $\phi_s$ ), needed to bring the electron up to the vacuum energy level, and finally the conservation of momentum requires an additional increment of energy to be lost in recoil as the electron actually leaves the surface. This latter component, the recoil energy, is a function of the reciprocal atomic number ( $1/Z$ ) ; it is in practice, relatively small for the lighter elements, and has been shown to be negligible for elements heavier than sodium<sup>(6)</sup>. Any remaining energy possessed by the electron after climbing these barriers is manifest as the kinetic energy ( $T_s$ ) of the free particle. This is the quantity measured by the analysis equipment, and from its value the other terms can be deduced. In practice the emitted electrons are collected by a metal plate in the spectrometer, and in consequence additional allowance must be made for the difference in work function between the sample and this plate. Thus the value of KE actually measured is normally slightly less than expected. Thus,

$$h\nu = E_b + T_s + \phi_s + \phi_{SA} \quad (3.1)$$

where  $\phi_{SA}$  is the work function difference between sample and analyser ; the

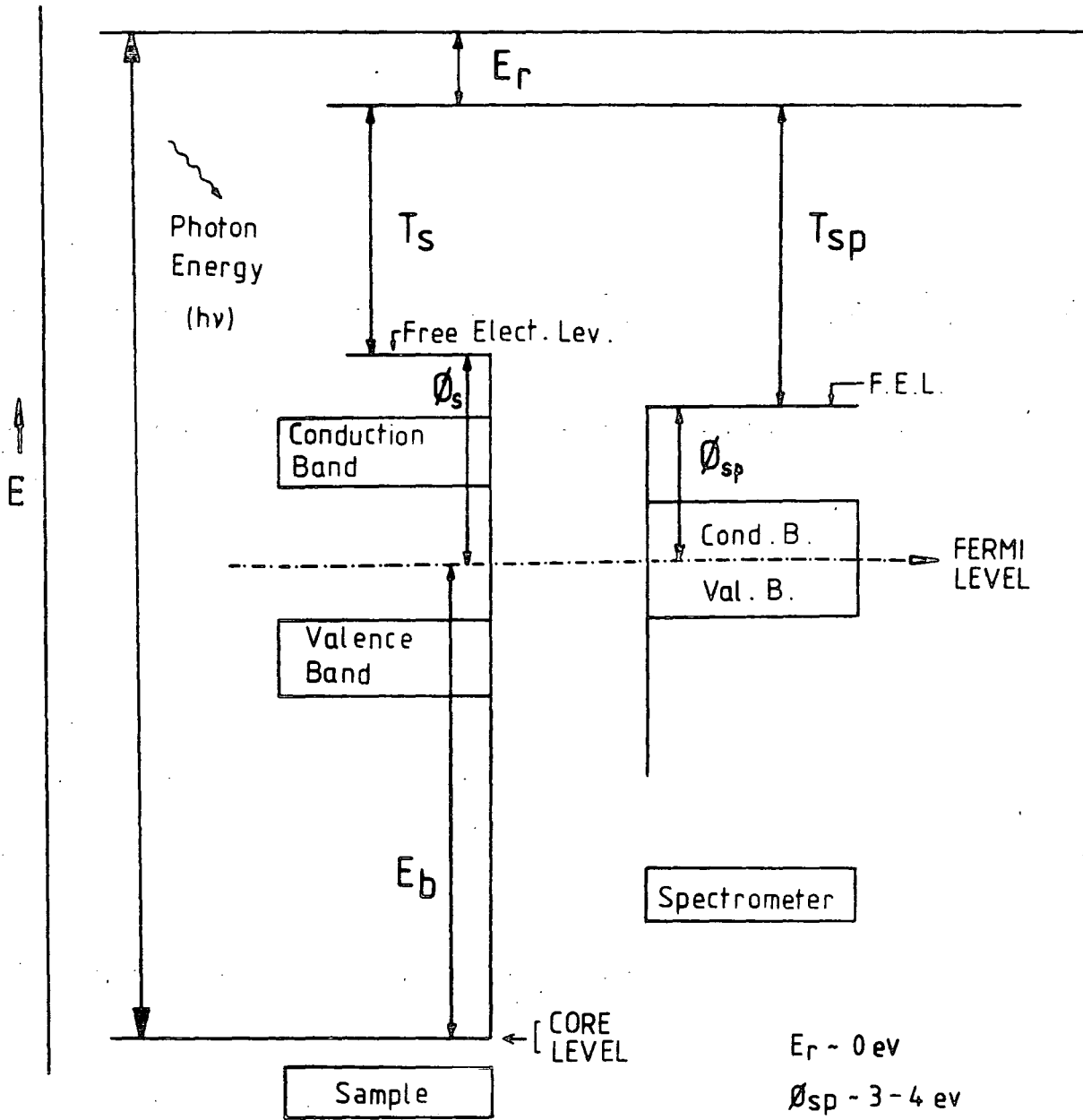


Figure 3.1 : Energetics of electron binding energy measurements in solid

$E_b$  = Binding energy     $T_s$  = Ejected electron KE

$T_{sp}$  = Measured KE.

recoil energy is neglected. From this expression,  $h\nu$ ,  $\phi_s$ ,  $\phi_{SA}$  and  $T_s$  are known, and thus  $E_b$ , the initial binding energy of the electron can be calculated.

In normal operating mode the deflection potential of the analyser (see Section 3.4) is scanned slowly upwards, and the number of electrons with each value of KE is plotted against the value of KE. Thus any one electron will ideally contribute to the magnitude of only one discrete peak. In practice, however, it is likely that about ten percent of escaping electrons will have less energy than expected due to either the splitting of the energy of the incoming photon, or the interaction of the core electron during expulsion. These lower energy electrons occur with bands of allowed energy and thus give rise to subsidiary shake-up lines<sup>(7,8,9)</sup>, observed at various lower energy points during the plot. In addition, there are a number of other phenomena which give rise to displacement and corruption of peaks, all of which must be taken into account during interpretation. The majority of these are, however, secondary effects, and are too complex in nature to be considered at this level of description.

### 3.1.3 Detailed Consideration of ESCA (2) : Data Interpretation

It has been previously shown that the bombardment of a sample with X-rays, gives rise to the ejection of core electrons with kinetic energy proportional to their original binding energy. This binding energy has been shown to be representative of the bonding environment of the source atom, and thus shifts in this value are indicative of changes in binding environment. A classic example of these shifts is given in Fig (3.2) after Siegbahn, where the different bonding environment of carbon gives rise to a whole series of  $C_{1s}$  binding energy peaks.

Before interpretation of the output plots can be undertaken, it is necessary to calibrate the energy axis of the X-Y recorder. This is normally done by using a sample of gold, whose  $4f_{7/2}$  peak at 84 eV is well defined and

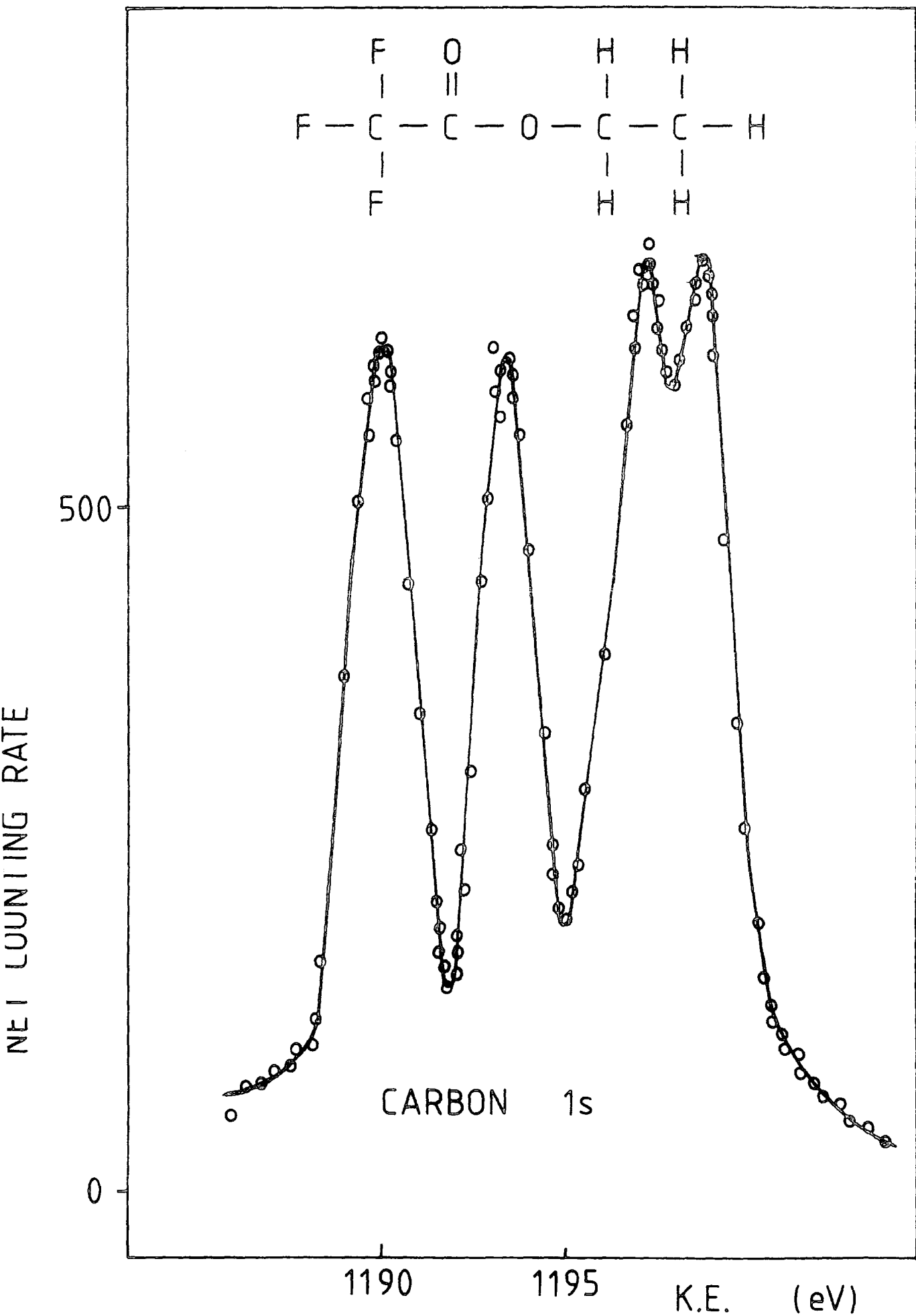


Figure 3.2 : Example of ESCA output data :  
 Photon-electron spectrum of  $C_{1s}$  shell, in ethyl trifluoroacetate -

easily reproduced. The known value of binding energy thus becomes a reference point on each graph, from which all positions along the X axis can be calibrated.

Practical output data are normally comprised of many different peaks, of various heights, originating from a variety of source materials. In order to interpret these data it is necessary to compare the energy positions of each peak with known values, both from reference tables, and from subsidiary data obtained from pure materials. This approach will normally give some idea of which elements and oxides are present on the surface of the materials. In addition various quantitative theorems do exist<sup>(10,11,12)</sup> ; these enable direct evaluation of atomic and molecular structure. They are, however, exceptionally complicated and it is therefore inappropriate to consider them in any detail here.

#### 3.1.4 Detailed Consideration of ESCA (3) : Instrumentation

The equipment used for the acquisition of ESCA data can be divided into five main parts : the X-ray source, the sample compartment, the energy analyser, the detection area, and the data recorder. A typical ESCA unit is presented schematically in Fig (3.3) ; this will now be considered in detail.

To produce the X-rays, a Marconi-Elliott GX14 high voltage power supply was used to accelerate electrons into a magnesium target ; this produced radiation at  $Mg_{K\alpha 1,2}$  (1253.6 eV). The total input power was normally about 200 W. In order to allow emitted electrons to reach the analyser, the sample was mounted inside a high vacuum chamber, normally held at  $10^{-7}$  torr, but able to reach much higher vacuum for high sensitivity measurements. This chamber was fitted with various access ports to allow not only insertion and removal of the sample, but also to allow the application of external treatment and analysis facilities. In addition, the sample port was fitted with an insertion lock and high vacuum gate, this allowed local access to the specimen

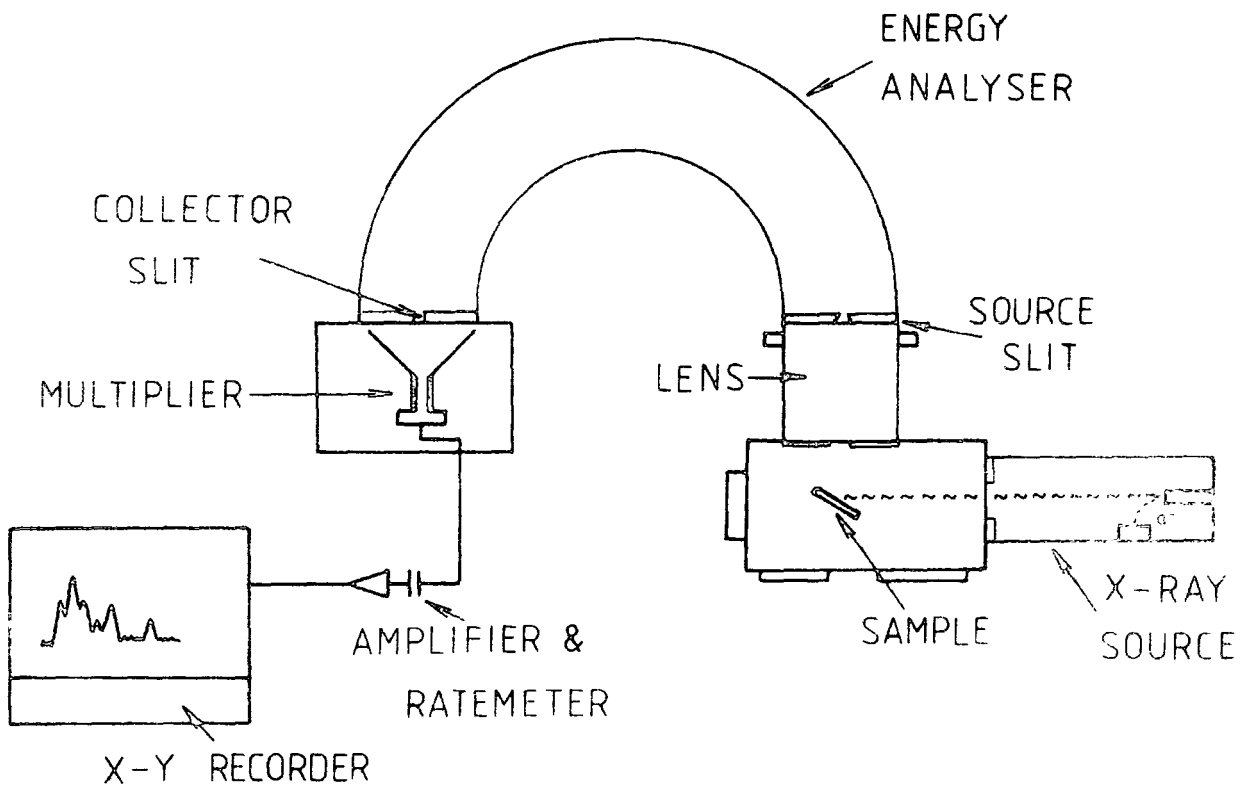


Figure 3.3 : Schematic diagram of AEl ES200 X-Ray photoelectron spectrometer.

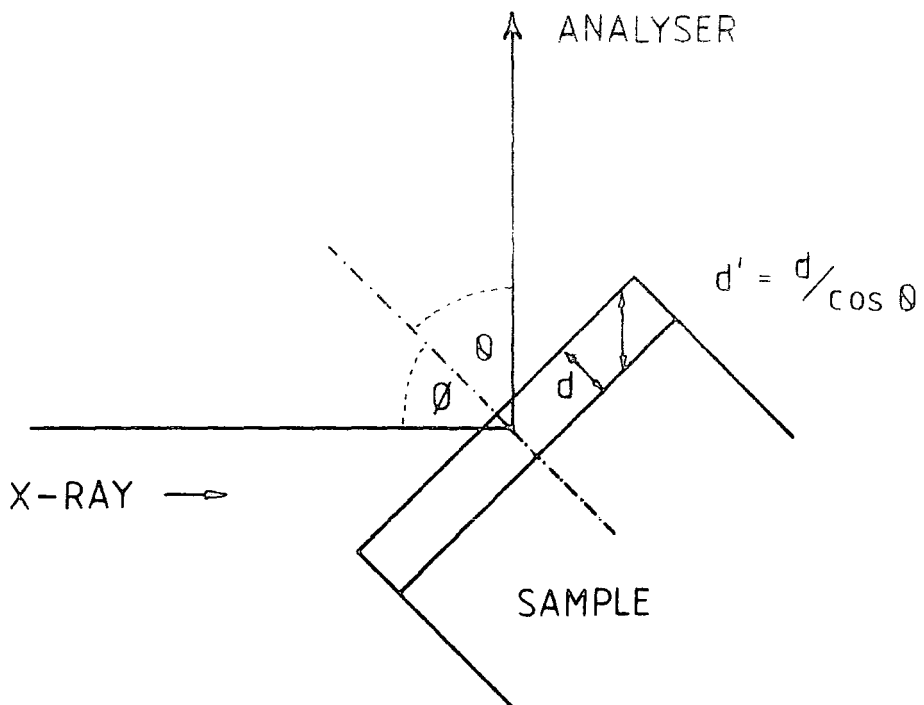


Figure 3.4 : Schematic representation of electron take-off angle  $\theta$ ,  $d$  = sampling depth,  $d'$  = transit distance in solid.

and avoided the need to raise the whole system up to atmospheric pressure during manipulation. In order to provide good electrical contact, the sample was mounted onto the probe tip with silver dag (section 3.2b), and allowed to dry thoroughly before measurements began. In addition, to provide some freedom of movement when in the chamber, this tip was subsequently mounted on an adjustable arm. This enabled the angle of incidence of the X-ray beam to be varied, (Figure 3.4), and thus allowed surface or bulk features of the sample to be specifically enhanced.

The electrons emitted from the surface of the sample were passed through an electromagnetic lens and slit system, and then into the analyser section. In the case of the ES 200, this was a double focussing instrument capable of a resolution of 1 in  $10^4$ . With this type of unit a potential difference across two concentric spheres deflects the incoming electrons by an amount proportional to their kinetic energy, and thus precisely selects the energy of the electron arriving at the output slit. The final detector was a multichannel electron multiplier, whose output was used to feed an amplifier and counter circuit. This signal was subsequently plotted on a Hewlett-Packard XY recorder. In normal operating mode the electrostatic field on the analyser was scanned continuously from the equivalent starting kinetic energy, up to the maximum required value. The output count rate for each voltage was then plotted against energy on the chart recorder. In practice the use of a multichannel detector, and double focussing analyser, allowed the simultaneous observation of many different bands of the energy spectrum, and so vastly reduced the sample measurement time. In consequence typical scans took no more than fifteen minutes for any one sample.

### 3.2 DEVICE FABRICATION TECHNOLOGY

This section is intended to cover the majority of general purpose preparation, cleaning and handling techniques applied during device manufacture. It is divided into brief sub-sections, which describe individual

stages of the operation ; these sections are approximately in order of normal application. The preparation and deposition of Langmuir-Blodgett films are covered in later chapters.

### 3.2.1 Surface Preparation (1) : Pre-cleaning

The simplest structures prepared during this work were metal-insulator-metal (MIM) devices. These were used primarily for the characterisation of the organic insulating films and their metal top electrodes. For these type of structures, the substrate was normally a thin evaporated layer of aluminium deposited on a glass microscope slide. Preliminary selection of these "chance select" slides was by optical inspection to ensure they contained no gross defects, or surface imperfections which might give rise to problems during film deposition. Initial degreasing and cleaning was carried out using a 5% solution of "Decon 90" (a general purpose alkali surfactant), with the aid of an ultrasonic bath for ten to fifteen minutes. This was followed by thorough rinsing three times in "Millipore" water, again with the aid of an ultrasonic bath, to remove all traces of the alkali cleaner. The ultra pure "Millipore" water referred to throughout this and other chapters was prepared as follows :-

Initial tap water was de-ionised by using an Elga B113 cartridge de-ionising system, this reduced the water to about 2 M $\Omega$  cm resistivity. The water was then passed through a Millipore "Milli-Q reagent grade" recycling purification system. This comprised of two "Super C" carbon (organic removal) filters, and one "Ion ex" mixed bed de-ionisation filter. In addition, there was a final 0.22  $\mu$ m membrane particle filter. This system was installed as a source of water for the Langmuir troughs, but was also used as a general purpose supply of pure water. The resistivity of the final output liquid was about 18 M $\Omega$  cm.



Secondary cleaning of the glass slides consisted of a series of degreasing operations in various organic solvents. This degreasing was carried out using soxhlet reflux units to boil and recycle the organic materials. The first solvent applied was trichloroethylene (BDH-Analar grade), this was followed by iso-propyl alcohol (BDH-Analar grade), both of which were used for about one hour to ensure thorough cleaning of the slides. In each case it was found to be advantageous to remove the samples from the reflux units whilst the solvents were still hot. This ensured total evaporation of residual liquid from the slides, leaving the cleanest surface possible<sup>(13)</sup>.

For the fabrication of semiconductor devices, substrates were obtained from Metals Research Ltd.(MR) or Mining and Chemical Products Ltd (MCP). The samples with epitaxial layers on highly doped substrates were supplied by R.S.R.E.(Malvern) or occasionally by Plessey Research Ltd. (Caswell). For this material, ultrasonic cleaning in Decon 90, or indeed any other liquid was found to be unsuitable due to its brittleness. Consequently, initial cleaning of "as received" semiconductor samples was restricted to reflux degreasing in organic solvents. Preliminary studies of various other solvent combinations of acetone, methanol and chloroform for use in pre-cleaning, failed to show any improvement on the trichloroethylene/IPA sequence.

In most cases the samples were etched immediately after this pre-cleaning operation, where this was not possible they were stored in a desiccator until required.

### 3.2.2 Surface Preparation (2) : Wet Etching

Following the initial pre-cleaning treatment, most semiconductor substrates were etched before the deposition of an insulating film, or the evaporation of metal contacts. In practice a wide variety of etchant

mixtures were tried during the production of MIS and Schottky barrier devices. A summary of the significant mixtures finally adopted is given in Table 3.3. The majority of the work was undertaken on MIS devices in an attempt to influence the chemical structure of the interface region, and thus the electrical device characteristics. The results of this investigation are presented later in chapter 9.

In each case the etchants were prepared freshly each day, using newly cleaned pyrex beakers and were stored in pyrex reagent bottles. All chemicals used were of Analar (BDH) grade or purer, and any water required for dilution or rinsing was obtained from the Millipore unit.

Following this wet etch treatment, samples were stored in Millipore water for the short time required to prepare the next stage of the process (i.e. Langmuir film deposition, or electrode evaporation).

### 3.2.3 Surface Preparation (3) : Dry Etching

The second type of surface preparation used for InP was glow discharge etching. This was applied in order to produce a chemically different surface from anything obtained by the use of wet etches. The technique of dry etching is in fact a relatively new process, but already plays a major role in the commercial production of integrated circuits<sup>(14)</sup>. In this application its convenience and greater flexibility are sufficient to justify its use in the place of wet etching. For the etching of silicon, glow discharges in  $\text{CF}_4$  are used to selectively remove material at various stages in the production process. In general, the technique requires the selection of a suitable plasma ; this must react with the species of interest, and form a volatile chemical compound that can easily be desorbed at the temperature and pressure used. With silicon, r.f. power is used to ionise  $\text{CF}_4$  into radicals of  $\text{F}$ ,  $\text{CF}$ ,  $\text{CF}_2$  and  $\text{CF}_3$ . These then react with the surface of the material and produce volatile  $\text{SiF}_4$ . In practice, many other gases are also being

Etch	Mixture	Etch Rate	Ref	Comment
$\text{Br}_2/\text{CH}_3\text{OH}$	0.2% Bromine by volume	$\sim 0.1 \mu\text{m}/\text{min}$	B Tuck + A J Baker J.Mat.Sci, <u>8</u> (1973) 1559	Leaves "orange peel" surface. Rapid ageing $\sim 1/2$ hr.
$\text{Br}_2/\text{HBr}/\text{H}_2\text{O}$	0.2:17:35 by volume	$0.4 \mu\text{m}/\text{min}$	D J Colliver Compound semicond.Tech. Artech House Inc (1976)	Used as polishing etch in dilute form.
HF	40% by volume	-	-	Oxide removal
$\text{HCl}/\text{H}_2\text{O}_2/\text{H}_2\text{O}$	1 : 1 : 10 by volume	-	(Personal communication) L D Irving RSRE, Malvern	De-oxidising etch.
$\text{HNO}_3/\text{HCl}/\text{H}_2\text{O}_2$	2 : 2.1 : 2	$\sim 5 \mu\text{m}/\text{min}$	R Becker Sol.St.Elect. <u>16</u> (1973) 1241	Reported as de-oxidising etch
$\text{H}_2\text{SO}_4/\text{H}_2\text{O}_2/\text{H}_2\text{O}$	4 : 1 : 1 by volume	$2500 \text{ \AA}/\text{min}$	Shiota et al. J Electrochem Soc. <u>124</u> (1977) 155	Used along with HF on GaAs to produce oxide free surface
$\text{NaOH}/\text{H}_2\text{O}_2$	1 : 1 by volume (1 molar : 0.76 molar)			

TABLE 3.3 Summary of wet chemical etches used on InP.

investigated<sup>(15)</sup> for use with a variety of additional metals and semiconductors.

For the dry etching of InP, a hydrogen plasma was used ; this reacts with the surface indium oxides to produce volatile material and thus leaves the remaining substrate phosphorous rich (as will be shown in chapter 8). This technique appears to be the only way of producing this type of surface.

The equipment used for this process consisted of a glass vacuum system, pumped by a standard rotary and diffusion kit. To establish the required gaseous ambient, the work chamber was fitted with an adjustable leak valve, fed from a cylinder of hydrogen. The r.f. discharge was excited by a 13.56 MHz radio frequency generator, tuned by an L.C. matching circuit and fed to an eight turn 60  $\mu$ H copper coil. This coil, 5 cm in diameter, was wrapped around the perimeter of the work chamber. In addition, the power output from the generator was monitored by a Heathkit HM 102 RF power meter. Access to the sample location in the work chamber was achieved via a demountable ground glass end piece, normally sealed in position by the external pressure, but removable when the chamber was not evacuated. The pressure of the system was continuously monitored by a Pirani thermocouple gauge. A schematic diagram of the plasma etching rig, as used, is given in Fig 3.5.

The surface preparation took place as follows :-

The sample (previously pre-cleaned) was inserted into the work chamber, and the latter pumped down to  $10^{-3}$  torr. The system was then flushed several times with pure hydrogen gas before an ambient pressure of 0.01 torr was established. Following this, the glow discharge was activated for the required time period, after which the sample was removed and stored in a desiccator until required. For surface characterisation work the glow discharge apparatus was connected directly to the ESCA work chamber, this enabled simultaneous etching and measurement of any sample.

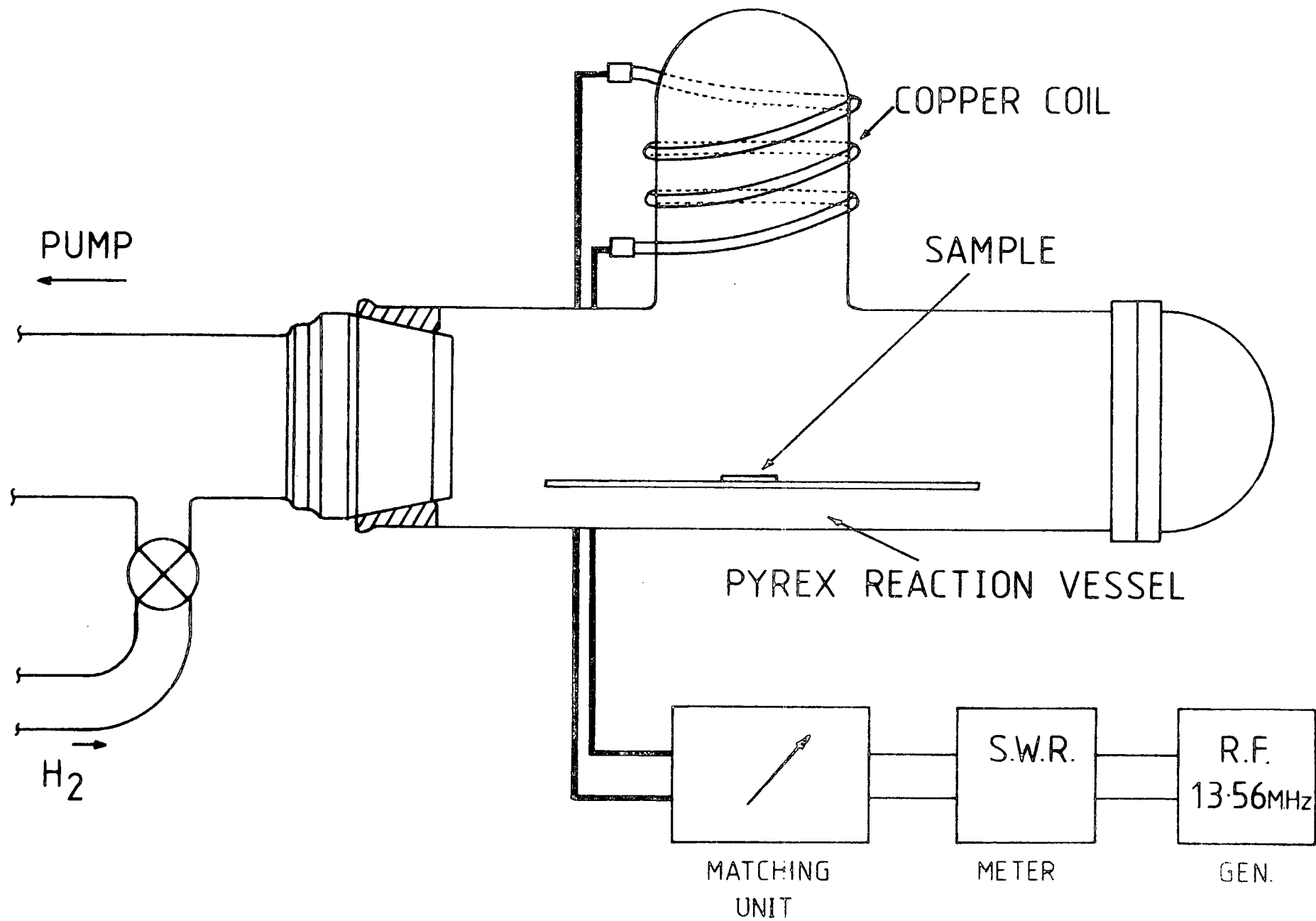


Figure 3.5 : Schematic diagram of glow discharge apparatus.

### 3.2.4 Electrode Deposition (1) : Semiconductors

The usefulness of any active device is generally limited by the method of inserting and removing the signal. In the case of semiconductors (working at low frequencies), the normal method is to use a metal electrode, deposited during device fabrication. The most common process used for this deposition is vacuum evaporation : this technique relies upon an electrically heated source boat, from which the metal electrode material is evaporated under high vacuum. Other methods are available, however, and are sometimes used for high melting points, and reactive metals. Sputtering is the main alternative, but vapour phase growth, electroplating and solution deposition all have applications under certain circumstances. In sputtering, the metal surface is bombarded with energetic charged particles, normally of a heavy gas such as argon. This causes the ejection of surface atoms which move through the vacuum and recondense onto the substrate to form the desired thin film. In addition, this technique has the advantage of not requiring a molten source, and this avoids problems due to interaction with the container.

In practice, vacuum evaporation is satisfactory for the majority of metals, as the use of high vacuum causes a sufficient reduction in the melting point to allow the materials to be easily evaporated. This approach also significantly limits oxidation of the metal, and the high mean free path of the evaporant allows the use of simple masking arrangements for contact definition. The vacuum systems used throughout this project were Edwards model 306 vacuum coaters, comprising of rotary and diffusion pumps evacuating a glass work chamber down to about  $10^{-7}$  torr. The state of the vacuum was monitored by integral Penning and Pirani gauges. During the deposition process, samples were mounted on a copper substrate holder attached to the metal lid of the chamber. The source boats, normally molybdenum, were

attached to a four pillar rotary table, and were powered by a low tension high current adjustable supply. In practice, certain metals were found to react vigorously with molybdenum ; in these cases a tungsten filament was used as the source. The normal shutter was replaced by a larger one with a 3mm x 30mm slit cut into it. This new shutter, when used in conjunction with different sources on the rotary table, enabled selective evaporation (different types of electrode on different areas of the sample) and laminated contacts to be easily produced.

This thickness of the resultant electrode was continuously monitored by a quartz crystal head mounted adjacent to the sample, whose output fed digital thickness and rate meters.

Under normal conditions, samples were taken straight from cleaning or etching and mounted on a brass mask. This was used to provide a simple and convenient form of contact definition. The mask was merely a small plate with holes cut in it of the same size as the desired electrode area. When inserted into an evaporant stream, the remaining metal shielded the majority of the substrate, allowing metal to reach the latter only through the holes. Edge effects were found to be negligible in most cases, except for very small holes (< 1mm), where care was needed to align the mask directly over the source.

For contacts to semiconductors, the chamber was pumped down to about  $10^{-6}$  torr, and the subsequent rate of evaporation used was about 1 - 5  $\text{\AA}/\text{sec}$ , depending upon the electrode material. The total thickness of the electrodes was between 500  $\text{\AA}$  and 1000  $\text{\AA}$ , again depending upon the material. In the case of some types of contact to semiconductors it was found that post evaporation annealing was required to activate or improve the characteristics. To achieve this, initial attempts were made at heating the sample directly after evaporation, whilst still in the evaporator. In

practice the results proved rather irreproducible and this approach was quickly abandoned in favour of post annealing in a normal temperature controlled furnace.

#### 4.2.5 Electrode Deposition (2) : Langmuir films

The organic insulating films used for the majority of MIS devices, produced during this work, are presently not as robust or thermally stable as more commonly used insulators like  $\text{SiO}_2$ . In consequence, special techniques had to be developed to enable electrode deposition by vacuum evaporation. The problems can be summarised as follows :-

Direct evaporation of hot metal onto the surface of the films would almost certainly cause thermal damage due to their relatively low melting point of about  $80^\circ\text{C}$ . Some form of cooling prior to evaporation was therefore required. But cooling the sample under only backing pressure (or higher) would cause rapid condensation of any water vapour, again causing damage. Thus an evaporation procedure combining both slow cooling and pump down was devised. Cooling was achieved by using an overhead tank of liquid nitrogen, this conduction cooled the lid of the evaporator and thus the substrate holder and the sample. In order to monitor the temperature, thermocouples were attached to the sample and the substrate holder, and lead-throughs used to take the output to Eurotherm temperature displays. This sample mounting and cooling arrangement is represented diagrammatically in Fig 3.6. The evaporation proceeded as follows :-

The sample, suitably mounted on the desired mask was attached to the substrate holder, the lid of the evaporator closed, and the chamber pumped down to backing pressure. To remove some of the residual gases and water vapour, the chamber was flushed three or four times with dry nitrogen, and again pumped down the backing pressure. The liquid nitrogen tank was now filled, and the fall in temperature of the sample closely followed. As



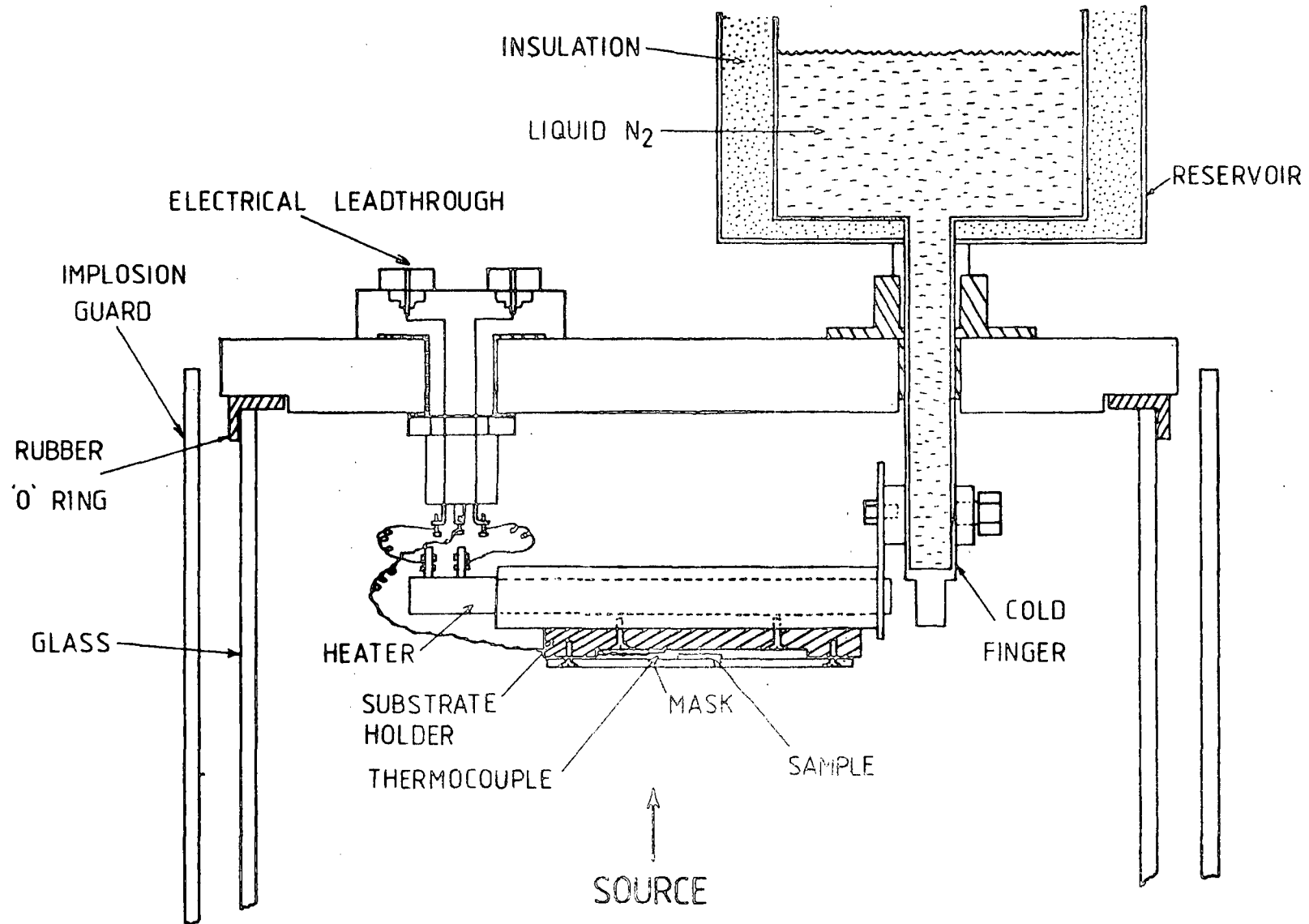


Figure 3.6 : Substrate cooling attachment for evaporator : showing coolant reservoir and sample location.

this passed through zero, the diffusion pump valve was slowly opened, and the pressure gradually lowered as the temperature continued falling. The sample was maintained at  $-80^{\circ}\text{C}$  for a considerable period of time whilst the pressure in the work chamber was reduced to the desired value of  $10^{-6}$  torr. Subsequent evaporation of the electrodes was carried out at the minimum practical rate, with periods of several tens of minutes not being uncommon for high density materials like gold ( $0.05 \text{ \AA}/\text{sec}$ ). The warm up procedure would ideally be the reverse of the pump down one, but in practice, the times involved were prohibitive. In consequence, the chamber was normally let up to backing pressure with dry nitrogen when the sample reached about  $-30^{\circ}\text{C}$ , and the equipment was then left overnight to fully warm-up before the sample was removed.

It must be emphasised that this process was developed in order to avoid "all possible" damage to the films during top contact deposition. In practice, it may be an over-reaction to the problem, as contacts have been evaporated onto uncooled films with little or no degradation in resultant characteristics. At present, however, results from this type of contact formation are not reproducible enough for general application.

### 3.2.6 General Device Handling

The degradation of devices under normal atmospheric conditions is a major problem for development engineers in the semiconductor industry. Any circuit on general sale must meet a basic specification for reliability and must thus have all degradation problems removed during development. At the research level, however, problems are much less severe as reasonable control of device environment is easily achieved.

In order to avoid most random and unpredictable device changes all samples not being used were stored in a desiccator under nitrogen at half atmospheric pressure. The outside of this container was blackened to reduce any long term optical effects, and the silica gel desiccant was thermally regenerated as required. The low pressure was used specifically to aid the drying of freshly dipped insulating films, as inevitably some water was picked up together with the stearic acid during the deposition process. This drying period was normally at least three days, and ensured the best insulating properties were obtained.

In order to facilitate reuse of the InP substrates a simple device mounting system was developed : this comprised of a small brass metal base in which were drilled two holes ; one for fixing the base in the sample cryostat, and another to enable access to the substrate contact. The sample was mounted on this base, fastened in position by two small strips of tape placed at the very edges of the substrate. One electrical connection to the device was made via the base, by connecting a wire from the substrate Ohmic contact to the back of the metal. This was held in place at either end by silver dag (a colloidal suspension of silver powder in an organic solvent ; Johnson Matthey FSP 306). The other contact, to the top of the device, was achieved by using a small gold ball probe which could easily be moved from electrode to electrode. In this way, rapid assessment of many

devices could be undertaken without the need for many "permanent" connections.

In order to control the environment of the sample during measurement a circular metal sample holder was constructed, this is shown in Fig 3.7. This comprised of a metal table, movable in the X and Y directions with the aid of small thumbwheels, and upon which the previously mentioned sample and base could be easily located. Adjacent to this was a small drop arm onto which the gold ball top contact probe was attached ; this could be moved vertically up or down and thus enabled control of electrical connections to previously selected devices. This metal table and drop arm were mounted on an insulating base of "tufnol", using plastic screws and mica spacing washers. The base was then similarly secured to the bottom of the cryostat. These relatively extreme measures were found necessary in order to avoid low current leakage between individual components during current-voltage measurements. Electrical leads were taken from the table and the drop arm via a ceramic leadthrough to external BNC sockets, and two gas pipe fittings were provided for connection to backing or nitrogen lines. In addition, a removable lid with a glass viewing window was included in the design to seal the whole vessel gas tight if required. For the acquisition of data, this sample holder was attached to some form of measurement equipment either AC or DC, as discussed in the next section.

The majority of measurement undertaken involved relatively short term operations, requiring the removal of samples from the desiccator for only a few hours at a time. In order to avoid degradation during this period, measurements were carried out whenever possible with the sample holder filled with nitrogen. In practice, however, it was shown by initial experiments that no significant degradation effects were produced by exposure to the normal atmosphere for this relatively short time.



- A. DROP ARM PROBE
- B. MOBILE TABLE
- C. SAMPLE
- D. TO ELECTRICAL LEADTHROUGH
- E. BULB
- F. GAS INLET

Fig. 3.7 Photograph of sample holder with lid removed

### 3.3 ELECTRICAL MEASUREMENT EQUIPMENT

In recent years advances in electronic instrumentation have played a very important role in device physics. The introduction of sophisticated equipment has considerably speeded up measurement operations, allowing the application of techniques previously thought impossible. These new methods lead to better devices, and thus superior equipment, and so the cycle continues. The availability of cheap, compact microcomputing power has significantly affected measurement techniques, providing easy automation and thus simplified long term testing. Even the relatively short three year duration of this project has seen new equipment become rapidly obsolete.

Due to this wide range of new apparatus there are now many techniques available to the device physicist for use in characterising a new product. Any given technique will, however, only yield information in a relatively restricted area, and so the pre-selection of equipment becomes very important. In practice, cost and availability of apparatus also have a significant influence on the final decision.

With MIS technology widespread use is currently being made of phase sensitive detection techniques to measure capacitance and conductance variation with bias and frequency. This type of data leads to important information about many aspects of the device interface region, and so is already a valuable technique. The same methods can of course be applied to other types of device. Indeed, A.C. measurements on both Schottky barriers and MIM structures have already yielded a great deal of useful information.

It must be emphasised, however, that those relatively new techniques have by no means taken over from the original simpler methods. Indeed, D.C. current voltage plotting is still a widespread technique and is very valuable for looking at conduction mechanisms in insulating and semiconducting materials.

Both types of measurement technique were, in practice, applied to the

devices produced during the project ; this section describes the apparatus used for each method.

### 3.3.1 D.C. Measurement

For current voltage plotting the standard sample holder (as described in 3.2) was used, in conjunction with a Keithley 410A picoammeter and a step variable D.C. voltage supply. BNC connections were used for the majority of wiring, with the shortest possible lengths to reduce noise and interference problems. The voltage output of the Keithley was taken to a Bryans 27000 X-T recorder to monitor the decay of current for each individual voltage and to ensure the recovery of the true data. This decay effect was in practice due to injected charge or trapped ions, moving in response to the applied bias. The output from these carriers was thus a displacement current, and the true D.C. conduction was represented by much lower values. Monitoring of the current decay until a constant value was obtained therefore, ensured that real current was being measured. The recording of the data was normally done on a point by point basis, often in conjunction with A.C. measurements to obtain the maximum amount of data from any one device. The values of voltage applied were rarely more than three or four volts ( $10^6$  V/cm), varied in 100 mV steps, and the power was switched off upon each change of bias to avoid transient spikes damaging the device and the equipment. At relatively low values of voltage, and thus low conduction currents ( $10^{-12}$  A), problems with noise become troublesome, and recovery of a steady state value from the random noise become very difficult. Of the various sources of this noise problem, some sources, like bad leads, and bad top contact probe connections could be overcome. Others, however, mainly external sources, had to be endured and measurements taken at times when the noise level was relatively low.

For the characterisation of FET type devices a dual channel battery

power supply was constructed with each channel having a meter and a vernier adjustable output up to a maximum of 10V. This supply was used to bias the source/drain, and source/gate connections of the device, and the current drawn from each channel was monitored by an ammeter. Data were recorded on a point by point basis, and the characterisation subsequently drawn out as required. In addition, a Tektronix type 575 transistor curve tracer was available for quick initial examination of device parameters, but the display was too small for any detailed data recording.

The final D.C. technique applied was the quasi-static method of capacitance plotting. The basic equipment required for this was a slow D.C. ramp and picoammeter. The ramp was used to apply a bias to the device and the resultant displacement current due to the semiconductor Fermi level being moved through the bandgap was recorded by the picoammeter. The output current was then plotted against applied bias to obtain a low frequency type C-V curve. In practice the signal magnitude is proportional to the ramp rate (see section 2.3) and therefore a compromise is normally required between high speed for large signal, and low speed to reduce non-linearity and hysteresis effects. In addition, the final current, even for relatively rapid ramping, are only about  $10^{-12}$  A, and so a low leakage current through the device insulator is essential. If this criterion is not met then the displacement current is masked by leakage, and the technique is useless.

### 3.3.2 A.C. Measurement

For the acquisition of C:V and G:V data as a function at bias and frequency, a Brookdeal 9502 two-phase lock-in amplifier was used. This instrument is quite a sophisticated piece of equipment, therefore a detailed explanation of its operation will be given. A phase sensitive detector can be considered as an A.C. voltmeter which can recover signals submerged in normally prohibitive amounts of noise<sup>(16,17)</sup>. To do this, the instrument



uses phase-lock-loop techniques to compare the magnitude, frequency and phase of the incoming signal with those of a known reference. In order to use the instrument to measure the A.C. characteristics of an MIS device, it is necessary to apply both a high frequency reference signal, and a variable D.C. ramp. The D.C. ramp performs the function of sweeping the Fermi level at the semiconductor surface through the bandgap region, enabling data to be taken at each point. The frequency of the low magnitude A.C. reference is variable over a large band width (10 Hz-120 kHz) to allow the eventual resolution of different time constant properties of the subject device. In practice these two component signals are mixed together and applied to the device simultaneously.

The phase sensitive detector in the lock-in amplifier can be thought of as a multiplier circuit<sup>(13)</sup>, the output  $v_o$  being the product of  $v_1$ , the input signal, and  $v_R$ , the reference signal. If we represent the signal in cosine form, then :

$$v_R = V_R \cos \omega_R t. \quad (3.2)$$

In reality, the normal input signal will consist of the synchronous signal to be measured, mixed with many random or discrete frequency asynchronous signals (i.e. noise). If we initially consider only the sample frequency component at  $\omega_s$ , then :

$$v_o = v_R \cdot v_s = V_R \cos \omega_R t \cdot V_s \cos \omega_s t \quad (\omega = 2\pi f) \quad (3.3)$$

If  $V_R$  is suitably scaled to unity then :

$$v_o = \frac{1}{2} V_s \left[ \cos 2\pi t (f_R - f_s) + \cos 2\pi t (f_R + f_s) \right] \quad (3.4)$$

In practice the noise frequency  $f_N = f_s$  can assume any value.

If a low pass filter of cut-off ( $f_c$ ) significantly less than  $f_R$  is applied, then only frequencies having :

$$(f_R - f_N) < f_c \tag{3.5}$$

will be passed, i.e. only frequencies very near to  $f_R$ . When  $f = f_R$ , as in the case of interest, then the output is merely a D.C. voltage proportional to signal amplitude and phase difference. That is, if :

$$v_1 = V_1 \cos (\omega_R t + \phi) \tag{3.6}$$

then  $v_o = V_1 \cos (\omega_R t + \phi) \cos \omega_R t \tag{3.7}$

$$= \frac{1}{2} V_1 \left[ \cos (2\omega_R t + \phi) + \cos \phi \right] \tag{3.8}$$

and after filtering out the  $2\omega_R$  component the output reverts to :

$$v_o = \frac{1}{2} V_1 \cos \phi. \tag{3.9}$$

This latter cosine term is finally eliminated by pre-calibration of the lock-in (see later) to adjust the value of  $\phi$  to zero and thus obtain the maximum output signal. In addition, quadrature components of the input signal can easily be measured by supplying the reference, now with an extra  $90^\circ$  phase shift, to another PSD. The 9502 is thus two PSD's in one box, with external reference and signal inputs, as given in Fig 3.8. The final improvement in signal/noise ratio over more conventional equipment depends largely upon the bandwidth of the final filtering applied. It is, for example, at least a factor of two hundred for time constants of about one second.

The input signal to the lock-in is normally the result of applying the mixed A.C. and D.C. signals to the terminals of the sample device. To

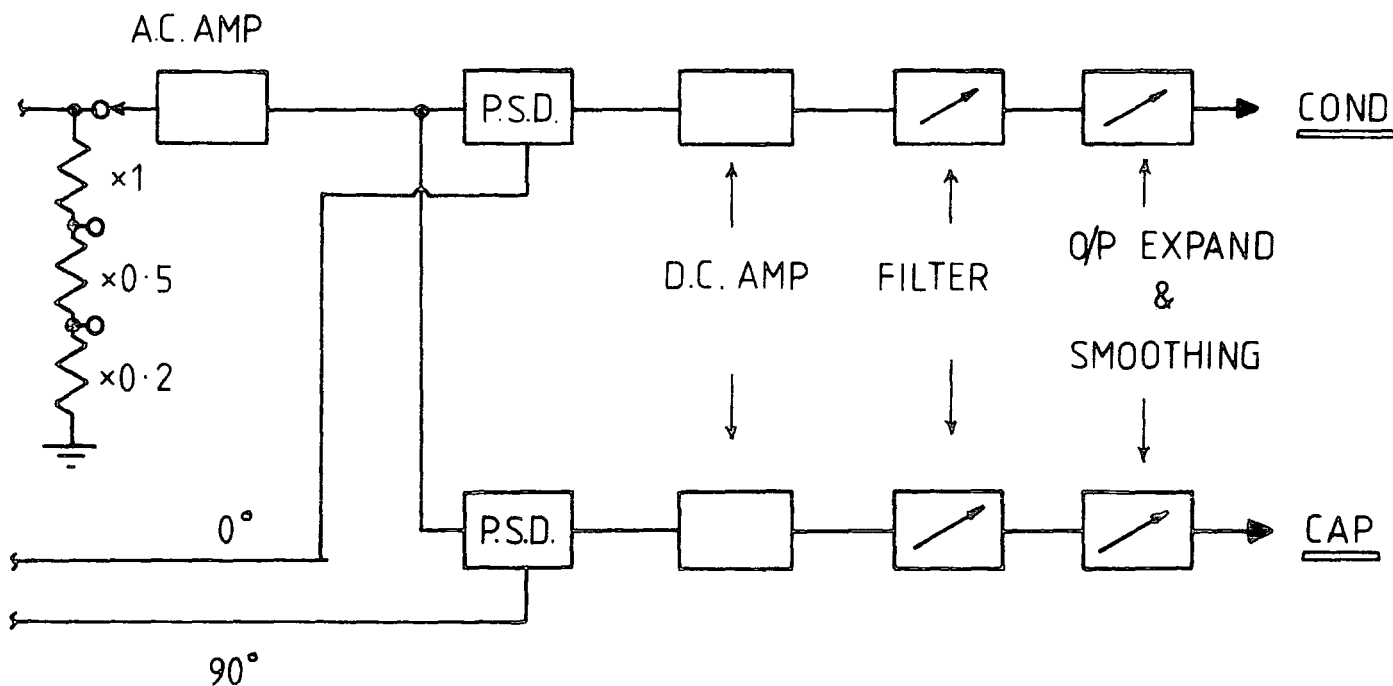
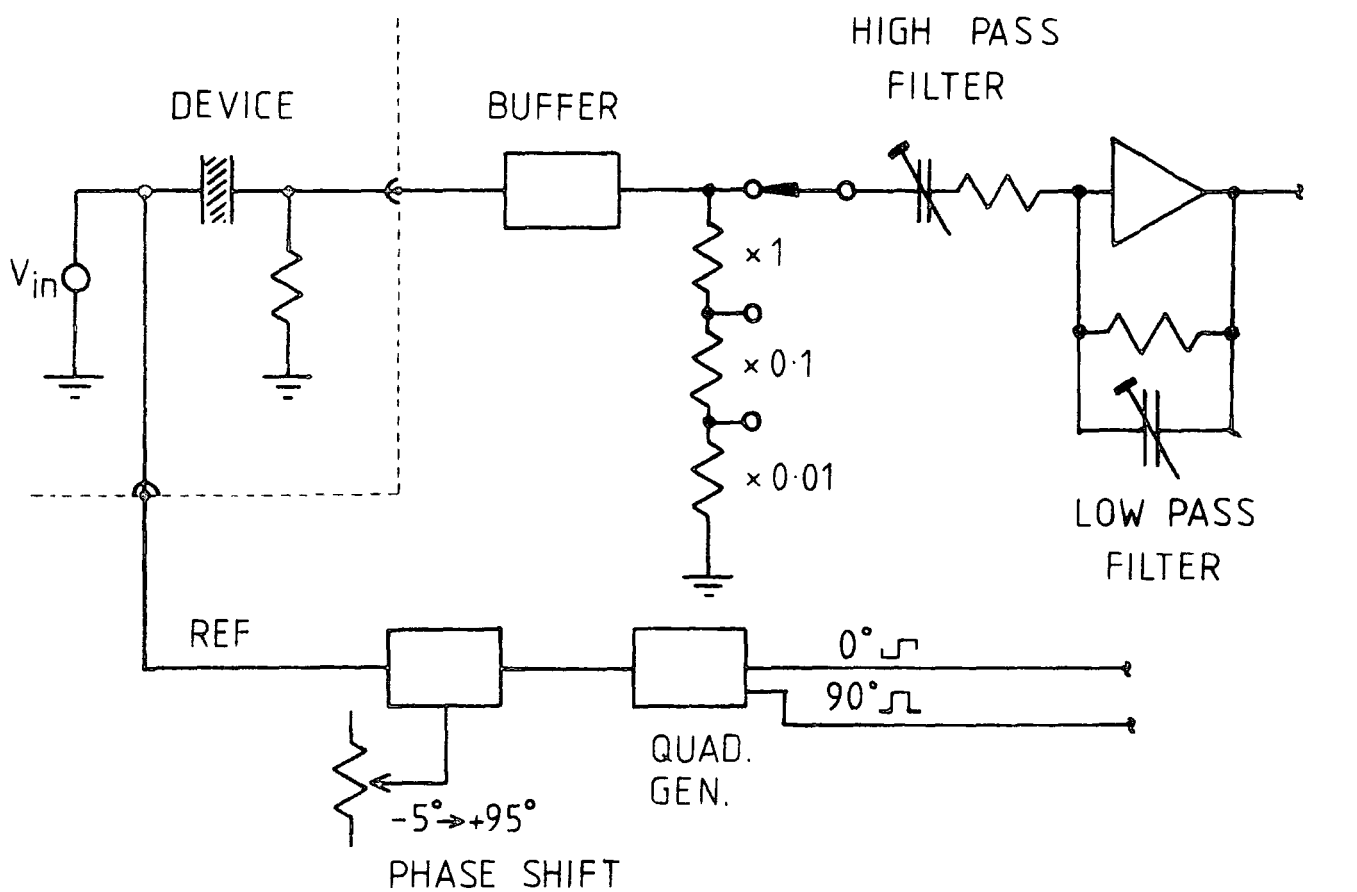


Figure 3.8 : Details of Brookdeal 9502 : Dual channel Lock-in Amplifier.

achieve these operations, special mixer circuits were designed and constructed as follows :-

In simple terms, an MIS device can be considered as merely an ideal capacitance in parallel with a high resistance (to represent leakage). If a voltage ( $V_s$ ) is applied to this device, and the A.C. current through the sample is measured by a resistance  $R_m$  <sup>(19,20)</sup>, (as shown in Fig 3.9),

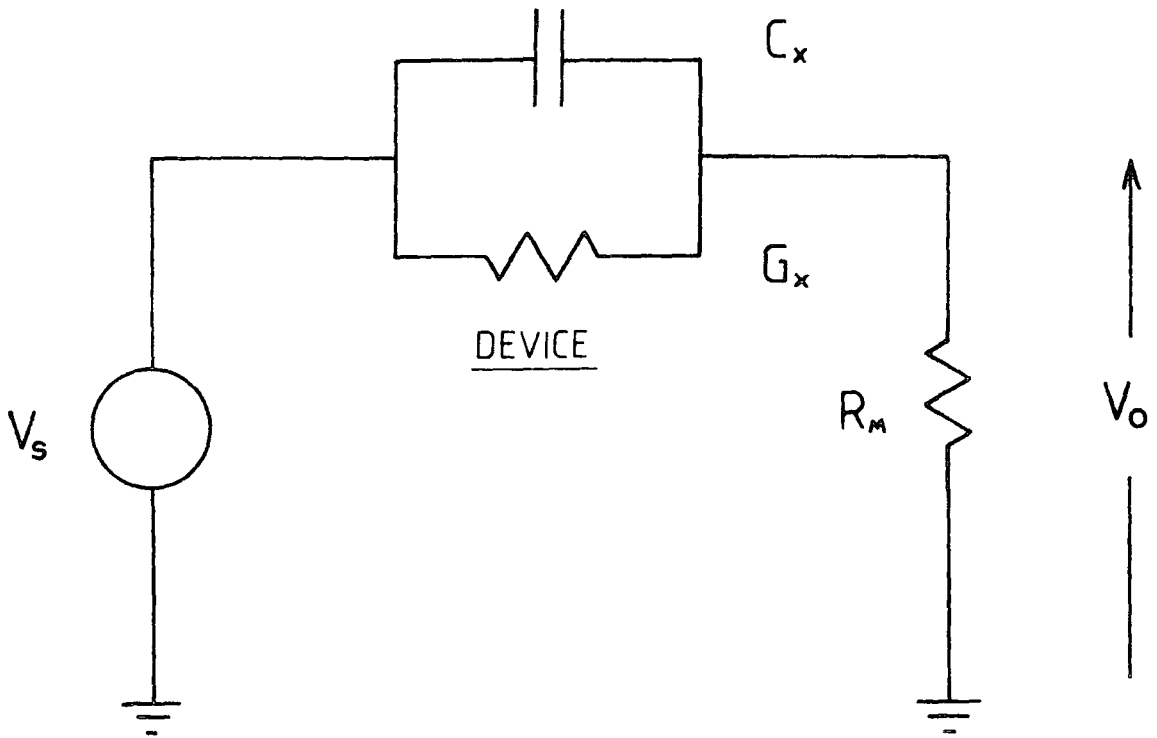


Figure 3.9 : Simplified representation of sample biasing.

it can be shown that ;

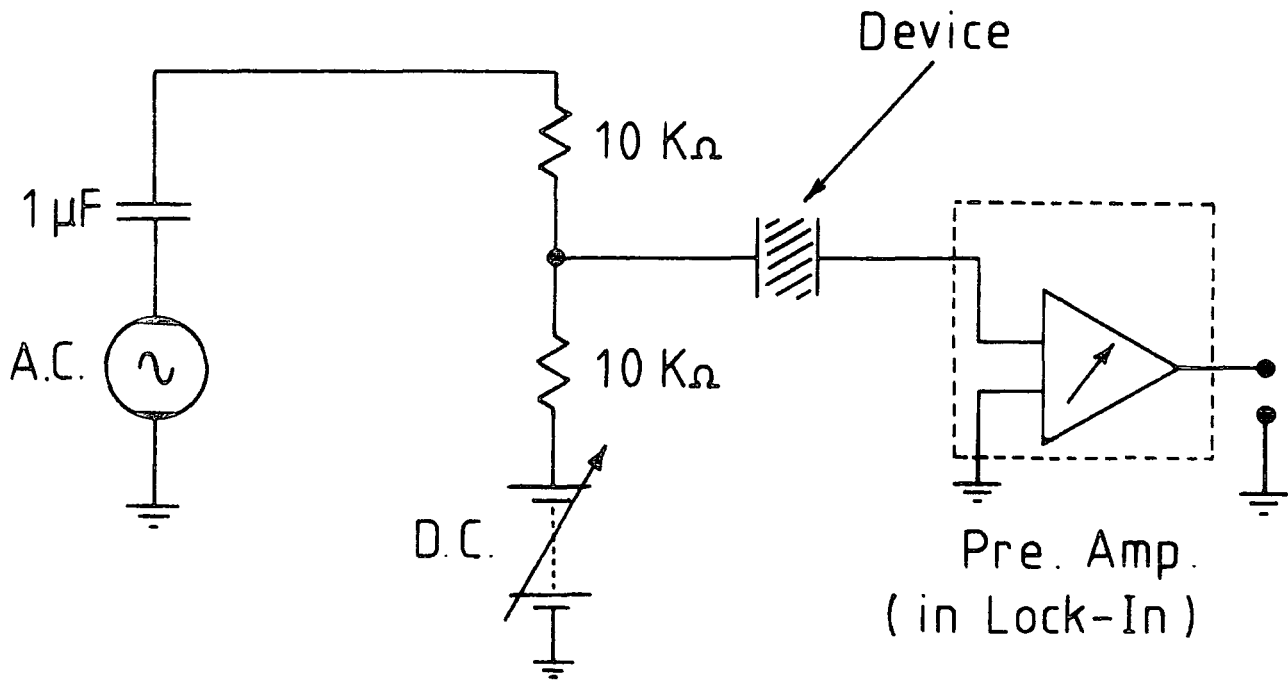
$$v_o = v_s \frac{R_m}{G_x + j\omega C_x} \quad (20) \quad (3.10)$$

providing ;  $R_m \ll 1/G_x$  (i.e. the sample has a high leakage resistance) and ;

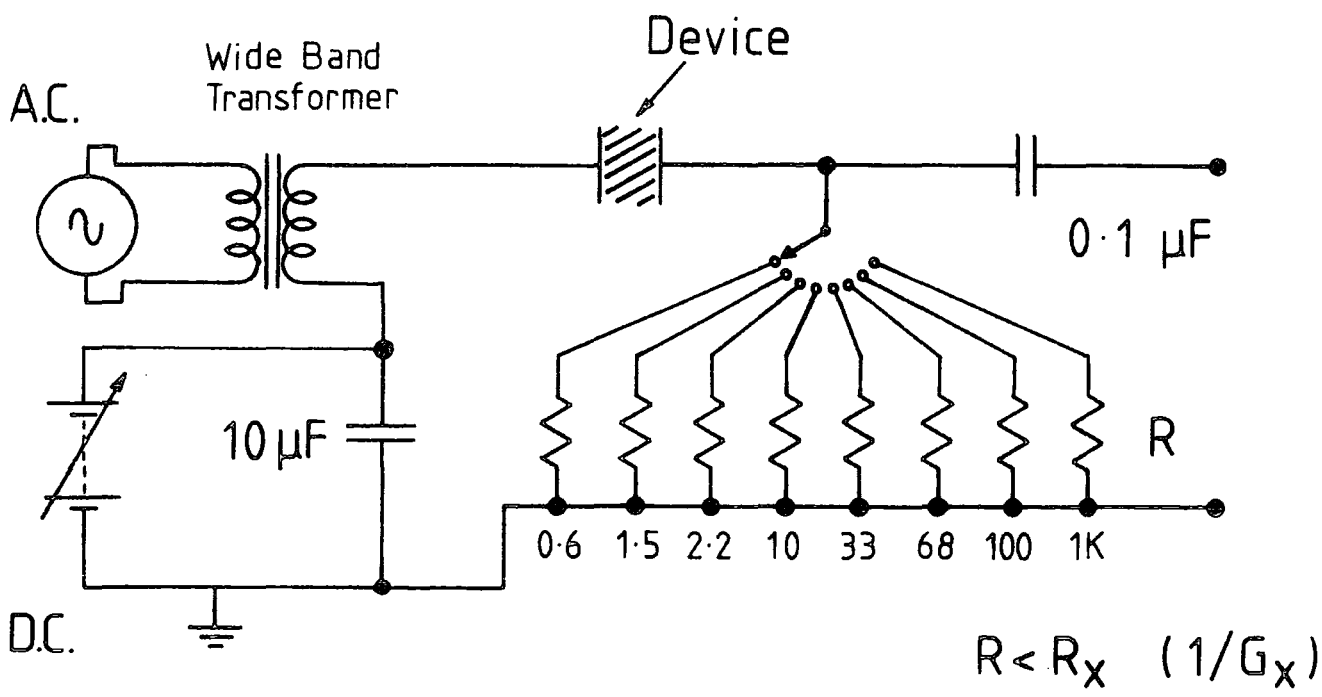
$R_m \omega^2 C_x^2 \ll G_m$ . That is the output voltage is directly related to the component values of the device, and feeding the signal directly into a lock-in will enable each term to be recovered. In practice, the additional conditions imposed by the full proof of the previous relation require the use of two mixer boxes, one for low frequency, and one for high frequency. The two circuits as designed and used are given in Fig 3.10 ; in each case the extra components added in addition to the basic circuit to carry out the AC/DC mixing are also given.

The majority of the remaining equipment used in the complete measurement system was relatively standard, and a complete schematic diagram is given in Fig 3.11 : A wide band oscillator was used as a source for the reference signal, and was attached to the rear of the lock-in for convenience. The necessary low impedance ( 50  $\Omega$  ), and high stability (0.1%/°C) were obtained from a Brookdeal 5012F oscillator. In addition it was necessary to keep the oscillator output to 50 mV (RMS) or less in order to avoid non-linearities occurring at the mixer circuit. The "fixed" D.C. bias used to ramp the device Fermi level under normal plotting conditions was provided by a custom made variable rate unit. This was designed to have a wide operating voltage ; + 15 V, and a variety of ramp speeds, down to 1 mV/sec, all of at least 1% linearity : This latter specification was achieved by the use of a high stability MOS operational amplifier in a feedback RC circuit, with variable value components. A Farnell autoranging digital voltmeter was used to display either channel of the lock-in, or the ramp voltage, as required. In addition, these outputs were recorded on graph paper, as real time plots, by a Hewlett-Packard 7046 A dual pen XY recorder.

At very low frequencies (< 30 Hz) it was found that large amounts of filtering were required in order to reduce the background noise to an acceptable level. This resulted in a relatively long time lag between any



LOW FREQ. ( $f \leq 1 \text{ kHz}$ )



HIGH FREQ. ( $f < 200 \text{ kHz}$ )

Figure 3.10 : Low and high frequency input mixing circuits.

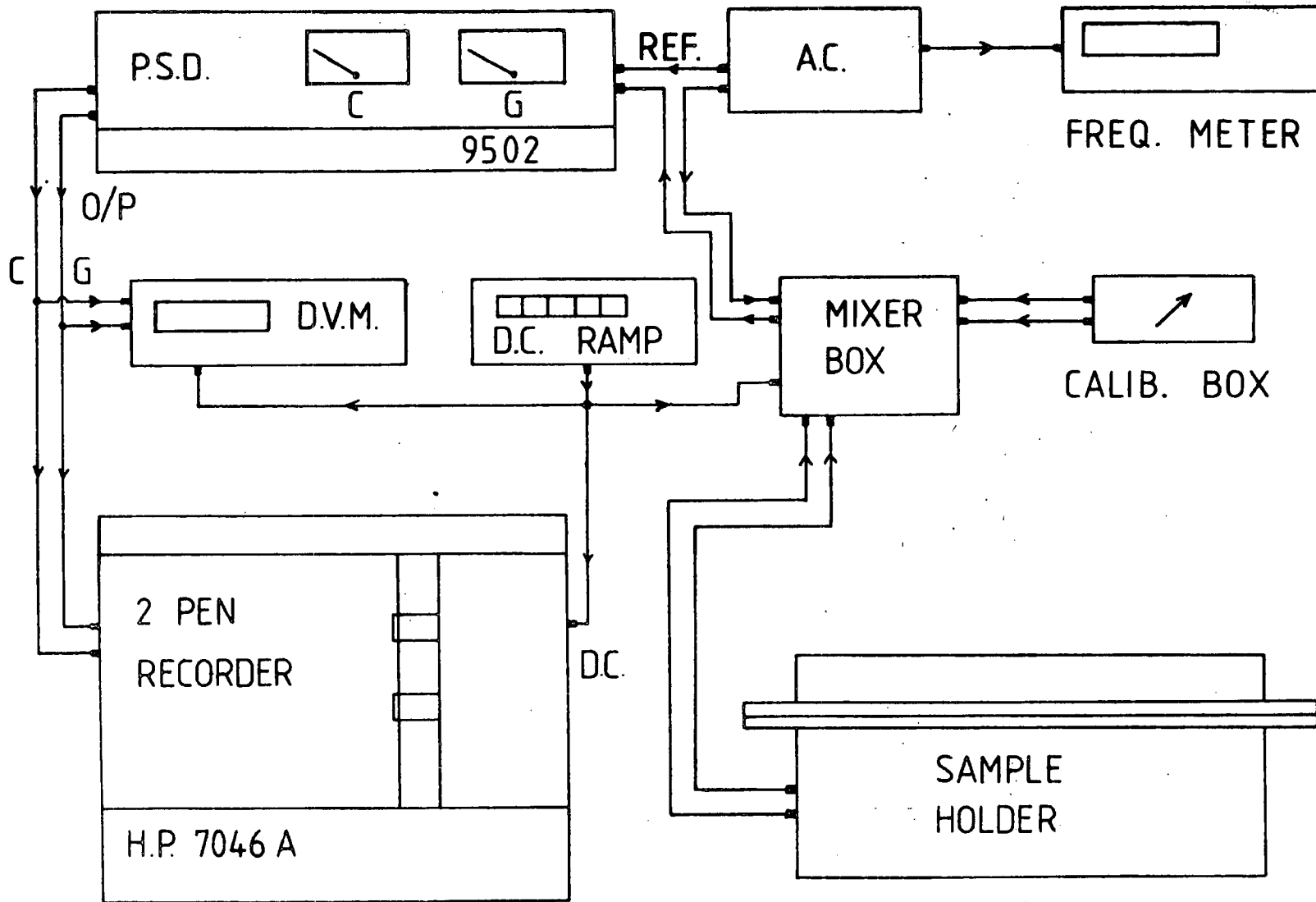


Figure 3.11 : Block diagram of major components in electrical measurement rig.

change in the lock-in input, and its subsequent effect on the output ; thus causing considerable problems during calibration. To ease the situation at these low frequencies a storage oscilloscope was used on a very slow time base to monitor the slow changes in each channel output.

With certain types of device configuration, problems were encountered due to hysteresis in resultant characteristics (see section 2.3). This effect was found to cause unpredictable shifts in both capacitance and conductance curves, and thus make results rather irreproducible. The method adopted to combat this problem was the use of a continuously cycling ramp generator. This function was obtained from a Farnell FG3 function generator, which was set to produce a continuous ramp of 100 mV/sec. In response to this type of signal, a pseudo-equilibrium condition was established in the device, where all the mobile charge moved through the same path on each cycle. This allowed consistent characteristic curves to be obtained and thus enabled some degree of comparison between different preparation paths to be undertaken.

In order to simplify the initial setting up and calibration of the lock-in, a special 'calibration box' was constructed. This consisted of two rotary wafer switches connecting various capacitance and conductance (resistance) values across the output BNC sockets. By switching this box into the input circuit of the lock-in, any value of device component could be artificially simulated during the calibration procedure.

At any given frequency the initial setting up of the measurement system was achieved as follows . Firstly, all residual lead capacitance and conductance were compensated for by using the zero offset controls on the lock-in amplifier. A known value of capacitance , similar to the expected device value, was then switched into the input circuit. The phase control was adjusted to remove any component of conductance occurring on the G channel ; this set  $\cos \phi$  in eqn ( 3.9 ) to unity. The voltage correspond-



ing to this value of capacitance was noted for subsequent use. A similar operation was carried out for the conductance channel, again noting the equivalent output voltage, and this process was repeated two or three times for each channel until each one became totally independent. The lock-in was now calibrated, and the subject device was switched into the input circuit and measurement commenced. Obviously the use of this relatively sensitive instrument created problems due to stray component values, and care was thus required to keep these to a minimum. Where this was not possible the values were recorded, and the device data compensated at a later state.

In normal use, the system was set up to plot capacitance and conductance against applied bias. This was undertaken at a variety of constant frequencies, with the lock-in requiring recalibration at each new one. In some cases, however, variation of C and G as a function of frequency were required, in these cases the bias was kept constant and data obtained on a point by point basis for each frequency.

In concluding this section, it should be noted that the overall accuracy obtained from the system was normally better than 7% ; the worst figures occurring at low and changeover frequencies where noise problems were prevalent. At high frequencies the results were considerably better. It should also be noted that, although most manufacturers claim, and probably provide accuracies of 2-3% in their lock-in instruments, the leads, and ancillary instruments do add considerably to stray components and overall error figures. In addition, instability due to temperature variation was found to cause drift in both offset and phase values for the lock-in, again adding to the overall system error.

In general, however, instrumentation improvement continues<sup>(21,22)</sup>, and newer, more refined equipment is gradually overcoming many of these problems.

### 3.4 ENVIRONMENTAL CONTROL

For the majority of their lifetime all samples were stored in a darkened, desiccated container, maintained under semi-vacuum. For measurement, they were removed and placed in a metal sample chamber (as previously described in section 3.2). This sample holder was maintained under similar inert conditions for the majority of the time ; except when access was required for contact changing, etc. In addition, the chamber could be totally evacuated or purged with dry nitrogen if required.

The investigations into the effect of gases on the MIS interface region inevitably involved dealing with toxic gases and vapours. In consequence special handling and mixing apparatus had to be developed : To this end, a custom glass mixing rig was constructed, with two input lines and a demountable final section. Each input channel was equipped with a flow meter and needle valve control, and the demountable section allowed a gas sample to be removed for mixture analysis.

Dreschel bottles were used for vapour pick-up and handling, normally with nitrogen as the carrier gas. This inert carrier was bubbled through the volatile liquid and thus inevitably picked up some vapour and transported it along to the sample chamber.

Standard 1.6 litre gas bottles<sup>(23)</sup> from BOC were used as sources for the majority of gases ; cylinders of hydrogen/nitrogen, CO/nitrogen etc. were all readily available. Toxic liquified gases in pure form were obtained in smaller lecture bottles ; the use of these was, however, avoided as far as possible, for reasons of safety.

Although long term characterisation of gas effects required continuous flow conditions, it was found useful in addition to provide the facility of impulse exposure. This exercise was relatively quick and thus proved useful for highlighting significant characteristic changes as a precursor to

longer tests. For impulse testing, a large non-porous rubber balloon was filled with a known volume of carrier gas ; normally nitrogen. It was then injected with another known volume now much smaller, of test gas. This was achieved by using a Hamilton<sup>(24)</sup> 0.5 ml precision gas tight syringe. The mixture in the balloon was now ready to supply the sample chamber as required. During exposure to toxic gases, the sample and sample chamber were placed in a sealed glove box to provide an additional safety envelope. The latter was also fitted with gas tight BNC lead-throughs and various gas supply and removal pipes. A schematic diagram of the whole system is given in Fig 3.12.

For a normal experimental run the pre-sealed sample chamber was placed in the glove box, and all the required electrical connections were made. Pipes were connected between the entry/exit feedthroughs on both the glove box and the sample chamber, with Dreschel bottles in line if needed. In addition, the final gas escape line was passed through another Dreschel bottle to indicate the gas flow rate through the sample chamber. After any gas run both the glove box and sample holder were thoroughly flushed with nitrogen before being opened to the atmosphere in order to avoid hazards from residual gases. Throughout measurements, special gas masks and safety spectacles were always worn to protect the operator at all times. It is worth noting in addition that early investigations with standard plastic piping showed that this material was in many cases porous to toxic gases, and indeed gases in general. In consequence, the majority of pipework was constructed from special rubber piping (Butyl XX synthetic- ESCO Rubber Co.Ltd, Teddington) which was guaranteed non-porous.

The overall system, although appearing rather untidy to the eye, worked very well in practice, and adequately served the purpose for which it was conceived . That is, to provide a wide range of stable or toxic environment, and allow exposure of the latter to any given sample over a variety of time periods.

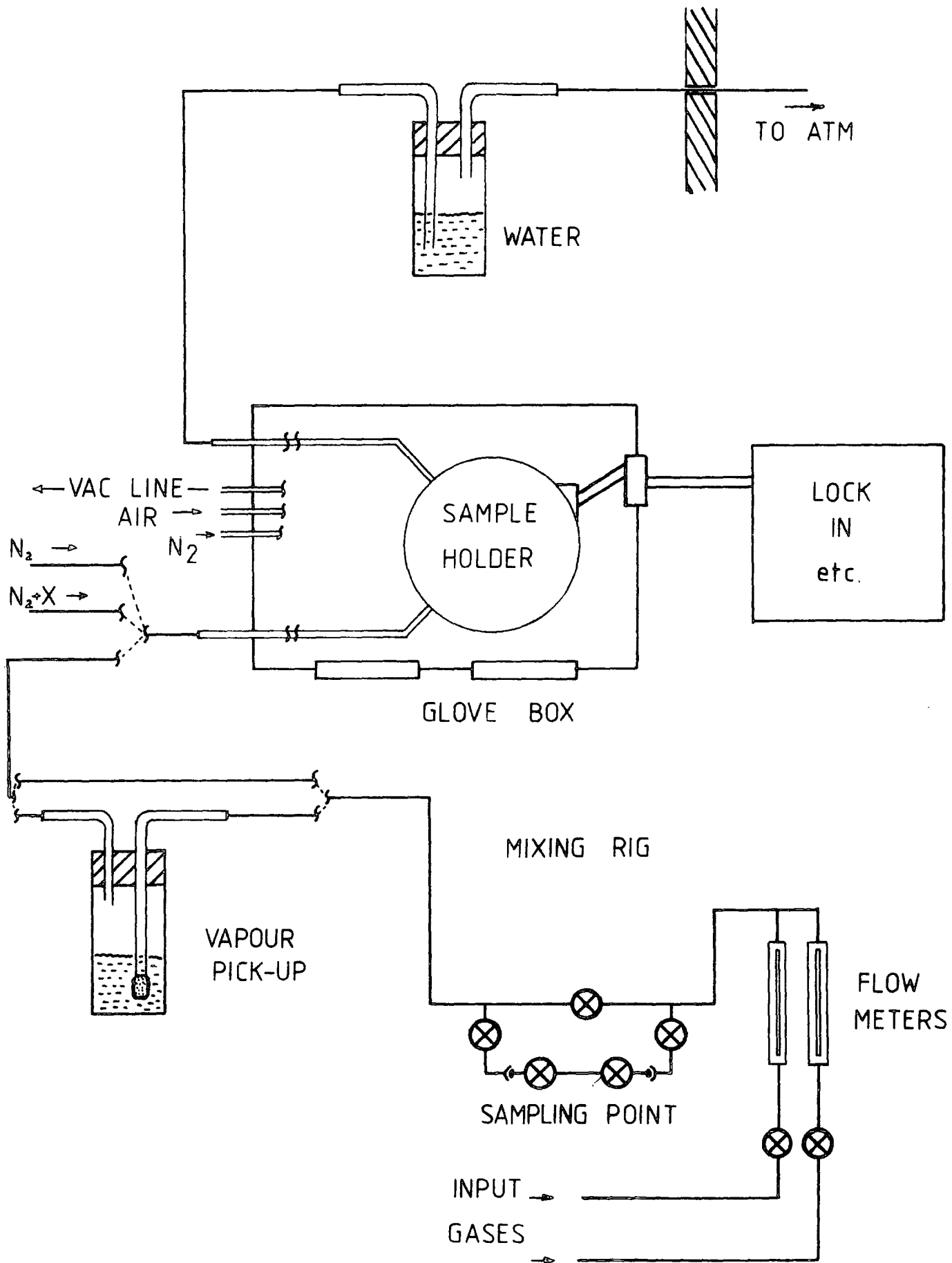


Figure 3.12 : Schematic layout of gas handling and mixing system.

## CHAPTER 4

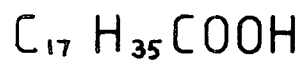
### LANGMUIR FILM TECHNOLOGY

This chapter is the first of four covering Langmuir films, their deposition and characterisation, and looks briefly at the history of the technology. In addition to introducing the concepts and terminology used throughout the thesis, this chapter aims to describe the development of the technique, and review some of the work already undertaken. Section (4.2) is an historical review, which discusses past contributions to Langmuir film technology beginning with the earliest reported work of Benjamin Franklin. This is followed by a section dealing with electrical characterisation results, which also gives a description of the current ideas concerning conduction in organic films. To conclude the chapter, some details of more recent applications of these materials in various fields of science are discussed, this is included to demonstrate the considerable interest currently being shown in Langmuir film technology.

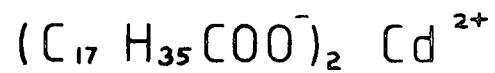
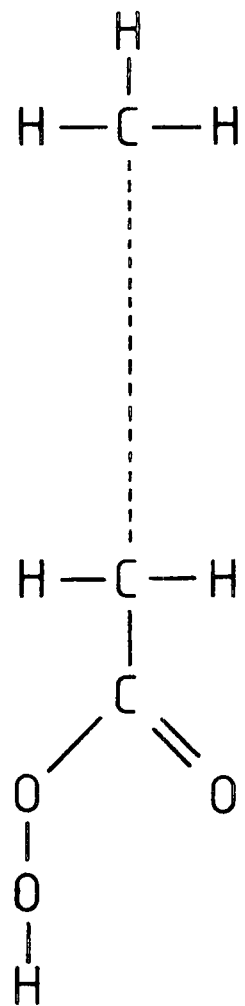
#### 4.1 SOME BASIC CONCEPTS

The production of a Langmuir film basically entails the compression of a thin layer of material, normally upon the surface of a liquid sub-phase, to form a monomolecular solid layer. This film is then transferred onto the substrate by repeatedly passing the latter through the monolayer, and picking up one layer on each transition. Using this procedure, a film of known thickness can be built up on many types of solid substrate.

The subphase normally used is water ; this is required to be extremely pure to avoid influencing the properties of the monolayer, and therefore usually undergoes considerable purification before use. The material used to produce the monolayer, and subsequently the Langmuir film multilayer must have certain properties ; in particular it must be amphipathic in order to align correctly on the surface of the water. This criterion requires that the molecule has a hydrophobic (water insoluble) group at one end, and a hydrophilic (water soluble) group at the other. This property, normally characteristic of long chain molecules ensures the material forms a regularly ordered structure when compressed to produce the solid monolayer. In practice there are many compounds which fulfil this requirement of which the majority are organic in nature. The work reported here however concentrates on one or two relatively simple materials, specifically stearic acid, and its salt cadmium stearate. Some of the other suitable materials and their particular usefulness are discussed in general terms in a later section. The chemical structure of stearic acid is shown in Fig 4.1, along with that of its cadmium salt, cadmium stearate. Once spread upon the surface of the subphase, the amphipathic material is compressed with the aid of a barrier ; in this case a constant perimeter variable area one. This compression causes the initially highly dispersed material to be concentrated into a solid monolayer , from which pick-up onto the substrate can be generated. During the compression operation it is, of course, very important to monitor the surface pressure of the spread monolayer. This ensures that the correct amount of barrier contraction is produced and that no collapse mechanisms are generated within the film. The monitoring of the surface pressure ( $\pi$ ) is normally undertaken by means of a Wilhelmy plate connected to a microbalance, whereby the plate generates a zero contact angle with the liquid surface, and so converts a horizontal pressure to a vertical one. In practice it is convenient to



ACID



SALT

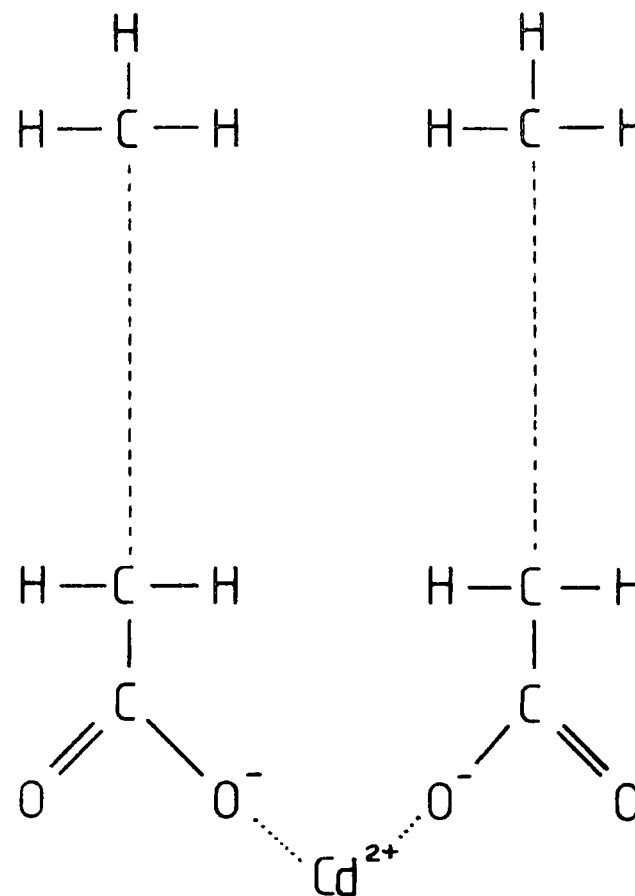


Figure 4.1 : Representation of chemical structure of stearic acid, and its cadmium salt.

draw an analogy between the compression of the surface monolayer, and the compression of a normal gas. In both cases, the materials pass through gas, liquid, and solid phases, the recording of which is normally called an isotherm. An example of this type of plot is given in Fig 4.2 ; in this case for a stearic acid monolayer.

Once compressed into a two dimensional solid, the monolayer is deposited onto the substrate by passing the latter through the interface region. During this operation, under ideal conditions there are three different modes of material pick-up. These are termed X, Z, and Y, and are respectively, pick-up on the way down only, on the way up only, and in both directions. These different deposition modes are illustrated diagrammatically in Figs 4.3 - 4.5. It is in this general deposition behaviour that the elegance of the Langmuir-Blodgett technique lies, for once the molecular length is known it is possible to predict or define the precise thickness of the resultant multilayer. Indeed, this technique is probably the only means of defining the thickness of a deposited film to the accuracy of less than one angstrom.

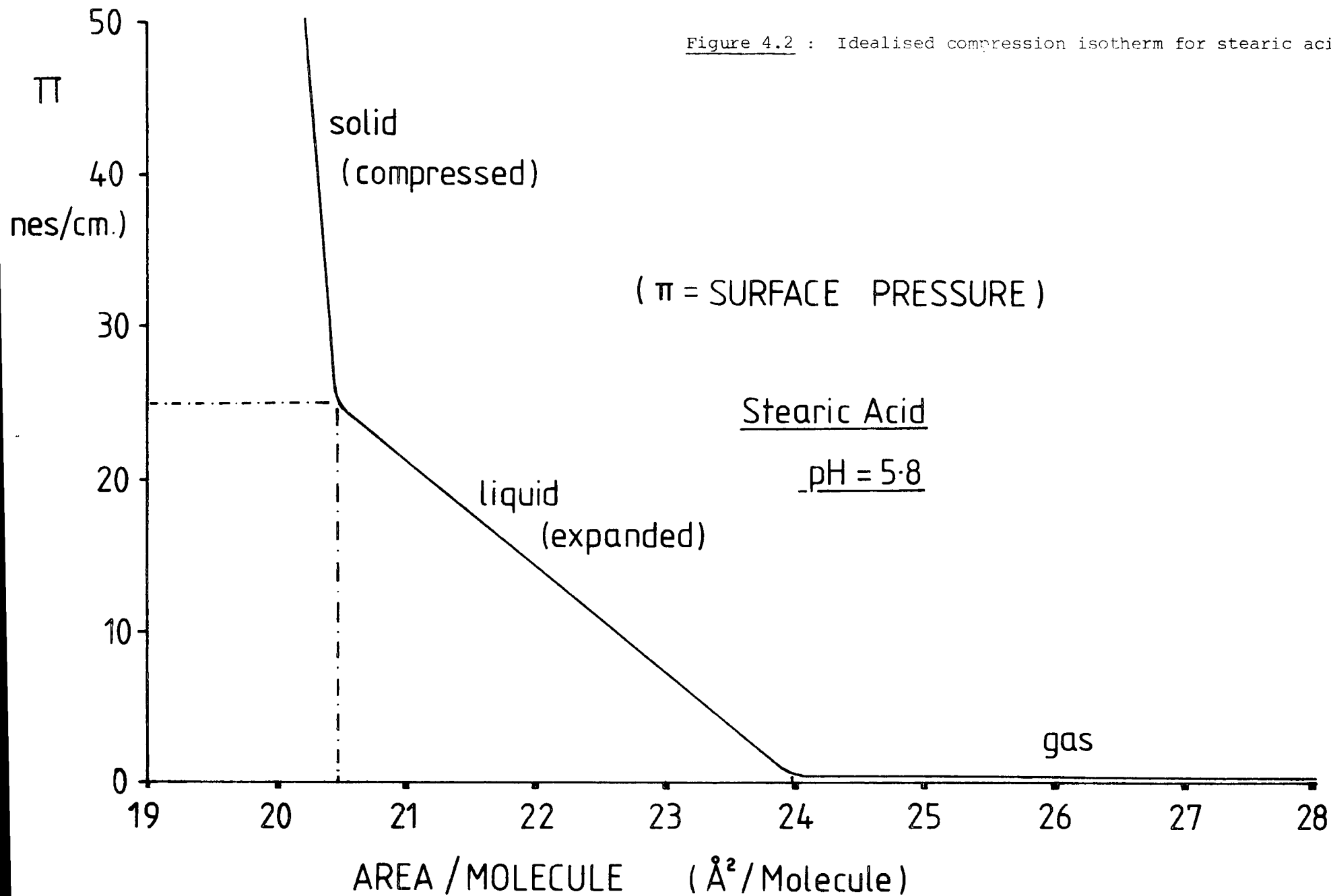
In concluding this section, it should be noted that the procedures mentioned here are relatively simplified, and in practice there are many additional details to be considered. In particular, the need for extreme cleanliness cannot be overstressed. These additional practical details will however be discussed at length in later chapters.

#### 4.2 HISTORICAL REVIEW

Before discussing in detail the results of recent electrical characterisation work, it is useful to look at the historical development of Langmuir films and their deposition.



Figure 4.2 : Idealised compression isotherm for stearic acid.



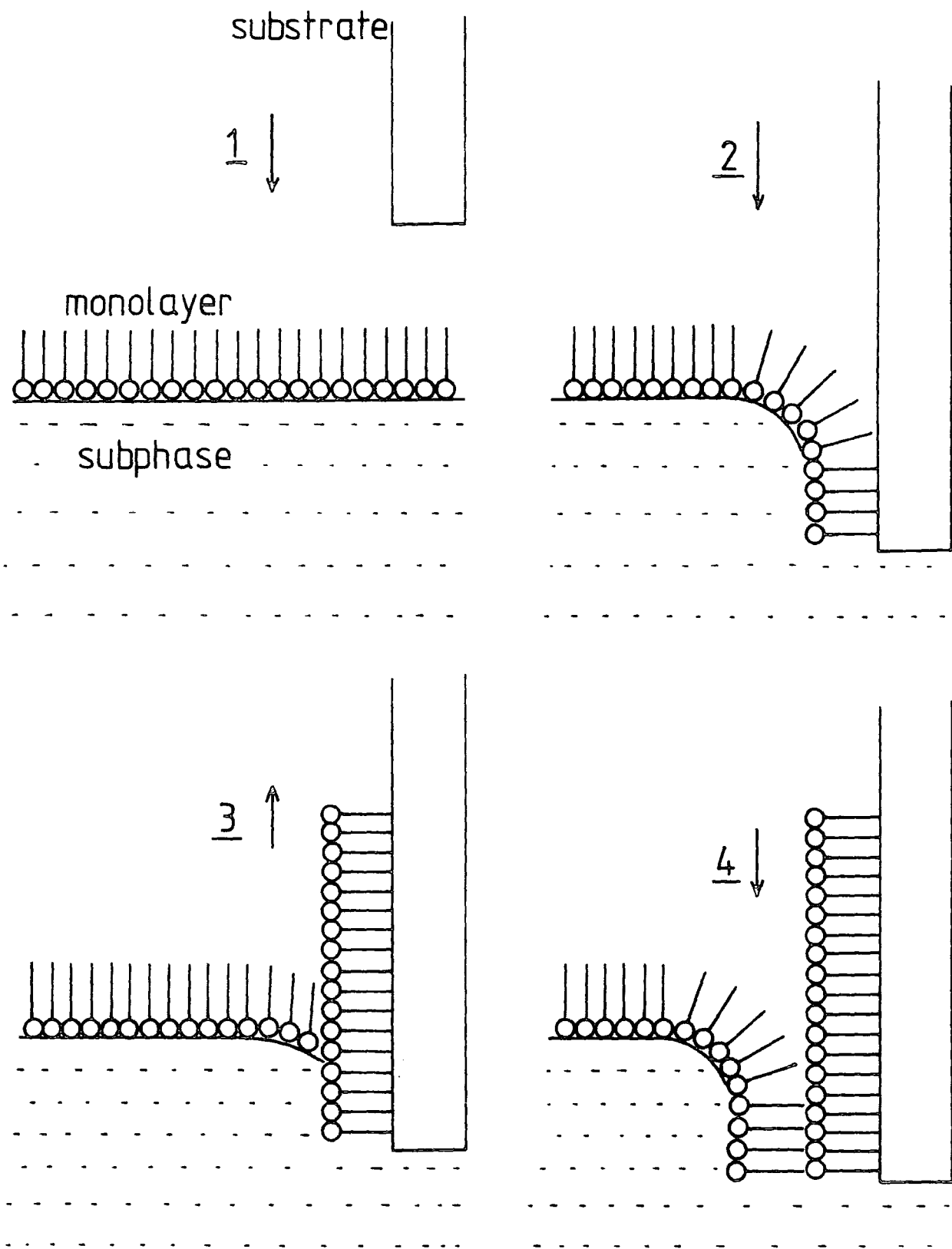


Figure 4.3 : Schematic representation of X-type deposition.

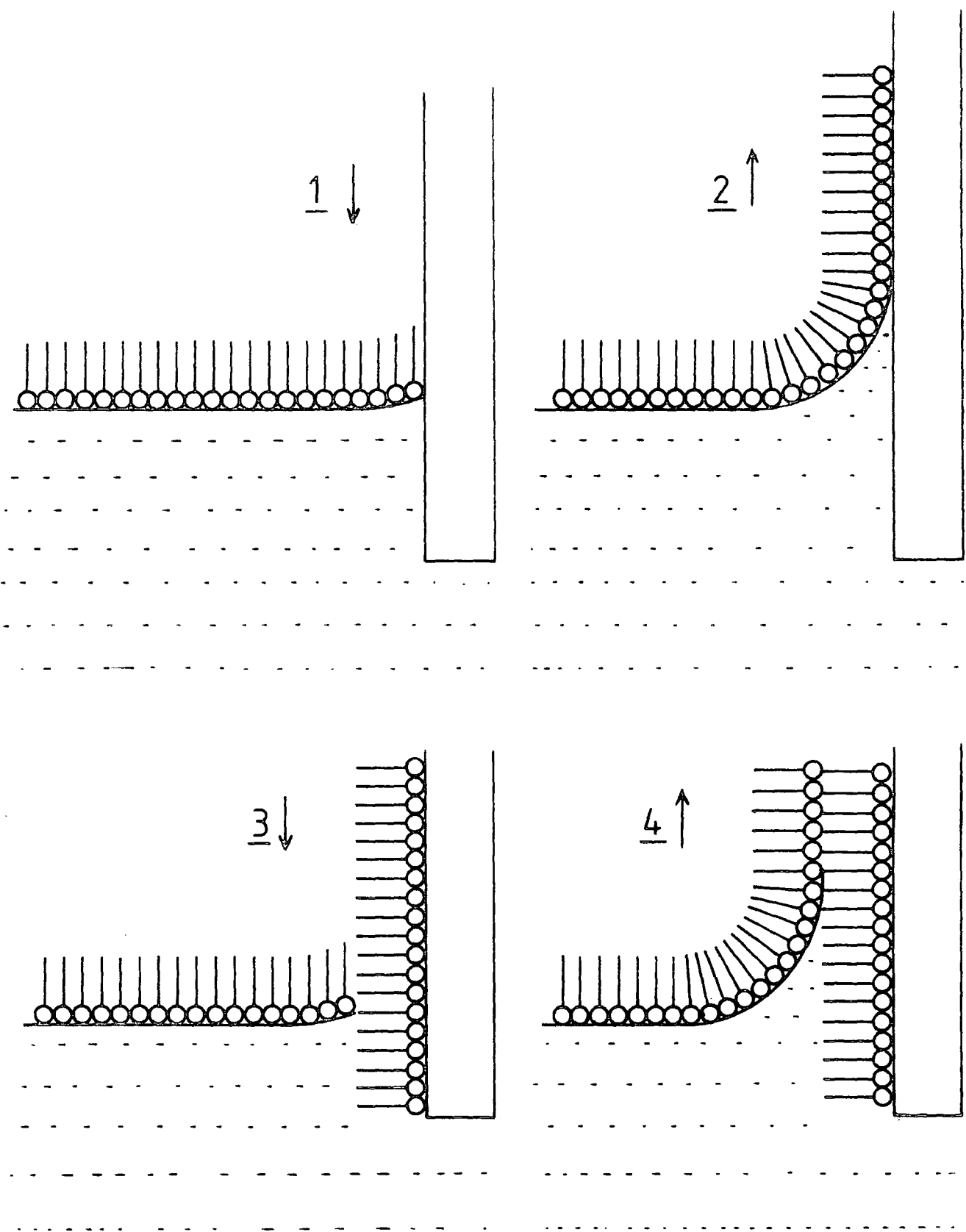


Figure 4.4 : Schematic representation of Z-type deposition.

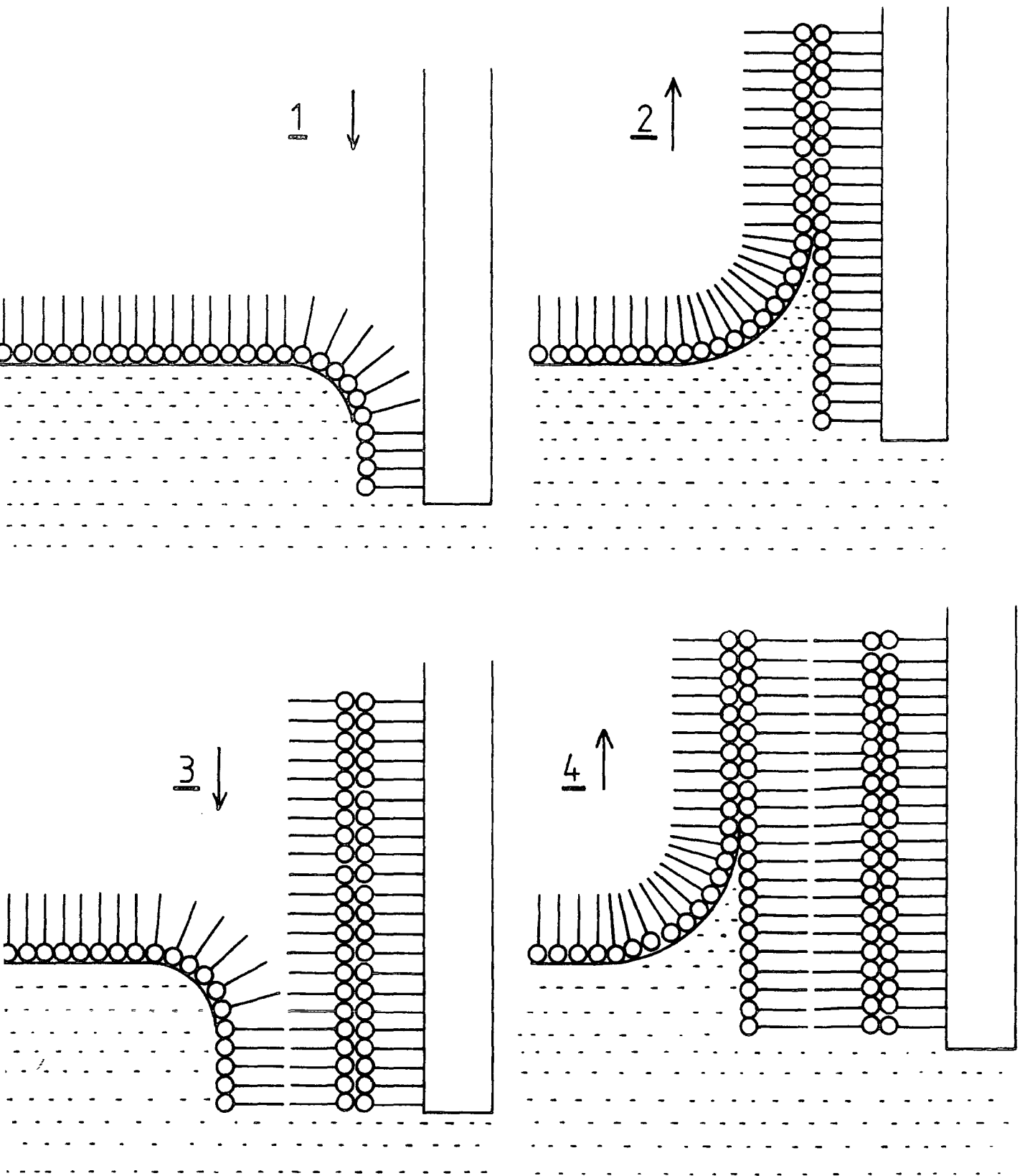


Figure 4.5 : Schematic representation of Y-type deposition.

The earliest reported experimental work pertaining to oil films on the surface of water was by Franklin<sup>(1)</sup> in 1774. During this work he noted "The amazing spreading of small amounts of oil over vast areas, causing considerable smoothing of the surface". It was many years however before any methods for control and manipulation of these films were proposed. The earliest record of this was by Fraulein Pockels, who in 1891<sup>(2)</sup>, used tin barriers laid across the top of brim-filled troughs to measure the variation of surface tension on contaminated water. Some ten years later, Lord Rayleigh<sup>(3)</sup> began to consider the structure of these "new" films, and concluded they were in fact only one molecule thick. The subsequent period until the classic work by Langmuir and Blodgett generated only minimal interest, and many workers remained unconvinced about the usefulness and structure of these films. It was in 1917 that Irvine Langmuir began to develop the theoretical concepts<sup>(4)</sup> that attempted to explain previous observations, and later with Katharine Blodgett<sup>(5,6,7)</sup> devised a process to control and transfer these monolayers onto solid substrates.

The original Langmuir Trough was a metal container brim filled with purified water in order to produce a convex meniscus. The inner faces of this trough, together with the metal control barrier, were rendered hydrophobic with a layer of paraffin wax. This aided the formation of the meniscus. A simple hand winder attached to a pivoted overarm was used to raise and lower the substrate. This was used because it was "difficult to lift a slide slowly with forceps held in the hand without an occasional backward hitching motion". A small pinch-clamp was used to hold the substrate. This was initially cleaned in hot sulphuric acid and potassium dichromate, followed by a rinse in distilled water. In order to achieve a constant surface pressure during film deposition, a tiny drop of oleic acid was added to the water at one end of the trough. This was separated from the stearic acid by a floating silk thread. The hydrophobic oil was found to have molecules that spread out

to consume all the available area thus exerting a defined pressure on the perimeter. The excess material remained gathered on the surface in small lense-like globules. Upon the barrier moving, and new space becoming available, the oil spread immediately from these lenses to occupy the new area. Thus the oleic acid spread at one end of the trough, acted as a piston to compress the stearic acid at the other side of the barrier to a constant surface pressure. In the case of oleic acid this value was 29.5 dynes/cm. Initial cleaning of the water surface to remove previous monolayers and any dust etc. was achieved by repeated passage of the metal barrier backwards and forwards over the subphase. The silk thread barrier was coated with wax to enable it to float on the water, and was anchored to the trough sides at each end. "The thread is waxed by being soaked in a benzene solution of paraffin wax and dried ; it must not take up so much wax that it becomes stiff". For deposition, the subphase was initially sweep cleaned, and a few drops of stearic acid dissolved in benzene were placed at one side of the barrier. The solvent was found to rapidly evaporate, leaving behind an invisible layer of stearic acid. The piston oil was then gently placed at the other side of the silk thread, as shown in Fig 4.6. Repeated passage of the substrate through the film resulted in removal of stearic acid onto the slide and the spreading of piston oil as the barrier was forced to contract. The pH of the water was controlled by the addition of alkali (calcium or sodium hydroxide) or acid (hydrochloric) and the resultant values were measured by indicators matched to La Motte standards. Reference to the original papers will show the necessarily meticulous attention paid to cleanliness in order to achieve acceptable results. All the chemicals were thoroughly purified, and tested for contamination by any means available. Liquids were filtered in sand, and solids were tested by melting point measurements, both as standard operations.

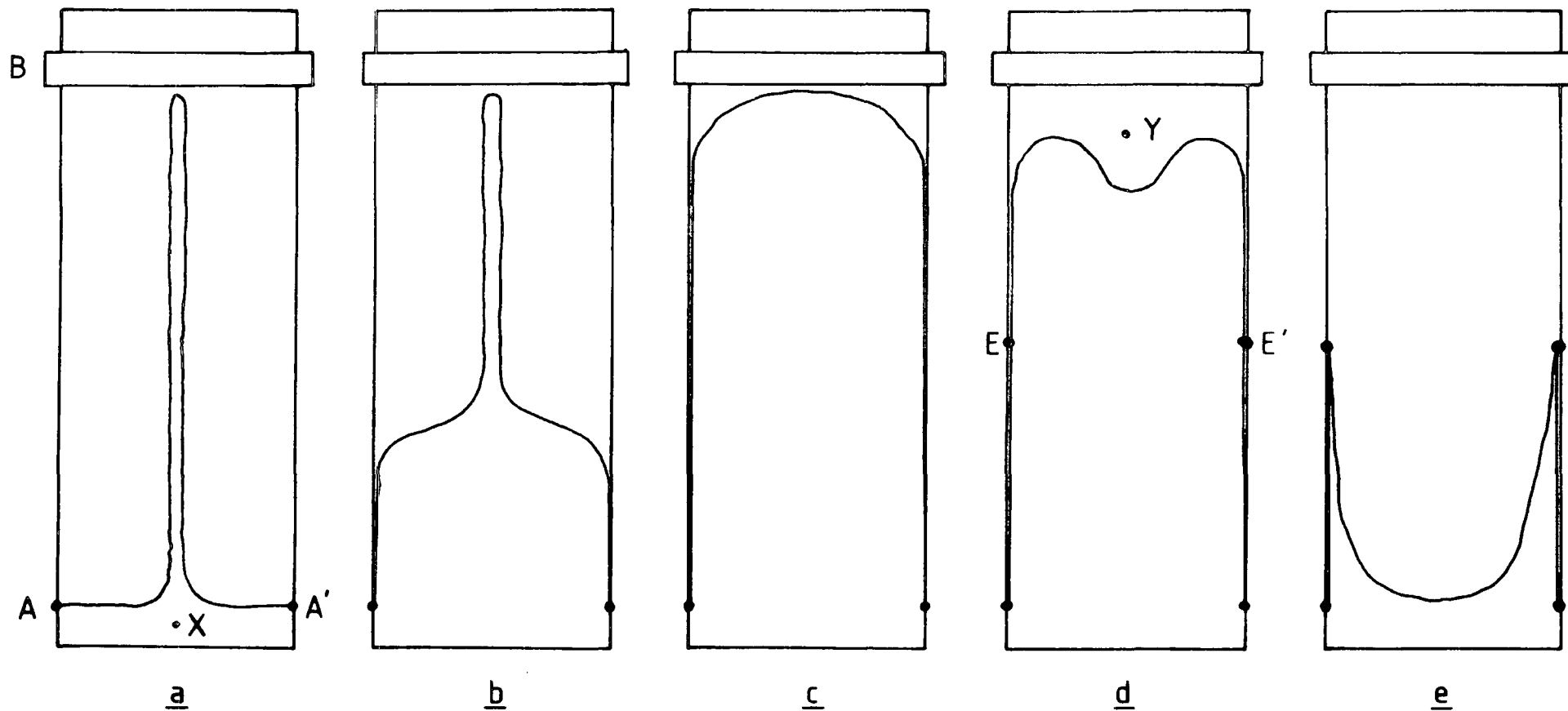


Figure 4.6 : Original Langmuir/Blodgett trough, showing (a) equilibrium, (b,c) after addition of fatty acid at X, (d) after addition of piston compression oil at Y, and (e) after removal of film onto substrate.

Langmuir and Blodgett found that the pH of the subphase, together with the metal ion type and concentration, both had marked effects on the properties of the resultant film. Together they undertook lengthy investigations to characterise these effects. They used optical and simple dielectric constant measurement procedures to test the effects of temperature, substrate variation, and film thickness, and even suggested potential applications in many cases. The majority of the results they obtained are correct to the present day, and this fact alone is no small tribute to their conscientious and dedicated approach to this new field. In fact the original Langmuir and Blodgett papers still remain a standard reference for anyone starting in this area.

In the years after this classic work, many more people began to look again at monomolecular films. Race and Reynolds<sup>(8)</sup> in the same General Electric Research Laboratory undertook more detailed electrical investigations of these organic materials. They looked mainly at changes in dielectric properties and their variation with frequency etc., by using a mercury drop as a top electrode. Also in America, Clark and Sterrett<sup>(9)</sup> looked at these new films using X-Ray diffraction techniques and provided valuable information about their ordered structure, stacking sequence, and molecular chain lengths. In England, the Department of Colloid Science at Cambridge was the home of work by Rideal and Schulman, whilst in France, Devaux and Marcelin continued to produce useful contributions. Books by Adams<sup>(10)</sup> and Rideal<sup>(11)</sup> were at this stage relatively new, and so contained summaries of current work. These included recent developments in surface potential, and surface viscosity measurements, both of which were found to be critical parameters in the investigation of film structure.

The Second World War caused the virtual termination of work in this field, and many years passed before any more significant developments were



made. In fact it is only in the last decade or two that investigations have restarted, and these have caused such a rapid expansion of interest that consideration of all avenues has become near impossible.

The monomolecular nature of the films along with their ordered packing arrangement has produced interest from all fields of science. In chemistry, their controlled molecular structure has enabled investigation of bonding mechanisms to be undertaken. Biologists meanwhile, have seen the useful resemblance of these films to biological cells and are attempting modelling of membrane behaviour. For physicists, the films are useful in optical and electronic devices, where their well defined thickness provides control previously unobtainable. In addition to all this high level work, basic properties like surface pressure, molecular packing, and stacking arrangements, are all still being actively investigated and show that a great deal about Langmuir films still remains to be understood.

It is interesting to note that in spite of modern day complications with measurement and analysis equipment, the basic trough and spreading system remain largely unchanged from the earliest design. Indeed some current workers, even today, use floating silk barriers and piston oil compression. Developments have of course occurred, but these are mainly in the area of barrier design and compression systems. An interesting deviation from the original rectangular design is a circular trough, using one or two centre pivoted radial arms as mobile barriers. The trough is still brim filled as before, but now precision engineering avoids any film leakage at the barrier/trough junction. Dipping is achieved in this design by the use of a mechanical screw drive system, and the surface pressure is monitored by a microbalance (see later). This development of the ability to measure surface pressure was one of the major steps forward in the history of Langmuir film technology. It allowed the monolayer compression to be measured directly, and thus avoided the use of piston oil compression. In addition, this advance allowed the adoption of independent

barrier compression systems, and so removed the need for crude silk waxed barriers. It should be noted, however, that at this stage the pressure measurement and barrier control were still totally independent, and largely manually operated. Automatic feedback control systems were not incorporated for many years to come.

In 1966, Gaines published his book "Insoluble monolayers at liquid-gas interfaces"<sup>(12)</sup>; this was a long in-depth review of current work on Langmuir films and other associated subjects. By dealing with all aspects of monolayers from the physics of surface tension, to multilayer deposition, Gaines produced a book that has become a classic in this field of work.

The following year, a paper appeared by Jaffe et al<sup>(13)</sup> proposing a radically different form of barrier system for use in Langmuir troughs. This idea used a constant perimeter glass fibre belt suspended on free running rollers. These rollers were attached to two mobile overarms, which, by clever geometry, could be moved to change the enclosed area (see Fig 4.7). In practice their application of this new barrier system was not particularly relevant to Langmuir films, but the suggestion had been made, and it was not long before the system was used by others.

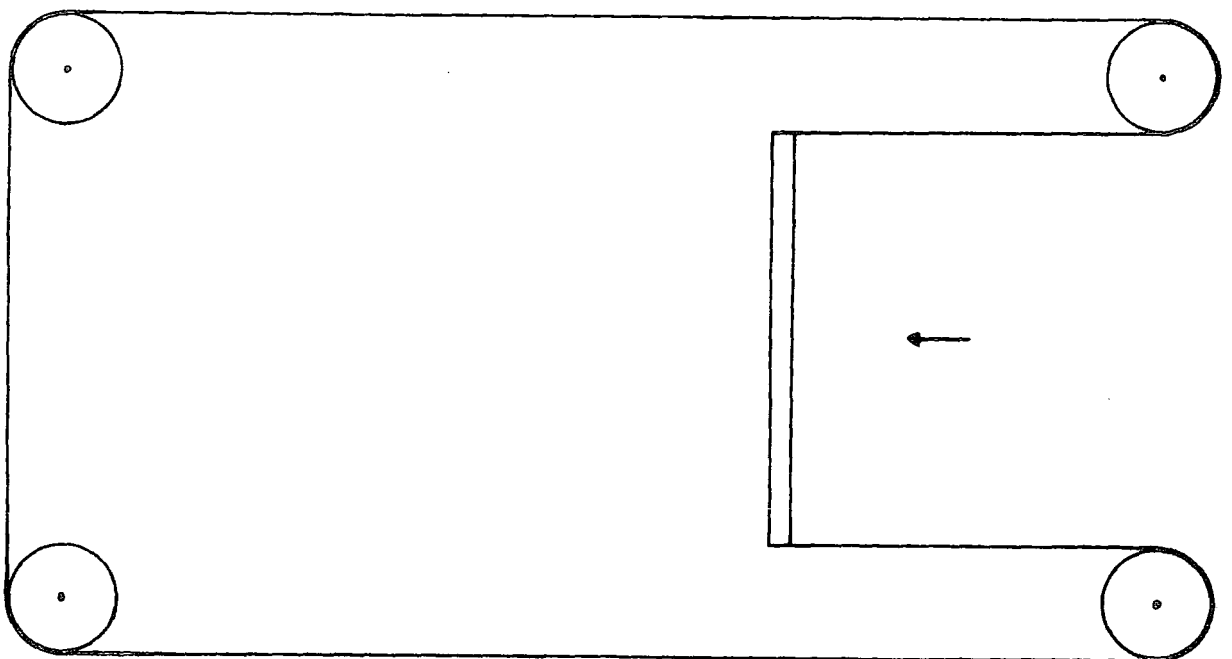


Figure 4.7 : Early example of constant perimeter compression barrier  
(After Jaffe et al, Ref.13).

The final stage in the development of the modern Langmuir trough was the adoption of automatic feedback to control the compression barrier. This was developed by Kuhn et al<sup>(14)</sup> for the circular trough, and by a collaborative effort between the ICI Corporate Laboratory (Runcorn) and the University of Durham<sup>(15)</sup> for the constant perimeter one. This final advance overcame persistent irreproducibility problems previously encountered with all electrical measurements, by enabling constant surface pressures to be maintained throughout the deposition. From this point forward, film quality and results were shown to improve considerably and the development of the Langmuir trough was complete.

This brief review has outlined some of the more important developments in this field. It is by no means comprehensive however, and the reader is therefore directed to one of the many recent review articles<sup>(16-21)</sup> for more detailed information.

#### 4.3 REVIEW OF PREVIOUS ELECTRICAL CHARACTERISATION

It is only relatively recently that meaningful electrical characterisation of Langmuir films has been undertaken; in consequence no single well defined explanation has yet become established. This section is, therefore, designed to briefly review and summarize the current ideas about electrical conduction in Langmuir films, in order to provide a background for the results obtained by the author, as presented in later chapters. It is convenient to divide this review into basically two parts, that is, AC and DC characterisation results.

In general, electrical characterisation requires considerably greater film perfection than is needed for optical or other work. Results obtained by early workers in consequence tended to be very irreproducible due to film defects, impurities, etc, and are thus only of historical interest<sup>(17)</sup>. The majority of useful measurements have therefore only been taken in the last

decade or so. In addition, it should be noted that although characterisations of a great variety of materials has been reported, this review will concentrate primarily on fatty acids and their salts, as these are the major subject of this investigation.

It has also been found by most authors that high quality films cannot be deposited onto substrates like gold and silver, due to their lack of surface oxide. The majority of studies have, therefore, used an aluminium film (with  $\text{Al}_2\text{O}_3$ ) on glass as a substrate, the oxide having been previously shown to be adequately conducting.

#### 4.3.1 DC Conduction : Tunnelling

The Langmuir-Blodgett technique lends itself very well to the investigation of insulator tunnelling properties. In this situation, the ability to produce thin films able to stand very high DC fields ( $10^6$ - $10^7$  V/cm) can be seen to be a useful property.

Measurements carried out by Kuhn et al<sup>(22,23)</sup> in 1971 demonstrated for the first time an exponential dependence of low field conductivity on insulator thickness. This was achieved by using one monolayer of a variety of different fatty acid chains. From the slope of the resultant plot, work function values were obtained which showed good correlation with photocurrent determined values. This work was extended by Polymeropoulos<sup>(24)</sup> who used a wider range of fatty acids and found a similar exponential dependence, with five orders of magnitude change in conductivity. He also found that the current-voltage behaviour was essentially temperature independent.

#### 4.3.2 DC Conduction: Multilayer Structures

Most experiments on thick multilayer structures appear to indicate barrier limited conduction mechanisms, with Schottky and Poole-Frenkel effects being prevalent. Space-charge-limited conduction has been reported but only for certain short chain substituted anthracene films.

Careem and Hill<sup>(25)</sup> have noted Schottky limited conduction for relatively thin films of N (number of monolayers) between three and nine, and have subsequently shown good correlation between theoretical and measured slopes of the  $\log J-V^{\frac{1}{2}}$  plot. In thicker structures the conduction was thought to be dominated by Poole, and Poole-Frenkel conduction, with the latter being dominant at higher applied voltages. Similar behaviour was noted by Nathoo<sup>(26)</sup>, with the normal logarithmic plot giving reasonable values of dielectric constant. Roberts et al<sup>(27)</sup> have reported weakly temperature dependent  $\log J-V^{\frac{1}{2}}$  behaviour for both  $Al_2O_3$  and InP substrates<sup>(28,29)</sup>. Their results were found to be polarity and electrode material independent and were thus interpreted as being due to Poole-Frenkel type behaviour. Once again, the dielectric constant calculated from the slope gave a reasonable value of about 2.5.  $\log J-V^{\frac{1}{2}}$  behaviour has also been observed by Honig<sup>(30)</sup>, but in this case the currents were electrode dependent and showed two distinct slopes, neither of which gave correct values of dielectric constant when fitted to Schottky or Poole-Frenkel behaviour. From these values of gradient the closest fit was to Schottky limited conduction, however no significant electrode dependence was observed which tends to indicate the Poole-Frenkel mechanism.

In general therefore it can be seen that  $\log J-V^{\frac{1}{2}}$  behaviour is a frequently observed phenomenon for fatty acid/salt films. The main problem however lies in the precise interpretation of this type of plot as it can be characteristic of various conduction mechanisms. Because of this, there is still disagreement as to precisely which of the two major alternatives is dominant since both Poole-Frenkel and Schottky behaviour appear to have been observed.

It is also interesting to note that although some consistency exists between measurements of gradient, the overall magnitudes vary quite markedly. These inconsistencies in the intercept value appear to be due to both film

and substrate variations ; effects which are not surprising in view of the wide range of specific differences in both preparation and deposition methods that exist between individual groups. In particular, the dryness of the film during measurement, and the state of oxidation of the interface appear to be quite crucial.

#### 4.3.3 AC Properties : Conductance

Measurements of AC conductivity as a function of frequency have been undertaken by a number of authors, and the majority has shown an  $\omega^n$  dependence with n between 0.5 and 1.0. Work by Jonscher and Nathoo<sup>(31,32)</sup> over a wide band of signals  $10^{-4}$  -  $10^2$  Hz consistently showed the exponent to be virtually unity and concluded the mechanism was some form of hopping conduction between localised states at each monolayer interface. In this situation, the carriers were thought to be injected from the contacts<sup>(33)</sup> and the resultant currents were therefore, electrode dependent, as observed at low frequency.

Similar results have been obtained by Sugi<sup>(34)</sup>, and Roberts et al<sup>(27)</sup> where the values of n were slightly less than unity, at 0.87, and 0.9 respectively. From these measurements, the mechanism proposed was also of hopping origin, although Roberts also concluded<sup>(35)</sup> that while values of n 0.5-0.9 were probably due to hopping, the higher values closer to unity were more likely lattice relaxation effects, and were indicative of high film quality. This latter idea was borne out by measurements from Careem et al<sup>(23,26)</sup> who showed two regimes of frequency dependent conduction. In these cases, the normal effect, observed at higher frequencies, (almost proportional to  $\omega$ ), was supplemented by a low frequency electrode dependent contribution, with n now much less than unity. This lower frequency effect was believed to be due to a hopping mechanism, whereas the normal regime was thought to be lattice dependent, and a function of relaxation of the dipolar COOH groups.

#### 4.3.4 AC Properties : Capacitance

One of the most common uses of capacitance measurement with fatty acid/salt films is the reciprocal (1/C) plot against film thickness. This has

been reported by many authors working on these materials, and allows dielectric constant and/or monolayer thickness to be obtained. These two parameters, being relatively easy to measure are thus reasonably well established, and agree with other sources, for example, X-Ray, and ellipsometry. The accepted values are,  $\ell = 25.8 \text{ \AA}$ , and  $\epsilon_r = 2.7$  for stearic acid/Cd stearate (at pH = 5.8), to within a few percent. In addition to these two constants, it is also possible to obtain the native oxide thickness from the Y axis intercept point. This enables some basic characterisation of the substrate/film interface region, given that the dielectric constant of the material is known. It appears from these measurements that the actual thickness is very "preparation" dependent, and thus there is little agreement between individual workers ; values anywhere between  $5 \text{ \AA}$  and  $80 \text{ \AA}$  being reasonable. For the majority of  $1/C-N$  plots the first monolayer and sometimes the second very rarely reside on the straight line<sup>(37)</sup>, and normally occurs above its expected value. This effect, often referred to as the "1st monolayer problem" is probably caused by differences between this layer and the remaining films due to its interaction with the substrate. Indeed, a recent paper by Barraud and Rosilio<sup>(38)</sup> has proved the existence of ion interchange between an aluminium substrate and the metal species in the film. This results in the first layer being aluminium, rather than cadmium stearate, and suggests that ion exchange can occur with other substrates, at both the interface and into the bulk of the film.

The majority of authors have found the dielectric constant, and thus the capacitance to be reasonably independent of frequency, up to  $10^6$  Hz, for good quality films. It appears, however, that bad (DC) electrical characteristics are associated with dispersion in  $\epsilon_r$ , which causes frequency dependence for both conductance and capacitance.

#### 4.3.5 Other Properties and Structures

##### Internal Voltage

Internal voltages for MIM structures have been observed by many authors, and produce displacement in the voltage dependence of most properties. Honig<sup>(30)</sup> has reported values up to 0.6 V for many different electrode materials, and Leger<sup>(39)</sup> noted up to 0.2 V, which disappeared at low temperatures. In both cases the authors proposed that the effect was due to work function differences causing ion movement across the insulator.

Srivastava<sup>(40-42)</sup> has reported detailed studies of the internal voltage effect, showing symmetrical displacement of J-V plots about the correct value. The voltage magnitude was found to decrease with numbers of layers (N), and was higher for asymmetric (odd N) structures. From this investigation, Srivastava concluded that the effect was due to net polarization of the molecules, supplemented by the previously proposed work function differences for unlike electrodes.

In general, the presence of internal voltages appears to be very preparation dependent, and even structures fabricated under apparently identical conditions may or may not show the effect. Moreover certain authors seem to be more fortunate than others in reproducing the effect. It can only be concluded from present evidence that the phenomenon is extremely sensitive to minor variations in technique, ionic content, planar packing, etc.

##### Dielectric Breakdown

The origin and effect of dielectric breakdown has been studied in depth by many authors, and although not directly relevant here, the subject is considered to be worth mentioning.

Agarwal and Srivastava<sup>(43-48)</sup> have shown that breakdown effects in fatty acids/salts, are a function of both temperature and film thickness, but found it necessary to distinguish between "onset" breakdown, and "destructive"



breakdown. In the former situation, sudden increases in current are observed, but no damage results unless considerably higher fields are applied to induce the latter effect. This initial stage shows a  $V^2$  current dependence and may well be associated with the onset of space charge limited conduction. Moreover at higher voltage, the J-V curve flattens off indicating high resistance effects due to electrode limitation. Agarwal and Srivastava also found, surprisingly, that the final breakdown voltage was thickness independent, which may well suggest that the  $Al_2O_3$  at the interface region plays more than a passive role in this mechanism.

Barraud and Rosilio<sup>(49)</sup> have also studied breakdown effects in both air and vacuum, but their results show the existence of a three stage process. Bubble formation at about  $10^6$  V/cm, due to electrostatic water expulsion, a sudden temperature independent current increase, ascribed to electrostatic thinning of the material, and finally proper breakdown causing electrode damage and capacitance decrease. This actual film damage appeared to be self healing in air, however, and the breakdown voltage showed considerably less increase with insulator thickness than noted by Agarwal and Srivastava.

#### Metal-Insulator-Semiconductor (MIS) Structures

Virtually no investigation has been carried out upon structures made on semiconductor substrates, and the little that has been done, used only silicon. Measurements reported by Tanguy<sup>(50,51)</sup> showed reasonable C-V curves, but only weak inversion, and quite significant amounts of ionic type hysteresis. In addition, the majority of these curves used orthophenanthroline, (a benzene ring complex) with added fatty acid chains, rather than simple fatty acids alone. No in-depth analysis of this system beyond the simple C-V curves was attempted. Experiments on silicon using fatty acids/salts have been reported by Lundstrom<sup>(52-54)</sup>. In these investigations the samples again showed good accumulation and weak inversion, but also charge

injection from the semiconductor into the insulator, and subsequent trapping at monolayer interface regions. This effect was investigated by time lapse C-V plotting and was concluded to be a low field Schottky limited process. Again, no detailed study of conductance or any other characteristics was undertaken.

Fatty acid deposition has also been achieved onto other semiconductor substrates by the Durham group<sup>(55)</sup>. Work carried out on InP will be considered in detail later in this thesis, but in addition, encouraging results have also been obtained on CdTe<sup>(56)</sup>. These data shows good accumulation, depletion and weak inversion, and also a sharp surface state conductance peak ; these effects are currently under more detailed investigation. In addition, the deposition of fatty acids and more complex materials on CdS, GaP; GaAs, and amorphous silicon is also being investigated ; this will be discussed in more detail in Chapter 10.

#### 4.4 GENERAL CONSIDERATION OF POTENTIAL APPLICATIONS

Before going on to discuss, in some detail, the specific equipment used at Durham, and its particular application to the study of electrical behaviour, it is perhaps useful to briefly mention other areas of current interest within Langmuir film technology.

The deposition of any material by the Langmuir-Blodgett process requires that the molecules used are amphipathic. This relatively minor constraint is not difficult to overcome with the help of modern chemical techniques ; so that, in practice it is now possible to use or adapt for use, quite a wide variety of different materials. The majority of materials so far considered are primarily electrically insulating, but it is possible to produce more conducting films<sup>(65)</sup>, some with anisotropic, and even semiconducting properties. In addition, the limitations upon chemical mechanical and biological properties are virtually non-existent, and, therefore,

allow an even wider variety of applications outside the field of electronics.

Perhaps the most important use (from the point of view of this thesis) of these films is in the semiconductor device industry, where the insatiable demand for smaller and faster devices is beginning to show some fundamental limitations in the Si/SiO<sub>2</sub> system. The on-going search for replacements to this material has shown certain III:V materials to be extremely promising, apart from their lack of native oxide. Thus it is here where the good electrical properties, and thickness control of Langmuir films may well prove to be extremely useful. In addition, although the process reported here is distinctly at the research level, there are no obvious obstacles to scaling the trough up to industrially useful proportions.

The excellent control of film thickness afforded by this technology also lends itself well to applications involving ultrathin films. It has been shown for example<sup>(57)</sup>, that the conversion efficiency of photovoltaic Schottky barriers can be considerably enhanced by the presence of an interfacial layer, whereby the thin layer permits control of the dark current magnitude, and the carrier injection ratios. Indeed, recent publications by Dharmadasa et al<sup>(58,59)</sup> have already shown good efficiency improvements for CdTe based devices.

Another application in the field of physics and electronics is that of optical waveguiding. In this area, recent publications have shown<sup>(60-62)</sup> that the good control of refractive index and film thickness afforded by Langmuir-Blodgett multilayers has given losses as low as 5dB/cm. Moreover, it is believed that further work will easily reduce this figure to 1dB/cm.

Other more complex chemical species are also being electrically investigated as Langmuir films, for example, aromatic compounds with benzene ring structures show particularly interesting properties<sup>(63,64)</sup>. These

lightly substituted anthracene derivatives exhibit a large anisotropy of conductivity, with in plane values being greater by a factor of  $10^8$ . In addition, double injection has been observed in these materials<sup>(65)</sup>, giving significant light output and opening up the possibility of future applications in large area electroluminescent panels.

More recent studies have led to the possible use of monolayers as photo-resists for microelectronics<sup>(65,67)</sup>. These specially synthesised organic materials (tricosenoic acid), are polymerised by electron beam and can produce extremely good resolution down to  $600 \text{ \AA}$  ( $0.06 \mu\text{m}$ ). These newer high resolution resists are projected to give an extra lease of life to conventional micro-lithography.

In addition to all this published exploratory work on physical applications, there are many even newer areas upon which no details have yet been published. Among these are work by IBM of America on the incorporation of ferromagnetic metal ions in mono/multilayer structures with a view to producing thin magnetic bubble structures, and exploratory work at RSRE, Malvern into the use of LB films for multilevel microwave coupling insulators.

Also, exploratory work is being undertaken by a variety of biochemists and biophysicists, using the Langmuir trough technique to build complex molecular structures in order to model biological processes. Multilayer systems containing chlorophyll and chromophores for example<sup>(68,69)</sup> have been produced and used to study the complex structures and mechanisms involved in photosynthesis. The structure and organisation of lipid molecules<sup>(70)</sup>, which are essential components of all cell membranes are being investigated using the LB technique. These molecules have inherently both fatty acid and polar regions and are, therefore, ideally suited for use in this field. Initially, lipid monolayers were extensively used to model cell membrane behaviour and investigate diffusion mechanisms for biological species<sup>(71)</sup>. More recently, however,

much more complex structures have been needed to move beyond this relatively simple approach, and again the LB technique has proved extremely useful<sup>(72)</sup>. The successful incorporation of proteins and other important cell membrane constituents into lipid bilayers and multilayers has been found to be essential to the development of useful biological models, and work is underway to produce these combined structures.<sup>(73)</sup> In the near future, this is expected to lead to the fabrication<sup>(74)</sup> of solid state biological sensors ( i.e. field effect devices for monitoring immunological response (IMFET) and enzyme-substrate reactions (ENFET) ). In these structures, active biological materials such as antibodies and enzymes are combined into the insulating region of the device and thus any reactions by these compounds have effects on the FET characteristics. This enables the monitoring of internal biological mechanisms both in the short term, and as permanent implants in the body to provide longer term measurements.

## CHAPTER 5

### DEPOSITION EQUIPMENT AND INSTRUMENTATION

Although the production of Langmuir films can be traced back to the original work of Langmuir and Blodgett in the 1920's, the quality and reproducibility of their insulators was far from impressive. From this original work, steady development has been undertaken to the point where the modern Langmuir trough is quite an advanced piece of equipment.

Two of the most significant steps during this period were the introduction of the constant perimeter barrier, and the application of methods of directly measuring surface pressure. In addition, recent work at Durham and I.C.I.Ltd., Runcorn, Cheshire, has resulted in electronic feedback instrumentation to link these two facilities and thus produce automatic pressure control. These three features, when combined with skilled engineering, result in a Langmuir trough capable of producing very high quality films from many different types of amphipathic materials.

The preparation and characterisation of these films will be discussed in later chapters ; as a precursor, however, a detailed description of the Langmuir trough as designed and constructed at Durham will be given.

#### 5.1 DETAILS OF THE LANGMUIR TROUGH

There are at present two Langmuir trough systems available at Durham, the initial 'large' one was built about three years ago, and has now been complemented by a smaller one designed to fit in a glove box. The latter is in fact a half-size version of the large one, built for use with more complex amphipathic materials, where tight environmental control is required. Both troughs use the superior constant perimeter compression system<sup>(1)</sup>, and are able to produce compression ratios of nearly 5 : 1. The use of feedback

control systems, developed at Durham and Runcorn, has produced maximum automation of both barrier control and dipping operations.

It was rapidly discovered during commissioning operations that extreme cleanliness was an essential prerequisite for good Langmuir film quality. From an equipment point of view, both troughs were stored and used in an air conditioned room, and each was further protected by an individual box to keep out airborne contamination. The use of standard anti-static clean room apparel (laboratory coats, face masks, hats and gloves ) was also undertaken in an attempt to further reduce contamination. In practice, the majority of stearic acid deposition was carried out using the large trough ; detailed consideration will, therefore, be mainly referred to this one, although all principles in general apply to both troughs.

#### 5.1.1 Trough and Barrier Construction

Due to the desired size of the large trough (36" x 8" x 3½") it was found to be impossible to acquire a complete single vessel. This problem was overcome by fabricating the container from a "U" section piece of glass, with end plates clamped in position and sealed with PTFE compression strips. A large cross-section metal frame was then used both as a base support, and as location for the screws clamping the end plates in position. At the beginning of the project, problems were anticipated in connection with out-leaking of contamination from the glass trough. To avoid this problem investigations were undertaken with a view to using a custom made silica basin for the base of the trough. In practice the latter proved far less suitable than ordinary glass, and contamination problems were considerably less than anticipated. Thus primary scouring of the new trough, accompanied by thorough weekly cleans proved to be adequate in avoiding any long term contamination build-up. Water for the pure subphase was obtained from a Millipore "Milli-Q" system (see section 3.2) which provided water of 20 MΩ<sub>cm</sub> resistivity, which was

piped to the trough through special polypropylene tubing. The latter was as recommended and supplied by Millipore (U.K.) Ltd. to avoid any pick-up of plasticiser or other undesirable chemicals during the transport of the water to the trough.

The PTFE coated glass fibre compression barrier\* was located by a system of six PTFE rollers, and these in turn were secured to two mobile overarms. A schematic illustration of this compression system is given in Fig 5.1. Points A and B are fixed, and therefore have rollers mounted with miniature ball bearings. The rollers at C/D and E/F are fixed, as the belt is not required to move relative to these points. These remaining two sets of rollers are fixed to their respective over-beams, which are in turn linked by a rubber toothed belt drive system. This novel belt drive is powered by a low geared motor, and is arranged to move the two overarms symmetrically inwards or outwards, and so maintain the barrier taut at all times. The overarms are located and suspended by concave vee section rollers, one at each corner, running on circular cross-section stainless steel rails. It was found in practice that the design shape of the beams was of critical importance, and a compromise for bearing spacing had to be evolved. This was between a maximum spacing for barrier stability, and a minimum spacing to give the smallest possible closed barrier area (for surface cleaning).

By using these glass fibre belts of 2cm depth, the need for critical water level control was removed, as any depth within the belt would still enclose the monolayer. This approach produced the need for clean inert support rollers, as they too would now suffer semi-immersion in the water. Extensive cleaning applied after the "dirty" fabrication and machining process, however, using various alkali solutions and organic degreasers was found to achieve the required level of decontamination. Throughout the design and fabrication period, attention was always paid to future cleaning needs, and to this end stainless steel and PTFE were used wherever possible. Larger pieces of

\* Fothergill and Harvey Ltd, Littleborough, Lancs.



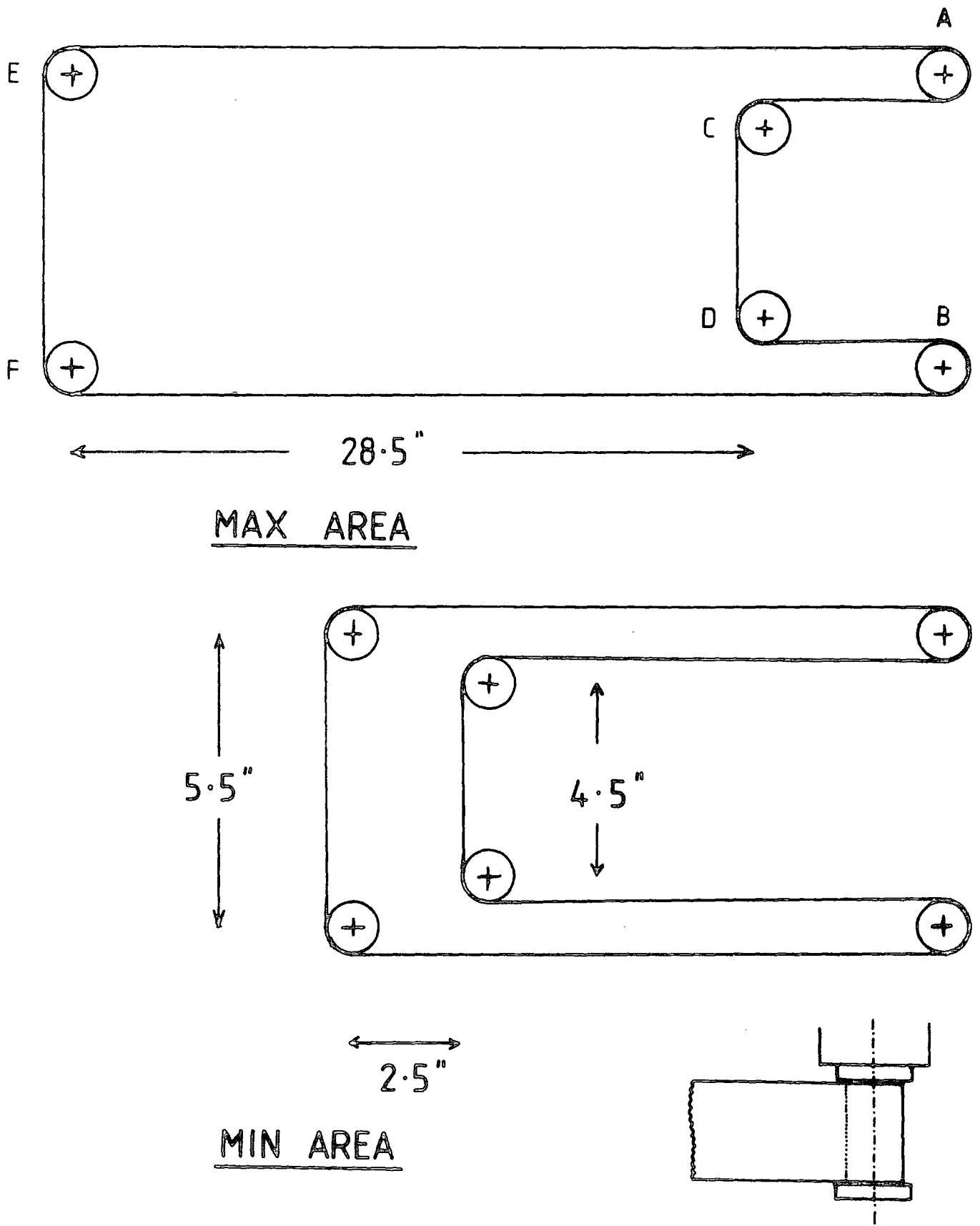


Figure 5.1 : Schematic representation of constant perimeter compression barrier, showing maximum and minimum areas.

SIDE VIEW

metal, over beams, base etc, were the main exception, but these were thoroughly cleaned and painted before final use.

### 5.1.2 Compression Ratio

In designing the Langmuir trough, one of the major initial considerations was that of compression ratio. The largest maximum area possible is needed from the point of view of dipping, to provide for larger substrates, and thicker multilayers. From a cleaning consideration, however, the smallest minimum area is desirable to ease removal of unwanted surfactant material. In practice, however, these are conflicting requirements since only one dimension is variable. A compromise can usually be achieved provided no additional limitations are imposed. In addition, it should be noted that since surface cleaning is carried out with a fine glass vacuum nozzle, the aforementioned minimum area must not be so small as to hinder access for cleaning.

The final dimensions arrived at are given in Fig 5.1, and from these values additional parameters can be obtained :

The maximum area, assuming the enclosed portion to be effectively three rectangles and allowing for the area of the rollers, is given by ;

$$A_{\max} = 879.1 \text{ cm}^2$$

The minimum area, by similar considerations is given by ;

$$A_{\min} = 187.6 \text{ cm}^2$$

Therefore the change in area  $\Delta A$  is ;

$$\Delta A = 709.5 \text{ cm}^2$$

and the compression ratio  $C_R$  is ;

$$C_R = 4.7 \text{ to } 1.$$

From these figures, and with the aid of some basic chemistry, the interpretation of isotherm and dipping data can be undertaken, as will be shown later.

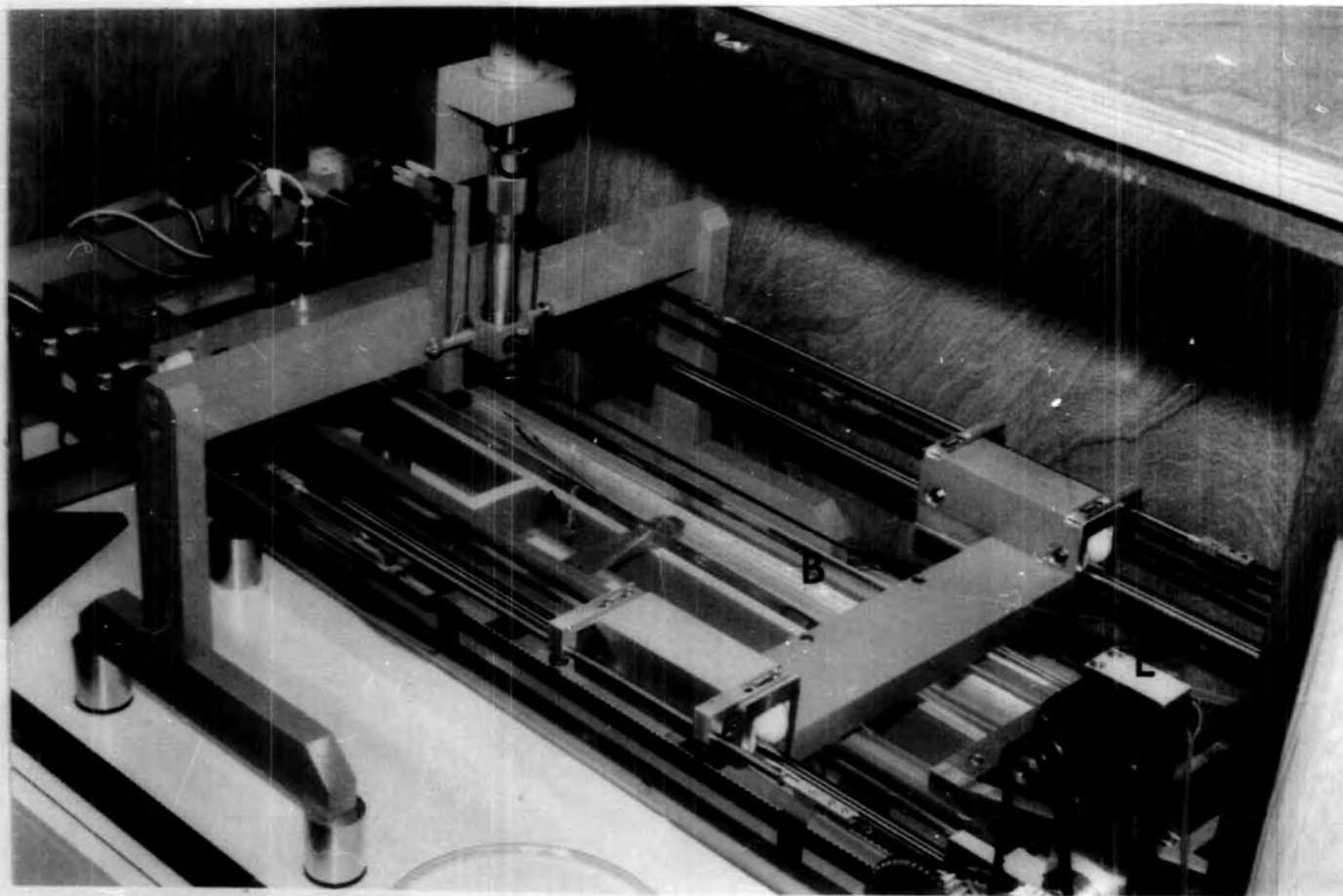
### 5.1.3 Dipping Mechanism

For the implementation of dipping, a novel screw drive system was developed. This uses a horizontal overarm, running perpendicular to the trough and supported on four independent legs. It is therefore totally independent from the trough and can be freely moved during cleaning operations. Attached to this arm is a motor powered micrometer for driving a vertical slide system up or down. The final design used here in fact needed considerable development to ensure smooth operation, as any vibration would obviously have considerable effect upon film quality.

A small pressure clamp was used for the final location of the sample, this was attached to the dipping arm by an adjustable metal rod to allow for different sizes of sample. Microswitches were located at each end of the slide travel, activated by moveable trip rods to permit a fully automatic dipping cycle. A photograph of the large trough is given in Fig 5.2, suitably annotated in order to clarify this layout.

### 5.1.4 Surface Pressure Measurement

For the automatic control system to be feasible, some method of surface pressure measurement was required. This was needed to provide information for a comparator circuit which in turn moved the barrier in response to changes in pressure. The measurement of surface pressure is in itself a substantial subject, with a relatively long history and origins in Langmuir's original surface tension observations<sup>(2)</sup>. Quantitative measurements are now normally based on one of two methods: the Wilhelmy plate technique as used here, or the Langmuir balance. The latter method utilizes the force on a partition between a clean area, and one with a monolayer, this force being measured with a microbalance arrangement<sup>(2)</sup>. In normal form, the Wilhelmy



- A. WILHELMY PLATE
- B. COMPRESSION BARRIER
- C. MICROMETER DIPPING MECH.
- D. pH. ELECTRODES
- E. BARRIER DRIVE MOTOR

Fig. 5.2 Photograph of Langmuir trough

balance<sup>(3)</sup> exploits a thin plate suspended semi-immersed in the subphase, and attached to a microbalance vertically above it. Values of weight can thus be related directly to surface pressure, providing the contact angle of the plate with the liquid is zero.

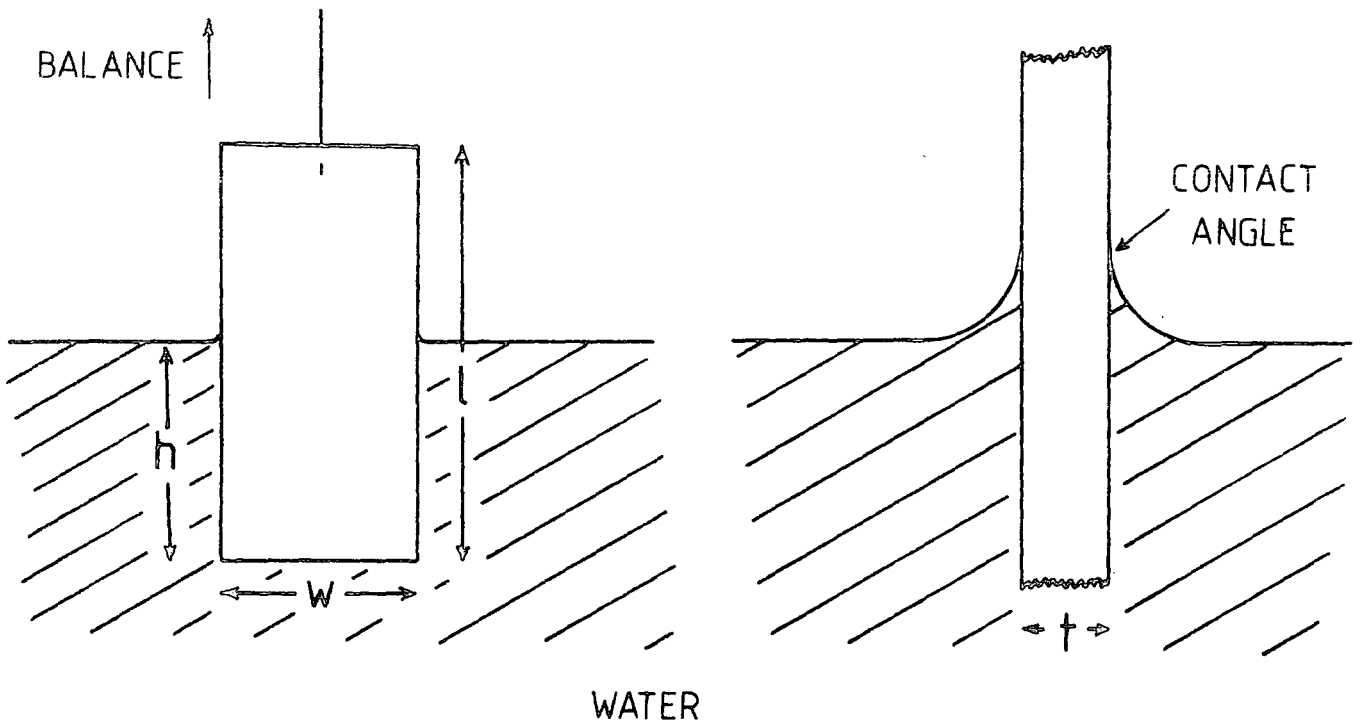


Figure 5.3: Representation of surface pressure measurement.

The forces acting on the plate consist of gravity and surface tension downwards, and buoyancy due to the displaced water upwards. Consider a rectangular plate of dimensions  $l$ ,  $w$  and  $t$ , and of density  $\rho_p$ , immersed in water

to a depth  $h$ , as shown in Fig 5.3. The net downward force  $F$  is given by,

$$F = \rho_p g l \omega t + 2\gamma(t + \omega) \cos\theta - \rho_w g t \omega h \quad (5.1)$$

where  $\gamma$  is the liquid surface tension,  $\theta$  is the contact angle (normally zero therefore  $\cos\theta = 1$ ),  $g$  is the gravitational constant, and  $\rho_w$  is the water density. It should be noted that this equation neglects the effects of the second phase, in this case air. The surface pressure  $\pi$ , is generally considered to be equal to the reduction of the pure liquid surface tension by the film, thus :

$$\pi = \gamma_o - \gamma_1 = \Delta\gamma \quad \text{dynes/cm.} \quad (5.2)$$

where  $\gamma_o$  is the surface tension of the clean liquid, and  $\gamma_1$  the surface tension of the liquid when covered with a film. Therefore, if a film is added to a clean subphase, all the plate dimensions remain constant :

$$\text{Initially } F = \rho_p g l \omega t + 2 \gamma_o (t + \omega) - \rho_w g t \omega h$$

$$\text{and with film } , \quad F' = \rho_p g l \omega t + 2 \gamma_1 (t + \omega) - \rho_w g t \omega h$$

$$\therefore \Delta F = F - F' = 2 (\gamma_o - \gamma_1) (t + \omega) \quad (5.3)$$

If the plate has negligible thickness, and width 1 cm, then ;

$$\Delta F = 2 (\Delta\gamma) \quad (5.4)$$

So the weight measured in milligrams is equal to twice the surface pressure in dynes/cm.

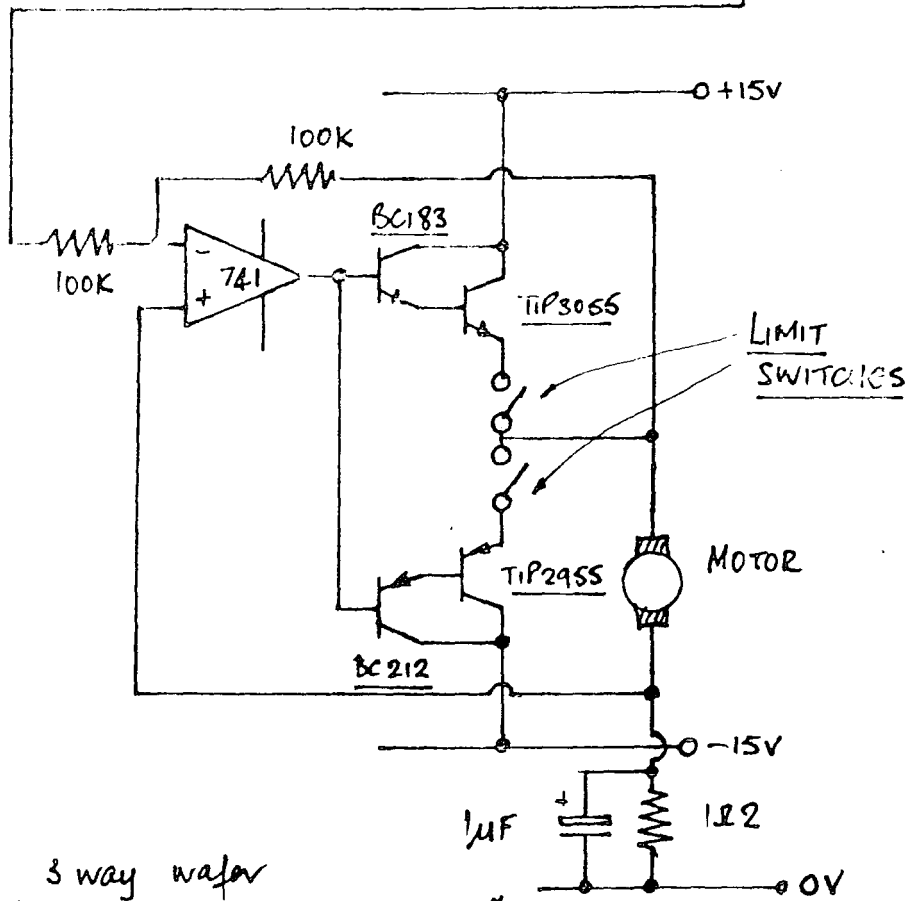
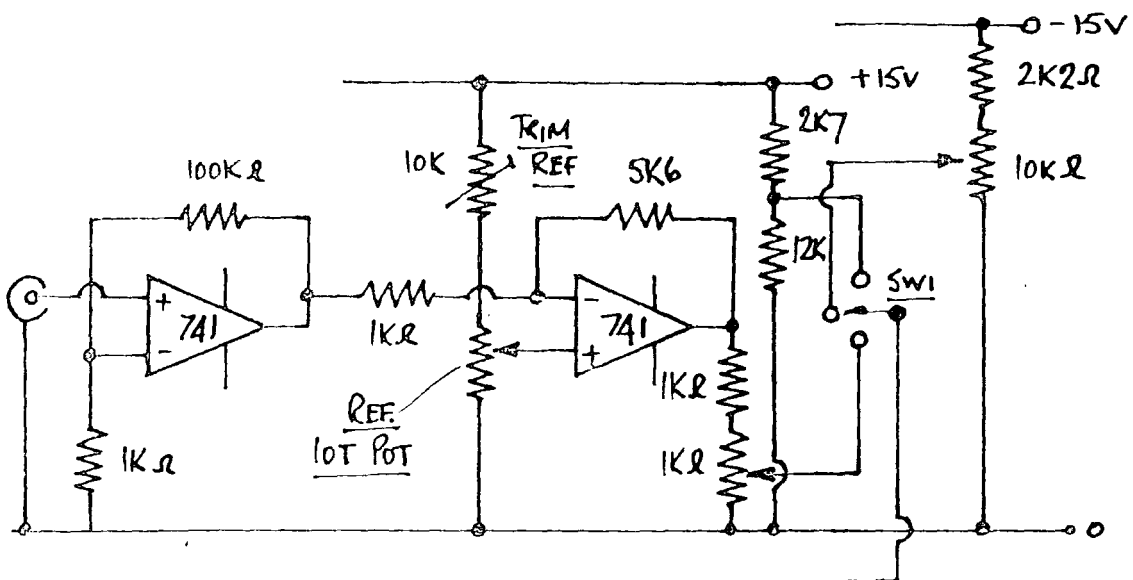
The major drawback of this method is the difficulty in measuring

contact angle to ensure it is zero, and also to prove it stays constant throughout measurements. Many different materials have been used for the Wilhelmy plate by workers in this field<sup>(3,4,5)</sup>, glass and a variety of metals being the dominant ones. With all these, stringent cleaning is required before use, however, in order to ensure the zero contact angle. In practice, after various feasibility tests, filter paper was decided upon as the plate material; this was cut from 1 cm wide reels of chromatography paper. It adhered well to all the previous requirements, and in addition was sufficiently light to avoid problems with the microbalance. The Wilhelmy plate was changed at regular weekly intervals to avoid any contamination build-up problems.

Measurement of the extremely small forces was achieved by using a Beckman LM 600 microbalance, with a detachable head located directly over the trough. The plate was attached to this head with a length of fine cotton thread.

#### 5.1.5 Instrumentation

For the automatic control of pressure, a unit was designed that compared the actual pressure with the desired value, and moved the barrier accordingly. The output of the Beckman balance, proportional to the mass reading (1 mV/mg), was taken to a control unit where a differential amplifier compared the value with a preset voltage. The output of this comparator was fed, after suitable scaling, to the barrier motor drive. The circuit was arranged to have a suitable zero output band where the two values were adequately similar, but becoming positive or negative if deviation occurred. Manual forward and reverse controls were added for use during surface cleaning, together with fail-safe microswitches at each end of the barrier track, to avoid damage by incorrect use of the manual control. A full circuit diagram of the resultant unit is given in Fig 5.4. Initial calibration of the "offset" control enabled direct dial-in of the required constant pressure to



SW1. 3 way wafar  
 "Reverse / forward / control"

Figure 5.4 : Circuit diagram of barrier control instrumentation.

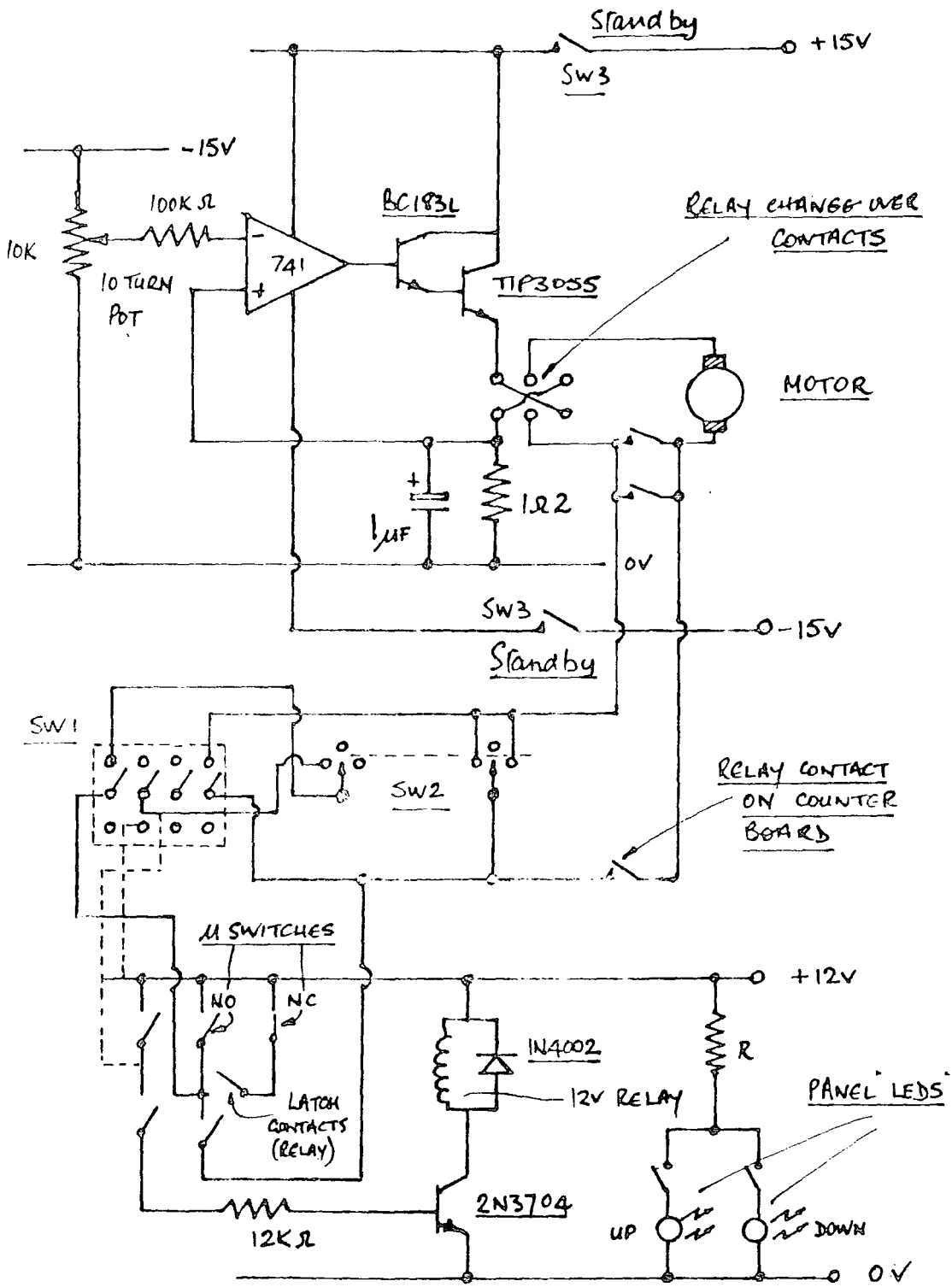


be achieved, once differences in water level had been allowed for with the zero control of the microbalance. These latter variations were due to changes in the value of  $h$  (immersion depth of the Wilhelmy plate) affecting the weight of the plate.

An X-Y recorder was used to plot the variation of surface pressure with barrier area ; this is normally termed an isotherm, and will be dealt with in the next chapter. Also considered in detail later is the monitoring of the change in area with time, to plot out the progress of the dipping operation. This was undertaken by using a Bryans ( W & W) 312 2X/T chart recorder.

In practice it was found that the pH of the subphase was of crucial importance due to its influence on the salt/acid ratio of the spread monolayer. Natural absorption of  $\text{CO}_2$  from the atmosphere was found to rapidly reduce the pH of fresh water by the formation of carbonic acid. To compensate for this dilute acid (HCl) or alkali ( $\text{NH}_4\text{OH}$ ) were added to maintain the pH at the ideal value of 5.8. Constant monitoring of pH was undertaken by using a Pye Unicam PW 9409 pH meter with a 401-EO7 combined glass and reference electrode, together with a 651012 platinum resistance thermometer for automatic temperature compensation.

The movement of the sample through the compressed monolayer was achieved by the use of a micrometer driven slide, as previously mentioned. This was controlled again fully automatically, by the circuit given in Fig 5.5. The control unit provided a variable voltage dual polarity signal for the drive motor, the sign being changed by interrupt signals from the microswitch end stops on the dipping head. A counter/decoder was arranged to trigger off each change of direction of the motor and thus count the number of layers being deposited. In addition, an autostop facility was provided by a three digit thumbwheel switch, the preset value of which was compared with the counter until the two were equivalent, at which point the motor was stopped.



- SW1 - 4 pole toggle "cycle/manual"
- SW2 - 3 way wafer "up/off/down"
- SW3 - 2 pole toggle "standby/operate"

Figure 5.5 : Circuit diagram of dipping mechanism control.

A photograph of the resultant instrumentation as used is presented in Fig 5.6. This full automation of both barrier control and sample dipping enabled precise control of many critical parameters and so allowed extremely high quality insulating films to be deposited in a very reproducible fashion.

This chapter has considered in some detail the technical aspects of the Langmuir troughs used by the author. Much of the background work both in design and construction was however undertaken by technical staff in the Department of Applied Physics at Durham. The author would therefore like to take this opportunity to extend a special thanks to Mr. B Blackburn, and Mr. P Friend for their considerable patience, effort and help throughout the construction of this equipment.

- A. MICROBALANCE
- B. BARRIER CONTROL UNIT
- C. DIPPING CONTROL UNIT
- D. pH METER
- E. CHART RECORDER



Fig. 5.6 Photograph of Langmuir trough control instrumentation

## CHAPTER 6

### LANGMUIR FILM DEPOSITION

Although the concept of Langmuir film deposition is an elegantly simple one, the practical techniques required to produce good quality structures are quite complex. This chapter presents details of these various procedures and discusses the reasons for their use.

The Langmuir-Blodgett process as applied during this work can be divided in four basic stages ; Subphase surface cleaning, monolayer production, monolayer compression and isotherm plotting, and film deposition. These steps will now be discussed individually.

#### 6.1 SUBPHASE CLEANLINESS

##### General Cleanliness

Because of the monomolecular nature of the deposition process, extreme care was required in preparing both the mixtures used, and the trough itself. To this end, all chemicals were of the highest purity, and the trough was cleaned on a regular weekly basis. This process involved washing in IPA, chloroform, and "Millipore" water, and for the belt and rollers, refluxing in trichloroethylene and IPA. In addition, the belt was replaced every three months.

The water for the subphase was supplied from a "Millipore" deionisation system (see section 3.2) via high purity polypropylene tubing, and was maintained at the required pH by daily addition of dilute alkali. The monolayer solution was mixed in a 10 cm<sup>3</sup> volumetric flask, using Aristar (BDH) chloroform, and stearic acid crystal (S4751-Sigma Chem. Co, St. Louis, U.S.A). This solution was replaced after two weeks, as apparent ageing of the mixture otherwise resulted in degradation of both isotherm and multilayer quality.

### Subphase Surface Cleaning

Initial cleaning of subphase prior to monolayer spreading was undertaken with the aid of a fine glass vacuum nozzle : this was attached to a water driven filter pump and thus worked like a miniature vacuum cleaner. To aid this cleaning the barrier was normally maintained in the closed position to minimise the area from which contamination was removed. Moreover the surface was usually cleaned three or four times with the barrier opened to full and then recompressed between each individual attempt. This procedure not only allowed the residual pressure to be monitored and recorded but also ensured some re-arrangement of the remaining surfactant material away from the less accessible areas to ease its subsequent removal. It was found in practice that residual pressures of less than 0.03 dynes/cm were required to enable the production of a reasonable quality monolayer.

### 6.2 MONOLAYER SPREADING

Stearic acid in its normal form is a crystalline powder, and will therefore not form a monolayer on water directly. To overcome this, the material is usually mixed with an organic solvent, in this case chloroform, to produce a weak solution. Upon contact with the subphase, drops of this mixture rapidly spread outwards, and the solvent evaporates, leaving behind relatively few well spaced stearic acid molecules. These molecules then align semi-perpendicular to the surface of the water due to their amphipathic nature. In practice, with stearic acid, it is the COOH group that is water soluble, and this is therefore the part of the molecule that resides closest to the subphase.

Even with a relatively dilute solution, the amount of liquid required to produce monolayer coverage of the subphase is still extremely small. In consequence it was necessary to use a micrometer syringe system (Alga micrometer syringe : Gallenkamp PMP 820-030 P) to deposit the required volume of solution on the subphase. From basic principles, it is possible to calculate the amount

of solution required for monolayer coverage :

If the required maximum area/molecule is  $40 \text{ \AA}^2/\text{molecule}$ , and the concentration of the solution is  $10 \text{ mg/cm}^3$ , then :

$$\text{Max. trough area} = 897 \text{ cm}^2 \equiv 40 \text{ \AA}^2/\text{molecule}$$

Molecular wt of stearic acid = 284.5 gm

$$= 6 \times 10^{23} \text{ molecules.}$$

$$\begin{aligned} \text{Now } 40 \text{ \AA}^2 &= 40 \times 10^{-20} \text{ m}^2 \\ &= 4 \times 10^{-15} \text{ cm}^2/\text{molecule.} \end{aligned}$$

$$\therefore \text{No. of molecules required} = \frac{897}{4} \times 10^{15}$$

$$= 224 \times 10^{15}$$

$$\therefore \text{Amount of stearic acid} = \frac{224 \times 10^{15}}{6 \times 10^{23}} \times 284.5 \text{ gm.}$$

$$= \underline{10.6 \times 10^{-2} \text{ mg}}$$

Thus with a solution of  $10 \text{ mg/cm}^3$

$$\rightarrow 10.6 \times 10^{-2} \text{ mg} = 10.6 \times 10^{-2} \text{ cm}^3.$$

In practice, the Elga syringe was found to dispense two drops or  $0.01 \text{ cm}^3$  per turn, therefore 10.6 turns were required for  $40 \text{ \AA}^2/\text{molecule}$ .

For the spreading operation, the syringe was normally precleaned in chloroform prior to being filled with stearic acid solution directly from the volumetric flask. The required amount of material was then spread, one drop at a time from very near to the water in a distributive manner. This ensured maximum evaporation of the solvent from the monolayer before any compression was undertaken. After use, the remaining solution was disposed of, and the syringe immediately rinsed in chloroform.

### 6.3 MONOLAYER COMPRESSION

It has been assumed up to this point in the discussion that the stearic acid is spread upon a pure water subphase and compressed to form a monolayer . Although this is possible, it is very rarely the case as stearic acid alone is relatively unstable when compressed and not only collapses at low surface pressures but also tends to dissolve in the water. To combat this problem, it is normal to add a small number of metal ions to the subphase to promote the generation of metal salts of the fatty acid. These salts normally combine two acid molecules together whereby ;



and so tend to stabilise the film. In practice the amount of metal required in the subphase is quite critical and the presence of too much appears to have a detrimental effect upon the multilayer stacking and quality. The metal ions, in this case cadmium (although the particular species is immaterial so long as it is divalent) were introduced in the form of  $\text{CdCl}_2$ , a few milligrams of which were added to produce the required  $2 \times 10^{-4}$  molar solution. It is of course important to ensure that residual anions formed after dissolving this material do not introduce any undesired contamination or subsidiary reaction.

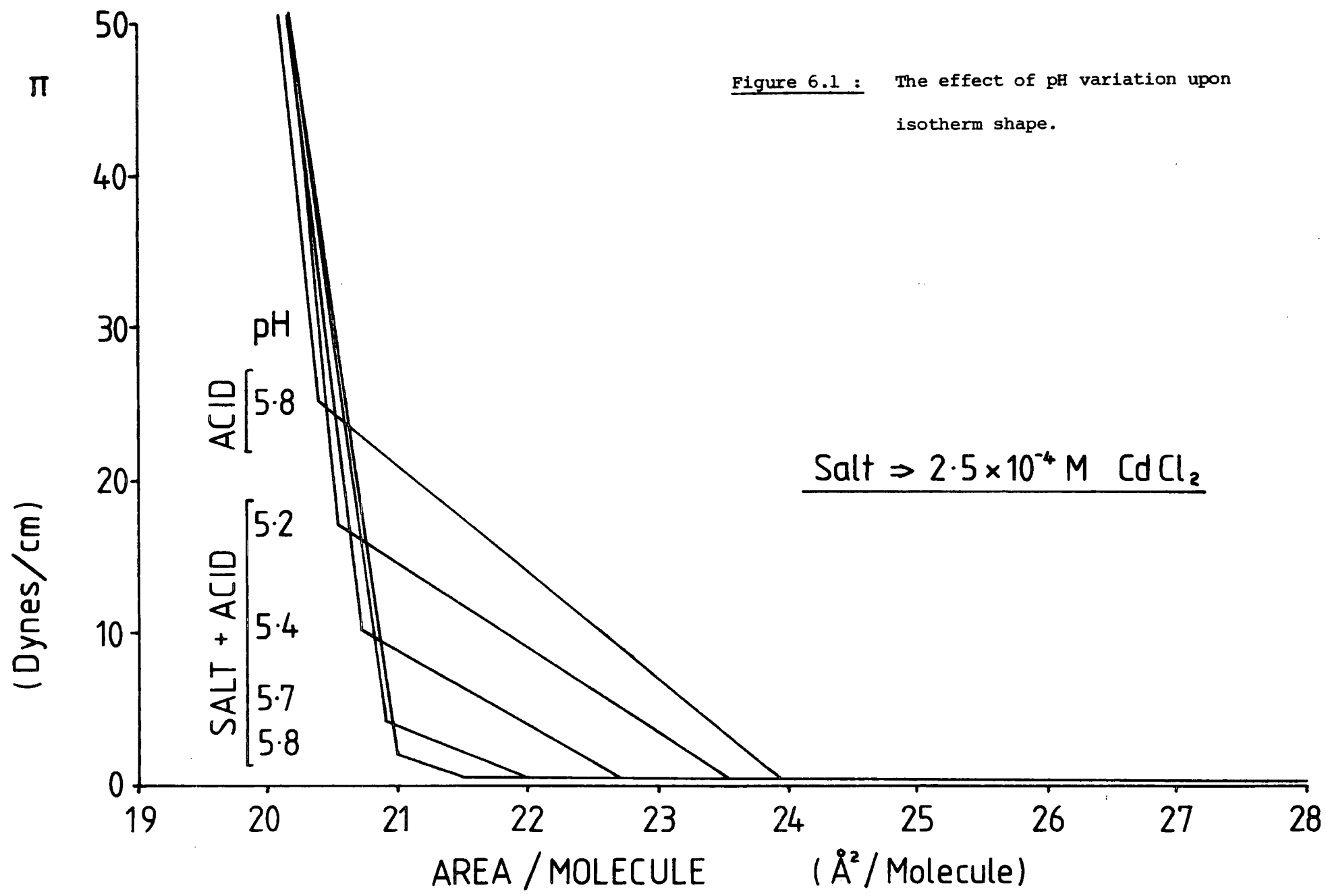
Because this reaction is a reversible one, and pH dependent, it is not surprising that any variation in the latter has a significant effect upon the isotherm shape : from Fig 4.2 it can be seen that for stearic acid alone the normal isotherm has three distinct straight line sections corresponding to gaseous, liquid (or expanded) and solid (or condensed), whereby the change in gradient between each line indicates the presence of a phase change. Up to a value of 5.5, the pH of the subphase has little effect on this isotherm; above this value, however, ionisation of the molecule

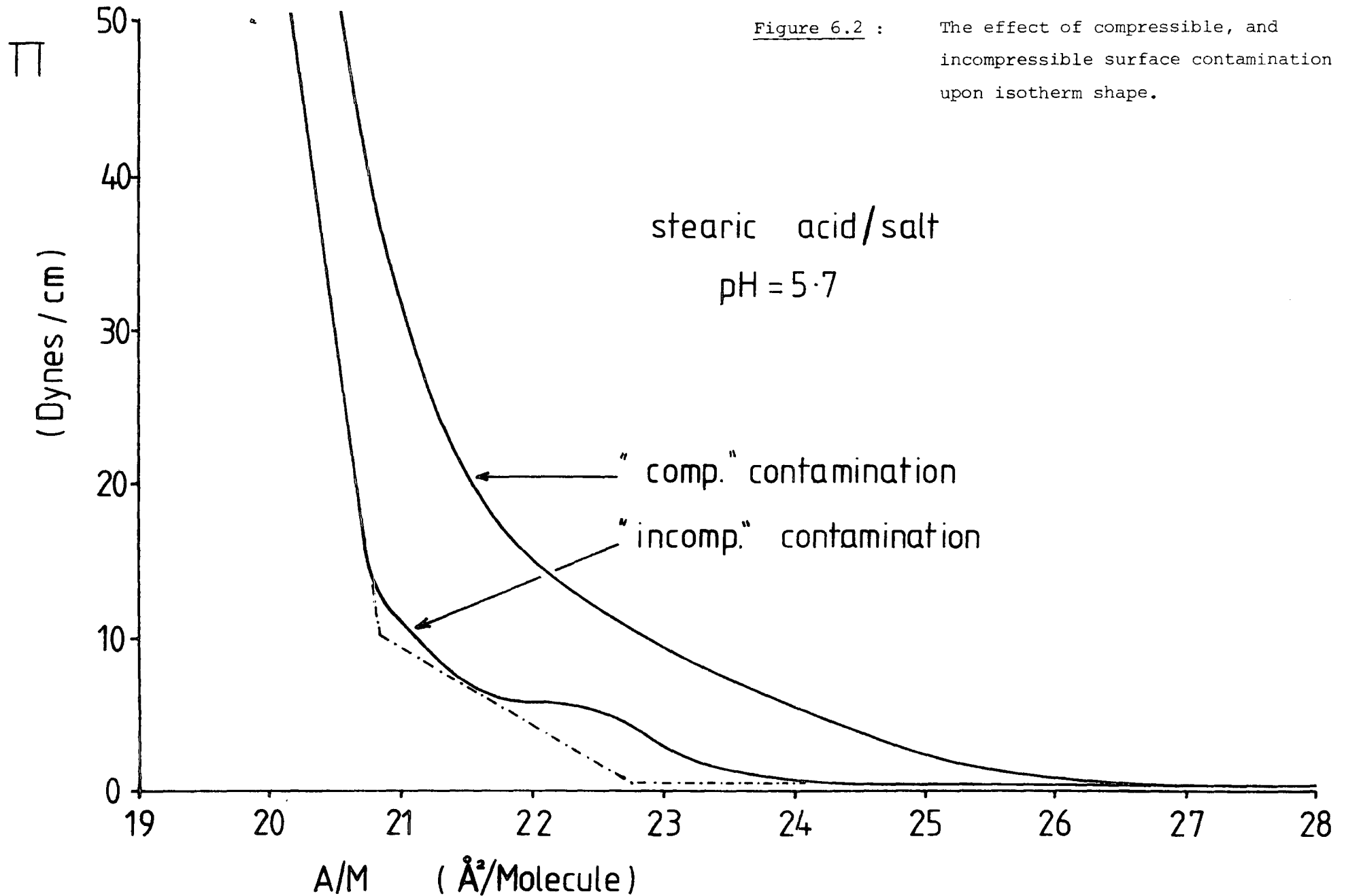


becomes significant and both resultant components are soluble. This is why the stearic acid alone is unstable and therefore unsuitable for serious deposition. With the additional metal ions in the subphase there is little effect upon the curve at less than pH 5, as the equilibrium is shifted totally to the stearic acid side. Above this value, however, the ionisation now results in the formation of cadmium stearate (Fig 4.1) and the isotherm shape is gradually changed. The main effect here is the enhanced stability of the monolayer reducing the duration of the liquid phase. This change increases with pH, and by 6.5 the mixture is dominated by the salt configuration, resulting in the liquid phase all but disappearing. Throughout this effect the solid phase part of the plot remains unchanged except for a lowering of the pressure at which the transition occurs. This is again symptomatic of the enhanced stability of the monolayer. In practice, considerable investigation was undertaken to assess the effect of pH upon isotherm shape and monolayer quality. Some examples of the effect of pH are given in Fig 6.1.

#### The Effect of Contamination

Up to this point, the considerations of isotherm plotting have been based on virtually ideal conditions and the resultant plot has been due to simple stearic acid/cadmium stearate. In practice, however, the plot is also extremely sensitive to the presence of additional (normally undesirable) material, which gives rise to deviation from the ideal shape. The effects recorded can be broadly grouped into two categories ; those due to relatively elastic contaminants, which influenced the entire compression, and those due to inelastic material which showed more localised effects on the isotherms. An example of each type is given in Fig 6.2. In the former case, the resultant isotherm was normally severely rounded, often to the point of completely masking the real break point. These effects tended to be rather irreproducible, however, but were usually removed by a thorough clean of the





entire system. The latter type by contrast showed a far more permanent effect, but this was restricted to a minor "bump" in the liquid phase portion of the plot. In this case the non-linearity was very resistive to cleaning, which normally reduced rather than removed the effect. This problem was resolved by the use of "recompression" ; this can be summarised as follows . The newly spread monolayer was initially compressed up to the solid phase portion of the isotherm - about 25-30 dynes/cm. This was followed by the opening of the barrier, back to a point just beyond the liquid/gas transition. The monolayer was now left to stand for about five minutes before being re-compressed as normal. This operation was found to not only affect the contamination bump , normally removing it, but also shift the isotherm slightly (reducing the area/molecule), and generally sharpen the shape of the plot, as shown in Fig 6.3. In general, the process could be repeated as often as required, but a maximum of three attempts was usually adequate to remove the majority of "bumps". It is likely that the resultant clean-up of the isotherm can be explained as follows : Initial compression causes phase changes in not only the primary monolayer, but also in the contaminant species. The latter material forming a condensed phase at a slightly higher area/molecule, whilst the stearic acid/cadmium stearate is still liquid. Increasing the pressure further, now causes ejection of this foreign material onto the surface above the monolayer, from where it has no further effect upon the isotherm. Subsequent reduction of  $\pi$ , by opening the barrier only partially, prohibits re-incorporation of the contaminant into the monolayer. Thus the re-compression run shows no signs of the initial problem. This treatment is of course unlikely to have any significant effect upon the initial group of elastic contaminants, as their wider compression range prohibits their ejection from the monolayer.

This model is of course only one of many possible explanations for

this phenomenon, but currently available evidence does tend to fit this idea . The isotherm shape, suggesting the compression of an additional phase, the return of the problem if the barrier is fully opened, and most of all, the gradual removal of the problem by frequent use of the trough. It is however at this stage not possible to identify the particular material responsible for this effect, and further work is therefore under way.

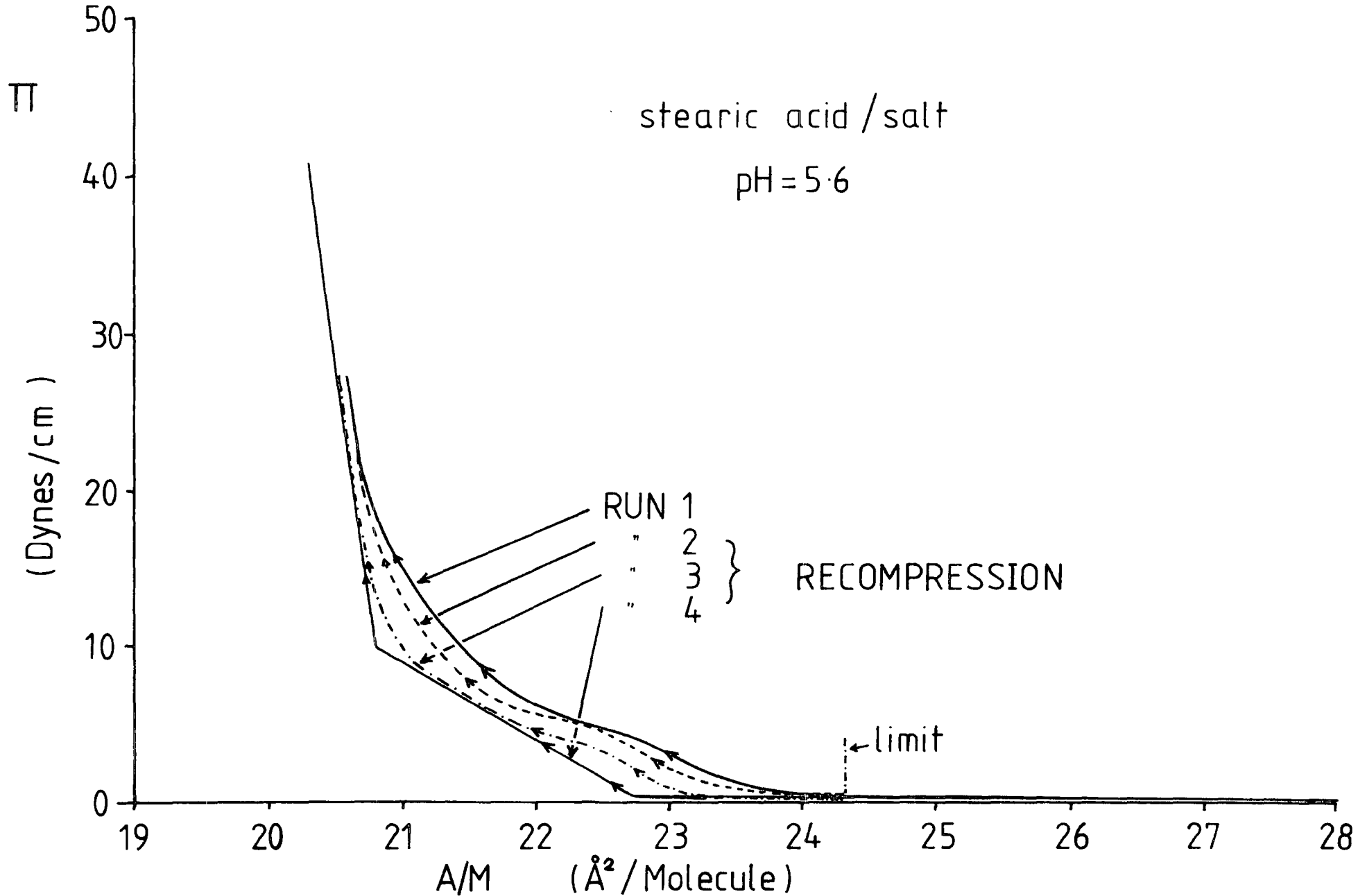
#### Other Isotherm Effects

In addition to contamination, there are several other minor influences that cause deviation from the ideal plot. Some of these will now be briefly mentioned.

The speed of compression of the barrier was found to affect the shape of the isotherm, and any increase over the normal 5mm/sec rate produced a pronounced rounding of the break points ; similar to the effect of "elastic" contaminants. This effect was concluded to be instrumental, due to the limited response of the microbalance. In addition, increases in barrier speed were accompanied by resonance effects causing pronounced surface ripple and subsequent monolayer damage. Because of these two effects, it was normal to avoid these higher compression speeds as far as possible.

The other significant variable which was found to affect the isotherm shape was that of time ; here however as with many time dependent situations the effects were very difficult to study. It was found that at various stages during the plotting there were potential time dependence effects ; for example, rate of spreading monolayer, time until initial compression, time until recompression, rate of compression (below non-linearity threshold) etc. The major relevance of these time effects can be traced to the use of organic solvents whereby the actual evaporation rate is not fully known, and it is highly possible that significant amounts remain for long periods ,thus being incorporated into the monolayer. In practice, experimental investigation

Figure 6.3 : The use of recompression to remove certain contamination.



into most of these time variables using different periods, and various solvents showed little degradation provided at least five minutes were allowed between critical stages.

#### 6.4 FILM DEPOSITION

For monolayer deposition, it was normal to spread considerably more stearic acid than was used for isotherm plotting (where X axis calibration requires the amount to be known and constant), in order to allow for area loss during compression and larger area substrates. The usual amount was about 20 turns. This layer was then compressed as with plotting an isotherm but only to a predetermined pressure, whereby the feedback electronics undertook to maintain the given pressure as material was removed. The normal pressure for dipping was 30 dynes/cm, although at extremes of pH this was sometimes reduced to allow for monolayer instability. In addition, it was usual during the initial compression to plot an isotherm simultaneously, this allowed real time monitoring of the monolayer to give an indication of film quality and identify potentially bad multilayers. Following the compression (and recompression if required) the monolayer was allowed approximately ten minutes to stabilise before dipping was commenced, during this period it was common for area losses of 2-3% to be recorded as final rearrangement of the molecules removed any remaining defects and voids in the film. Where no stabilization was achieved, and the area continued to collapse (albeit at a slow rate), this symptom was normally due to excess amounts of undesired surfactant material in the monolayer, and the only solution was to clean off the layer and begin again.

As has been discussed previously, there are basically three different modes of monolayer pick-up, normally termed X, Y, and Z as shown in Fig 4.2. Which particular mode is present at any given time is defined largely by the subphase pH and the substrate final treatment, i.e. the type of surface

presented to the monolayer. In the latter case, if the substrate was hydrophilic, it was found to be advantageous to begin with the sample immersed in the water prior to the spreading and compression of the monolayer. This procedure avoided the downward passage of the substrate through the compressed monolayer (without any pick-up), and thus appeared to produce a better interface region. In general, the deposition of the first monolayer was found to be the most critical part of the whole operation. Not only was the bonding at this point fundamentally different to that in the rest of the structure, but also any problem or defect occurring here would be multiplied by each subsequent layer, throughout the structure. The bonding of the molecules in the bulk of the film can be seen to be a relatively strong interaction due to the head/head and tail/tail stacking sequence. By contrast, however, the adhesion of the initial layer is far more tenuous and reliant upon weaker interactions. To ensure a good initial monolayer therefore, a much slower dipping speed was used at the beginning of the operation ( $\sim 1$  mm/min), and subsequently increased by a factor of three or four after the initial layers. This latter increase was required to reduce the overall operation time, which would otherwise take many days for large samples.

Throughout the deposition operation, a 2X-T recorder was used to monitor the surface pressure and barrier area, the former normally remaining constant during the whole operation. By contrast, however, the area slowly decreased as material was removed from the monolayer and deposited onto the substrate. This decrease, when amplified was found to provide an excellent real time monitor of the dipping operation, from which the absolute quantity picked up in each direction could be measured. Some examples of recorded pick-up for various types and deposition are given in Figs 6.4-6.6, showing how not only the particular mode could be distinguished, but also any changes occurring as the dipping progressed due to pH and other variations. In



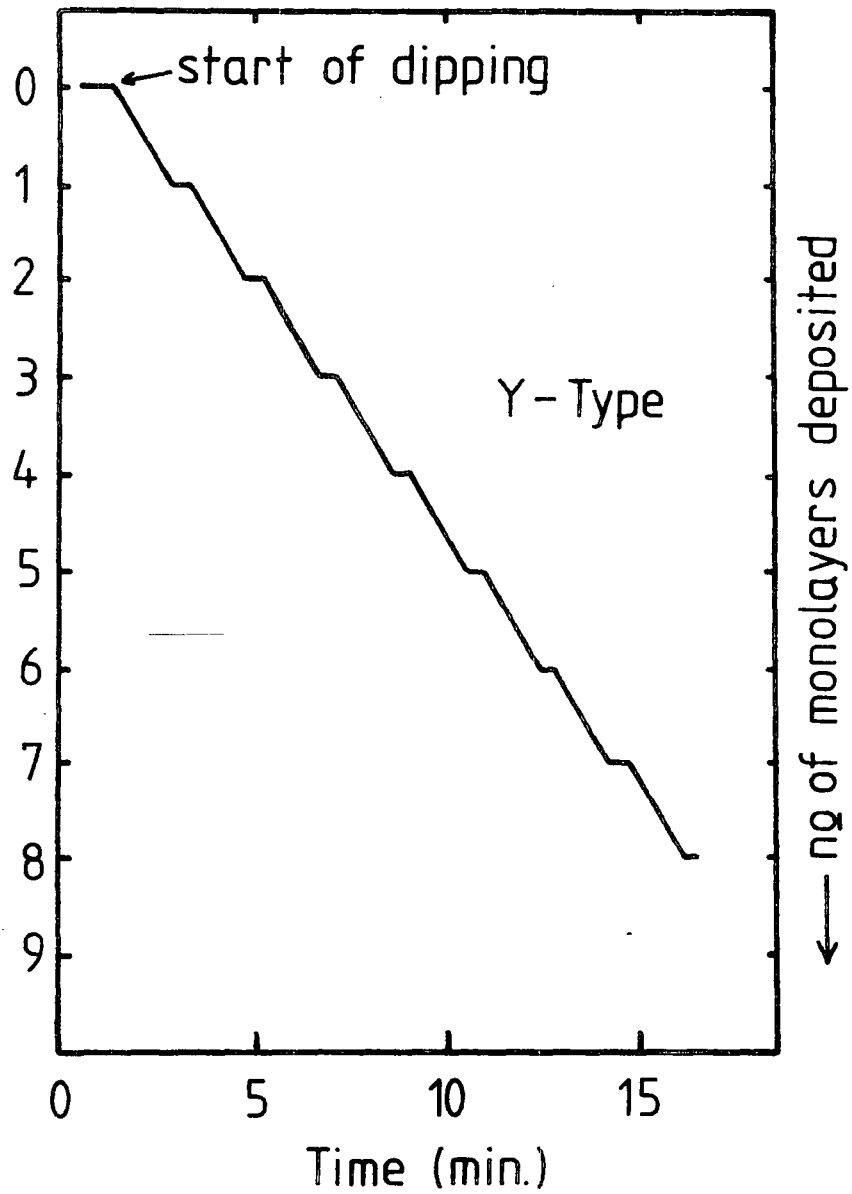


Figure 6.4 : Area-time plot for good Y-type pick-up.

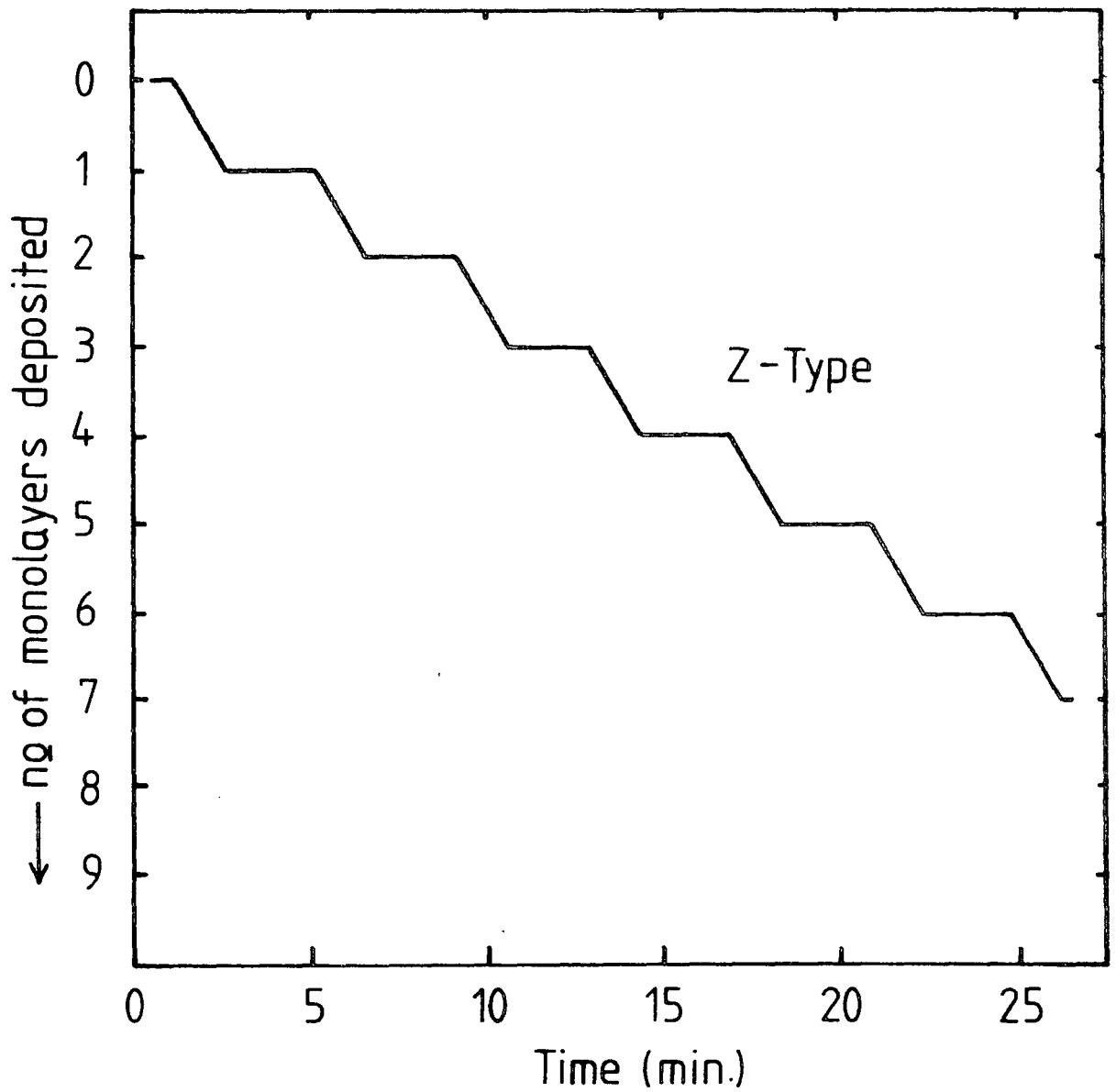


Figure 6.5 : Area-time plot for Z-type pick-up.

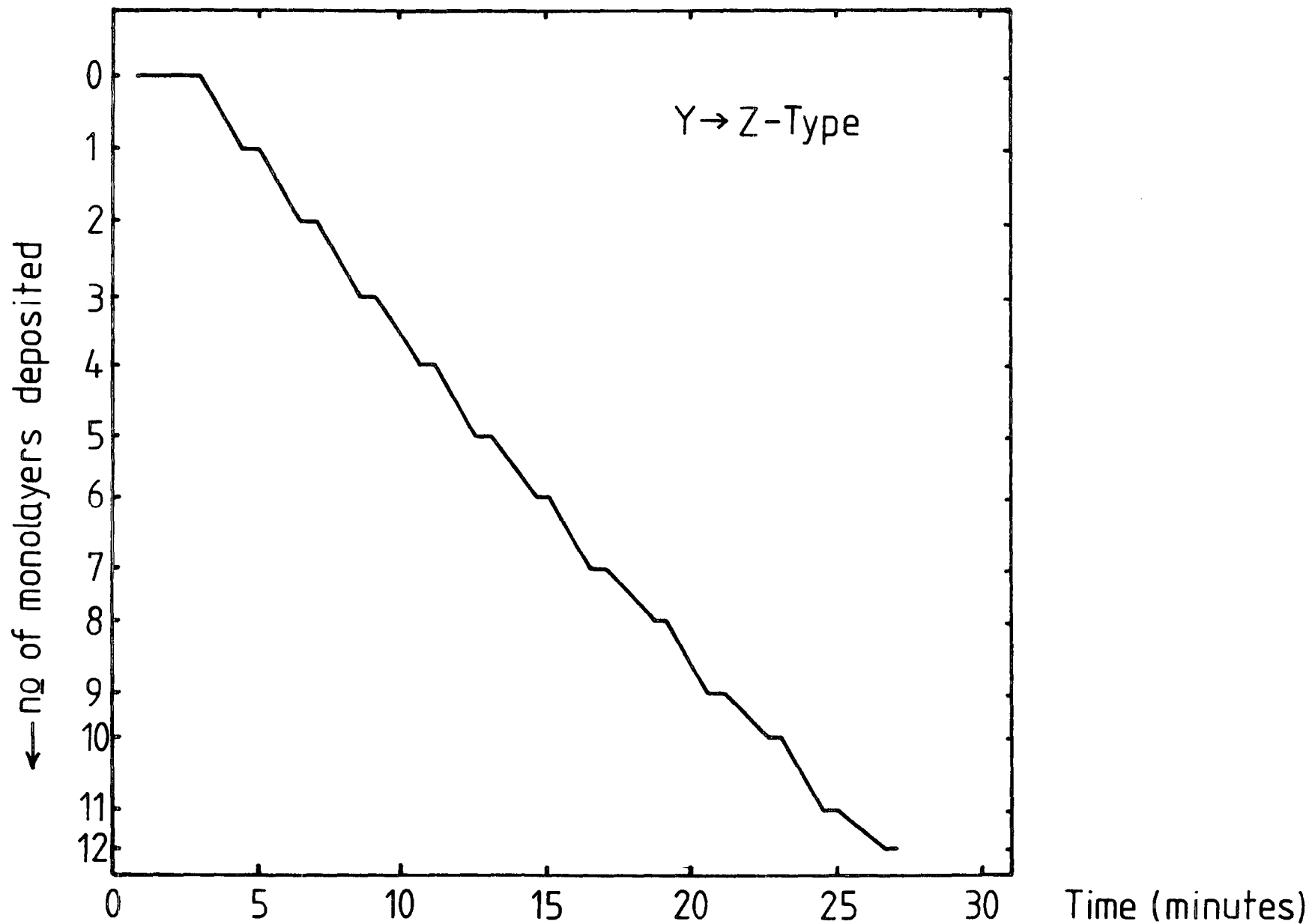


Figure 6.6 : Area-time plot showing apparent change from Y → Z type deposition.

addition, by comparing the reduction in monolayer area with the size of the substrate it was possible to ascertain if the required 100% pick-up was being achieved.

#### Discussion of Monolayer Stacking

The discussion of the basic dipping mechanisms in the earlier chapter divided the process into three possible types ; X, Y and Z. This division was originally conceived during the early work of Langmuir and Blodgett<sup>(1)</sup>, where the normal mode was Y ; X was observed at extremes at pH, and Z not at all (its definition being basically speculative). More recently, however, these basic distinctions have come under severe criticism as the real process is seen to be extremely complex. The major problem is that in spite of both Y and X type deposition being observed (from the area reduction with time), associated studies of the resultant films<sup>(2,8,9)</sup>, show the spacing of the acid groups to be inevitably twice the molecular length. This evidence therefore suggests that independent of the pick-up mode, the resultant films are always Y type. In addition, more recent detailed studies of this process<sup>(6)</sup> have proposed the existence of another mode of deposition referred to as XY, which as its name suggests, is a cross between the two original extremes. Before going on to discuss the results obtained here, it is perhaps useful to consider some of the various explanations proposed by ~~other~~ authors :

Even at the beginning of work on multilayer films it was thought quite probable that the molecules were partially mobile and thus able to move around. This idea led to Langmuir<sup>(1)</sup>, and later Gaines<sup>(3)</sup> suggesting that overturning may occur at some point during X deposition mode to account for the apparant Y type resultant film. Sometime later, in a detailed study of monolayer properties, Charles<sup>(4)</sup> proposed the overturning of every other downward layer during pick-up as a means of producing Y type films. This idea was developed further by Honig<sup>(5)</sup> who correlated a large number of practical observations and concluded that the overturning occurred actually

under the water, after the initial pick-up. In his model, about half the new layer revolved, causing the built-up film to be produced in a rather ragged and uneven fashion. More recently, a paper by Hasmoney<sup>(6)</sup> as well as reporting the existence of XY deposition, developed a model to explain both this and X deposition without invoking any ideas of overturning. Here the formation of two distinct forms of salt is proposed, the final form  $Pb St_2$  (the author used  $Pb^{2+}$  ions rather than  $Cd^{2+}$ ; the arguments are otherwise identical), and an intermediate form  $Pb^+ St$ , where only the latter species is present in the surface monolayer. Pick-up is suggested to occur only onto  $Pb^+ St$  sites in the multilayer during the upward motion, but onto all available carbon chains on the downward transition. Thus the ratio of  $Pb St_2$  to  $Pb^+ St$  in the film defines the extent to which pick-up occurs. This model is probably the best to date, but it is clear that many problems still remain, and further work is necessary before a total understanding of the process emerges.

The majority of dipping undertaken by the author showed Y, and what at first sight appeared to be Z, with occasionally X at extremes of pH. The Y and X were not hard to explain as they were the types noted by other workers, but the occurrence of Z has not been reported by anyone else. Thus one of two conclusions can be drawn; either the effect was real and a function of the relatively uncharacterised substrate, or alternatively the effect was merely instrumental. This latter possibility can be explained as follows: Many of the substrates dipped were not identical on both faces, due to the preparation techniques of the semiconductors; the use of epitaxial layers, or even the use of evaporated aluminium on glass for MIM structures. It was therefore possible that a different mode of pick-up may have existed for each face. If adhesion to the back surface was particularly bad, any monolayer deposited during the upward motion, would come off again on the downward trip, leading

ultimately to no net pick-up or area loss. The front face by contrast may have picked-up X-type, or on the downward traverse only. The net area record for the combination of these two faces will therefore show apparent Z, as the downward pick-up and loss cancel, leaving only the upward pick-up showing on the trace. As detailed investigation has yet to be carried out it is not possible to prove either explanation. It is doubtful however that minor differences in the substrate surface are enough to produce this marked deposition dichotomy.

In practice, little or no previous work has been done attempting to deposit films onto III-V, and II-VI compounds, it is possible that this fact alone is enough to explain our observations. Furthermore, the majority of our depositions onto aluminium and silicon tended to be Y type and thus in agreement with other workers, as would be expected.

If Z type deposition has been observed, then ideally a model must be proposed along with it, to explain the stacking sequence. This has unfortunately not been undertaken in any detail apart from cursory suggestions. The overturning models proposed earlier for X-type stacking are quite applicable providing the movement occurs during the pick-up or upon re-insertion into the subphase. Otherwise the sequence would require overturning to happen with the substrate out of water - a rather unlikely event. No pick-up would of course occur on the downward traverse. In practice, the aforementioned types of "mixed" films were also quite often noted, but of YZ rather than XY type. Similar explanations can however be invoked by combining ideal Y pick-up with some overturning, and thus Z pick-up.

#### Monolayer Collapse

It has been previously mentioned that under certain conditions, collapse of the spread monolayer can occur. The most frequent origin of this effect is in isotherm plotting where the excess pressure is applied to obtain

the final low area portion of the curve. Under normal dipping conditions, the application of a relatively low constant pressure can also induce collapse over long periods of time. This effect is normally shown by thin white lines appearing on the surface (of the normally invisible monolayer), in a random pattern. These lines become longer and more numerous as time passes. The collapse mechanism is thought to involve some buckling of the layer<sup>(1,7)</sup>, and the two resultant chains rising vertically upwards with hydrophilic groups together. These normally then break off when several tens of molecules long and lay on the surface - thus appearing as white lines. The collapse mechanism in practice requires some form of nucleation, normally a particle within the film, or more likely in the case of the long term effect, air-borne material landing on the film. It is also likely that some ageing or hardening of the spread monolayer occurs with time, as visible structure becomes apparent after more than ten hours. This crystallisation process could also aid the nucleation and progression of the collapse. Because of these observations it became normal to avoid slow deposition runs as far as possible, and otherwise renew the monolayer after a maximum of three hours on the subphase.

This chapter has described in detail the Langmuir film deposition process, and some of the practical difficulties resulting from the required operating conditions. It has also discussed the solutions evolved to overcome many of these problems. From this discussion, it can be concluded that providing care is taken at all stages of the process, the resulting Langmuir film will be a uniform insulator of known thickness. If these conditions are not met, then the result is less satisfactory.

CHAPTER 7

QUALITY ASSESSMENT AND ELECTRICAL PROPERTIES OF

LANGMUIR-BLODGETT FILMS

The Langmuir-Blodgett deposition process, although simple in concept, is very sensitive to contamination at all stages of the operation - a problem not uncommon in the semiconductor industry. Because of this susceptibility it was considered useful to monitor the resultant multilayer structures to ensure that no unwanted material was being incorporated into the film. This chapter therefore briefly describes the simple techniques used to check each individual film.

In addition, before these materials could be incorporated into MIS structures, it was necessary to investigate their electrical behaviour separately, as MIM structures, in order to help the understanding of the final device. The measurements undertaken, and the results obtained during this electrical characterisation are also presented in this chapter.

7.1 INSULATOR FILM QUALITY AND ASSESSMENT

Because the deposition of Langmuir films is essentially a surface process, the detection and observation of most types of contamination is relatively easy. Indeed, not only do the various monitoring steps applied during the deposition process (isotherms, pick-up records) give a very good warning of sub-standard film quality, but the contaminants themselves give rise to significant effects upon the films. Thus it is by the observation of these latter defects that overall film quality can be monitored and predicted. The origin of these defects can be explained as follows : The initial compressed monolayer floats on the surface of a water subphase, thus any soluble contaminants will be dissolved in the water, and unless present in large amounts will

have little effect upon the film once it is removed. Any significant contamination must therefore be surfactant in nature, and will thus lead to significant voids in the monolayer as it replaces stearic acid/Cd stearate at certain points in the layer. When picked up onto the substrate this material will interrupt the normal stacking and adhesion not only in the one layer, but at the same point on all subsequent layers. Thus it can be seen that any species present in the first few layers, or indeed initially present on the substrate will generate a void all the way through the multilayer. It should be noted that it is of course possible to incorporate additional species into the film that are contaminant but not surface active; their effect is however relatively minor as their sphere of influence is only one or two monolayers and thus does not grossly affect the electrical properties of the film.

The most convenient method found to detect the effect of these surface active materials was optical microscopic examination, as this was relatively quick, and the majority of features occurring were normally relatively large. This approach, although proving excellent for thick films ( $\sim 30$  layers), on InP, did create some problems with thinner structures, and ordinary metal substrates. In both of these latter cases, the trouble was caused by the extreme thinness of the film and its resultant inability to scatter significant amounts of light to build-up contrast patterns. With InP, the refractive index was fortuitously the correct value to produce a good image. The microscope used had a maximum magnification of X300, and therefore allowed the observation of particles or holes down to around  $10 \mu\text{m}$  in size. Some examples of the various features noted are given in Figures 7.1 - 7.3. The first photograph (Figure 7.1) shows a typical good quality film, this exhibits good overall uniformity with very few defects, and only very small ones. These latter holes were very likely caused by small dust particles landing upon the monolayer during the dipping process, and their density and size are insufficient to affect the electrical characteristics. The presence of somewhat



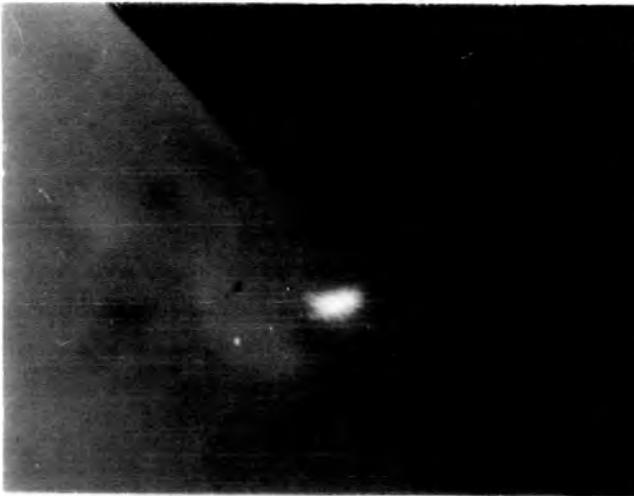


Fig. 7.1 Typical good quality film

(  $\longleftrightarrow$   $\sim 0.1\text{mm}$  )

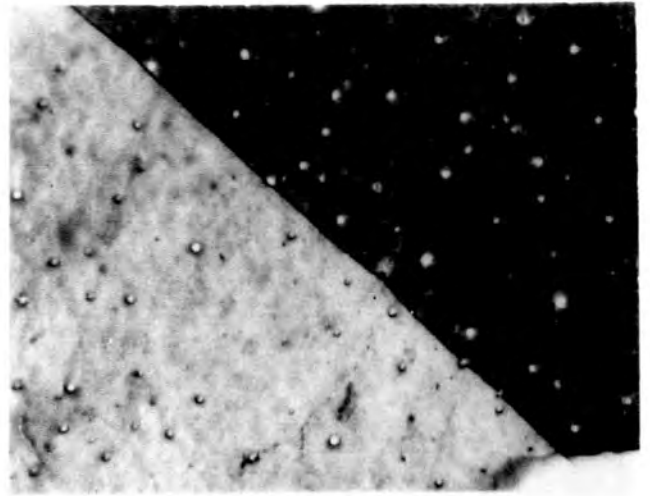


Fig. 7.2 Poorer quality film : Showing significant pinhole density.

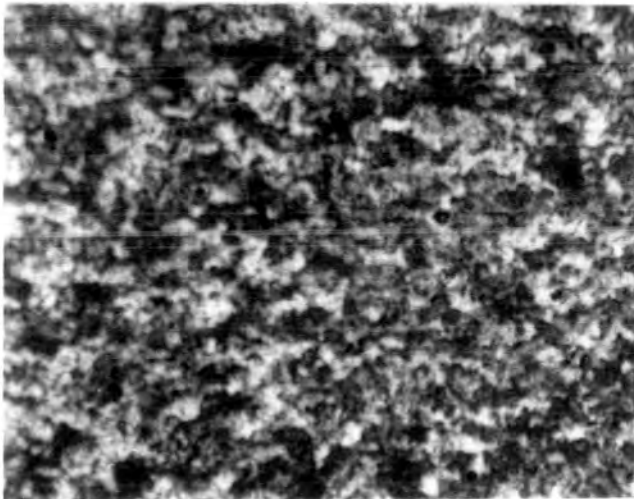


Fig. 7.3 Bad quality film : with amorphous appearance



Fig. 7.4 Typical good quality top electrode



Fig. 7.5 Diffuse dark ring around electrode, indicative of poor sealing.

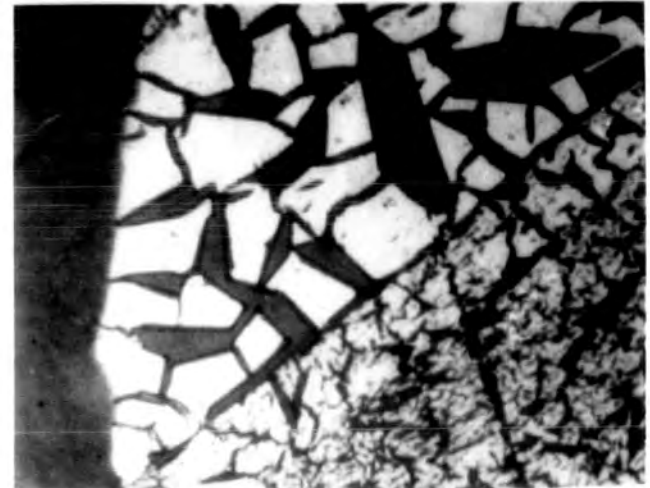


Fig. 7.6 Cracked electrode indicative of thermal expansion problems.

larger holes, normally with a higher density was observed occasionally, as shown in Figure 7.2. In this case the defects were caused by a combination of inadequate surface cleaning of the substrate, resulting in surfactant materials deterring film deposition, and excess undesirable contamination in the film, again inhibiting film adhesion. Both these situations were found to give rise to similar effects, although in any given case, one was normally dominant. The density and size of the defects were of course a variable quantity, and with some structures usable devices could still be produced. In most cases, however, these bad films were discovered immediately after the dipping operation, and were thus processed no further. The final example, in Figure 7.3, shows a very bad quality film, this has a film to hole ratio of virtually 50% and indicates major contamination problems. These types of film were very rarely due to the substrate except where little or no prior cleaning had been undertaken. In most cases, therefore, the origin of the problem was the film itself, and normally resulted in extremely bad pick-up records, and/or poor quality isotherms. These effects were found to originate either from bad contamination, normally of the subphase or the stearic acid, or alternatively from extremes of pH, normally very high, causing full ionisation of the acid and thus bad adhesion to the substrate. In the case of contamination, the situation was rectified by the application of a thorough equipment clean and subphase change. For all films of this category the large hole structure precluded the production of useful devices, and in all cases the film was observed to be largely amorphous and unstructured.

The effect of the evaporation process was also monitored by the optical microscope, this allowed any damage caused by the procedure to be discovered before characterisation was attempted. In most cases, the effect of evaporation was found to be insignificant providing that the required precautions (see section 3.2) were taken. A typical sample with a satisfactory electrode, in this case gold, is shown in Figure 7.4. When the required cooling

process was not fully adhered to, the inevitable result was some form of thermal damage to the film, often manifest in the presence of a diffuse dark ring around the electrode, as shown in Figure 7.5. This effect was usually caused by too short a cooling period prior to evaporation, or bad thermal contact of the sample to the liquid nitrogen reservoir. Again, the degree of the damage was found to vary considerably, and in some cases the apparent effect upon the final characteristics was negligible. In the majority of cases, however, some degradation of performance was encountered, and often the structure was found to be short circuit. Another effect noted to arise from the evaporation process was that of cracked or flaking contact electrodes, as shown in Figure 7.6. This problem was particularly prominent where more than one contact material was used ; for example gold on lead, and was thus concluded to be a symptom of different thermal expansion rates. The solution in this case was found to be a reduction of metal thickness as far as possible, and a reduction in the rate of evaporation. In practice, the former effect, whilst alleviating the cracking problem did lead to trouble during the measurement stages of the characterisation, making the electrodes quite fragile, and in some cases making their area unpredictable.

In conclusion, it has been shown that providing the strict cleaning and preparation procedure is adhered to, insulating film of good uniform appearance and quality can be produced. Moreover, damage due to the thermal deposition of electrodes can be kept to a minimum by cooling the substrate during the evaporation process.

## 7.2 ELECTRICAL CHARACTERISATION

This section presents typical electrical data obtained from various structures incorporating Langmuir-Blodgett films. The emphasis is mainly upon MIM structures, from which AC and DC conduction results were obtained. Also included, however, are some characteristics from films deposited upon InP substrates ; these exhibited somewhat different data.

### 7.2.1 Reciprocal Capacitance Plots

The ability to deposit monolayers of well defined thickness allowed a variety of stepped structures to be deposited on both aluminium and InP substrates. From these structures graphical plots of  $1/C-N$  could be generated ; where N is the number of monlayers built up to produce the given capacitance. If x is defined as the thickness of each monolayer, then nx is the total insulator width at each point. Equation 2.31 can therefore be modified to account for this effect, and becomes ;

$$\frac{1}{C_T} = \frac{d}{A\epsilon_O \epsilon_{OX}} + \frac{NX}{A\epsilon_O \epsilon_{LF}} \quad (7.1)$$

where  $\epsilon_{LF}$  is the relative permittivity of the organic films. From this expression it can be seen that a plot of  $1/C_T - N$  will give a straight line from which  $\epsilon_{LF}$  and d can be obtained.

For most samples an array of 1mm diameter top contact electrodes was used, although in practice the resultant area was not quite constant. This variation was concluded to be due to edge effects during the evaporation reducing the electrode thickness at the perimeter, and thus reducing the effective area. The average value of contact area was found to be  $\sim 5 \times 10^{-7} \text{ m}^2$  (i.e. 0.8mm diameter) although a variation of  $\pm 10\%$  was not uncommon. Because of this inconsistency, the majority of capacitance values plotted were the average of between five and ten individual measurements. A typical example of a  $1/C - N$  plot is presented in Figure 7.7 ; from this line, if the molecular chain length is taken as  $25.8 \text{ \AA}$ , the resultant value of dielectric constant becomes 2.7. This value agrees well with results obtained by others. Also, from this plot it can be seen that the Y axis intercept is at a capacitance of 7140 pF, which corresponds to an interface oxide ( $\text{Al}_2\text{O}_3$ ,  $\epsilon_r \approx 4^{(1)}$ ) thickness of  $30 \text{ \AA}$ . Once again this value is consistent

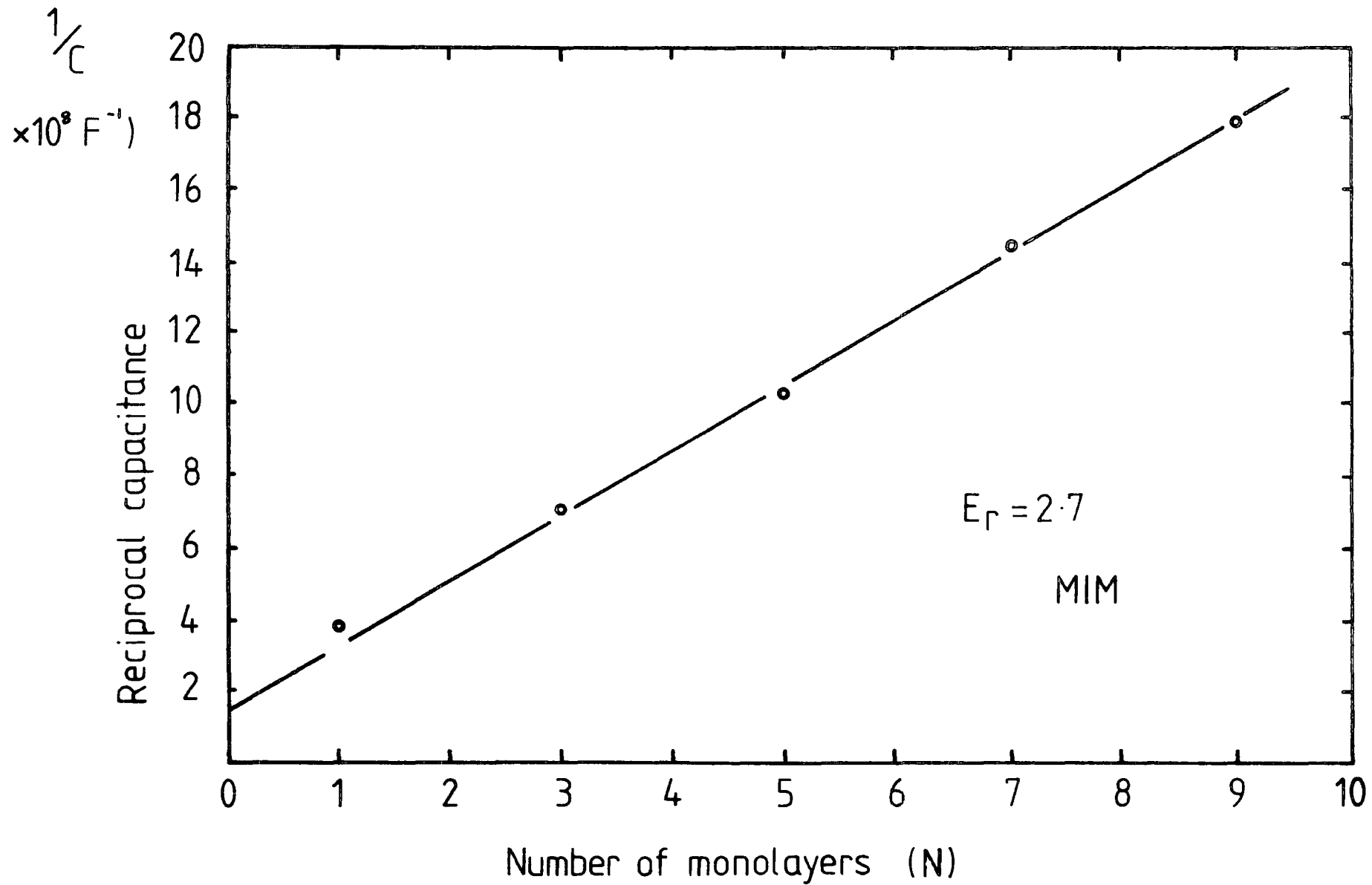


Figure 7.7 : Typical reciprocal capacitance plot for thin stearic acid/Cd stearate film.

with other results. In practice the evaluation and interpretation of this intercept point should be undertaken with extreme care as it is quite common for the first monolayer of a structure to be rather different from the remainder of the multilayer. This effect is not yet fully understood but it may well generate a different dielectric constant for this first layer which leads to the point at  $N = 1$  not lying on the expected line. Differences in structure and resistivity of this first layer can also lead to shifts in the whole plot, and it is often necessary to measure  $R$  (resistance) against  $N$  (no. of monolayers) in order to characterise an unsatisfactory first monolayer. In this situation an intercept of  $n=1$  would indicate that the first monolayer was quite conductive. This point is illustrated in Figure 7.8, which shows a typical plot, in this case for Cd Arachidate, along with data obtained by Sugi et al (see Chapter 4). It can be seen clearly from this plot that while the first monolayer of our data is not quite as resistive as the rest of the structure, for Sugi's multilayer the first two monolayers are very highly conductive. Possible explanations for this first (or more) monolayer effect have been discussed in section 4.3

It is of course possible to deposit much thicker films using the L/B technique, as illustrated in Figure 7.9. This diagram again shows the representation of  $1/C-N$  and from the gradient a similar value of dielectric constant is deduced. With larger steps between layers, the resolution of the intercept point is reduced somewhat and thus only an approximate value for interface oxide can be obtained. In this example the substrate is in fact InP, and taking the dielectric constant as  $11^{(2)}$  gives an oxide of  $\sim 40 \text{ \AA}$  which corresponds reasonably to data obtained from surface analysis procedures (see Chapter 9). Similar plots on  $\text{Al}_2\text{O}_3$  (not shown) have been undertaken and give values of gradient and intercept that agree well with those presented in Figure 7.7.

As previously mentioned, the majority of work undertaken involved the use of stearic acid/Cd stearate, however some structures were fabricated with

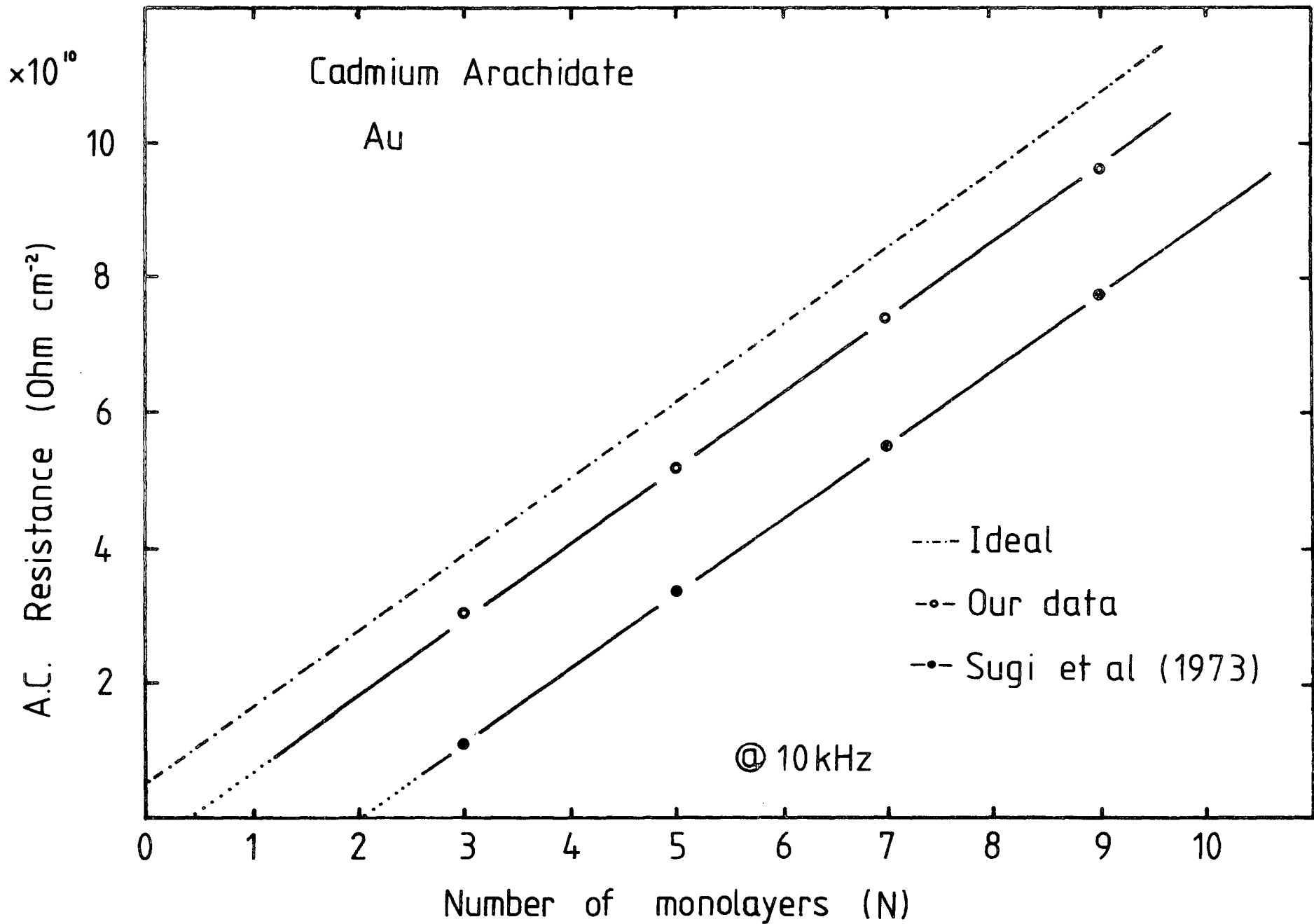


Figure 7.8 : AC resistance plot for thin arachidic acid/Cd arachidate film along with ideal, and data of Sugi et al (Ref. 2.34)

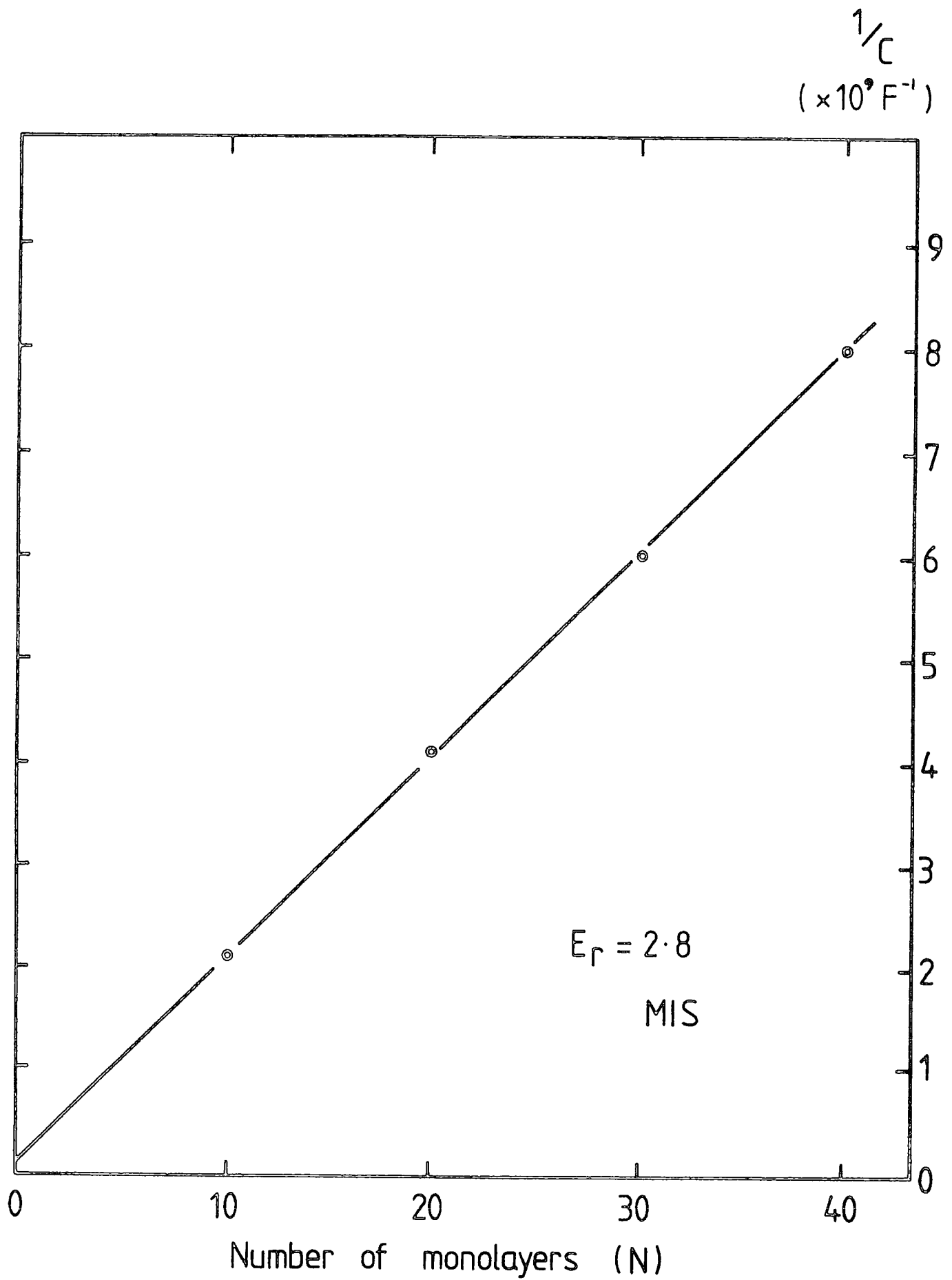


Figure 7.9 : Typical reciprocal capacitance plot for thick stearic acid/Cd stearate film.



arachidic acid. This material has a slightly longer ( $C_{19}$ ) carbon chain than stearic acid, and therefore a lower dielectric constant. An example of a reciprocal capacitance plot for this material is shown in Figure 7.10. From these data it can be seen that the dielectric constant is deduced as 2.5, and the  $Al_2O_3$  thickness 35 Å.

In general the use of stepped multilayer structures can be seen to be ideally suited for simple investigation of surface oxides, enabling some estimation of their thickness. Indeed, this approach is probably exclusive to the L/B technique as no other process can compete with its defined monolayer/multilayer thickness.

### 7.2.2 DC Conduction Properties

In this section, DC conduction effects in Langmuir film structures are investigated. These were undertaken on MIM structures for simplicity and ease of deposition. Conduction in certain MIS structures is also discussed towards the end of the section.

#### (a) Metal-insulator-metal structures

##### Monolayers

Although no detailed investigation of ultra-thin tunnelling structures was undertaken, several exploratory samples were fabricated. With these, one monolayer was deposited onto an aluminium (on glass) substrate, followed by gold top electrodes. An example of the characteristics obtained is given in Figure 7.11, in this case with  $CdAr_2$  as the insulator. These types of structures were found to exhibit a rather surprising  $\log J-V^{1/4}$  dependence as opposed to the usual  $\log J-V$  behaviour. No perfect explanation has yet been proposed for this effect, but a similar dependence is generated by leakage due to image force lowering in a Schottky barrier, as shown in Equation 2.12. This expression can be seen to exhibit temperature dependence and so could in practice be easily checked. Further measurements have shown the characteristics

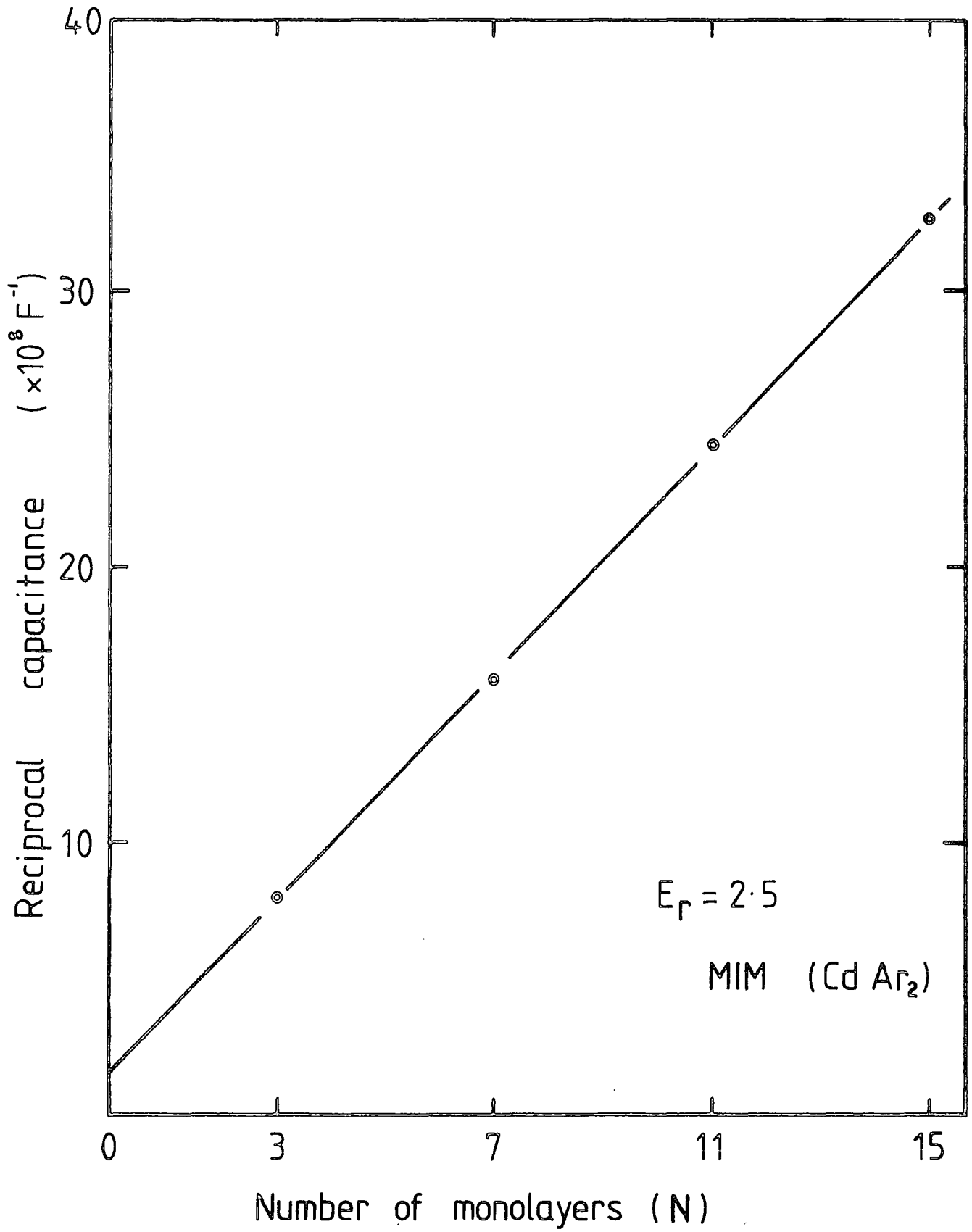


Figure 7.10 : Typical reciprocal capacitance plot for arachidic acid/  
Cd arachidate film.

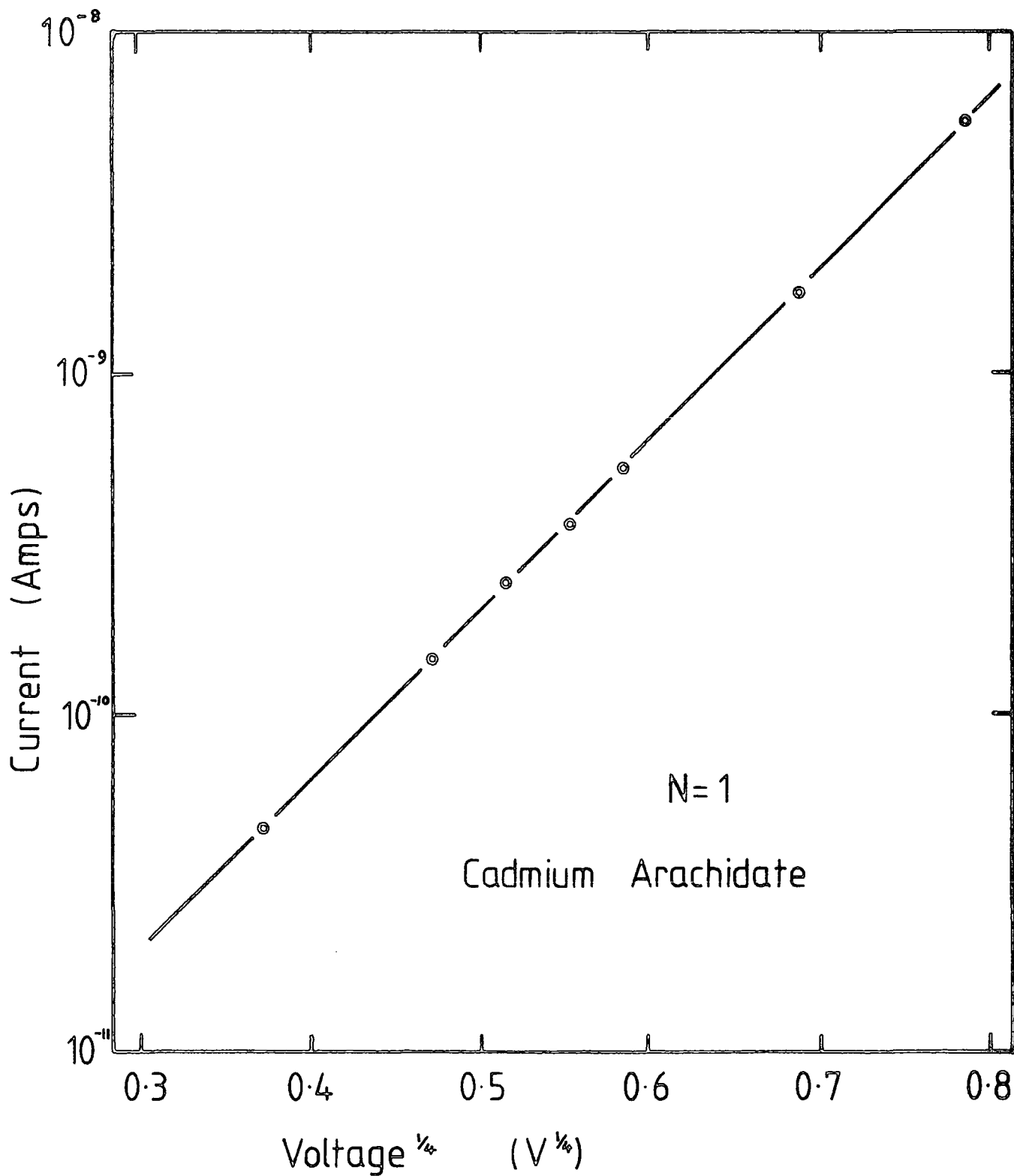


Figure 7.11 : D.C. current through a single monolayer of Ar Acid/Cd Ar<sub>2</sub>

to be contact independent, which therefore disagrees with the Schottky barrier idea. In consequence, no adequate explanation for this effect can be presented at this stage, however the fact that it follows the general  $\log J \propto V^{(n/n+1)}$  scaling law as discussed in section 2.3 does imply the current is barrier limited in some way. A similar  $\log J-V^{1/4}$  behaviour has also recently been observed by Ginnai et al<sup>(3)</sup> at Leicester, however no adequate explanation has been proposed yet by the authors for their observations either.

### Multilayers

The majority of multilayer structures investigated showed  $\log J-V^{1/2}$  behaviour, as observed by other workers, with reasonably consistent values of gradient being obtained at all times. A typical set of data for various different electrode materials is shown in Figure 7.12, for 30 layers of CdSt<sub>2</sub> on an aluminium substrate. As discussed in Chapter 2, this type of plot is characteristic of either Schottky or Poole-Frenkel conduction, although which particular mechanism is responsible is rather more difficult to prove. Given that the insulator thickness is known with sufficient accuracy, then from the gradient of any one of the lines in Figure 7.12, the dielectric constants as calculated from equations 2.19 and 2.22 are found to be ;

For Schottky conduction or Poole-Frenkel (with neutral traps),  $\epsilon_r = 2.6$ ,  
for ordinary Poole-Frenkel,  $\epsilon_r = 10.3$  ;

so from these figures it appears that one of the former mechanisms is more probable. From this evidence alone, however, it is impossible to distinguish the two.

It can also be seen from the MIM characteristics that the use of different electrode materials has a significant effect upon the magnitude of the conduction current ; this is indicative of barrier limited (Schottky) conduction. However, reference to equation 2.18 will show that due to the exponential dependence of the current upon barrier height, a mere 0.1 eV

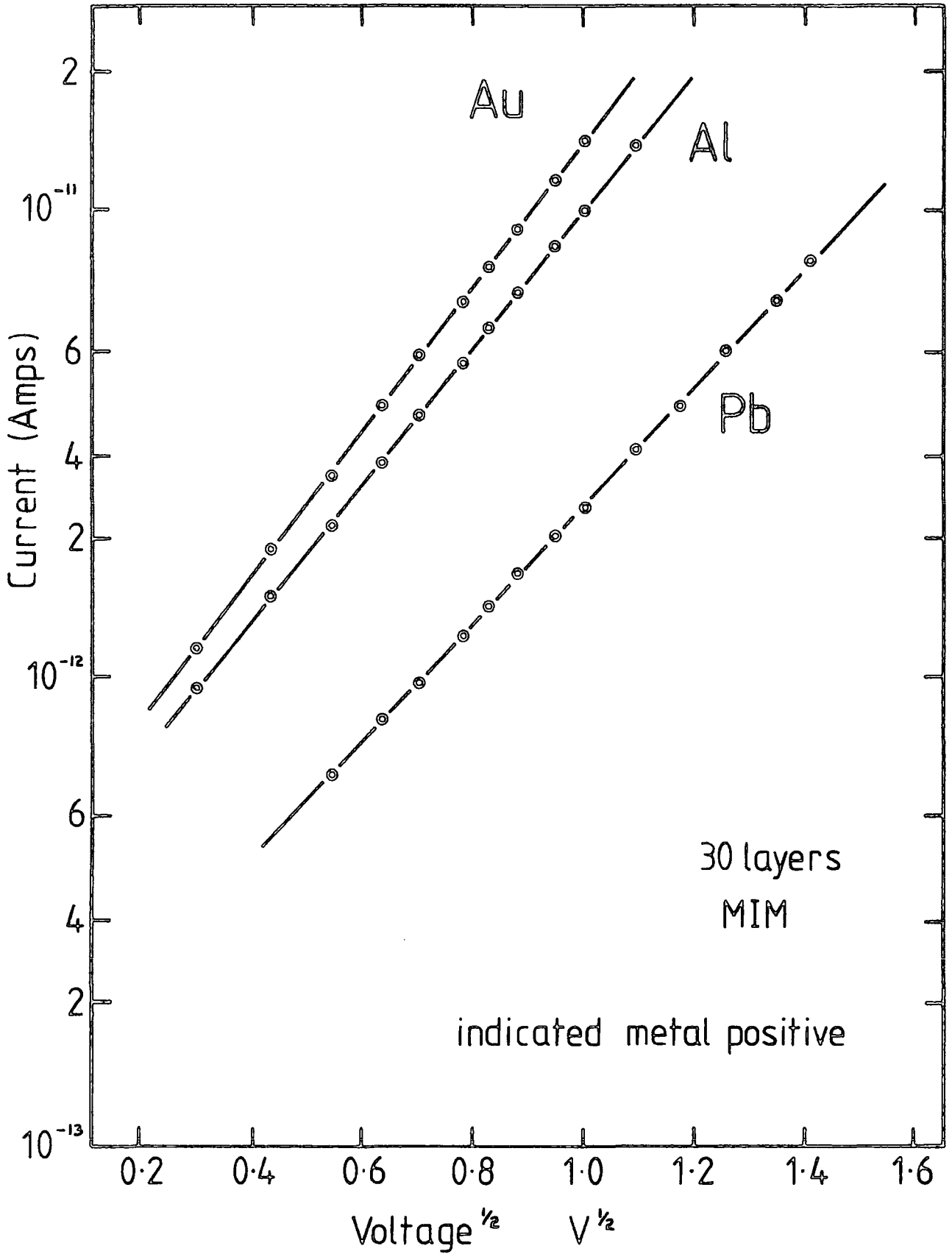


Figure 7.12 :  $\log J-V^{1/2}$  plot for MIM structure, showing three different electrode materials.

change (equivalent to 0.1 V change in work function) will produce a factor of fifty variation in the current magnitude. Moreover, the actual difference in work function between even aluminium and gold is 0.55 V. Thus it can be seen that even though electrode dependence is exhibited it is not large enough to be due to barrier effects. In consequence, it is reasonable to conclude that the mechanism of conduction is Poole-Frenkel, and that minor variations in current are due to electrode oxides (particularly Pb), small inconsistencies in contact area, and possibly local inhomogeneities in the insulator.

In addition to this deduction, various other effects were noted :

(i) The current was found to scale with insulator thickness due to the conduction mechanism being field dependent. This effect varied as (thickness)<sup>1/2</sup> as expected.

(ii) Variations in resultant dielectric constant  $\epsilon_r$  were usually above rather than below the normal value of 2.7. This was reflected in shallower straight line gradients than expected.

(iii) On occasions where damage to the films was produced by poor electrode evaporation, the resultant thinner film showed a steeper gradient than expected. In addition, this effect was usually associated with premature breakdown at low ( 1.0V or less) applied bias.

(iv) The phenomenon of internal voltage (as discussed in section 4.3), was found to be rather difficult to characterise. Values up to 200 mV were noted for 30 layer structures on occasions, and produced lateral shifts of the current-voltage curve. Insufficient detailed investigation was carried out to correlate this effect with any particular preparation parameter.

(b) Metal-insulator-semiconductor structures

During the investigation of Langmuir films deposited on semiconductors, it was noticed that on many occasions the current-voltage characteristics did not show  $\log J-V^{1/2}$  behaviour. The origin and effect of these different mechanisms

will now be discussed.

(i) N-type - Forward Bias

A typical current-voltage plot for a 30 layer insulator on n-type InP is presented in Figure 7.13. From this graph, on  $\log J-V^{1/2}$  axes, it can be seen that although the reverse bias current shows a straight line dependence, albeit with two distinct gradients, the forward bias current does not. By replotting this latter data on various axes it was found that a straight line was generated for  $\log J-\log V$ , as shown in Figure 7.14. This new plot can be seen to exhibit a gradient of two, implying  $J \propto V^2$ , which is indicative of space-charge-limited conduction. Thus it appears that some form of charge injection is present. Because this effect occurs only in forward bias, then the source must be electrons injected from the semiconductor, or holes from the top electrode. Further investigation showed that the effect was not top electrode dependent, which suggested the injected species were electrons from the semiconductor. Moreover by depositing a film onto the reverse side of an epitaxial sample (i.e. the  $n^+$  layer, which behaves as a good conductor) it was possible to fabricate an  $MIn^+$  or effectively an MIM on indium phosphide. With this structure the injection effect was still present, showing that it was not a function of the semiconducting properties of the InP or its depletion layer, but more a result of the surface oxide and interface structure.

The number of sub-standard insulating films resulting from deposition onto InP was found to be significantly higher than for films on  $Al/Al_2O_3$ . This fact reflects the strong dependence on surface oxide character of the deposition quality, and although oxidised under most conditions, the InP oxide was obviously not as ideal as  $Al_2O_3$ . The formation and effect of InP oxides will be discussed in greater detail in Chapter 9. A typical plot for these poorer quality structures is presented in Figure 7.15, showing the rapid increase in forward bias current with applied voltage. These data in fact show a straight

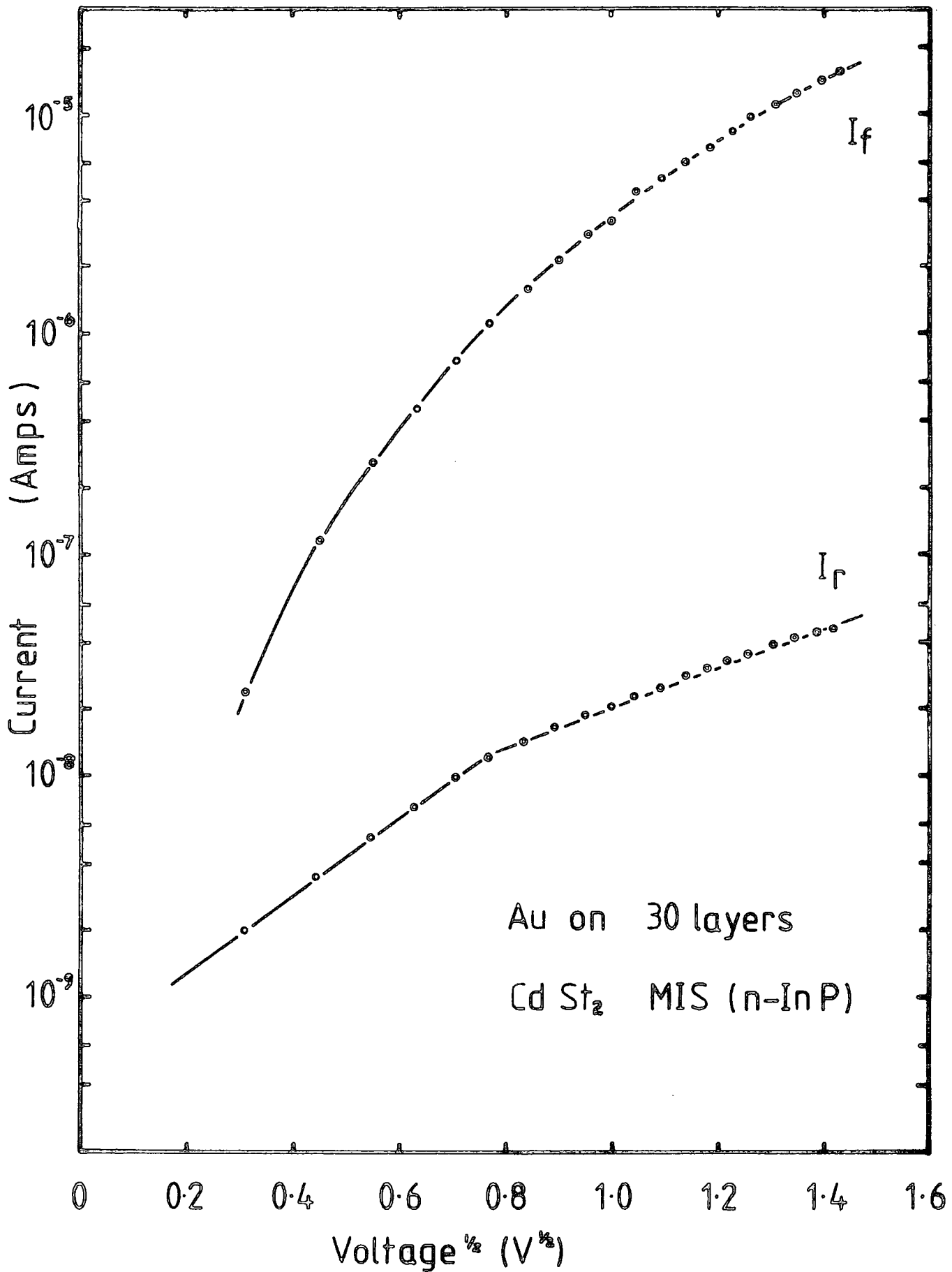


Figure 7.13 : Log J-V<sup>1/2</sup> plot for n-InP/Langmuir film MIS structure.



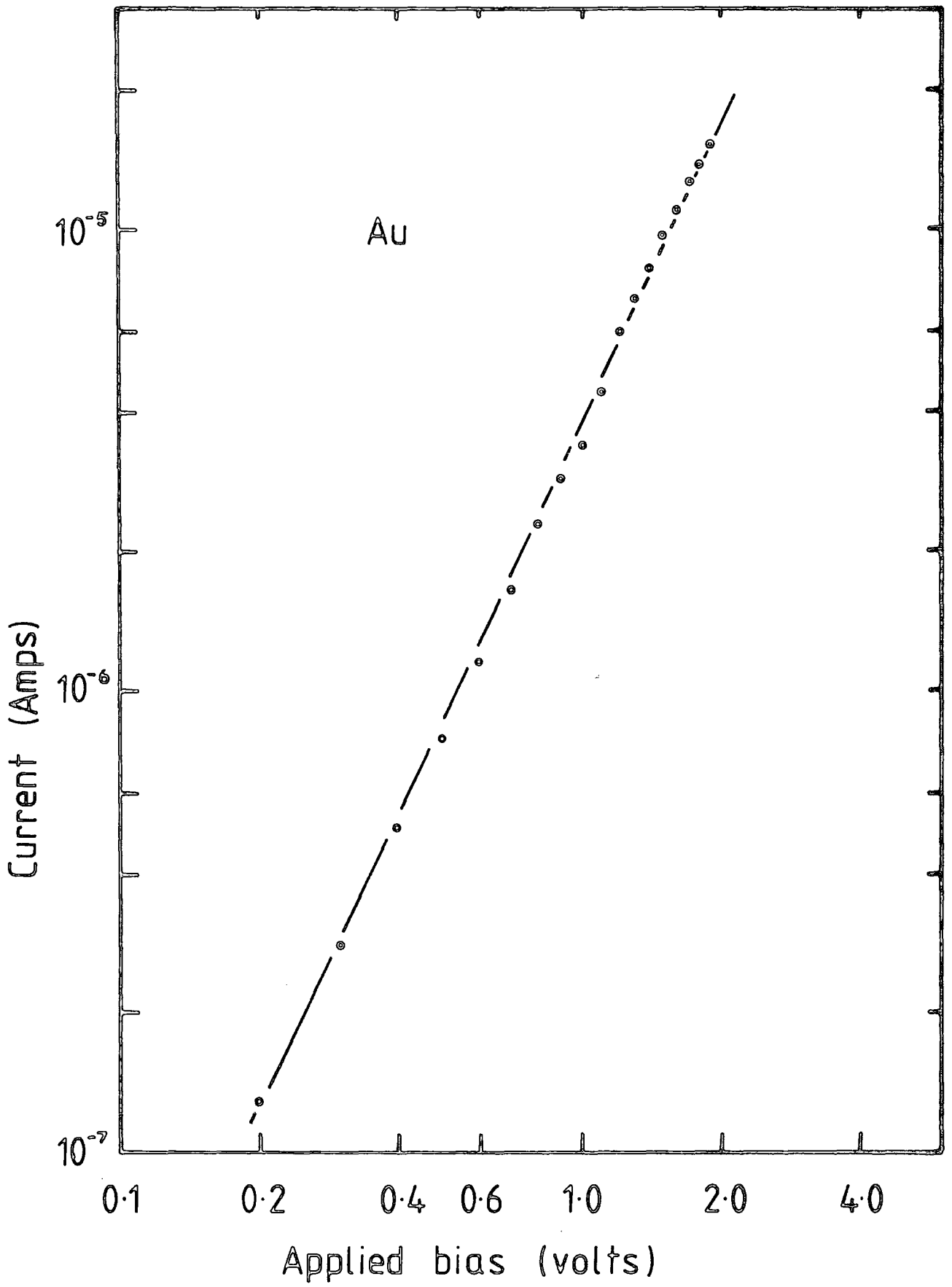


Figure 7.14 : Forward bias n-InP MIS data replotted on log-log axes.

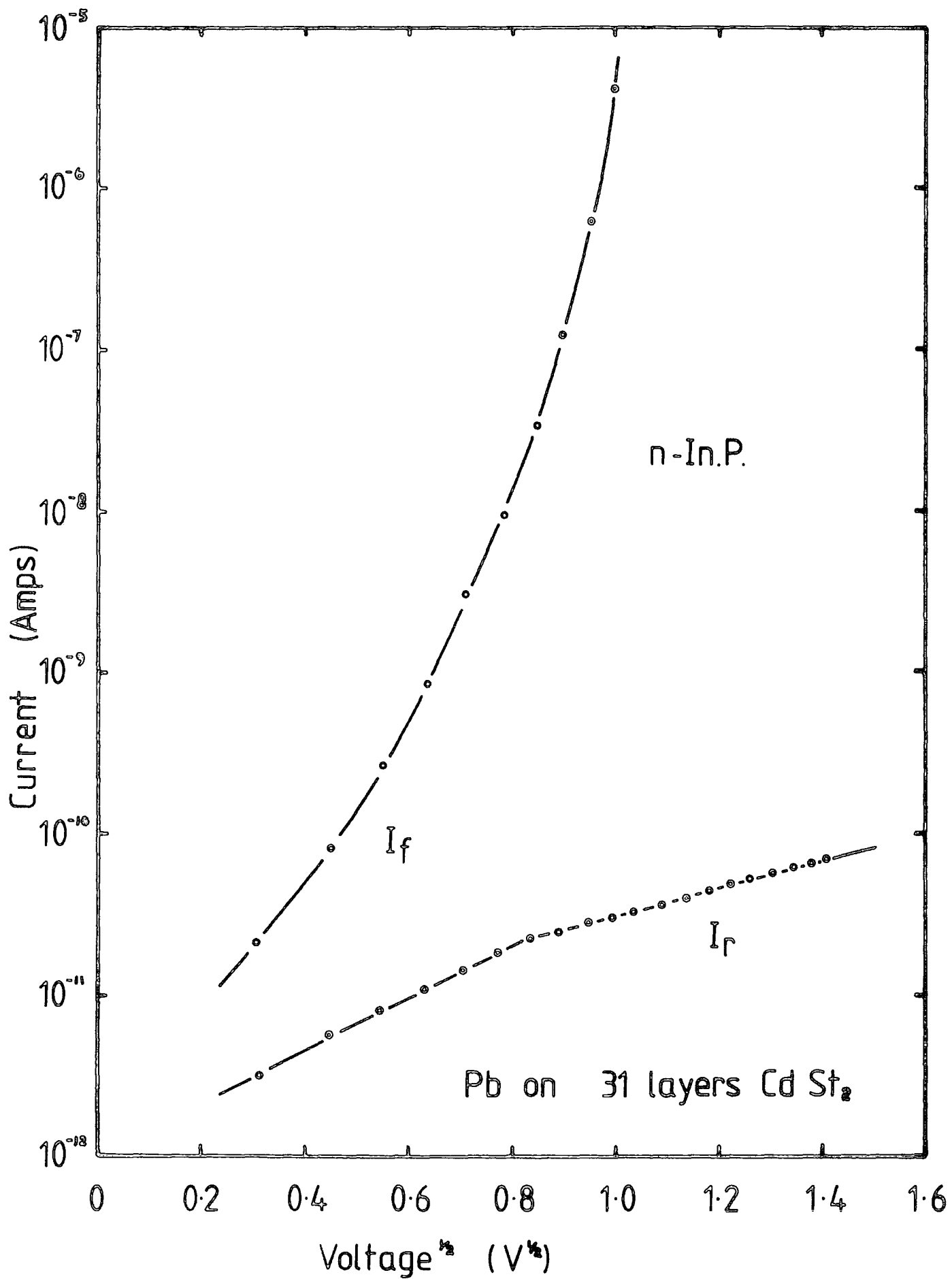


Figure 7.15 : Typical characteristics for poor quality n-InP MIS device.

line when replotted on Log J-V axes, suggesting the presence of a forward biased Schottky barrier as modelled by equation 2.7. In this situation, however, the current magnitudes are considerably reduced when compared to a lone Schottky barrier, suggesting the insulator is having some effect.

#### Reverse Bias

The initial reverse bias current is shown as  $I_{R1}$  and exhibits the same dual gradient structure as with good films. Upon replotting after the forward bias however, these currents are significantly increased suggesting that the damage occurs during the forward biasing operation. In general, the subsequent magnitude of this reverse bias current was rather irreproducible, and depended to a large extent upon the damage caused by the forward bias "breakdown", and the type of semiconductor substrate (doping, epi/bulk etc). No increase of this type was noted for "good" structures which showed  $J-V^2$  behaviour in forward bias. This dual gradient reverse bias dependence is not easy to explain and does not readily fit any simple model. The lower current region has a gradient corresponding well to the data obtained on MIM structures, this suggests that at low fields the voltage is being dropped totally across the film, and Poole-Frenkel conduction is dominant. At about one volt, however, the gradient appears to change to approximately one half the previous value (the magnitude of this shift is quite consistent). This new line corresponds to a dielectric constant of twice the original value, if the same conduction mechanism is assumed to be present. This explanation alone is highly unlikely, however, as the effect is never present in simple MIM structures, and no corresponding step change in AC capacitance values is ever observed.

In practice, as the effect was only observed where the insulating film contained considerable amounts of charge (see also section on P-InP MIS), introduced either by injection, or by some breakdown mechanism, it could

reasonably be assumed to be associated with the formation of a depletion layer in the semiconductor. Thus in this higher field region the structure could be represented as two resistances in series, one for the film, and one for the semiconductor depletion layer. There is however no common mechanism for reverse bias leakage through a depletion layer which shows  $\log J-V^{\frac{1}{2}}$  behaviour ; the closest is  $\log J-V^{\frac{1}{3}}$  (equation 2.12), produced by image force lowering. The high field data in Figures 7.13, and 7.15 when replotted on these new axes does, however, still correspond to a reasonable straight line, over the limited range available. Moreover, from equation 2.12 the gradient of this line gives a dielectric constant of approximately the correct value for InP. Thus it is possible that this reverse bias effect is indeed associated with the semiconductor depletion layer. It should be noted, however, that this explanation is very tentative, and considerably more work is required to verify it, before it can be proposed with any great degree of confidence.

(ii) P-type

For p-type InP substrates quite normal current-voltage characteristics were obtained, as illustrated in Figure 7.16. This plot shows quite good  $\log J-V^{\frac{1}{2}}$  behaviour for both directions of applied bias, and by similar reasoning to that outlined previously, the mechanism here is likely to be Poole-Frenkel (with conduction between neutral trapping centres in the film). Although considerably fewer MIS structures on p-type substrates were investigated, the majority showed this good symmetrical conduction behaviour. As with films on  $Al_2O_3$ , slight variations of gradient were encountered, but normally to a lower rather than higher value. This lack of forward bias injection on p-type material enhances the aforementioned proof of electron injection from n-type substrates.

As with n-type material poorer quality films showed a rapid rise in forward bias current and the same dual gradient reverse characteristic, as illustrated in Figure 7.17.

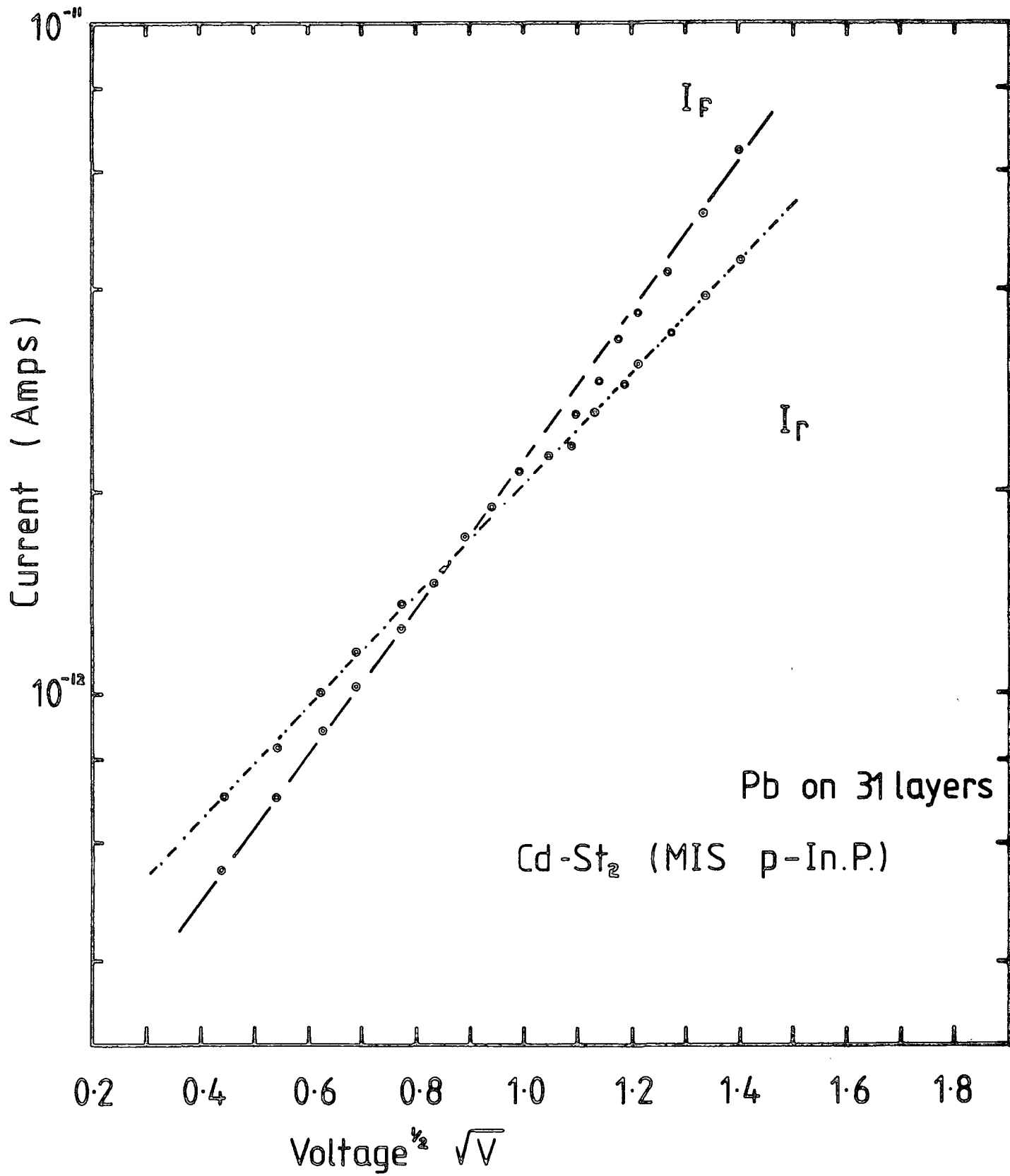


Figure 7.16 : Typical log  $J-V^{1/2}$  plot for p-InP MIS device.

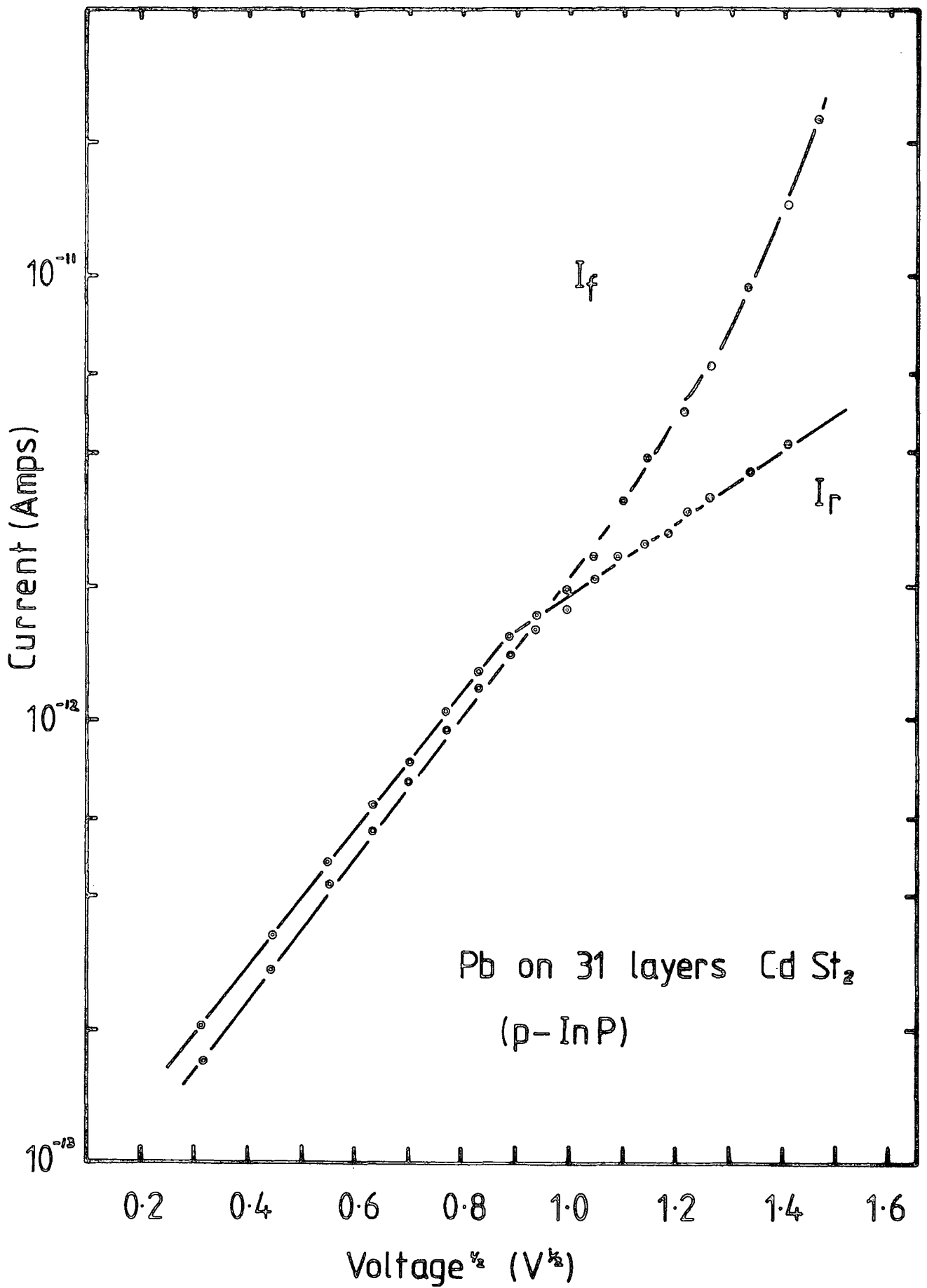


Figure 7.17 : Typical characteristics for poor quality p-InP MIS device.

### 7.2.3 Frequency Dependence of AC Characteristics

Phase sensitive detection techniques were used to evaluate the variation in both capacitance and conductance of MIM structures with frequency. For convenience the results obtained and their discussion are divided into two groups : high and low frequencies. This division is defined by the existence of a break point to a higher power dependence and not by a specific value of frequency.

#### (a) Low frequency effects

In the low frequency régime a conductance variation of  $\omega^n$  was always observed, where the value of  $n$  was normally between 0.7 and 1.0. For the capacitance in this region the dependence was found to vary as  $\omega^{n-1}$ . By correlating the AC characteristics with DC and MIS data, it was found that higher values of  $n$  were synonymous with good quality films, and lower values with more conducting structures. In consequence, the process of looking for any change in capacitance with frequency was used as a rapid method of quality appraisal for the resultant films. The mechanisms proposed by various authors to explain this frequency dependence have already been discussed in section 4.3, however no one appears to have correlated this effect with film quality. The lower values of  $n$  reported by Jonscher et al were thought to be due to hopping conduction between defect sites ; in this case it is quite reasonable to assume the presence of a higher density of these sites in a "poorer" film. The near unity exponent has also been observed by other workers, and this is usually explained by the existence of dipolar processes. This effect is also not surprising when the structure of the film is considered, and as dipolar processes are usually associated with more ordered structures this will reflect the better "quality" of the film. An example of each type of resultant data is presented in Figures 7.18 & 7.19.

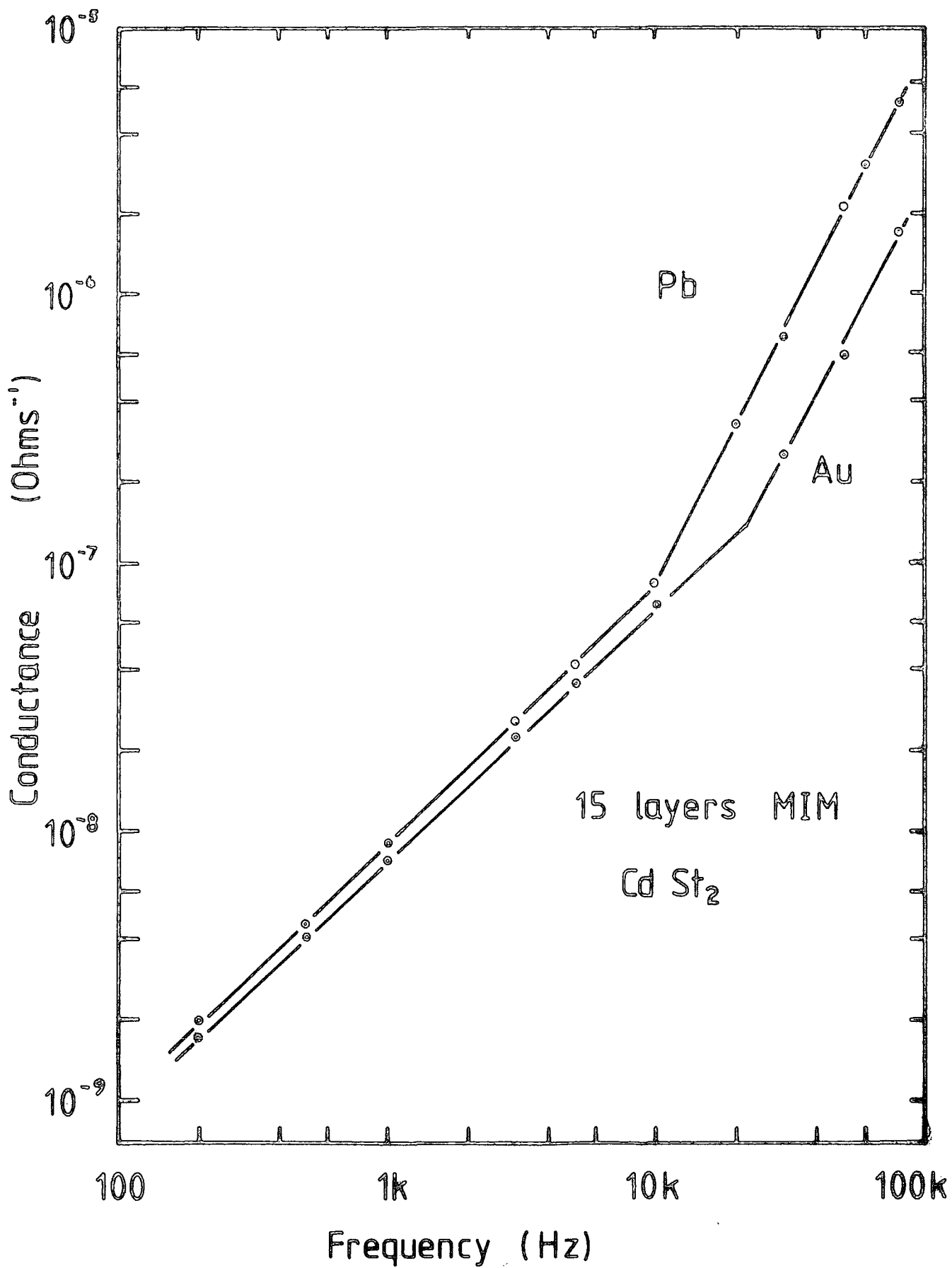


Figure 7.18 : Variation of A.C. conductance with frequency for good quality film.



Conductance ( $\text{Ohms}^{-1}$ )

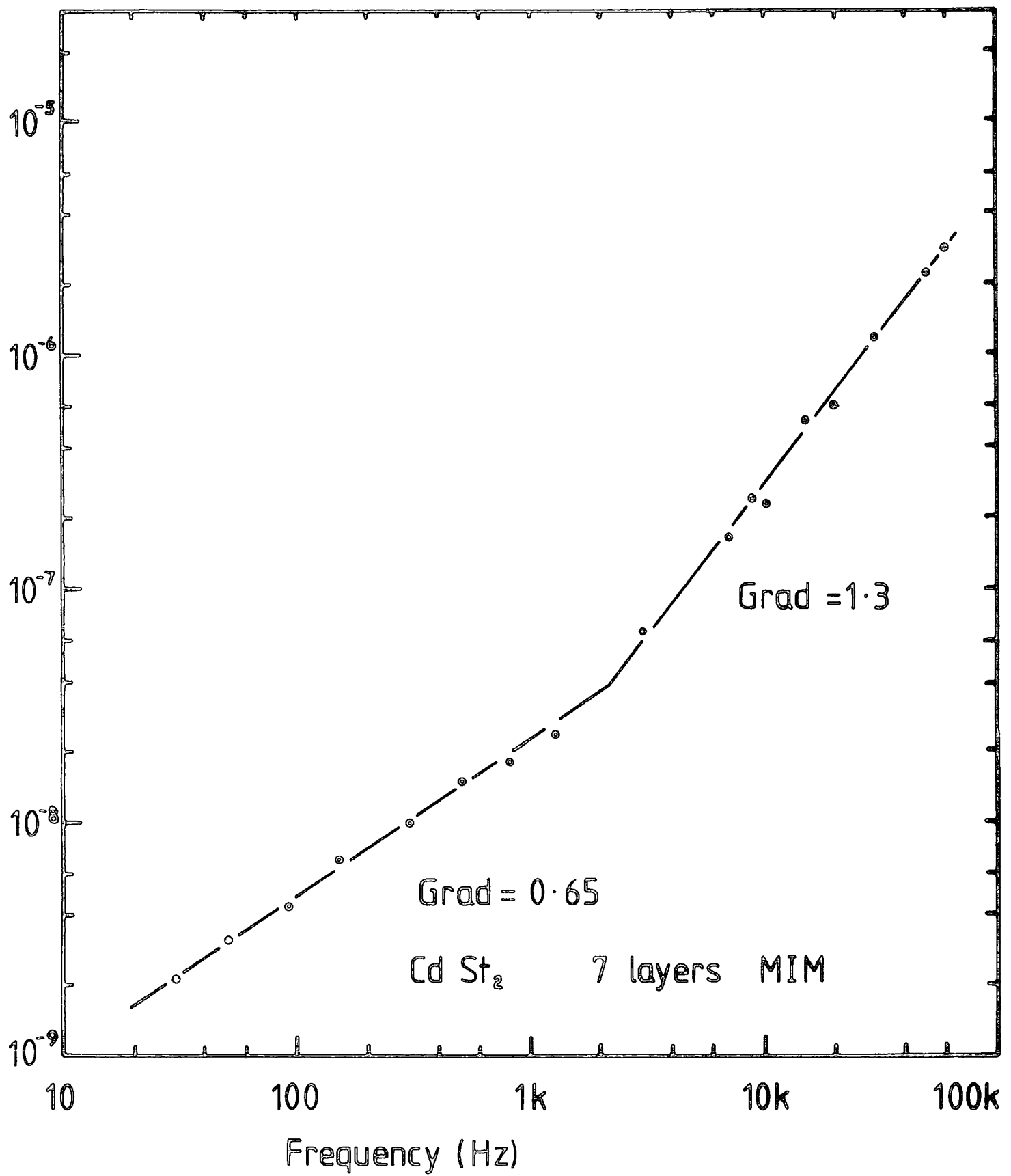


Figure 7.19 : Variation of A.C. conductance with frequency for poor quality film.

(b) High frequency effects

It was found with most samples that a second, higher power dependence of frequency was also present. With this steeper gradient the exponent was closer to, but not always equal to two. Rather than being real effects and functions of conduction in the material these steeper gradients were found to be due mainly to contact and/or substrate resistance. These resistances, which become more important at higher frequencies, add extra components to the basic equivalent circuit, as discussed in chapter two. From Figure 7.18 it can be seen that when the lower frequency régime shows  $G \propto \omega^1$ , then at about 10 kHz the gradient breaks to  $\omega^2$ . This effect is precisely as predicted by equation 2.45, which shows the resistance proportional to  $\omega^{-2}$  in this "mid" frequency range. Throughout this change the capacitance remains independent of frequency. Moreover from the aforementioned equation, it is possible to calculate the value of the extra resistance generating this break point :

For the Pb contacts  $f_{\text{break}} \approx 10\text{kHz}$

$$\rightarrow R \approx 200 \Omega ,$$

whereas for the Au contacts  $f_{\text{break}} \approx 30 \text{ kHz}$

$$\rightarrow R \approx 40 \Omega$$

With this particular sample the substrate material was Al/Al<sub>2</sub>O<sub>3</sub>, in consequence the 40  $\Omega$  recorded for the Au electrode very likely originated from the substrate oxide. Thus the resistance due to the Pb electrode must be reduced to around 160  $\Omega$ . Even with this reduction, however, the value is surprisingly high, and may thus be a function of lead oxide rather than the metal itself. This additional resistance was also found to have significant effect upon the characteristics of MIS devices when compared to normal Au contacts. These

effects and anomalies will be discussed further in Chapter 9.

If we look at an example of the poorer quality films [ Figure 7.19 ], it can be seen that in this case the original  $\omega^{0.65}$  dependence is transformed to  $\omega^{1.30}$ , and, as previously mentioned the capacitance will show a continuous  $\omega^{-0.35}$  variation. These effects can again be shown to be consistent with the presence of additional series resistance :

From equation 2.45 it can be seen that in the higher frequency regime ;

$$G \propto \omega^2 C_s^2 R_c$$

thus if  $C_s$  is frequency independent,  $G$  will break to  $\omega^2$ , as found with "good" quality films. If however  $C_s$  is frequency dependent, in this case proportional to  $\omega^{-0.35}$ , then ;

$$C_s^2 \propto \omega^{-0.7}$$

$$G \propto \omega^{2-0.7} = \omega^{1.3} ,$$

and this is indeed what is found. It should be noted that although a significant variety of exponential dependences were recorded with poor films, the higher power after the break inevitably corresponded well to this model.

#### 7.2.4 Summary of Results

In concluding this section on AC and DC conduction properties in Langmuir films, it is useful to summarize the detailed remarks and results given previously.

For DC characteristics :

- (i) In good quality insulating structures, Poole-Frenkel conduction between neutral traps is the dominant mechanism.

(ii) For films deposited on n-type InP structures, forward bias gives electron injection into the insulator, and thus space-charge-limited characteristics.

(iii) For rather poorer quality insulators on semiconductors, forward bias produces high levels of charge motion through the film and thus Schottky diode type data. Reverse bias appears to lead to the formation of a depletion layer and current limiting is by a combination of the film and this depletion layer. In the case of these poorly insulating films it is likely that conducting channels are produced in limited areas of the film.

For AC characteristics :

(i) At lower frequencies (below  $\sim 1$  kHz) good quality films show a conductance dependence of  $\omega^1$ , with no variation in capacitance.

(ii) An  $\omega$  dependence of substantially less than unity along with capacitance variation is a sign of a poor quality film.

(iii) At higher frequencies series resistance effects cause a break to  $\omega^2$  for conductance, or slightly less than this in the case of poorer films.

A more detailed discussion of many of the effects associated with semiconductor substrates will be given in Chapter 9.

## CHAPTER 8

### INTRODUCTION TO InP MIS DEVICES

This chapter serves as an introduction to InP, looking at the basic properties of the material, and reviewing some of the previous surface characterisation and MIS work carried out. It should be noted, however, that to date not a great deal of detailed work on either of these two areas has been undertaken. In consequence, considerable disagreement exists with respect to many of the ideas presented here.

#### 8.1 INTRODUCTION TO INDIUM PHOSPHIDE

##### 8.1.1 Band Structure and Electrical Properties

Indium phosphide is a  $\text{III-V}$  semiconductor with a zinc blende type lattice structure. It is very brittle and has a shiny silver metallic appearance. Like GaAs, it is a direct gap material with a value of about 1.35 eV<sup>(1)</sup> at room temperature and also, like GaAs, it has subsidiary minima in the conduction band, accessible to electrons of moderate energy. For these reasons the primary effort in InP work has been directed towards the production of transferred electron devices, and only more recently have other areas of device technology been considered.

The electrical properties of resistivity and Hall coefficient are perhaps the most widely studied characteristics of this material, with extreme ranges of temperature and doping variation having been investigated<sup>(2)</sup>. For the majority of work reported here, the bulk samples of n and p type material had room temperature resistivities of typically 0.2 and 3.0  $\Omega$  cm respectively with the  $n^+$  substrate for epitaxial layers being an order of magnitude less. At low temperatures, these values are of course reduced, with a factor of five being usual for a liquid nitrogen (77 K) ambient. In

addition, from these basic measurements, other important parameters have been deduced. Again for typical samples used, the electron and hole mobilities were found to be 4000-4500 and 140-160  $\text{cm}^2 \text{V}^{-1} \text{sec}^{-1}$  respectively. These basic properties, along with other useful ones are summarized in Table 8.1.

By contrast with silicon, freshly cleaved InP and indeed most III-V materials, have no intrinsic surface states in the band gap, and so to a first approximation should be ideal for surface active devices. However, recent evidence has led to the proposal that the adsorption of small amounts of material causes the expulsion of native atoms and the generation of very dense levels of interface states. These levels are now thought to explain many of the Fermi level pinning effects observed on InP devices. In addition, the states produced by lattice cleaving, which normally reside in the conduction and valence bands are now thought to be drawn into the band gap under certain conditions of surface relaxation. These effects, and the recent investigations are, in practice, of crucial importance to MIS device performance, and because of this, will be discussed and reviewed in greater detail later.

#### 8.1.2 Material Growth

The melting point of InP is  $1070^\circ \text{C}$ ; at this temperature the vapour pressure of phosphorous is between 20 and 30 atmospheres. This fact, along with the highly toxic and corrosive nature of the latter material makes the growth of InP rather less than easy. The established way of overcoming these problems for the growth of bulk material is to use liquid encapsulation in association with normal Czochralski methods. This approach was first developed for InP by Mullin et al<sup>(3)</sup>, and involves the use of a layer of inert boric oxide ( $\text{B}_2\text{O}_3$ ) held over the melt by a suitable overpressure of nitrogen. The crystal is then grown on the end of a seed slowly pulled through the encapsulating layer. To provide the necessary control over carrier concentration, dopants are added at the growth stage in small known amounts. For

TABLE 8.1 Summary of properties of InP

Property	n-type	p-type	units
Density		4.7	$\text{g/cm}^3$
Band gap		1.34	eV
Relative permittivity		12.30	-
Lattice constant		5.07	$\text{\AA}$
Orientation		(100)	
Mobility (max) @ 300K	4000-4500	140-160	$\text{cm}^2/\text{V-sec}$
@ 77K	$\sim 44,000$	$\sim 1,200$	$\text{cm}^2/\text{V-sec}$
Effective mass	0.07	0.69	
Resistivity @ 300K	0.02	3.0	$\Omega \text{ cm}$
@ 77K	0.08	$\sim 1.0$	$\Omega \text{ cm}$
Carrier concentration ( $N_D$ )	$5 \times 10^{15}$	$2 \times 10^{16}$	$\text{cm}^{-3}$

n-type material, tin or germanium are normally used, with zinc and cadmium for p-type. In addition, semi-insulating properties can be produced by the use of chromium. After growth, the crystal, typically 6 cm in diameter, is cooled slowly and the boric oxide removed by washing. The boule is then orientated to the desired plane and sawn into individual wafers.

For many applications it is necessary to produce surface regions of differing doping concentration, sometimes with other dopants and even with the opposite carrier type. This can be achieved by epitaxial growth from either the vapour<sup>(4,5)</sup> or the liquid phase<sup>(6)</sup>, but currently the former is the most common. In this process the substrate material, necessarily scrupulously clean and smooth, has additional material grown onto it from the local reaction of indium with phosphorous trichloride. For this process, the latter is carried in hydrogen gas and passed over liquid indium prior to incidence with the InP. Growth rates are normally very slow, typically about 10  $\mu\text{m/hr}$ . Once again, controlled impurities can be introduced into the vapour stream to vary the doping of the epitaxial layer. It should also be noted that considerable investigation is currently underway into the use of molecular beam epitaxy upon InP, i.e. the direct controlled deposition of material onto the substrate.

The majority of substrates used in the work reported here were bulk (100) oriented materials of both p and n-type. In addition, frequent use was made of n-type epitaxial layers  $\sim 10\mu$  thick, grown on  $n^+$  (highly doped) substrates. For the InP, typical carrier concentrations were  $5 \times 10^{15} \text{ cm}^{-3}$ , and  $2 \times 10^{16} \text{ cm}^{-3}$ , for n and p-type material respectively.

### 8.1.3 InP Devices

Initial interest in InP as a device material was due to its superior peak to valley ratio band structure over GaAs which could in theory lead to higher efficiency transferred electron oscillators. This difference, proposed



in 1970<sup>(7)</sup> by Hilsum and Rees, was quickly observed on n-type bulk samples<sup>(8)</sup> which were found to exhibit controlled oscillation of up to 14 GHz. Since the original proposal, considerable development and optimisation work of these diodes have been undertaken<sup>(9)</sup>, resulting in operation at frequencies up to 75 GHz. For most devices the active layer is grown on an n<sup>+</sup> substrate (for ease of producing an Ohmic contact), and a tin bead is alloyed onto the top surface for the barrier<sup>(10)</sup>. In addition, however, recent investigations into evaporated Ag/Sn and Au/Ge/In contacts have shown promising results<sup>(11)</sup>. As a consequence of this concentrated effort, it appears that InP Gunn effect devices are now very near to commercial exploitation.

Since the original development work for microwave devices, many other potential applications for InP have been envisaged, in particular, the most promising areas include high speed FET's, solar cells, and miniature lasers. In the field of fast FET's structures have already been fabricated<sup>(12)</sup>, and the higher mobility is expected to yield response times far superior to the best yet obtained on silicon. To date, however, structures have been limited to depletion mode (MESFET) devices with their inherently high current drain, as the lack of a suitable insulator presently precludes the fabrication of MISFET devices. This topic is considered in greater detail later in the thesis.

The production of solar cells on InP is an attractive proposition due to its near optimum band gap for solar energy absorption<sup>(13)</sup>. Because of this, theoretical efficiencies of nearly 30% have been proposed<sup>(14)</sup>, but to date the best achieved is 3%<sup>(15)</sup>. Considerable effort is still being directed towards this type of device, however, and along with normal Schottky barrier structures, MIS thin films and heterostructures are also being looked at.

In the field of optical communication, the need to produce lasers in the 1.1-1.3  $\mu\text{m}$  region to match the transmission fibres has led to the use of GaInAsP quaternary material grown on bulk InP substrates. Of the many systems

investigated this configuration seems to be the most favourable<sup>(16)</sup> with the good lattice match considerably easing growth and the optical discontinuity acting to confine the light to the active region. In addition, a second overlayer of InP is usually grown to prevent losses in the upward direction, both layers being produced by LPE. To date, operating lifetimes of 1500 hr continuous usage have been achieved<sup>(17)</sup>.

## 8.2 REVIEW OF CURRENT IDEAS ABOUT THE InP SURFACE

This section serves the purpose of reviewing the previous surface and interface characterisation work carried out on InP. The work covered can be divided into three approaches. The purely chemical work carried out by Kirk et al at Nottingham, looking at surface degradation, thermal and chemical, as a function of environment variation. This was mostly undertaken using Auger analysis, as a precursor to Schottky barrier formation and investigation. The second approach is also a chemical one, but more related to MIS and device work. It deals with the influence of various atomic species, oxygen in particular, and their effect upon the surface of the material; chemical reactions, Fermi level pinning, barrier height variation, etc. The final approach reported is the direct result of MIS work by the Naval Ocean Systems Centre in San Diego (reviewed in 8.3). This involves chemical surface analysis and profiling at the various oxides and insulators used for MIS devices. By this approach, not only is the composition of the dielectric recorded, but also the state of the interface region. It is this latter information that is most relevant here.

It will be seen from this section that the extent of work so far carried out is relatively small, and as such not a great deal of consistency yet exists. This point is significant, as much of the original work to be presented in the next section differs in conclusions to that presented here.

It should also be noted that considerably more work has been undertaken on other III:V materials, and GaAs in particular. This work shows many similarities between the material from a chemical point of view, and it is likely that trends can be extrapolated to cover InP. For a variety of reasons, however, this review is restricted to purely InP work, and that directly relevant to MIS device fabrication.

(a) Auger analysis

A series of papers have been presented by Kirk et al between 1975 and 1980<sup>(18-21)</sup>, all dealing with the surface degradation of InP. The majority of these involve chemical surface analysis using LEED, scanning Auger and occasionally ESCA, all on (100) surfaces of n-type material. Initial investigations looked at the thermal degradation properties (i.e. change in surface chemistry and stoichiometry as the temperature is increased), and found serious decomposition above 300° C. This resulted from the loss of phosphorous, and the subsequent restructuring of the surface leaving islands of pure elemental indium. In fact these measurements were carried out at ultra-high vacuum ( $10^{-10}$  t) and so caused a reduction of the threshold temperature ; later results<sup>(22)</sup> show that 350° C is a more realistic figure for normal pressures. Kirk concluded that this out-diffusion of phosphorous would leave a large density of surface defects which may seriously degrade any subsequent device performance. In addition, it was found that pre-etch treatment had no effect upon this change in the surface stoichiometry. Later papers looked in more detail at the effect of storage and cleaning procedures, again on (100) surfaces, but now with epitaxial layers as well as bulk materials. As received samples were found to show the presence of significant amounts of oxygen and carbon along with the expected indium and phosphorous. Storage in dry nitrogen for ten days reduced this oxygen concentration and increased the indium ; suggesting the decomposition of surface oxides, and a subsequently

cleaner surface region. However, storage in the normal atmosphere showed the opposite effect, with an increase in both carbon and oxygen components, and thus a thicker oxide. Vapour degreasing in a variety of organic materials showed little effect upon the oxide, except for an increase in the carbon, which was to be expected due to pick-up from the organic materials. In all cases these surface contaminants were found to be uniformly arranged over the surface. This even distribution was markedly altered by HF etching, however, which was found to reduce the oxygen content (removing oxide) but increased and localised the carbonaceous material. Prolonged etching had no effect on the island size, only the carbon concentration. In addition, the intermediate areas were found to be very clean indeed, showing only indium and phosphorous and no sign of any other material. Subsequent investigation of these areas of carbon showed them to be extremely resilient, resisting most forms of attack, and giving a very low sputtering yield by comparison with the intermediate clean regions. They were thus concluded to be thin layers of diamond structure. More recent papers from Kirk have concentrated upon the epitaxial growth process, and looked at the effect of termination procedures on the final surface. These investigations have shown a depletion of phosphorous from the top few monolayers due to the maintained high temperature following the cessation of growth. This leads to local areas of free indium which are chemically active and will tend to form  $\text{In}_2\text{O}_3$  and various other oxides. In addition, the tetra valency of carbon is suspected to lead to its incorporation into the lattice in the absence of phosphorous.

It was the early discovery of the useful microwave generation properties of Schottky barriers on InP that in practice led to the investigation of the chemistry of barrier formation, and analysis of the preliminary and subsequent structures. In consequence there are many reports similar to the work of Kirk et al, but none quite as detailed. Of particular interest are

the various publications of Williams et al<sup>(23)</sup>. These will not, however, be considered in detail as many of the conclusions are similar to those of Kirk et al.

(b) Vacuum Cleaved (110) Samples

In the last few years, workers at Stanford (USA), led by Professor Spicer, have published a number of papers<sup>(24-26)</sup> dealing with the chemisorption of materials onto the InP surface. These investigations used synchrotron radiation to excite emission from both core and valence levels to obtain detailed information about the bonding of initially oxygen, and later various metals to the InP surface. Atomically clean surfaces were exposed to oxygen in gradually increased amounts, and its effect was monitored by looking at the binding energy variation of the surface atoms. It was thus established that InP had no intrinsic surface states, only ones caused by lattice defects and other extrinsic sources. These defects being similar to those causing Fermi level pinning in other  $\text{III-V}$  materials, and GaAs in particular<sup>(27)</sup>. These investigations were restricted to mainly chemisorption reactions, where no bond breaking was induced and the oxygen attached itself to the dangling indium or phosphorous bonds. In practice, it was found that reaction was with group V elements alone, and that even fractions of a monolayer of oxygen produced Fermi level pinning. The locus of this pinning was shown to depend upon the doping type of the material(p or n), and on the actual amount of oxygen present. This proposed variation of pinning position with oxygen is shown in Figure 8.1, where it can be seen that both n and p type Fermi levels eventually reside very close to the conduction band minimum. From these results it was concluded by Spicer that n-type MIS devices would be hard to invert, but easy to accumulate and deplete, whereas p-type devices would be pinned in inversion and would thus be difficult to accumulate and deplete. These postulates were found to fit very well with device results then being

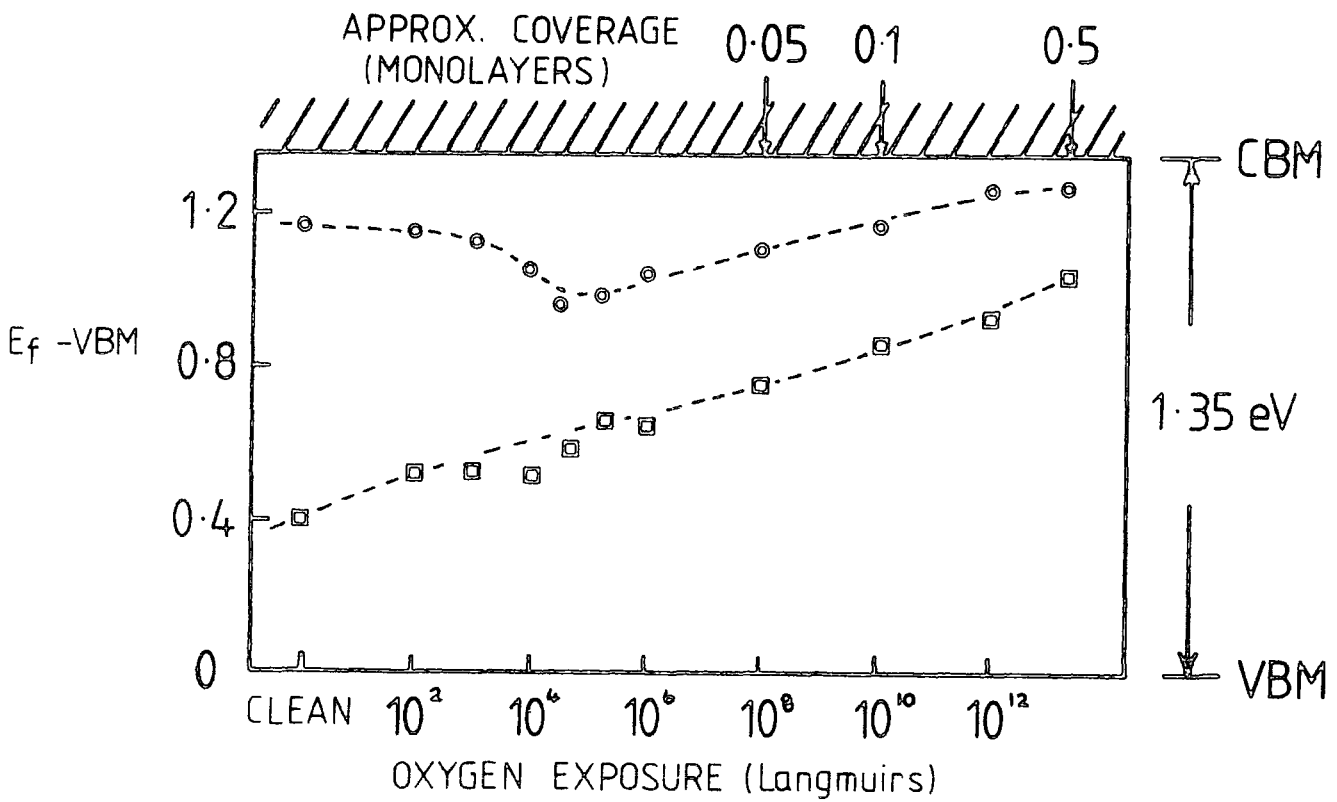


Figure 8.1 : Displacement of the Fermi level of (110) cleaved, n-type (●), and p-type (◻) InP as a function of oxygen exposure, (After Spicer et al, Ref. 26 ).

reported by various workers at San Diego (see section 8.3).

Later publications looked at the effect of metals chemisorbing onto the InP, and produced good correlation between the final pinning position of the Fermi level and the measured Schottky barrier height. The proposed model for this effect envisaged the condensation of the ad atom (oxygen or metal) releasing enough energy to cause the expulsion of native materials from the already highly strained lattice. This was required to occur for only one in every hundred incident atoms in order to produce the observed defect density, and thus produced a diffuse interface region between either the metal or the oxide and the semiconductor. This more detailed model proposed the existence of two pinning positions for oxygen adsorption ; a donor level 1.2 eV above the valence band, due to missing indium for n-type material, and an acceptor level at 0.9 eV due to missing phosphorous in p-type material. These two levels were therefore concluded to be superimposed on the normal U-shaped strain

induced density of states in the band gap, leading to additional peaks at 1.2 eV and 0.9 eV depending upon the material doping.

(c) Oxide and Interface Profiling

The final characterisation work reviewed here, is that carried out by Wilmsen et al<sup>(28-31)</sup>, in connection with MIS device fabrication. Reasonably standard surface analysis techniques (Auger and later ESCA) were applied, and when used in association with low energy ion sputtering, enabled systematic profiling of the oxide and interface to be undertaken. Initially, two types of anodic oxide (KOH and ethylene glycol) grown on a bromine/methanol etched surface were investigated.

The former type of oxide was composed of mainly  $\text{In}_2\text{O}_3$ , with little phosphorous appearing until the relatively wide interface region, where both  $\text{In}_2\text{O}_3$  and  $\text{P}_2\text{O}_5$  were present. It was also found that the majority of the oxide was of reasonably constant composition with linear emission signals. The ethylene glycol oxide by contrast had no uniform outer layer but a steady increase in  $\text{P}_2\text{O}_5$  content up to the interface region. With this oxide the overall amount of  $\text{P}_2\text{O}_5$  was much larger than with the KOH material. In both cases the oxide region was found to be quite diffuse, around  $200 \text{ \AA}$ , and was therefore concluded to be not a function of growth conditions, but rather of some other limiting mechanism. Later work used both Auger and ESCA to depth profile and compare KOH anodic oxide with thermal oxide grown at  $450^\circ \text{C}$  in an oxygen atmosphere. The anodic oxide again showed a diffuse interface region, with the majority of the dielectric being  $\text{In}_2\text{O}_3$ , and  $\text{P}_2\text{O}_5$  appearing at the interface with the semiconductor. By contrast, the thermal oxide showed large amounts of elemental phosphorous at the interface but a similar  $\text{In}_2\text{O}_3$  bulk composition, with possibly slightly larger amounts of  $\text{P}_2\text{O}_5$ . This interface region was concluded to be a function of thermal degradation of the InP during the oxide growth. The investigation of  $\text{SiO}_2$  as a possible dielectric for InP produced a shift in effort, and subsequent papers from then on concentrated

upon the analysis of this new interface region. The  $\text{SiO}_2$  was pyrolytically deposited at a variety of different substrate temperatures, and the resulting structured depth profiled as before. In each case the substrate was pre-etched in bromine methanol before the deposition process. A higher temperature of deposition appeared to produce a broader interface region, and above  $350^\circ\text{C}$  indium was found to diffuse through the insulator and considerably degrade its electrical properties. This indium in practice appeared to exchange oxygen with the  $\text{SiO}_2$ , and as no free silicon was shown in the insulator; it was concluded that it diffused back to the InP where it would behave as an n type dopant and so additionally degrade the device performance. From this work it was concluded that low temperatures were required ( $\sim 350^\circ\text{C}$  or less) in order to avoid indium diffusion causing device problems. At this low value, however it was found to be considerably more difficult to deposit the oxide uniformly, and so further work on the process was required.

### 8.3 REVIEW OF InP MIS WORK

The investigation of InP MIS devices began as late as 1975, when the growth technique had been sufficiently developed, and the properties of the material looked extremely promising. A variety of different insulators have been tried, anodic oxide, aluminium oxide, and  $\text{SiO}_2$  being the major contenders ; no one has however so far proved significantly superior to the others.

#### (a) Anodic Oxide

The first reported MIS device on n-InP was fabricated by Wilmsen<sup>(32)</sup> in 1975 ; his dielectric was anodic oxide produced from 0.1M KOH soln., with a thickness of about  $600\text{ \AA}$ . He found however that this oxide was quite leaky, and in consequence, deposited an additional layer of sputtered  $\text{SiO}_2$  on top to reduce the leakage problems. The resultant characteristics were found to be reasonable, showing accumulation and depletion, but not inversion. In addition, analysis by Terman's method (see 2.3) produced a relatively low



surface state density of about  $10^{11}/\text{eV cm}^2$ . In a later paper, Wilmsen and Kee<sup>(33)</sup> developed these measurements by the use of ESCA, and found that the anodic oxide was largely  $\text{In}_2\text{O}_3$ , with relatively little  $\text{P}_2\text{O}_5$ . The interface region was concluded to be quite thick  $\sim 200 \text{ \AA}$ , within which the amount of phosphorous steadily fell, and the amount of indium and oxygen steadily rose, as the distance from the interface increased. Early in the year following Wilmsen's initial investigations, Lile and Collins<sup>(34)</sup> reported the use of wet chemical anodic oxidation based upon salicylic acid, to produce a dielectric on the surface of n-type InP. They used a bromine/methanol initial etch, and produced a low leakage layer, again of what was thought to be  $\text{In}_2\text{O}_3$ . Its breakdown strength was found to be  $10^6 \text{ V/cm}$ , and the resultant device showed good accumulation, depletion, and even weak inversion characteristics. In addition, analysis again generated an inherently low surface state density  $4 \times 10^{11}/\text{eV cm}^2$ , but considerable dispersion and non-uniformity of the insulator proved to be significant drawbacks.

This latter problem was highlighted by sputter Auger profiling, which showed an oxygen rich layer close to the interface, and significant amounts of carbon near the surface region. Subsequent investigation of this type of oxide by Ota and Horikoshi<sup>(36)</sup> showed it to be composed of a double layer structure, of which the upper component is responsible for the majority of the dispersion. The lower region, a highly oxidised "native" oxide was found to have a reasonably constant thickness which was concluded to define the properties of the device. Anodic oxides based on glycol solutions have also been reported by Hartnagel<sup>(35)</sup>, who noted anomalously high values of accumulation capacitance and significant dispersion of the insulator dielectric constant. These problems were apparently removed by low temperature annealing at  $150^\circ\text{C}$  in nitrogen, and the resultant curves showed good accumulation, depletion and weak inversion. The hysteresis was, however, found to remain and the devices were depleted at zero bias. More recent work by colleagues of Hartnagel<sup>(37)</sup>

has shown similar conclusions to those reached by Ota<sup>(36)</sup>, and they have produced good MIS devices on both InP and GaAs by initially growing a native oxide layer, and covering this with another insulator ( $\text{Al}_2\text{O}_3$ ) to produce the final structure.

(b) Aluminium Oxide

As well as the growth of anodic native oxides, various investigations have been carried out on aluminium oxides, with a view to using these as dielectrics in MIS structures. Electron beam evaporation of alumina has been reported by Favennec<sup>(38)</sup>, who obtained a good quality insulator with high breakdown strength ( $10^6$  V/cm), and low leakage ( $< 10^{-8}$  A/cm<sup>2</sup>). The resultant MIS characteristics on n-type material showed normal accumulation and depletion, and in addition, exhibited low frequency inversion returning to the accumulation value. However, these devices also showed significant clockwise hysteresis, again indicative of electron injection and trapping at the interface region. The pyrolytic deposition of alumina has been demonstrated by Kamimura et al<sup>(39)</sup>, who used an argon carrier gas to deposit the insulator from  $[\text{Al}(\text{OC}_3\text{H}_7)_3]$  onto a substrate heated to  $350^\circ\text{C}$ . The surface was initially etched with bromine/methanol, and the resultant film had a breakdown strength of  $5 \times 10^6$  V/cm. In practice the device characteristics showed accumulation and depletion, but no inversion. In addition, considerable variation of the accumulation capacitance with frequency was noted, this was however not due to the dielectric, as no problems were encountered with silicon as a substrate. It was therefore concluded that the effect was a function of the  $\text{Al}_2\text{O}_3/\text{InP}$  interface, and probably an injection phenomenon. Measurements undertaken to characterise the interface showed a low surface state density of  $10^{11}/\text{eV cm}^2$ , which increased markedly as the substrate temperature during the initial deposition was increased, up to  $10^{12}$ - $10^{13}/\text{eV cm}^2$  for  $400^\circ\text{C}$ - $500^\circ\text{C}$ . This was thought to be due to the surface disassociation of the InP at higher temperatures.

(c) Silicon Dioxide

The third type of insulator investigated, has been  $\text{SiO}_2$  ; this is normally deposited by the pyrolysis of silane ( $\text{SiH}_4$ ) and oxygen, onto a heated substrate. This type of structure was first produced by Messick in 1976<sup>(40)</sup>. The insulating layers were found to be hard and glassy at room temperature, with high resistivities, and breakdown strengths of almost  $10^7$  V/cm. However, these films were found to exhibit voltage dependent instabilities, produced by charge injection and trapping of electrons in the oxide. Analysis carried out by Terman's method yielded surface state densities of around  $2 \times 10^{11}$  /eV  $\text{cm}^2$ , and Auger analysis showed the interface region to be quite clean and uniform over about  $250 \text{ \AA}$ . Fritsche<sup>(41)</sup> found that the addition of HCl to the silane in a low temperature CVD reactor, produced much lower surface state densities at the conduction band edge. He also found evidence of deep donor states ; neutral in accumulation, and positively charged in depletion, which were thought to limit the excursion of the Fermi level to 0.5 eV below the conduction band. This preparation technique, also led to approximately 500 mV of hysteresis, of the clockwise variety, again suggesting injection problems. Later work by Meiners<sup>(42)</sup>, utilized a similar technique of pyrolytic deposition to the one developed by Messick<sup>(40)</sup>. In this investigation, good accumulation and depletion were obtained, but considerable problems were encountered with frequency dispersion, and surface state analysis gave relatively high densities of  $10^{12}$  /eV  $\text{cm}^2$ . These problems were concluded to be due to non-optimisation of the deposition technique.

More recently, a paper by Meiners, Lile and Collins<sup>(44)</sup> has presented the first investigation of p-type devices. These structures used pyrolytic  $\text{SiO}_2$  as previously described<sup>(42)</sup> deposited onto a heated substrate ( $300^\circ\text{C}$ ) to produce the insulating layer. Both n and p-type devices were fabricated, and measurements undertaken in light and dark conditions. It was concluded that pinning of the Fermi level restricted n-type devices to accumulation and

depletion, and p-type devices to inversion only. Some inversion was, however, produced on n-type devices under illumination, but at only low frequencies did the value return to  $C_{\max}$ . In addition, this pinning at the p-type device in inversion, although not particularly good for normal MIS work, was inferred to be potentially useful for FET's.

Another method of depositing  $\text{SiO}_2$  has been reported by Grant et al<sup>(43)</sup>, this uses plasma oxidation of tetraethylorthosilicate within the reaction vessel, to produce an insulating layer on the InP at room temperature. This is one of the few techniques available for low temperature deposition, and as such has the potential for producing significantly better interface properties (see later). The results so far obtained again show reasonable accumulation/depletion, and indeed signs of low frequency inversion, but they also show frequency dispersion of the oxide capacitance and clockwise hysteresis.

This summary has covered the majority of early investigations involving MIS on InP, and has looked at most recent work up to mid 1980. It should be noted, however, that interest and activity in this area is rapidly expanding, and significant breakthroughs may soon be forthcoming. Indeed, the author knows of useful amounts of as yet unpublished information which may well prove quite interesting. From this overall view, a number of general conclusions and trends can be inferred. None of these three major insulators appear to be particularly ideal, and individual variations in technique tend to significantly affect the overall characteristics. In particular, problems with dispersion of accumulation capacitance are very irreproducible, but on the whole  $\text{SiO}_2$  seems the most promising in this respect. Virtually all n-type devices show clockwise hysteresis, again ranging in magnitude, depending upon individual techniques, but always indicative of electron injection, and trapping in the oxide interface region. These conclusions fit very well with the work of Ota<sup>(36)</sup>, and Hannah and Livingstone<sup>(37)</sup> whose results point to the

initial native oxide layer of the InP substrate being critical in defining the interface properties, and thereby leading to the hysteresis. The anodic oxide layers, although easily grown, seem inevitably to show quite high leakage ; again this requires further investigation, but suggests their unsuitability for widespread device application.

With respect to device characteristics, the majority of papers all show accumulation and depletion, but very few show weak or strong inversion. This tends to reinforce the general conclusions of Meiners et al<sup>(44)</sup>, who suggested that extrinsic surface states restricted the movement of the surface Fermi level. Reports of apparent inversion are, however, available, in particular Pande and Roberts<sup>(45)</sup> with anodic oxide, and Favennec et al<sup>(38)</sup> with Al<sub>2</sub>O<sub>3</sub>, both of which show a reverse bias increase in capacitance almost up to C<sub>ox</sub>. It is interesting to note that both of these are low temperature deposition techniques, i.e. they do not require any heating of the substrate during deposition. For p-type material, the only work so far shows considerable pinning of the Fermi level above the mid band gap position (inversion), so limiting the excursion of the CV curve. Results presented later, in the next chapter, for organic insulators on p-InP in fact show significant variation to these characteristics, and both accumulation and depletion are observed. The surface state density measurements appear to give reasonable consistency, all showing 1-5 x 10<sup>11</sup>/eV cm<sup>2</sup> for good devices, and slightly higher when problems with preparation were encountered<sup>(39,42)</sup>. The majority of analyses however use the simple capacitance approaches of Terman or Berglund, and no consideration of conductance data is normally presented.

In addition to simple MIS devices, many of the more recent workers have proceeded to fabricate FET structures, using their particular insulator technology. These devices are however beyond the consideration of this section.

CHAPTER 9

THE CHARACTERISATION OF InP-LANGMUIR FILM MIS DEVICES

This chapter considers the experimental characteristics of structures fabricated on substrates of InP. The main emphasis has been placed upon MIS type devices utilizing Langmuir/Blodgett insulating films, but details of chemical surface analysis and Schottky barriers are also given. In particular, because the low temperature deposition process induces no surface damage, the effect of various etchant preparation upon device performance has been investigated. From the results obtained, a model of the states in the band gap of InP has been proposed.

9.1 CHEMICAL ANALYSIS OF THE InP SURFACE

In order to produce useful devices, precise control of the semiconductor /insulator interface is required. To achieve this, an extensive study of the InP surface before and after various etchant treatments was undertaken. The results obtained from this investigation are divided into three sections : the initial surface, and the surface after various wet and dry etching processes. In each case the volume of information precludes detailed description, but summary tables of important data are presented, along with example curves and brief discussion of significant elemental features. From this information, comparison of elemental peak heights with those of reference materials, before and after etching, has enabled the chemistry of the surface to be determined. In particular the ratio of indium and phosphorus components due to oxide and non-oxide configuration has allowed the extent of oxidation of the surface to be established.

For this study, the model compounds used for reference and calibration are summarised in Table 9.1, where contributions to indium, oxygen, and phosphorus are given, along with the relevant binding energy in each case.

TABLE 9.1 : Spectral characteristics of model compounds

Sample	O <sub>1s</sub> Binding energy (eV)	C <sub>1s</sub> Binding energy (eV)	In <sub>3d</sub> Binding energy (eV)	P <sub>2p</sub> Binding energy (eV)
P <sub>4</sub> O <sub>10</sub>	(0.39) 533.5 (0.61) 535.0	(0.83) 285.0 (0.17) 286.3	- -	(1.0) 135.4
AlPO <sub>4</sub>	(1.0) 533.0	(1.0) 285.0	-	(1.0) 133.1
(C <sub>6</sub> H <sub>5</sub> O) <sub>3</sub> PO	(0.25) 532.3 (0.75) 534.3	(0.83) 285.0 (0.17) 286.7	- -	(1.0) 133.8
(C <sub>6</sub> H <sub>5</sub> ) <sub>3</sub> P	-	-	-	(1.0) 130.7
In (metal)	(0.26) 530.4 (0.52) 532.0 (0.21) 533.5	(0.75) 285.0 (0.13) 286.3 (0.05) 287.5 (0.06) 289.0	(0.34) 443.6/451.2 (0.52) 444.7/452.2 (0.14) 445.8/453.4	-
In <sub>2</sub> O <sub>3</sub> (BDH)	(0.49) 530.5 (0.37) 532.0 (0.14) 533.3	(0.82) 285.0 (0.09) 286.3 (0.09) 288.3	(0.83) 444.8/452.3 (0.17) 446.0/453.6	
In (metal) O <sub>2</sub> plasma 2 min 10 W. 0.1 Torr	(0.16) 530.5 (0.74) 532.6 (0.10) 533.8	(0.81) 285.0 (0.12) 286.3 (0.07) 289.2	(0.04) 443.6/451.2 (0.34) 444.6/452.2 (0.62) 445.8/453.4	-
InPO <sub>4</sub>	(0.72) 532.2 (0.28) 533.8	(0.74) 285.0 (0.16) 286.3 (0.05) 287.6 (0.05) 289.2	(0.19) 443.7/451.3 (0.81) 446.0/453.3	(1.0) 133.3

N.B. Binding energies normally  $\pm$  0.15 eV. Figures in brackets represent contribution of each component within a given core level.

### 9.1.1 As Received Samples

In general, the initial surface of the InP samples showed considerable variation of chemistry ; perhaps reflective of the growth termination procedure and packaging rather than any bulk variability. A summary of typical data, showing variation in carbon, indium, oxygen and phosphorus, for a variety of Malvern epitaxial samples, is given in Table 9.2. The dominant features for each element will now be discussed separately.

#### C<sub>1s</sub> Levels

As received samples showed significant intensity of the C<sub>1s</sub> level, indicative of surface contamination. The major component at 285 eV originates from the C-H bond, and along with subsidiary peaks at 286.5 eV and 289.0 eV associated with C=O and C<sub>2</sub>O<sup>o</sup>, is indicative of a fatty acid type overlayer. The angular dependence suggests the acid portion resides closest to the InP.

#### In<sub>3d</sub> Levels

The indium levels revealed basically two main peaks at 444.8 eV and 445.8 eV, plus additional ones at 7.6 eV higher in <sup>each</sup> case, both due to spin orbit splitting. Comparison of these values with the data obtained from the model materials showed the main peak was 1.0 eV higher than that due to In metal, consistent with an origin in the indium to phosphorus bond. This higher energy component was found to be essentially the same as that for indium in In<sub>2</sub>O<sub>3</sub>, but the overall intensities and observed energies for oxygen and phosphorus were found to disagree with this assignment. The lower energy peak, from comparison with model compounds is proposed to originate from InPO<sub>4</sub>, which is therefore the dominant oxide on the InP surface.

#### P<sub>2p</sub> Levels

The two distinct peaks observed in the phosphorus spectrum showed a binding energy difference of 4.5 eV. The component at 128.5 eV, shifted



TABLE 9.2 : Spectral characteristics of some "as-received" n-type substrates

Sample	Take-off Angle	In <sub>3d</sub>	C <sub>1s</sub>	O <sub>1s</sub>	P <sub>2p</sub>	InP/ <sub>In ox</sub>	InP/ <sub>P ox</sub>
CV 792	30°	1.0	5.85	1.75	1.36	3.7	7.4
	70°	1.0	49.7	6.94	2.25	2.1	1.6
LV 505 (1)	30°	1.0	4.81	3.18	1.02	2.7	2.9
	70°	1.0	21.9	7.39	1.38	1.1	0.85
LV 502 (2)	30°	1.0	5.62	3.04	1.06	3.2	2.9
	70°	1.0	18.4	4.86	1.27	1.2	0.9
LV 764	30°	1.0	5.94	3.02	1.44	2.2	3.6
	70°	1.0	28.1	6.95	1.27	1.1	0.9
KV 456	30°	1.0	10.08	3.16	1.5	2.4	1.24
	70°	1.0	51.3	6.75	2.1	0.75	0.33
LV 505 (3)	30°	1.0	4.45	2.64	1.36	2.0	2.2
	70°	1.0	21.8	6.45	1.95	0.9	0.7

down approximately 2 eV from that of phosphine, was found to be consistent with an attachment to indium, as in InP. Contrary to results reported by many other workers, no evidence of  $P_4O_6$  or  $P_4O_{10}$  was observed, indeed, subsidiary experiments showed these materials to readily sublime at room temperature under normal measurement conditions. In practice, the higher binding energy at 133.0 eV was consistent with a high oxidation state of phosphorus (as in  $AlPO_4$  for example), and thus agreed with the proposed existence of  $InPO_4$ .

From the angular dependence studies (Table 9.2), it was found that the oxide layer was located at the outermost surface of the material, but varied considerably in thickness from sample to sample. In addition, it can be seen that the surface always has an indium to phosphorus stoichiometry less than unity.

The results of this pre-etch surface characterisation can be summarised as follows :

- (i) The outmost few layers of the surface corresponded to oxidised material, approximately 10-15 Å thick.
- (ii) The lower binding energy indium peak was due to InP, but was at the same value of binding energy as  $In_2O_3$ , (of which there was very little present).
- (iii) The lower binding energy signal for indium, along with the values for  $P_{2p}$  and  $O_{1s}$  suggest that the dominant oxide species was  $InPO_4$ .
- (iv) Considerable quantities of carbon, mainly as fatty acid structures were observed.

It should be noted that these conclusions are not consistent with those reached by other workers as discussed in (8.2). The significant differences are the lack of  $P_2O_5$  and  $In_2O_3$ , and a proposed dominant surface oxide of  $InPO_4$ .

### 9.1.2 The Effect of Wet Etching

From the summary of wet etching results given in Table 9.3, and in particular from the indium/indium oxide and phosphorus/phosphorus oxide ratios, it was found that the majority of etches used could be placed in one of two categories producing either an oxidized or a de-oxidized surface. The following discussion gives more detail of the surface chemistry differences which lead to this conclusion.

#### (a) De-Oxidising Etches

From Table 9.3 and the corresponding output data in Fig 9.1, it can be seen that the de-oxidising etches were primarily the mineral acids and peroxide mixtures, (labelled 3-6). The resultant surface was found to be quite clean, and virtually oxide free, with the dominant signals being those for In and P bound as InP. It can also be seen that HF gives the cleanest surface, and an indium to phosphorus ratio closest to unity. In all cases, however, the drawback of these acid etches is that the resulting surface appears to accumulate fair amounts of hydrocarbon, on the outermost layers, probably due to an increase in the sticking coefficient of the surface. From the angular dependence data this layer is estimated to be about  $10 \text{ \AA}$  thick ; this is however an average value as the distinctly patchy nature of the coverage, makes an absolute thickness rather meaningless. It was found that this carbon coverage could be reduced considerably by the application of a three stage etch of different acid/peroxide mixtures, as shown in Table 9.3.

#### (b) Oxidising Etches

The two bromine etches (1 and 2 in Table 9.3) were found to produce a thin uniform oxide, about  $20 \text{ \AA}$  thick (see later), although the absolute magnitude and growth rate were found to depend largely upon solution concentration. In addition, from the data obtained there appeared to be no significant chemical difference between the two oxides (apart from a faster

TABLE 9.3 : ESCA intensity data for some wet etched InP substrates

Sample	Take off $\theta$	In <sub>3d</sub>	C <sub>1s</sub>	O <sub>1s</sub>	P <sub>2p</sub>	InP/ <u>In</u> ox	InP/ <u>P</u> ox	Etch concentrations given in Table 3.3	
CV 792	30°	1.0	4.9	2.5	1.45	1.6	2.1	(1) Br <sub>2</sub> /CH <sub>3</sub> OH (1 min)	
	70°	1.0	21.6	4.8	2.04	0.55	0.89		
LV 505 (1)	30°	1.0	9.7	9.5	2.02	0.36	0.2	(2) BR <sub>2</sub> /HBr/H <sub>2</sub> O (1 min)	
	70°	1.0	16.3	8.2	2.28	0.26	0		
LV 505 (3)	30°	1.0	10.6	3.1	1.18	V.Large	V.Large	(3) HF (1 min)	
	70°	1.0	37.3	8.1	1.38	10.0	8.14		
LV 764	30°	1.0	7.7	2.0	1.98	7.5	10.8	(4) HCl/H <sub>2</sub> O <sub>2</sub> /H <sub>2</sub> O (4 sec)	
	70°	1.0	31.5	6.3	1.68	6.6	4.8		
KV 456	30°	1.0	8.3	2.9	2.29	V.Large	8.0	(5) HNO <sub>3</sub> /HCl/H <sub>2</sub> O (15 sec)	
	70°	1.0	23.6	5.4	2.17	12.0	2.1		
LV 505 (2)	30°	1.0	2.2	0.9	1.06	12.0	10.4	(6) H <sub>2</sub> SO <sub>4</sub> /H <sub>2</sub> O <sub>2</sub> /H <sub>2</sub> O (3 min)	
	70°	1.0	14.4	2.2	1.39	4.7	1.95		
	30°	1.0	2.6	0.6	0.93	V.Large	V.Large	HF (5 min)	
	70°	1.0	7.6	1.3	1.90	10.5	V.Large		
	30°	1.0	3.9		2.3	1.29	4.7	5.0	NaOH/H <sub>2</sub> O <sub>2</sub> (1 min)
	70°	1.0	15.3		3.5	1.35	2.2	2.35	

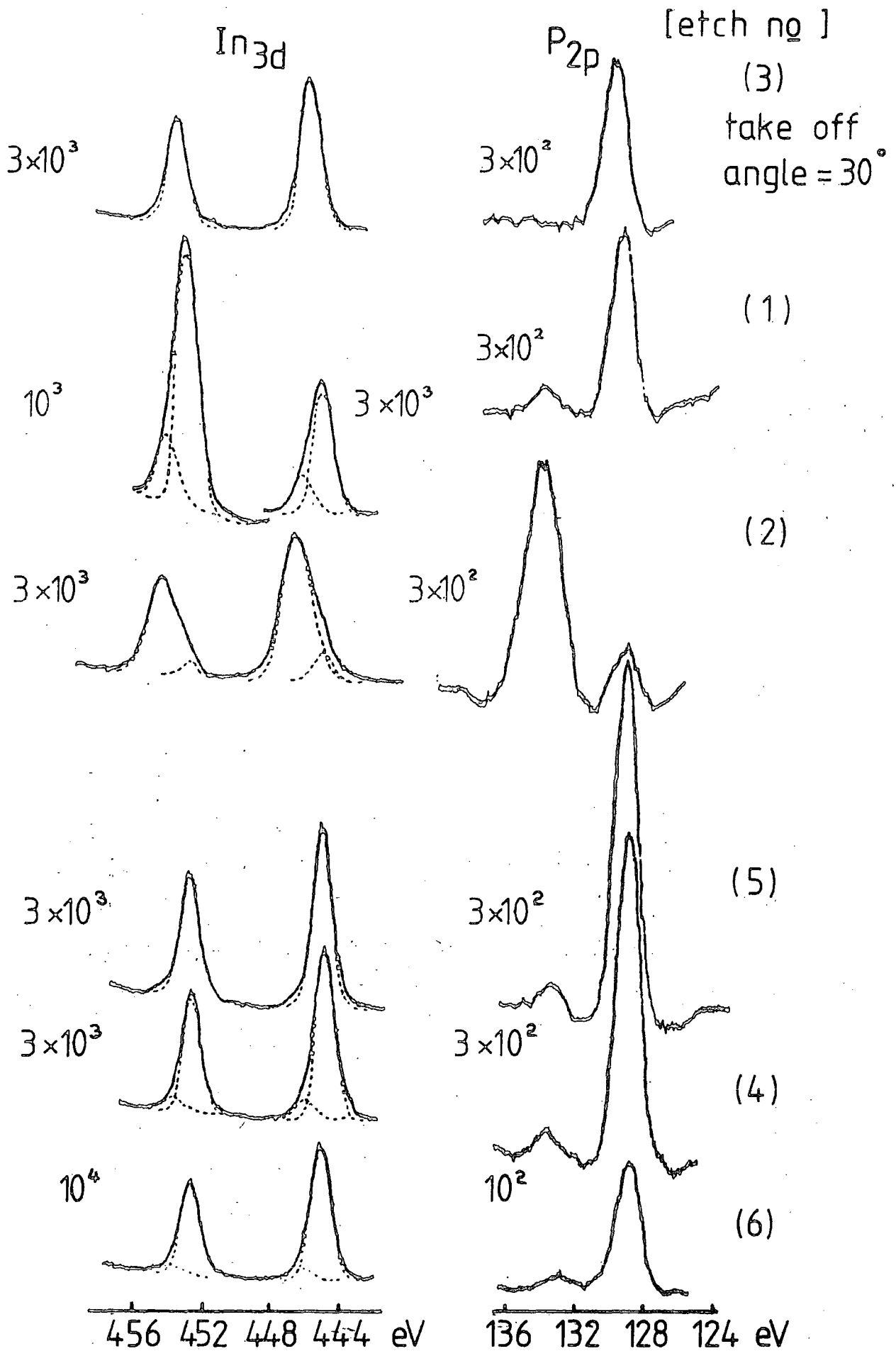


Figure 9.1 : Sample ESCA output data for  $\text{In}_{3d}$  and  $\text{P}_{2p}$  levels- after various wet etches.

growth rate for the Br/HBr). Because of the similarity between these two etchants, only HBr/Br was analysed in detail. For this investigation after a detailed evaluation of the output spectra, the effect of 5% and 20% solutions of the 1-17-35 mixture were noted as a function of time.

In<sub>3d</sub> Levels

For the In<sub>3d</sub> levels, a similar pattern to the one described previously was noted, with two peaks being dominant, the lower one corresponding to InP, and the higher one InPO<sub>4</sub> or InO(OH). Samples of the output data for various times are shown in Figure 9.2, where it can be seen that after 15 seconds the characteristics are dominated by the oxide peak. In general, the intensity and width of this component was found to be directly related to etch time.

P<sub>2p</sub> Levels

The phosphorus output data showed two well separated components, attributable to InP in one case and some form of phosphate (PO<sub>4</sub><sup>3-</sup>) in the other. Again, no peaks corresponding to P<sub>4</sub>O<sub>6</sub> or P<sub>4</sub>O<sub>10</sub> were observed.

After compensation for the emission factors, the ratio of indium to phosphorus was found to be greater than unity, suggesting that the oxidised surface was phosphorus rich.

O<sub>1s</sub> Levels

The component peaks of the oxygen data were observed to show a similar pattern to those of the unetched samples. Based on these data, the major level was concluded to correspond to oxygen bound as a phosphate (PO<sub>4</sub><sup>3-</sup>), but there were no peaks attributable to either In<sub>2</sub>O<sub>3</sub> or P<sub>4</sub>O<sub>10</sub>.

C<sub>1s</sub> Levels

It was found that significantly less hydrocarbon contamination existed upon the etched surface, which suggests that the presence of the oxide

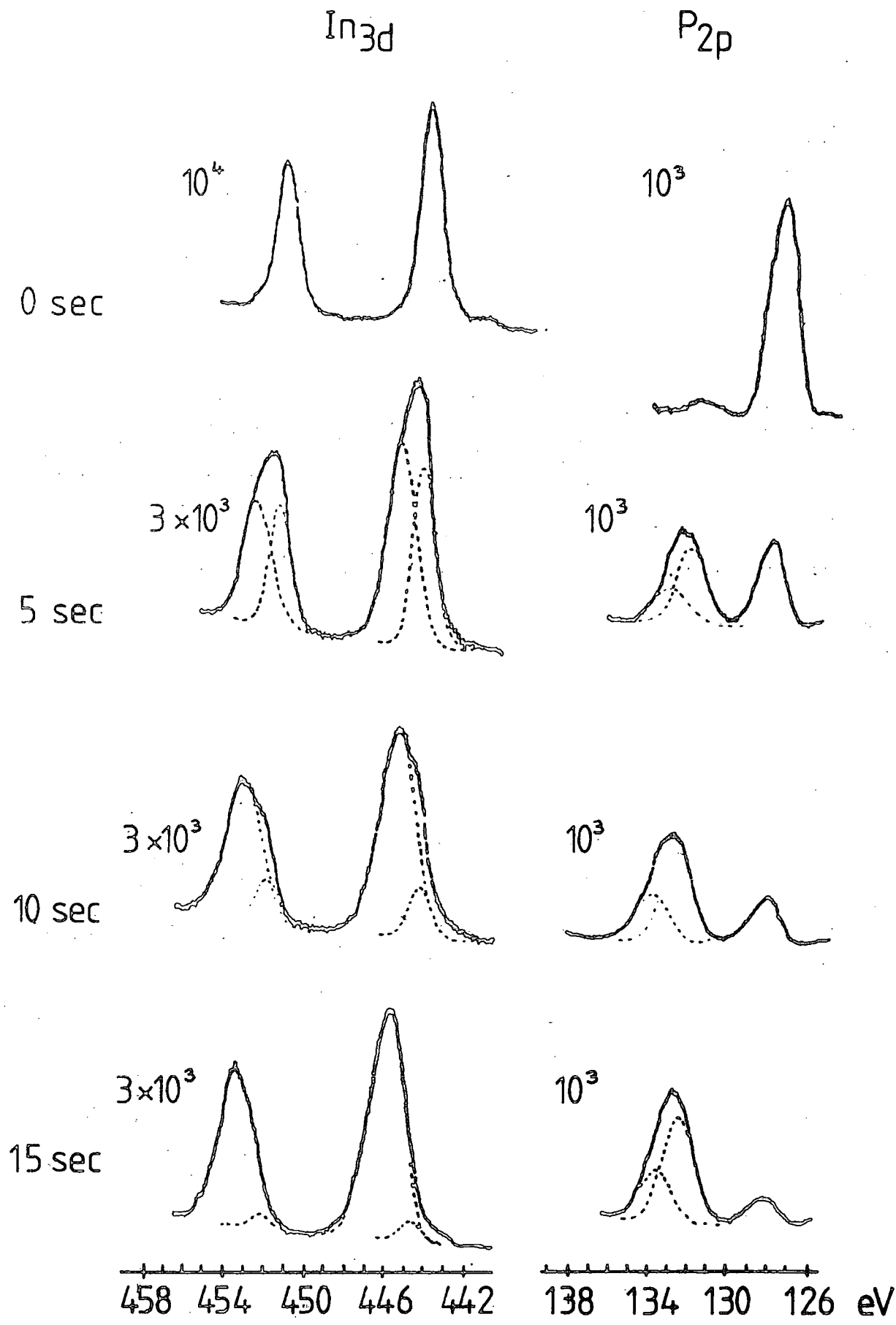


Figure 9.2 : Sample ESCA output data for time dependent 20% Br/HBr etch.

considerably reduces the sticking coefficient for these hydrocarbon materials. Once again, the angular variation measurements showed that the carbon was distinctly a surface feature, corresponding to the top few angstroms of the analysed area.

#### Variations with etch time

A summary of the effect of time on 5% and 20% solutions HBr/Br etches are given in Tables 9.4 and 9.5. With the 20% solution, the oxidation rates were found to be very rapid, and times of only a few seconds produced a total oxide coverage (as determined from the  $\text{In}_{3d}$  levels). Samples treated for longer periods showed more uniform coverage, and as expected, the weaker etchant exhibited a slower growth rate. In both cases the hydrocarbon contamination showed an approximately steady increase with time, but became thicker rather than more uniform. In addition, the changes in the  $\text{O}_{1s}$  level suggest that the oxide layer becomes more uniform with time, especially within the top 10-15 Å. It was also apparent that changes in surface stoichiometry increased the phosphorus dominance with prolonged etching; this was probably a symptom of the higher diffusion and reaction rate of indium.

#### Depth Profile of Surface Oxide

In order to gain more information about the chemical oxide, an argon ion gun was used to sputter profile a Br/HBr etched sample. The resulting output data as a function of time (and therefore sample depth) are given in Figure 9.3. The main features of this profile can be summarised as follows :- The surface stoichiometry was found to progressively change through the oxide, and was equivalent to InP at a depth of around 12 Å. The oxide, probably  $\text{InPO}_4$  was found to be very much a surface feature, and decreased rapidly after a few angstroms, as did the surface hydrocarbon. Elemental indium was also observed in small amounts, uniformly distributed through the oxide. For the  $\text{P}_{2p}$  contribution, a total of four oxidation states were noted, but the



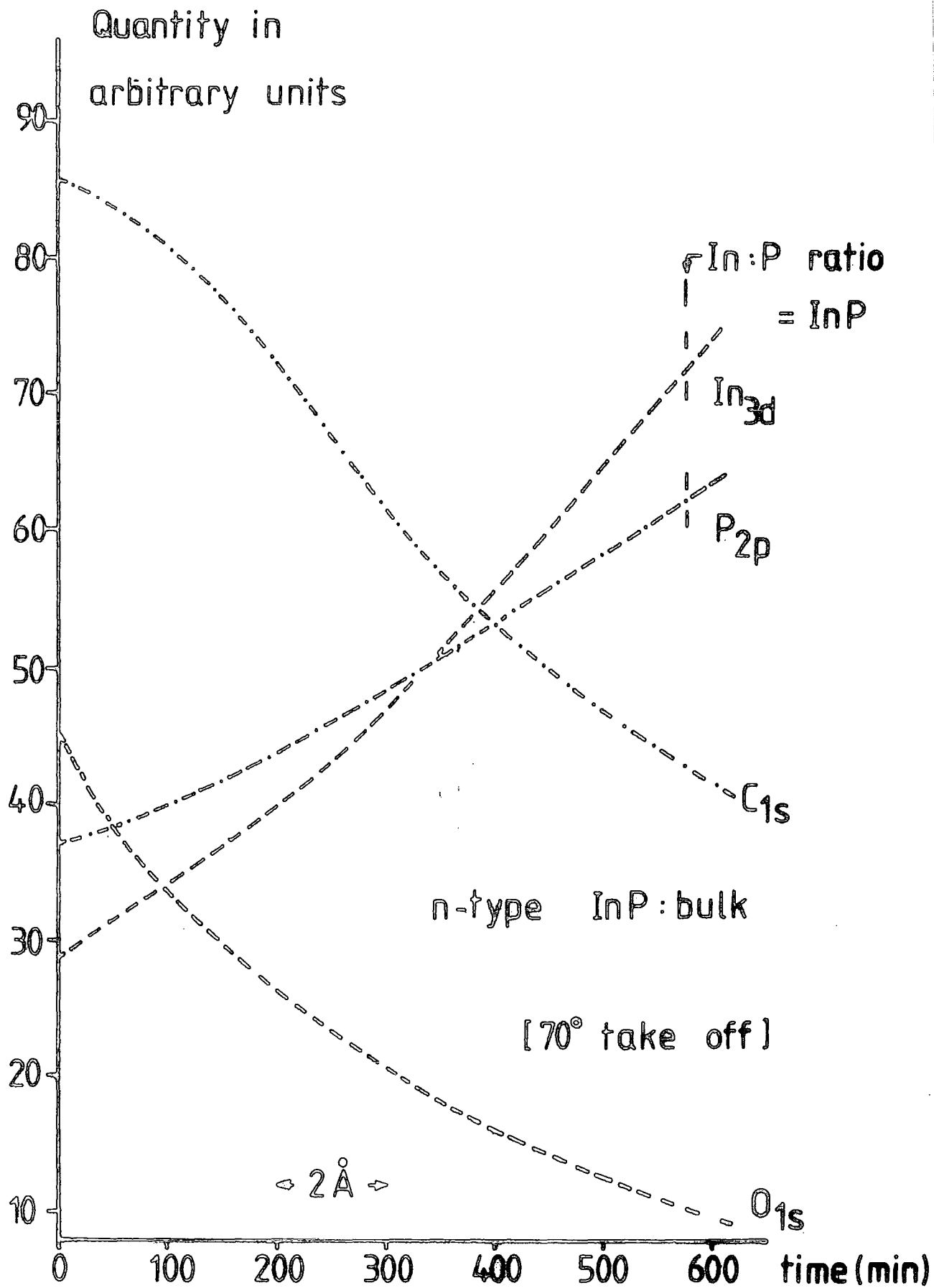


Figure 9.3 : Output data for argon ion depth profile of wet (Br/HBr) etched oxide.

**TABLE 9.4** : Spectral characteristics of sample LV 505 etched with 5% Br<sub>2</sub>/HBr/H<sub>2</sub>O solution.

Treatment time	Take off Angle	In <sub>3d</sub>	C <sub>1s</sub>	O <sub>1s</sub>	P <sub>2p</sub>	InP/In ox	InP/P ox
0	30°	1.0	2.7	0.94	1.05	10.1	V. Large
	70°	1.0	10.1	2.02	1.2	6.1	11.5
5 sec	30°	1.0	4.5	2.7	1.5	1.4	1.5
	70°	1.0	11.7	5.13	1.95	0.58	0.5
10 sec	30°	1.0	4.27	4.72	1.8	0.47	0.5
	70°	1.0	6.3	5.67	1.95	0.15	0.15
30 sec	30°	1.0	4.95	5.67	2.1	0.3	0.2
	70°	1.0	6.52	6.48	2.1	0.09	0.09
60 sec	70°	1.0	11.92	7.15	2.4	0.04	0.06

TABLE 9.5 : Spectral characteristics of sample LV 505 etched with 20% BR<sub>2</sub>/HBr/H<sub>2</sub>O solution.

Treatment Time	Take off Angle	In <sub>3d</sub>	C <sub>1s</sub>	O <sub>1s</sub>	P <sub>2p</sub>	InP/In ox	InP/P ox
0	30°	1.0	2.02	1.08	1.2	V. Large	13.3
	70°	1.0	7.87	2.56	1.2	9.6	8.1
3 sec	30°	1.0	6.3	4.32	2.1	0.39	0.78
	70°	1.0	14.8	4.99	2.2	0.17	0.3
5 sec	30°	1.0	5.85	4.59	1.65	0.67	0.67
	70°	1.0	13.05	5.8	2.4	0.16	0.2
10 sec	30°	1.0	3.82	5.94	1.95	0.16	0.3
	70°	1.0	11.02	6.61	2.25	0.06	0.09
15 sec	30°	1.0	7.42	5.53	2.1	0.04	0.15
	70°	1.0	10.8	6.21	2.25	0	0.06

additional ones were found to be directly due to the profiling process<sup>(1)</sup>, and not real configurations. For this ion bombarded surface, in the absence of hydrocarbon, a more accurate estimate of the oxide thickness was possible, this gave a value of 14 Å ; the average of 12 Å and 18 Å from In<sub>3d</sub> and P<sub>2p</sub> spectra respectively.

The results of this characterisation of wet etches can be summarised as follows :

- (i) The etchants employed can be categorized into two groups ; giving a clean surface, or an oxidized one ( ~ 15 Å). In the latter case, the thickness was governed by the substrate type, and the duration and concentration of the etching process.
- (ii) HF treatment was the only method of producing a stoichiometry close to unity, it also produced significantly larger amounts of surface hydrocarbon. This could however be reduced by a three stage etch process.
- (iii) All other surfaces were phosphorus rich.
- (iv) The oxides produced by the Br<sub>2</sub> etches were predominantly InPO<sub>4</sub>, with possibly some InO (OH) and H<sub>3</sub>PO<sub>4</sub> being present.
- (v) Contrary to results obtained by other workers, no In<sub>2</sub>O<sub>3</sub> or P<sub>4</sub>O<sub>10</sub> were observed throughout this study.

### 9.1.3 The Effect of Dry Etching

In order to investigate the effect of glow discharge etching upon the InP surfaces, two different ambient gases were used, oxygen and hydrogen. The resultant surface in each case was examined directly and after exposure to the atmosphere, and the salient features observed can be summarized as follows :

#### (a) Hydrogen Plasma

For initially clean (pre-etched in a de-oxidising etch) InP surfaces the hydrogen was found to behave as a very effective reducing agent, reacting

with the surface phosphorus to produce volatile  $\text{PH}_3$ . This was subsequently removed by the vacuum pump. The remaining surface was found to become gradually indium rich as witnessed by a shift in the binding energy of the indium component to a value corresponding to that for indium metal. Exposure times of greater than 50 seconds were found to leave the surface totally covered in indium metal. In addition, the hydrogen plasma was found to be very effective in removing hydrocarbon contamination causing a factor of three reductions in peak height over a period of 20 seconds.

Upon exposure to the atmosphere the indium surface layer was found to rapidly oxidize to  $\text{In}_2\text{O}_3$ , thus leaving the topmost layer fundamentally different to any surface produced by wet etching.

For a sample pre-etched in a wet oxidizing liquid, the effect of the dry etch was found to be rather more complex. In this situation, the plasma cannot reduce  $\text{InPO}_4$  which therefore stays intact and protects the underlying material. However, for short etch times the resultant  $\text{InPO}_4$  layer was patchy and so the intermediate area was reduced by the hydrogen, leaving it indium rich. Subsequent exposure to the atmosphere was found to give the anticipated oxidation of the indium areas leaving a patched overlayer mixture of  $\text{In}_2\text{O}_3$  and  $\text{InPO}_4$ .

Because of these effects, the majority of device fabrication using dry etching was undertaken upon clean, rather than wet, oxidised surfaces.

#### (b) Oxygen Plasma

The use of oxygen plasma to prepare the InP surface was found to give an effect very similar to that resulting from a wet oxidizing etch. The oxide growth, primarily  $\text{InPO}_4$ , was found to saturate after an exposure time of approximately 1 minute and resulted in a terminal thickness of about 25-30 Å. This oxide was found to be relatively stable, and exposure to the atmosphere produced very little change in the surface chemistry. In addition,

the use of both types of wet etchant as pre-treatment was found to have no significant effect upon the resulting oxide layer.

The results of the dry etch characterisation can be summarised as follows :

- (i) A hydrogen plasma was found to reduce an initially clean InP surface by forming volatile  $\text{PH}_3$ . This resulted in the remaining surface being indium rich and oxidising to  $\text{In}_2\text{O}_3$  upon atmospheric exposure.
- (ii) Longer etches produced metallic like properties due to the large amounts of indium generated.
- (iii) The use of hydrogen plasma on a wet oxidised surface produced a mixed overlayer of  $\text{In}_2\text{O}_3$  and  $\text{InPO}_4$ .
- (iv) The use of oxygen plasma produced a surface very similar to that resulting from a wet oxidising etch.

## 9.2 METAL-SEMICONDUCTOR CONTACTS

### 9.2.1 Ohmic Contacts

For n-type InP, Ohmic back contacts were produced by using an alloy of indium with 5% tin<sup>(2)</sup> (by weight), at a thickness of 500 Å. In most cases two electrodes were evaporated (to enable I-V checking), and were annealed at 200°C in nitrogen for about five minutes. For bulk substrates a resistance between these electrodes of a few Ohms was found to signify a good contact. With epitaxial samples, however, the increased doping of the substrate removed the requirement for thermal annealing.

For p-type substrates a laminated structure of nickel (50 Å), zinc (500 Å), and gold (5000 Å)<sup>(3,4)</sup> was found to be necessary, followed by a five minute anneal at 300°C. In this case, the typical resistance between contacts was  $\sim 10\Omega$ .

It should be noted, however, that there are many different recipes for Ohmic contacts, the majority of which have been developed empirically, but most of which are satisfactory. For more details of these additional

approaches an excellent summary is given by A.G.Milnes and D.L.Feucht in "Heterojunctions and Metal Semiconductor Junctions" (Academic Press, 1972).

### 9.2.2 Schottky Barriers

In order to supplement the chemical characterisation information, a number of metal/semiconductor junctions were fabricated on both oxidised and deoxidised surfaces. In all cases the substrates used were bulk rather than epitaxial.

#### (a) P-type Structures

P-type Schottky barriers were fabricated using a gold barrier electrode, and both current-voltage and capacitance-voltage characterisation were undertaken.

Typical log (current)-voltage curves for both oxidised and de-oxidised interfaces are shown in Fig.9.4, in these cases prepared using HBr/Br and  $H_2SO_4/H_2O_2$  mixtures respectively. In each case the forward bias data can be seen to show an excellent straight <sup>line</sup> as expected, and from Eqn. 2.13 the ideality factors were calculated to be,

For the oxidised interface  $n \approx 1.08$ ,

and for the de-oxidised interface  $n \approx 1.20$ .

From the capacitance-voltage data, it was possible to plot  $1/C^2 - V$ , and thus from Eqn. 2.9, assuming the dielectric constant to be  $\epsilon_r = 12$ , the value of Nd was calculated to be  $1 \times 10^{17} \text{ cm}^{-3}$ . This agrees adequately with values obtained from Hall effect measurements. In addition, from Eqns. 2.9 and 2.10 the intercept point upon the X-axis in each case was used to calculate the approximate barrier heights.

From the reciprocal capacitance plots shown in Fig.9.5 for the samples previously mentioned, it was found that  $\phi_B = 0.8 \text{ eV}$ , with no significant variation in value for different etchant preparations. It should also be noted that the slight variation in slope apparent for different electrodes is merely a function of area variation due to the contact evaporation process.

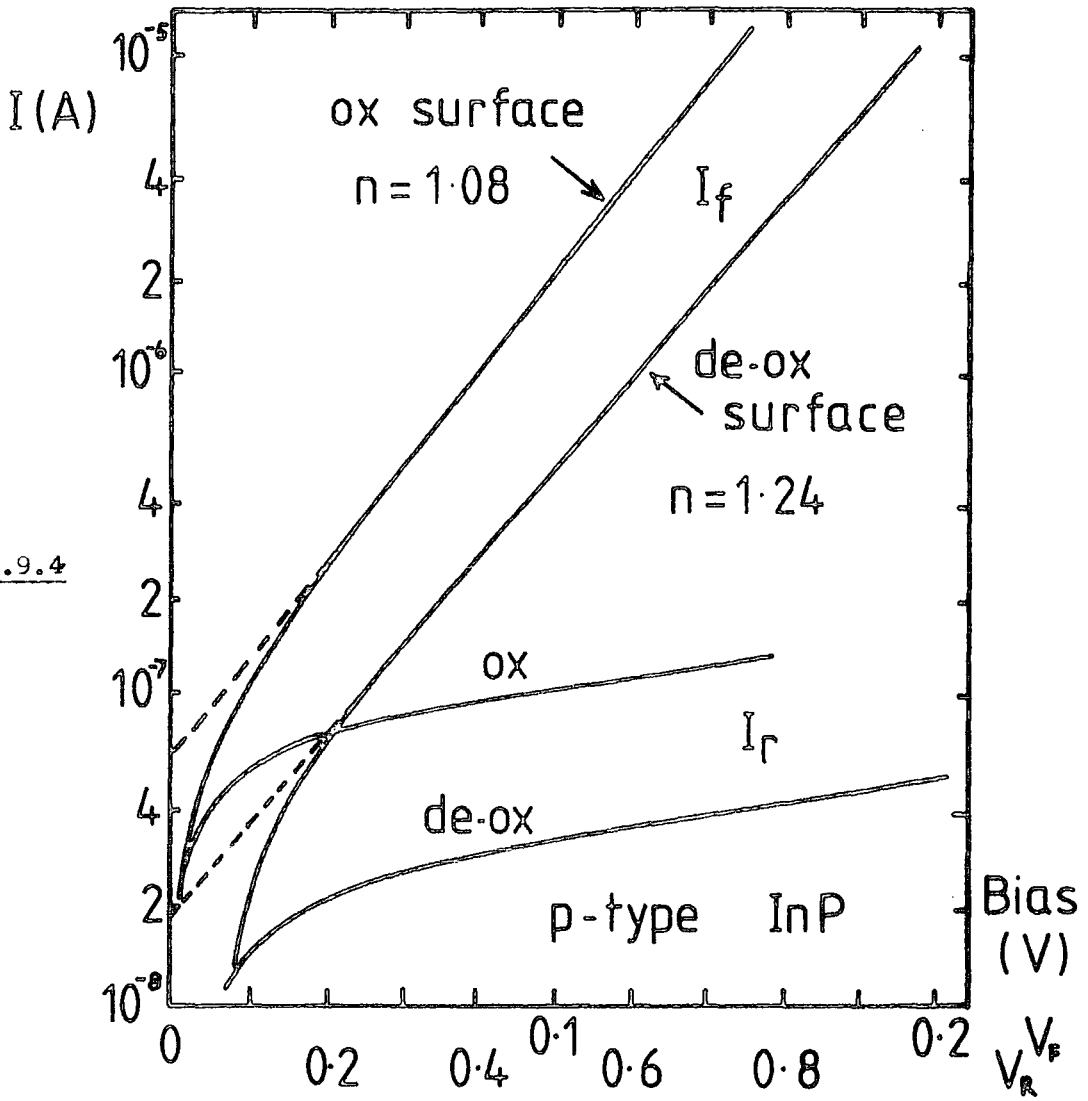


Fig.9.4

Figure 9.4 & 9.5 : Schottky barrier data for p-type InP substrate.

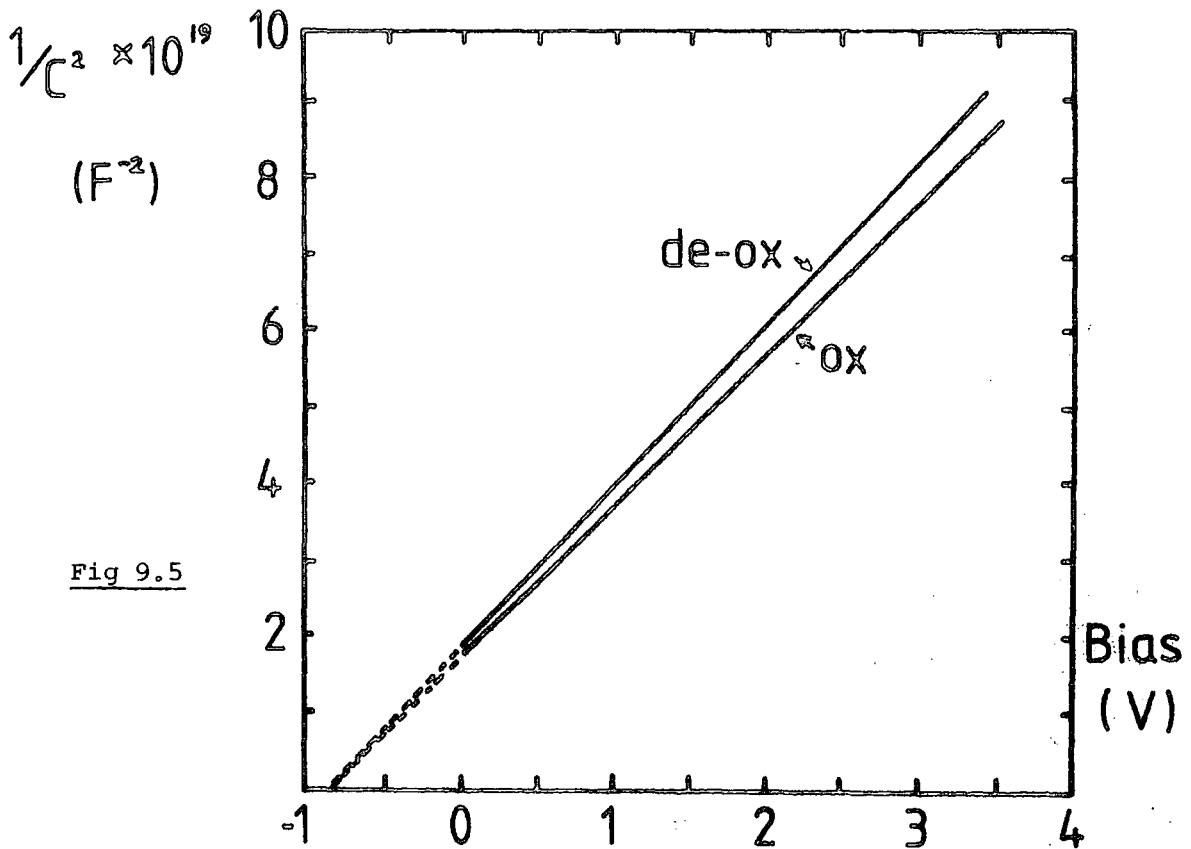


Fig 9.5



(b) N-type Structures

Devices on n-type substrates were prepared using gold barrier electrodes, however the slightly lower conductivity of bulk n-type material led to problems with series resistance. Typical log (current)-voltage characteristics for both oxidised (HBr/Br) and de-oxidised ( $H_2SO_4/H_2O_2$ ) interfaces are shown in Fig. 9.6, from which it can be seen that there is no straight line portion. However, when the series resistance values of  $4.4 \Omega$  are compensated for (as discussed in section (2.2) ), straight line portions are revealed. From the gradient of these, the ideality factors were calculated to be ;

For the oxidised interface  $n \approx 1.08$ ,

and for the de-oxidised interface  $n \approx 1.15$ .

These values can be seen to correspond well to the ideality factors obtained from the p-type devices without series resistance. This suggests that the compensation approach is quite valid.

Typical reciprocal capacitance plots for these two samples are shown in Fig.9.7, from which the doping density  $N_D$  was calculated to be  $1 \times 10^{16} \text{ cm}^{-3}$ , and the barrier heights were  $\phi_B = 0.43 \text{ eV}$ . Once again, no significant variation with etchant preparation was noticed.

(c) Discussion

The characteristics obtained from both p and n type Schottky barriers appear to be etchant dependent, but not to the extent expected. The lower ideality factors obtained from oxidised interfaces agree well with the concept of a gradual transition region and the relative lack of surface damage. They do, however, conflict somewhat with the normally accepted rule of interfacial oxide increasing the value of  $n$  as discussed in Chapter 2, as the clean, oxide free interface gives a higher ideality factor. It must therefore be concluded that the abrupt, damaged nature of the transition region is an important factor in the case of the "clean" interface. This point is further supported by the relative lack of variation of barrier height

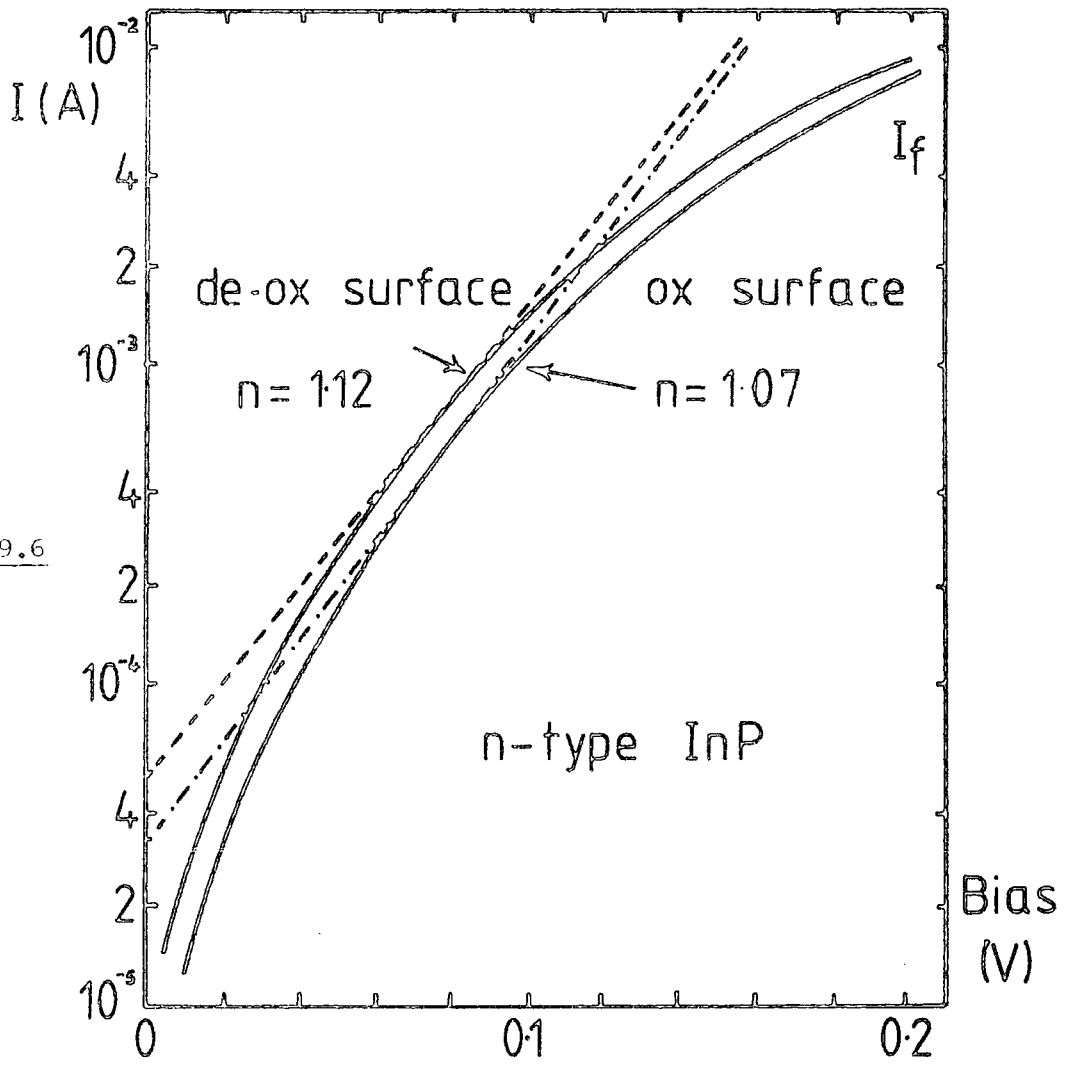


Fig 9.6

Figure 9.6 & 9.7 : Schottky barrier data for n-type InP substrate.

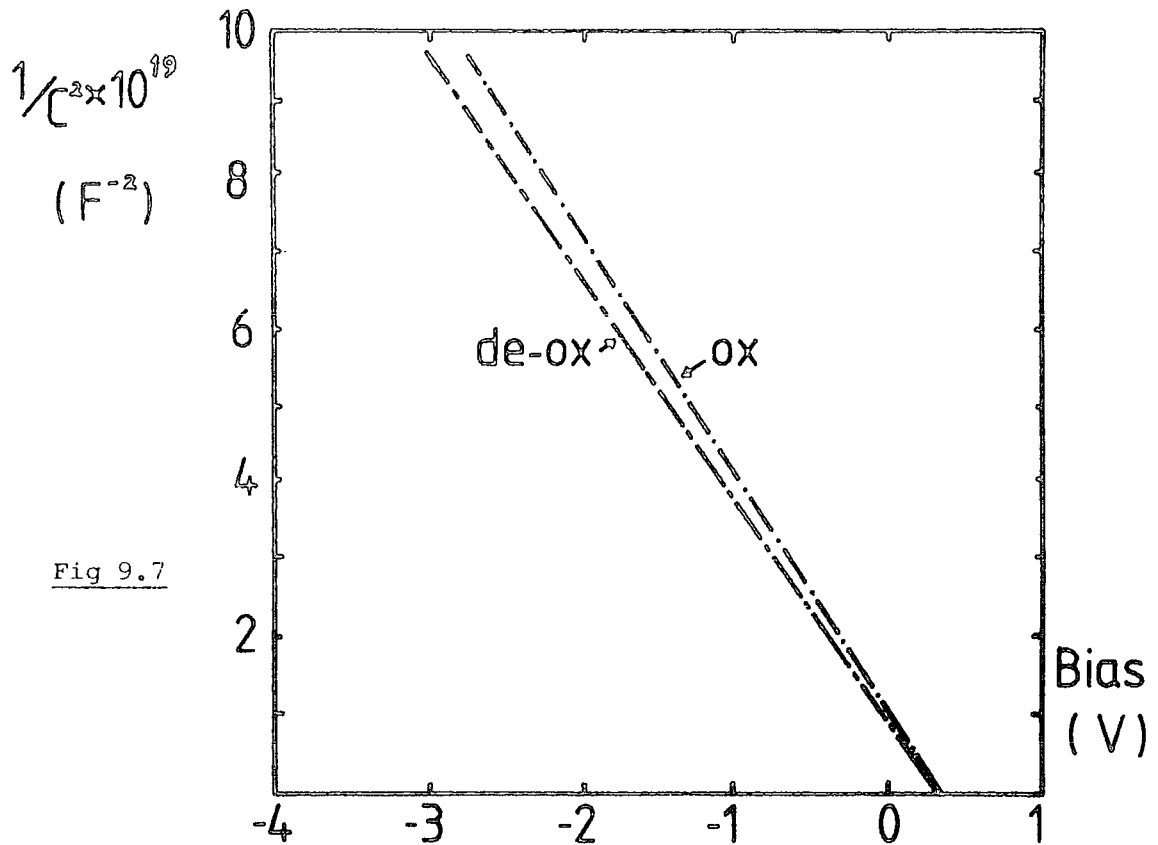


Fig 9.7

as a function of etch preparation, in spite of good agreement with values obtained by other workers<sup>(5,6)</sup>. This indicates that the barrier height is influenced by damage caused during evaporation of the metal electrode. Indeed, the values obtained for p-type material suggest that the Fermi level is located in the upper half of the band gap.

It appears therefore that for Schottky barriers both etching and electrode damage contribute to the overall characteristics and the presence of an oxide layer, although buffering the effect somewhat, cannot prevent the introduction of some damage. These damage effects emphasise the sensitive nature of the InP surface and are in some respects comparable with the ones discussed later in the chapter caused by high temperature insulator deposition processes. Moreover, these results provide excellent contrast with the MIS data obtained by Langmuir film incorporation where little or no damage is produced.

### 9.3 N-TYPE InP : MIS CHARACTERISATION

Because of the passive nature of the Langmuir film deposition process, MIS structures have <sup>been</sup> fabricated with little perturbation of the semiconductor surface. This has allowed detailed investigation into the effect of the two etchant types upon the device characteristics, and has enabled a correlation to be made between the surface chemistry and the device performance. The results of this investigation (presented in this section) are divided according to surface preparation, but in general were rather different to the ones obtained by other workers using more energetic insulator deposition processes (as discussed in Chapter 8).

#### 9.3.1 Wet Etchants

A typical set of capacitance and conductance curves for both an oxidised and a de-oxidised surface are shown in Figs. 9.8 and 9.9. The differences between these two sets of data, although not very marked, do show

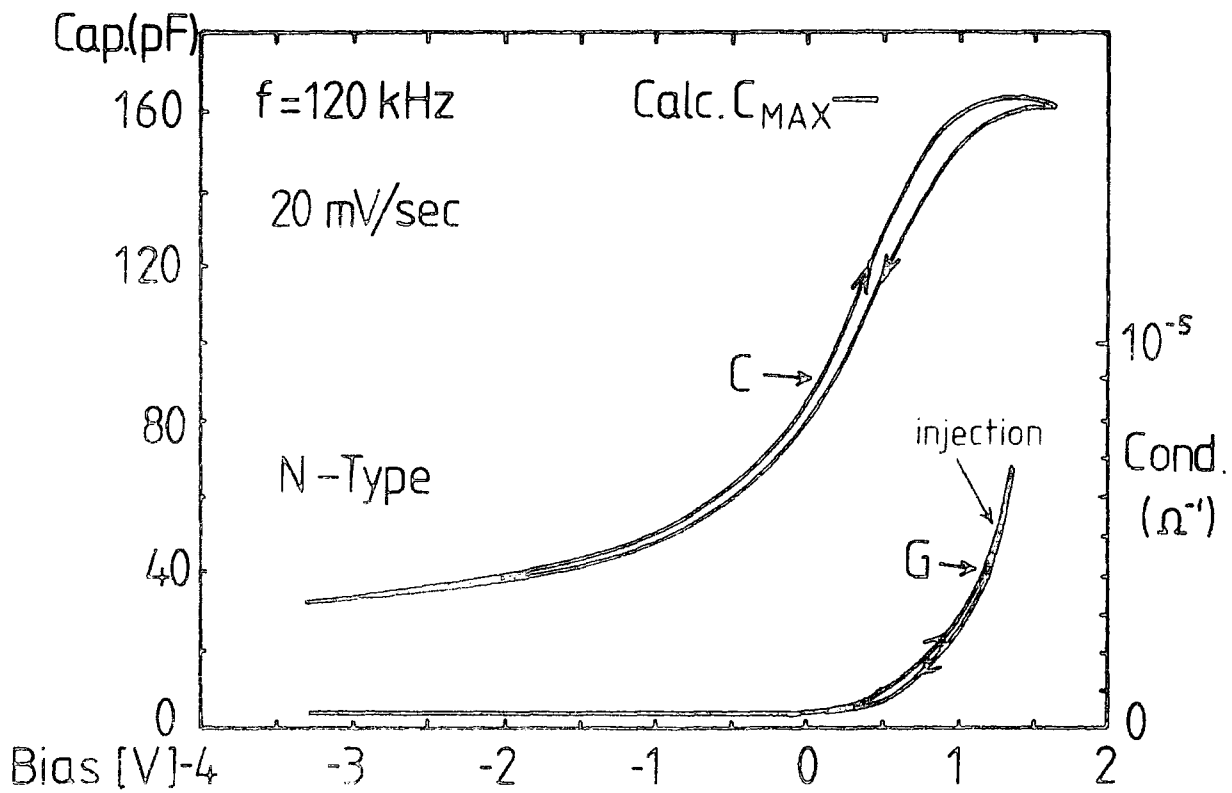


Figure 9.8 : Typical output MIS data for oxidised InP interface.

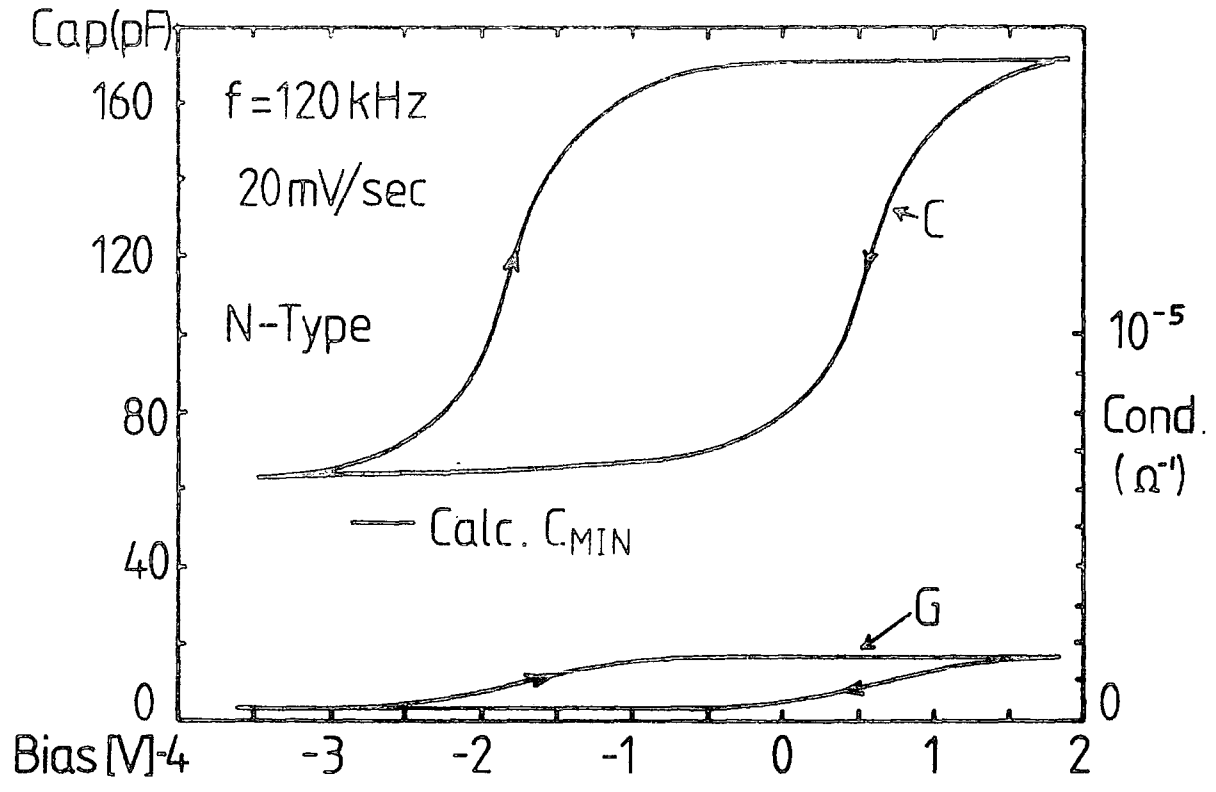


Figure 9.9 : Typical output MIS data for de-oxidized InP interface.

significant discrepancies ; these will now be discussed.

(a) Oxidised Interface

The major feature of this type of data was found to be the rapid increase in conductance under forward bias conditions that occurred frequently. This was initially assumed to be a breakdown effect, but comparison with I-V and p-type MIS data showed it to be due to electron injection into the insulator. Otherwise the conductance data showed no significant structure, with totally flat reverse bias output, and no surface state peak even at the lowest frequency.

The capacitance data usually showed deep depletion type characteristics, with no inversion even at low frequency. In forward bias some levelling at the calculated accumulation value was observed, but the onset of forward bias injection inevitably removed the charge and so lowered the measured capacitance. It should be noted that with certain samples this injection effect was less dominant enabling stronger accumulation to be produced. This inconsistency only occurred for older samples obtained from Malvern, and therefore is probably connected with some overall variation in sample quality.

In all cases, the hysteresis was clockwise, and small ( $\sim 100$  mV) in magnitude. The curve shape was also different for each direction, with a much sharper transition occurring from accumulation to depletion.

(b) De-Oxidised Interface

The de-oxidised surface appeared to be much more abrupt in structure and thus possessed a higher density of damage at the interface region. In this situation, the conductance data showed flat characteristics for both directions of applied bias, and frequently the film could be exposed to more than  $10^6$  V/cm without the onset of any breakdown effects.

The capacitance data were found to show adequate accumulation, and what to a first approximation appeared to be weak inversion. Comparison of

the value with the calculated  $C_{\min}$  however suggested the effect was more likely due to Fermi level pinning as the value measured was not low enough. For this type of interface the characteristics were dominated by hysteresis, of the same sense as before, but now considerably larger in magnitude. The effect of frequency upon these data was virtually zero, and thereby provided further evidence for the  $C_{\max}$  to be due to accumulation, and the  $C_{\min}$  to be due to pinning (see Fig.9.9).

(c) Additional Observations

In all cases the application of light was used as a method of ensuring that the maximum value of capacitance was due to the onset of accumulation rather than any other effect, it was also used to increase the density of free carriers and so aid the observation of a conductance peak. For n-type samples, however, the effect was negligible.

The dominating influence of the interface was confirmed by the removal of the insulator followed by re-deposition without additional pre-treatment. For this operation, the solvent (chloroform) appeared to remove most of the insulator but was thought to leave one interfacial monolayer, upon which the new film was built. This "wiping and re-dipping" was found to have no effect upon genuine characteristics, but did enable the re-deposition of particularly bad films without re-etching and other pre-treatment operations.

In order to clarify the injection effect, a thin layer of fluorocarbon polymer was deposited upon partial areas of selected substrates as a barrier layer. Subsequent comparison of two halves of any sample showed the total removal of the injection wherever the polymer had been deposited. In addition, however, as is well characterised for polymers, the extra layer generated significant hysteresis and was therefore useless for any further development. The application of bias-stress to normal MIS devices was also used as evidence for the presence of injection, as shown in Fig. 9.10. From these data, it can be

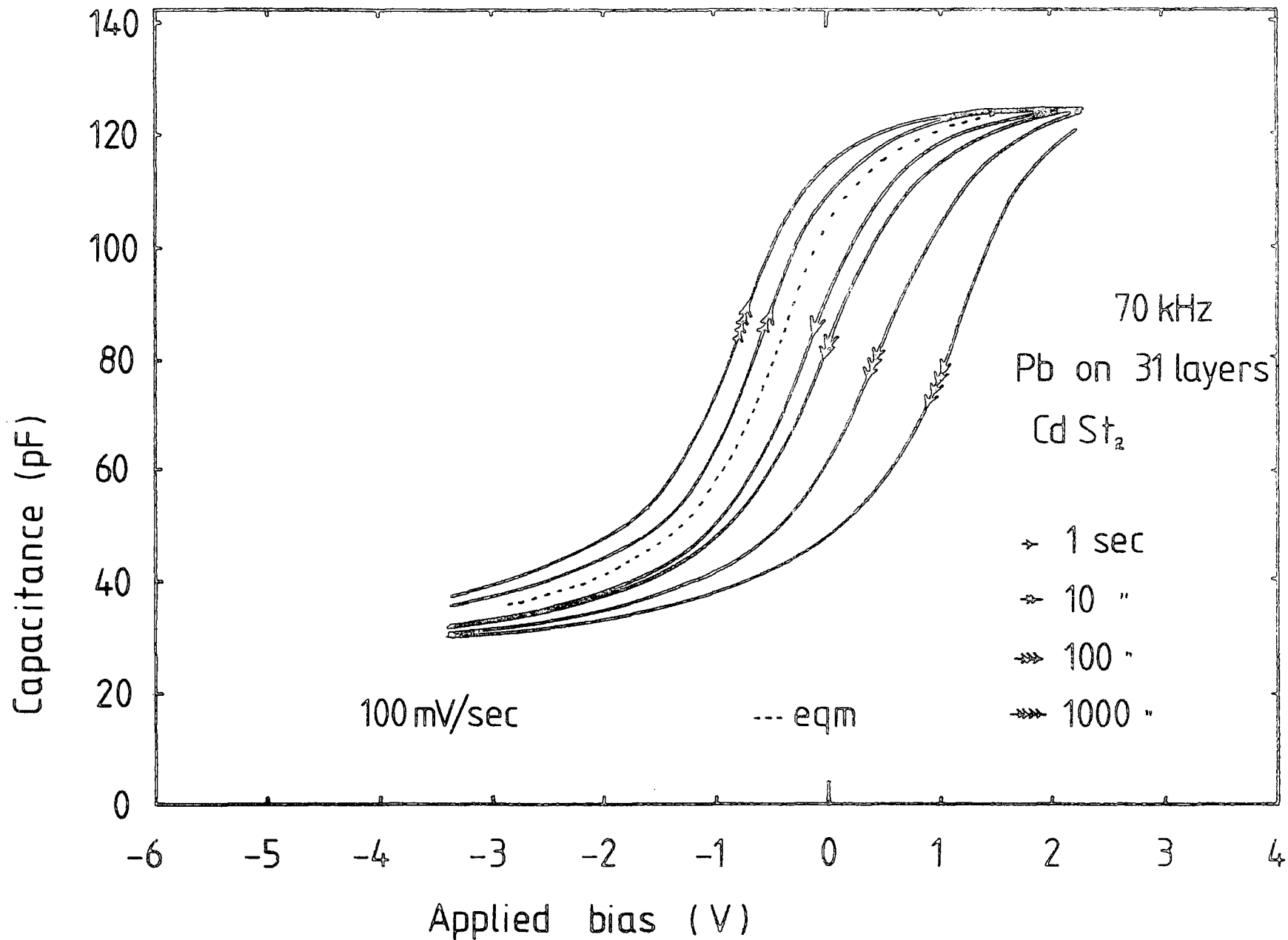


Figure 9.10 : The effect of bias-stress upon an n-type MIS structure : showing dominance of electron injection.

seen that forward biasing for long periods produces a gradual shift as electrons are injected into the insulator. By contrast, the application of reverse bias has considerably less effect upon the curve position. Experiments were also undertaken on  $n^+$  substrates, prepared with oxidising etchant, but here again the injection effects dominated showing the forward bias increase as observed in ordinary low doped material. This result was concluded to indicate that the injection was not due to the semiconducting properties of the InP, but was more a function of its chemical nature, interface oxide, etc.

For both interface types, frequent use was made of Hg top contacts to quickly test samples prior to electrode evaporation. In practice this approach did not allow any quantitative evaluation to be undertaken (due to the unknown contact area), but it did quite effectively show the presence of the two contrasting types of characteristic.

(d) Optimisation of Etching

For the purposes of this investigation, the optimum capacitance characteristics would show accumulation, depletion, and weak inversion, demonstrating that the Fermi level was relatively free to traverse the band gap. Up to this point however the characteristics described, although containing some of these requirements were far from the optimum. Further investigation of the preparation techniques showed that a combination of first a de-oxidising etch, followed by a short oxidising etch generated a very thin oxide layer which combined certain features of both extremes. A typical example of this type of data is shown in Fig. 9.11, in which it can be seen that accumulation, depletion and some weak inversion are present, and, in addition, although still present, the injection effect is less extreme in its onset. Moreover the hysteresis is considerably less than that normally associated with a de-oxidising etch, and the effect of illumination is to increase the reverse bias capacitance, further confirming the presence of



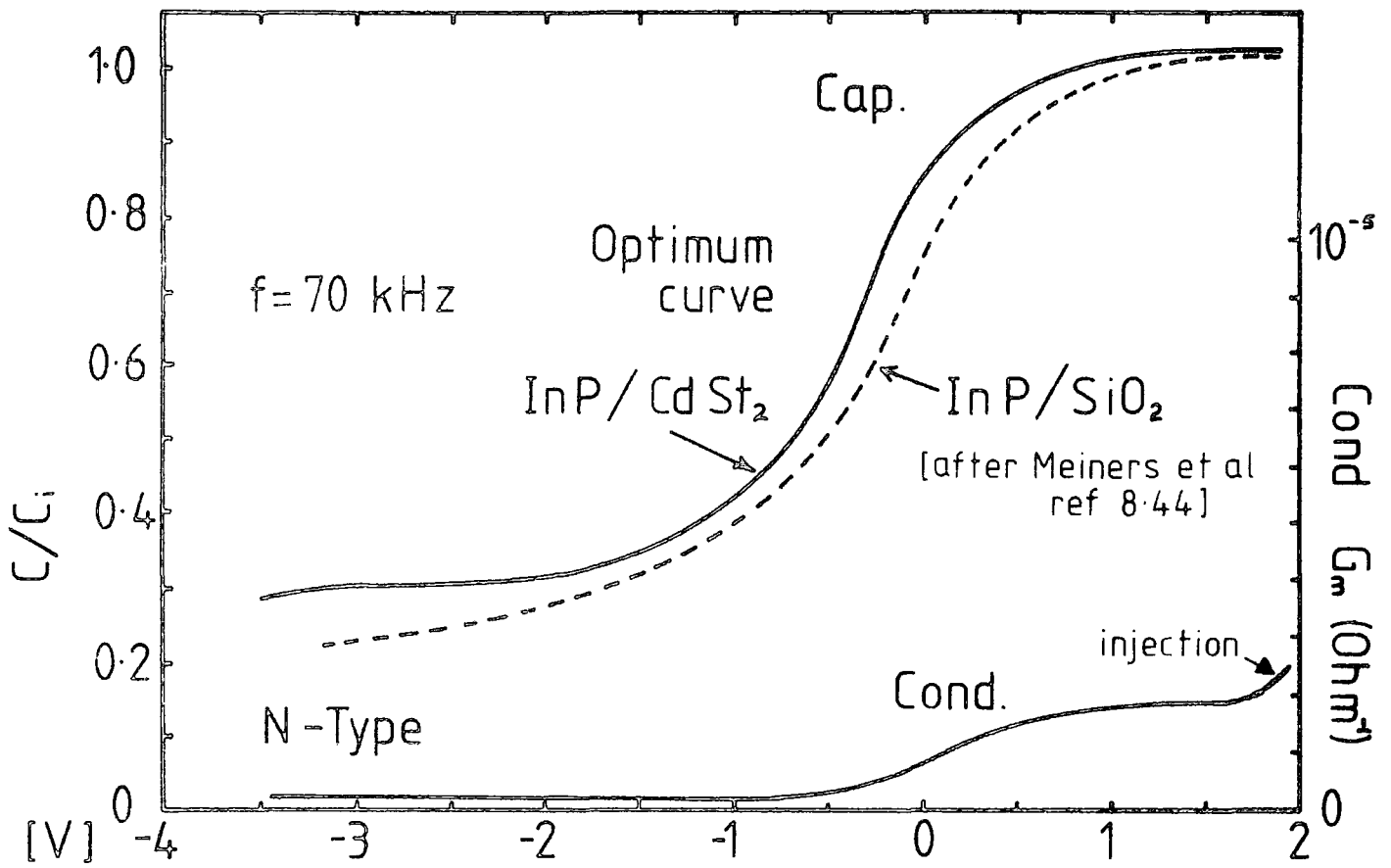


Figure 9.11 : Example of optimum sample data obtained by using both oxidising and de-oxidising etches. Also shown for comparison is a typical curve obtained using a high temperature insulator deposition process.

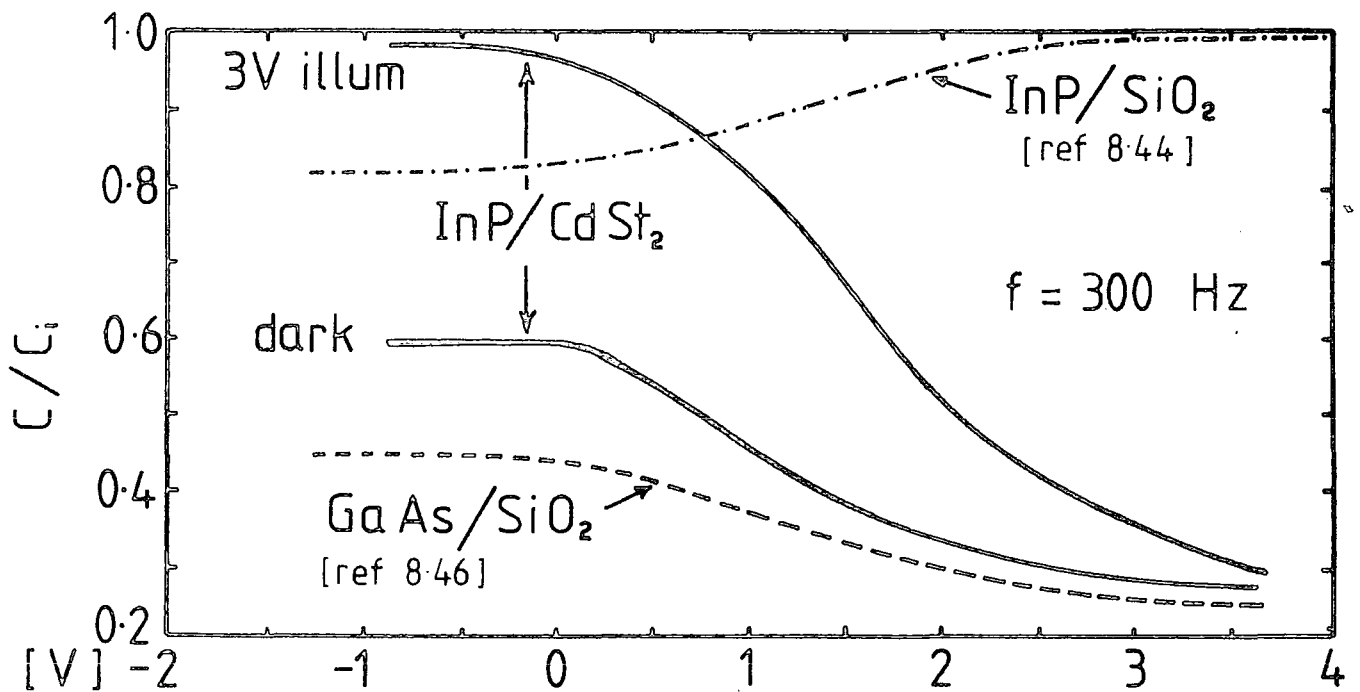


Figure 9.12 : Typical capacitance characteristics obtained using oxidised p-type interface. Also shown for comparison are typical GaAs and InP (high temp. insulator) curves.

weak inversion. Also shown in this diagram for the sake of comparison are typical data obtained using a high temperature deposition process.

(e) Estimation of Interface State Density

Because of the lack of structure in the conductance data it was found impossible to employ any sophisticated surface state analysis procedure. Moreover the absence of strong inversion at low frequency prohibited the use of many of the simpler approaches. It was however possible to obtain some indication of the interface state density from Terman's method as described in Chapter 2, applied to the "optimum" device characteristics. In this method, comparison is made between the high frequency "ideal" capacitance curve, and the low frequency curve with "surface states". The difference in these two can thus give an indication of the interface state density.

From the comparison of data obtained at 120 KHz, with that measured at 30 Hz, the maximum displacement in the depletion region was found to be ; For epitaxial material  $\Delta V \approx 1.2$  V, and for bulk material  $\Delta V \approx 1.7$  V. Thus from Equation 2.63 the total number of states at the interface can be calculated to be ; For epitaxial material  $N_{ss} \approx 2.3 \times 10^{11}$  states/cm<sup>2</sup>, and for bulk material  $N_{ss} \approx 3.3 \times 10^{11}$  states/cm<sup>2</sup>. In each case these values are relatively large when compared to silicon, but agree with the estimate obtained by other workers (see Chapter 8). Moreover, the slight difference in values between bulk and epitaxial material were quite reproducible and are thus more likely to reflect differences in bulk chemistry rather than induced etchant effects.

9.3.2 Dry Etchants

In general the use of dry etchants on n-type material showed no great improvement over the best obtainable with wet etches. This was in fact quite surprising in view of the significantly difference chemical surface obtained. The technique is however considerably cleaner and more controllable than with wet etching.

Two types of glow discharge were used, oxygen and hydrogen, both of which ultimately gave characteristics very similar to those of a slightly (wet) oxidised surface. Of the various exposure times used, 10 seconds was found to give the best results for the oxygen plasma, after which the thicker oxide induced considerable injection. For the hydrogen plasma, an exposure of 25 seconds gave the best characteristics, above which the indium dominance of the surface stoichiometry led to a gradual reduction in the  $C_{\max}/C_{\min}$  ratio and the interface becoming virtually metallic in nature.

In practice, the two different types of oxide present,  $\text{InPO}_4$  from hydrogen, and  $\text{In}_2\text{O}_3$  from oxygen appeared to have little effect upon the injection characteristics usually observed with n-type oxidised substrates.

#### 9.4 P-TYPE InP : MIS CHARACTERISATION

This section investigates the p-InP-Langmuir film interface, as a function of various surface preparations. In many respects, comparisons can be drawn between the n-type, and p-type results, there are however significant differences. Moreover, as shown in certain diagrams, these results are markedly different to those obtained using any high temperature deposition process.

##### 9.4.1 Wet Etchant

As expected, the two groups of etchants investigated produced characteristically different results. However, the results were overall less ideal than those for n-type devices.

##### (a) De-Oxidised Interface

For the clean interface, capacitance variation occurred only in the depletion region, with the value levelling off in forward bias at a capacitance corresponding to slightly over half the expected  $C_{\max}$ . In reverse bias the capacitance continued to reduce with increasing voltage, showing no sign of weak inversion. For this type of structure, the hysteresis was

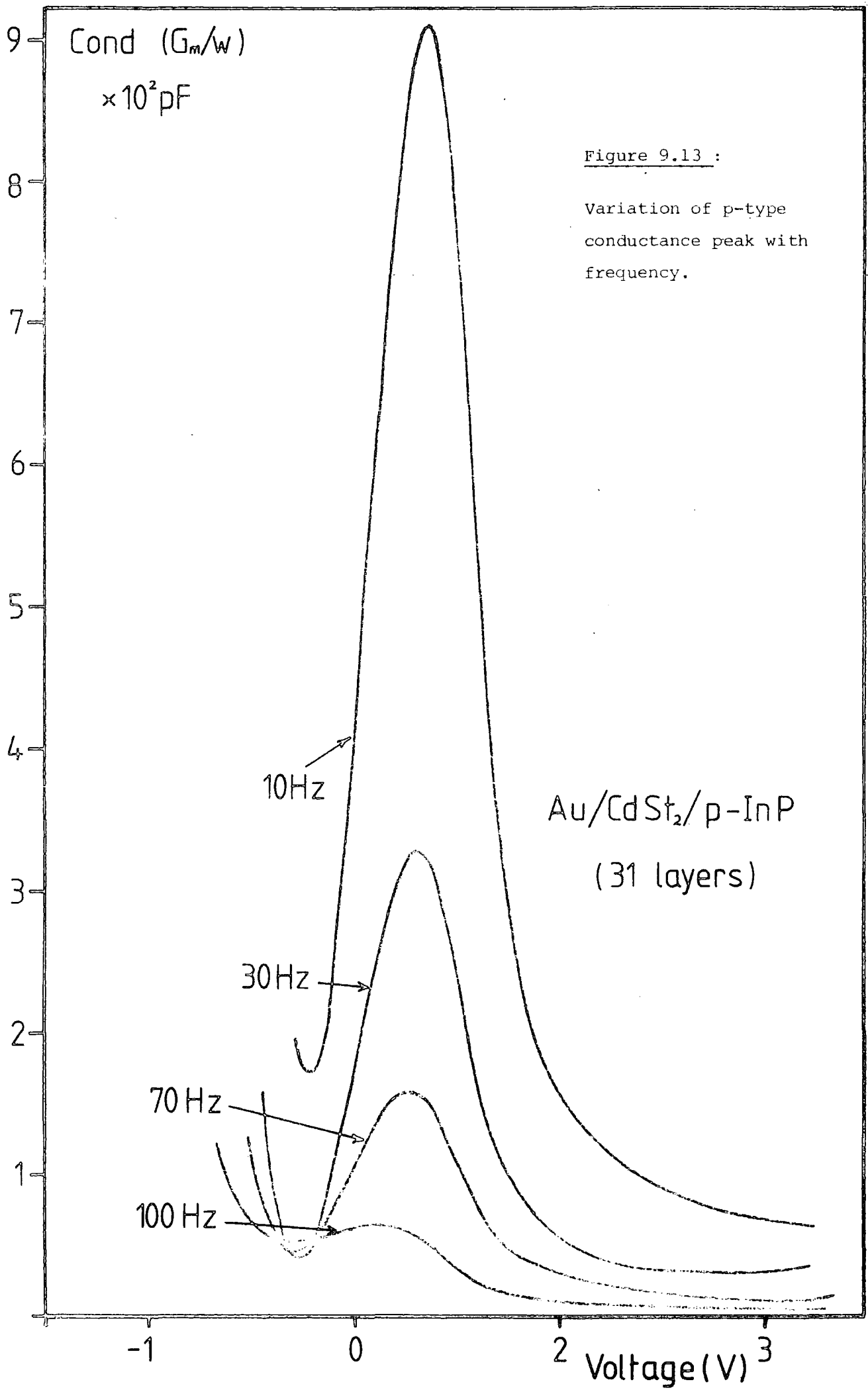
comparatively small, normally only a few hundred millivolts, and was of the opposite sign to that encountered in n-type structures.

The conductance data were flat for both directions of bias and showed no signs of the usually familiar forward bias injection. The "apparent" accumulation capacitance value was found to be frequency and light sensitive, both effects producing increases of about 10%. The application of weak illumination was also found to induce a peak in the conductance data at lower frequencies. This feature however was relatively broad and small in magnitude, it also showed the correct variation with frequency and was thus assumed to be due to surface state effects.

(b) Oxidised Interface

A similar capacitance levelling off in forward bias was noted with bromine-type oxidising etches, but now the curves were much sharper and the change considerably more abrupt. This is shown in Fig. 9.12 along with a C-V plot for GaAs under similar conditions. Also shown in this diagram is a curve obtained for InP by Meiners et al, using SiO<sub>2</sub> as the insulator ; the dominance of inversion at low frequency can clearly be seen. In reverse bias the capacitance fell quickly into depletion but again showed no inversion. The conductance data were found to exhibit no structure in the dark, but illumination produced a much sharper, narrower peak, as shown in Fig.9.13, again likely to be due to surface state effects. In addition, the hysteresis produced by this type of interface was found to be significantly reduced over that for the de-ox type, to the point where it was virtually zero, even at quite high ramp rates (> 50 mV/sec).

As the bias frequency was lowered, the constant plateau capacitance value was found to increase, but by a considerably larger amount, and when low frequency was used together with weak illumination, the C<sub>max</sub> value obtained corresponded well to the calculated C<sub>max</sub>.



From the experience gained on n-type devices, the "optimum" surface preparation approach was used on p-type samples. In this case, however, the improvements noted over the normal "ox"-type characteristics were rather less significant.

#### 9.4.2 Dry Etchant

Both oxygen and hydrogen glow discharge surface preparations were used for the p-type substrates, for a variety of different exposure times. With the oxygen plasma, the results were found to be very similar to those for the normal bromine etches; the hydrogen plasma however produced significant improvement. In this latter case, exposure times of 20 seconds were found to give sharp levelling of the capacitance in forward bias, rapid depletion, and an extremely narrow optically excited conductance peak. In addition, a second frequency independent peak, nearer accumulation was noted on certain occasions, as shown in Fig. 9.14, but as yet this feature is rather irreproducible and may be due to surface conduction effects. Moreover, for the hydrogen plasma interface it was found that the capacitance value could easily be increased to accumulation at significantly higher frequencies than before (under weak illumination).

In general, more notable improvements were produced using hydrogen plasmas for p-type material than were noted with n-type substrates, and in particular the narrowness of the conductance peak suggests a reduction in the width of the band of levels responsible. This effect may well be linked with the different oxide produced by this approach.

#### Summary of the effect of etching upon MIS characteristics

##### (a) N-type MIS

- (i) Using optimised etching, n-type structures show accumulation, depletion and under certain conditions, weak inversion. Strong inversion could only be induced with illumination however.

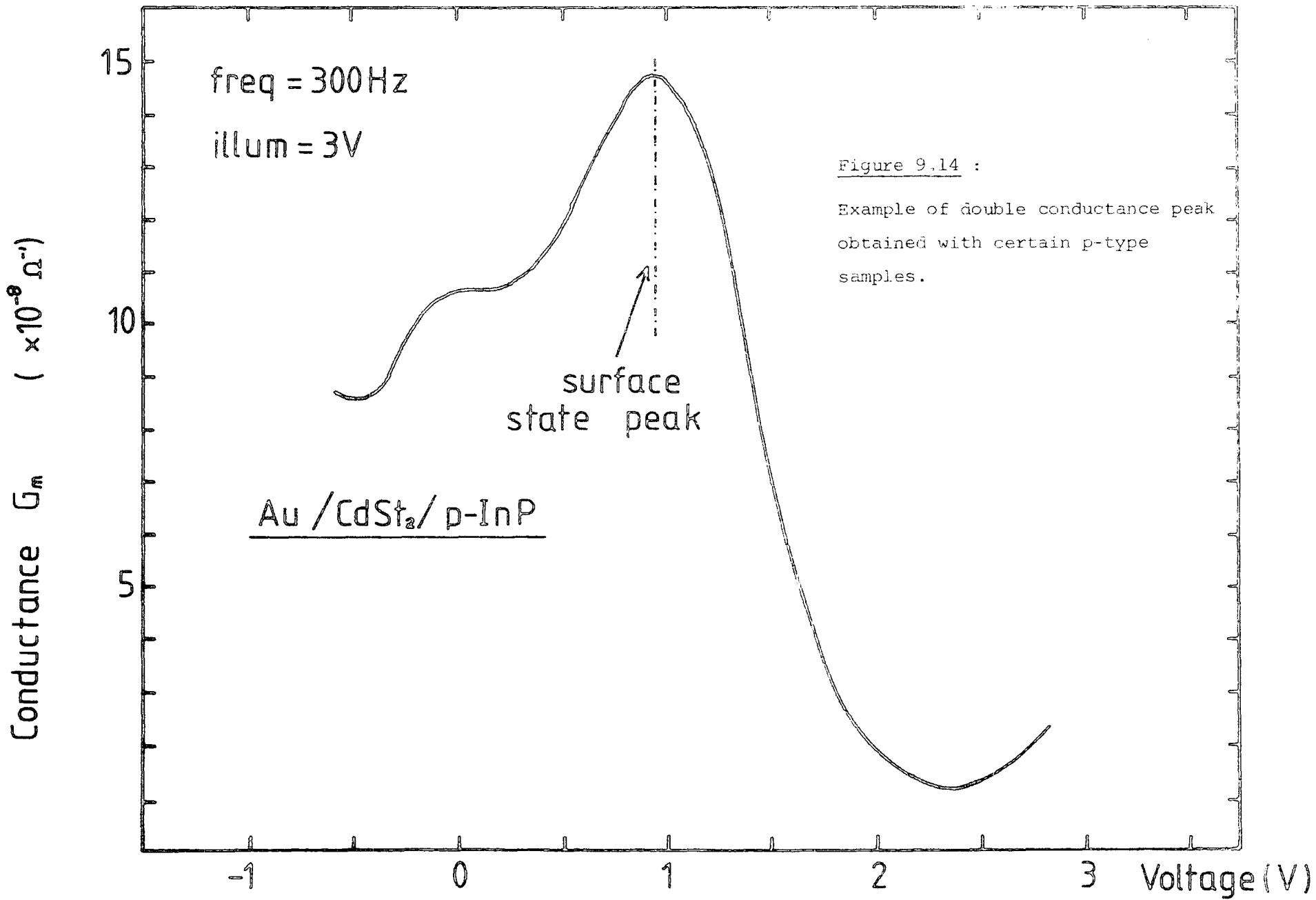


Figure 9.14 :

Example of double conductance peak obtained with certain p-type samples.

(ii) De-oxidised interfaces exhibited large clockwise hysteresis and capacitance levelling off in reverse bias.

(iii) Highly oxidised interfaces showed much less hysteresis, but also showed electron injection in forward bias.

(iv) Dry etching produced only marginal improvement over (i) but was significantly more controllable.

(b) P-type MIS

(i) P-type material could not easily be accumulated or inverted but did however show different characteristics for ox, and de-ox etched interfaces.

(ii) The use of low frequency and weak illumination induced accumulation and a surface state conductance peak with certain interfaces, particularly a hydrogen plasma produced one.

(iii) No forward bias injection of carriers from the semiconductor was observed.

9.5 ADDITIONAL EFFECTS ON InP MIS DEVICES

As well as the semiconductor/insulator interface, it was found that various other features of the device and its environment affected the output characteristics. Some of these effects will now be described, prior to their discussion and explanation in Section 9.5.4.

9.5.1 Series Resistance

Although the majority of characteristics discussed so far have been considered to have virtually flat conductance (in the dark), it was found that in the majority of cases a slight plateau or upward step occurred upon the onset of accumulation. This effect was found to be due to the presence of additional series resistance, as discussed in Section 2.3, of a value calculable from the height of this plateau. The resistances obtained using Equation 2.74 were found to be higher than initially expected, typically  $100\Omega$  for gold top electrodes, and slightly more for lead. These values were



also found to be frequency dependent, increasing markedly at lower frequencies. In addition, the variation in these values from bulk to epitaxial substrates was relatively small.

#### 9.5.2 Electrode Material

Although gold was initially used as the main material for top electrodes, its relatively high melting point significantly increased the chances of thermal damage to the film during the evaporation process. Because of this, a variety of other metals were investigated as potential top electrodes; among these were silver, indium, zinc, lead, aluminium, bismuth, indium/tin alloy (5% Sn by wt), chrome, and gold/germanium alloy (5% Ge by wt). Of these various possibilities it was found that lead in particular gave significant improvement in device characteristics, but it was found necessary to use an additional thin gold overlayer to ease probe contacting.

The use of different top electrode material was found to produce corresponding flat band voltage shifts in both the C-V and G-V curves as shown in Fig. 9.15. These shifts were found to correspond to the material work function differences, as discussed in Chapter 2.

In addition to improving the overall characteristics, the use of Pb top electrodes was found to increase the series resistance and add extra hysteresis above that present with gold alone. On n-type substrates the normal clockwise sense was increased by up to a factor of two, indicating the presence of additional trapping centres, presumable at the electrode-insulator interface. For p-type structures, particularly with the oxidised interface, the effect was more marked as the normal characteristics showed no hysteresis.

#### 9.5.3 Insulator Effects

In the majority of structures where the insulator quality was adequate the accumulation capacitance showed negligible variation with frequency (as discussed in Section 7.2 for MIM structures). Where the film quality was suspect the AC conductance showed significant increase with voltage for both

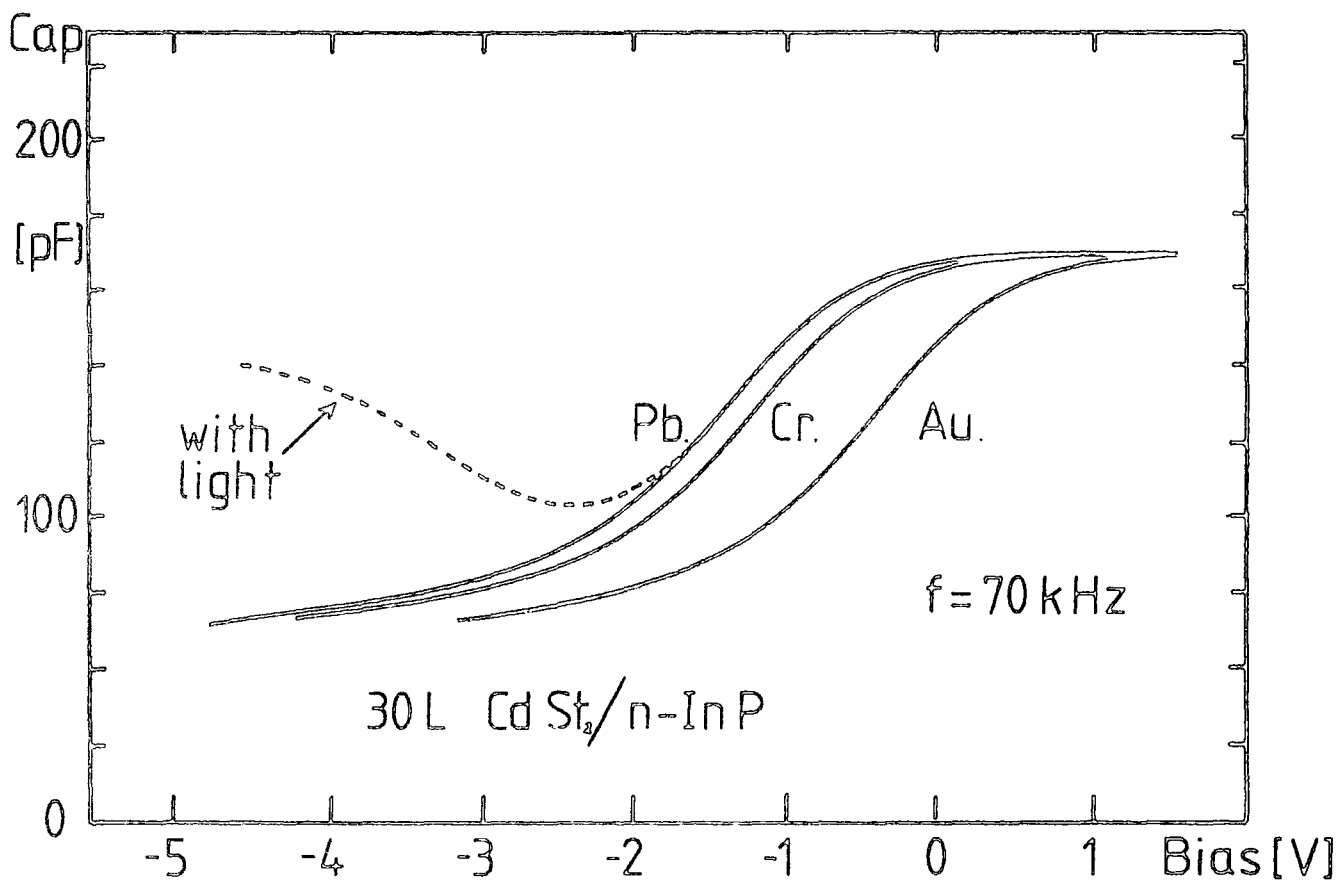


Figure 9.15 : The effect of different electrode materials upon the MIS capacitance curves.

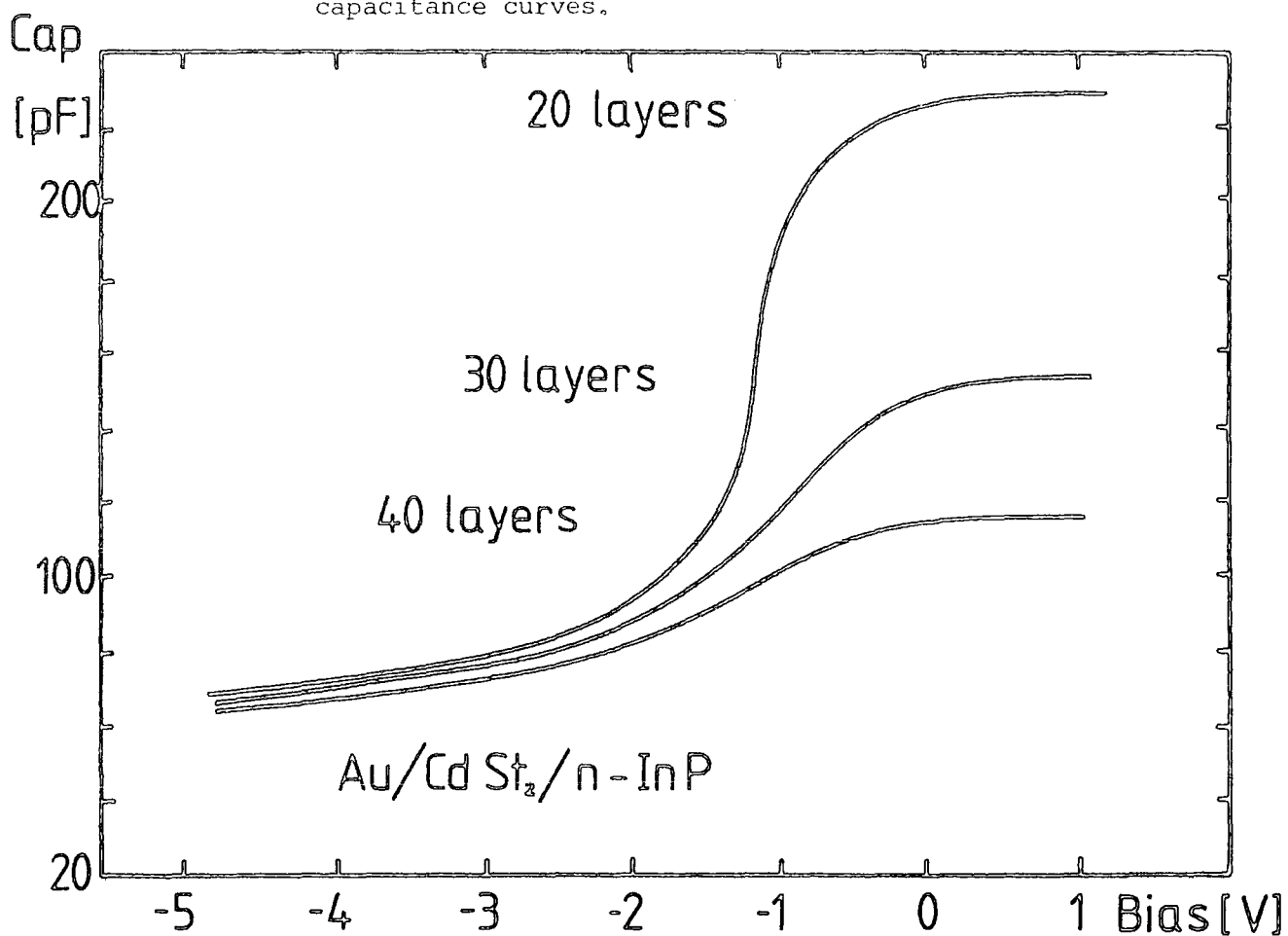


Figure 9.16 : The effect of insulator thickness.

directions of applied bias. In forward bias this effect was more rapid than the normal injection feature noticed with most n-type substrates. In reverse bias it is likely that the formation of a depletion layer buffered the breakdown of the film. These effects were obviously extremely variable, and a whole spectrum of characteristics from Schottky barrier type, to good device, were observed.

The effect of insulator thickness on the device capacitance is shown in Fig. 9.16, where the accumulation value can be seen to scale inversely with a number of monolayers (as discussed in Chapter 7). In addition, the conductance plateau can be seen to be a function of thickness.

During the investigation of MIS devices, it was found that the characteristics could be markedly improved by annealing the structure after fabrication. The temperatures required were quite low due to the melting point of stearic acid being  $\sim 380$  K, and the values finally used were obtained rather empirically by using increases of 1 K and testing the device between each 12hr anneal. Typical results of this process are shown in Fig. 9.17, where it can be seen that an initially de-oxidised interface exhibits gradually reduced hysteresis. This is probably due to the increased mobility of the film enhancing ion motion and removing usually mobile charge into interface trapping centres. At higher temperatures, the advantages of the process become outweighed by the onset of injection effects. In practice, although this was an interesting way of improving de-ox characteristics, better results could be obtained by other approaches, and in consequence the effect was rarely utilized.

Before concluding this section, it is perhaps worth noting a significant long term effect observed with the majority of Langmuir film structures. This was the definite improvement in characteristics from all aspects, over a period of months rather than weeks or days, and makes an interesting contrast to normal long term degradation effects. These improvements, particularly in breakdown field strength, and injection problems were probably due to a very slow drying

Capacitance (pF)

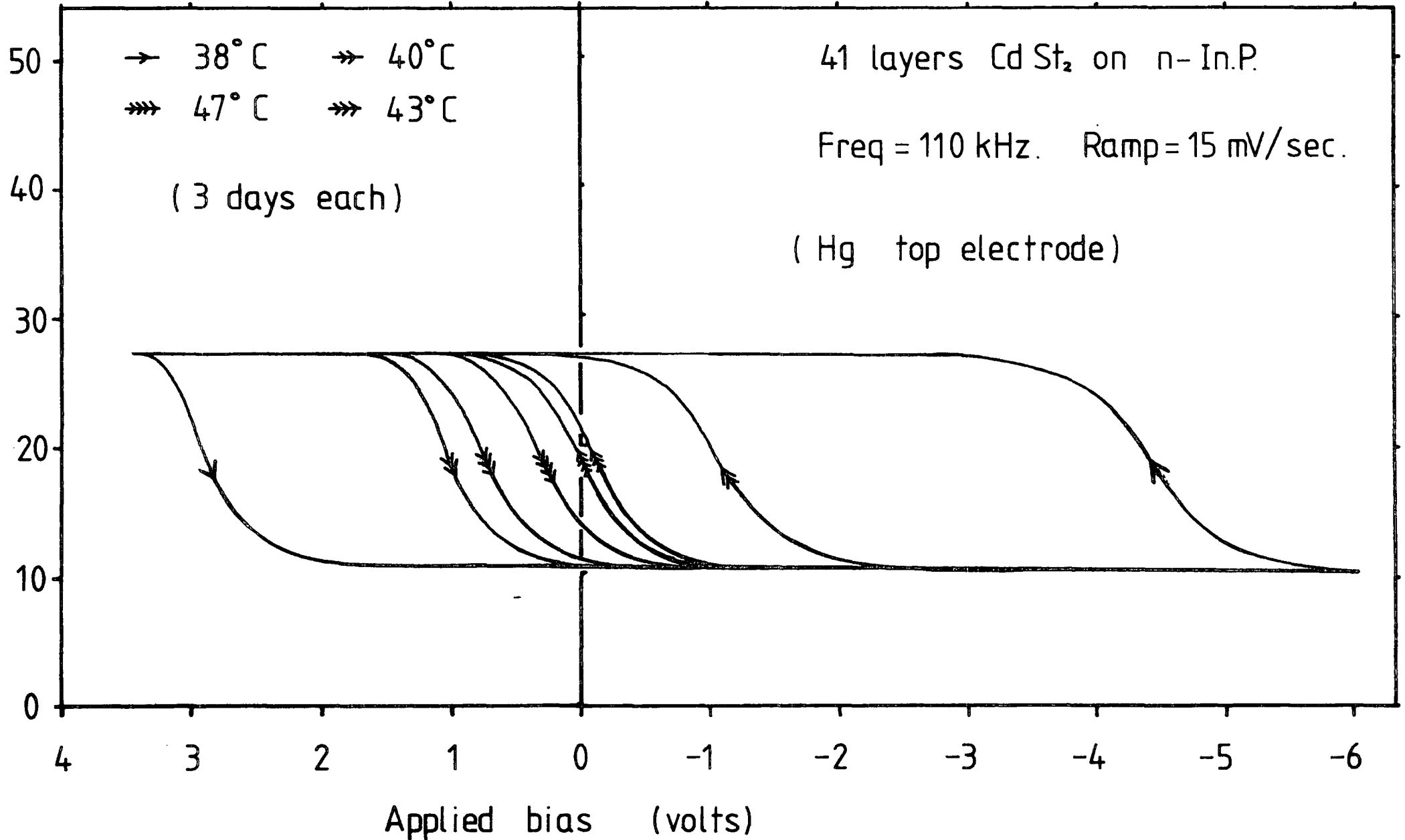


Figure 9.17 : The effect of low temperature annealing upon capacitance data.

out of the film, as the normally tightly bonded water molecules (between the hydrophilic ends) were slowly removed by the desiccation. This effect obviously requires further investigation.

#### 9.5.4 Discussion of Additional Effects

By bringing together various results presented previously it is possible to explain the majority of the additional effects discussed in this section.

##### (a) Series Resistance

From the results obtained on both bulk and epitaxial Schottky barriers, where the series resistance compensation values were only a few Ohms, it can be deduced that the anomalously high resistance values produced by MIS devices do not originate in the substrate or the back contact. Equally, the use of Pb top electrodes although affecting  $R_S$  cannot account for the large value. In view of these points it can be concluded that the semiconductor/insulator interface, and particularly the first one or two monolayers of Langmuir film are the likely origin. Moreover, the frequency dependence of the effect, and the evidence from  $1/C : N$  plots can be seen to reinforce this conclusion. From this argument it appears that the first few monolayers are rather more conducting than the rest of the insulator thereby requiring a slight adjustment of the original equivalent circuit given in Fig. 2.12. This modified version, shown in Fig. 9.18, has additional capacitance and resistance components between the insulator and the semiconductor, to represent this new interface region.

From this circuit, given that  $C_I < C_L$ , and  $G_I \ll G_L$ , simple analysis can be used to show that the equivalent admittance will be dominated by  $C_I$  and  $G_L$ . Moreover, the other series conductance values  $G_E$  and  $G_S$  will add linearly to the  $G_L$  and the circuit will follow the observed device behaviour.

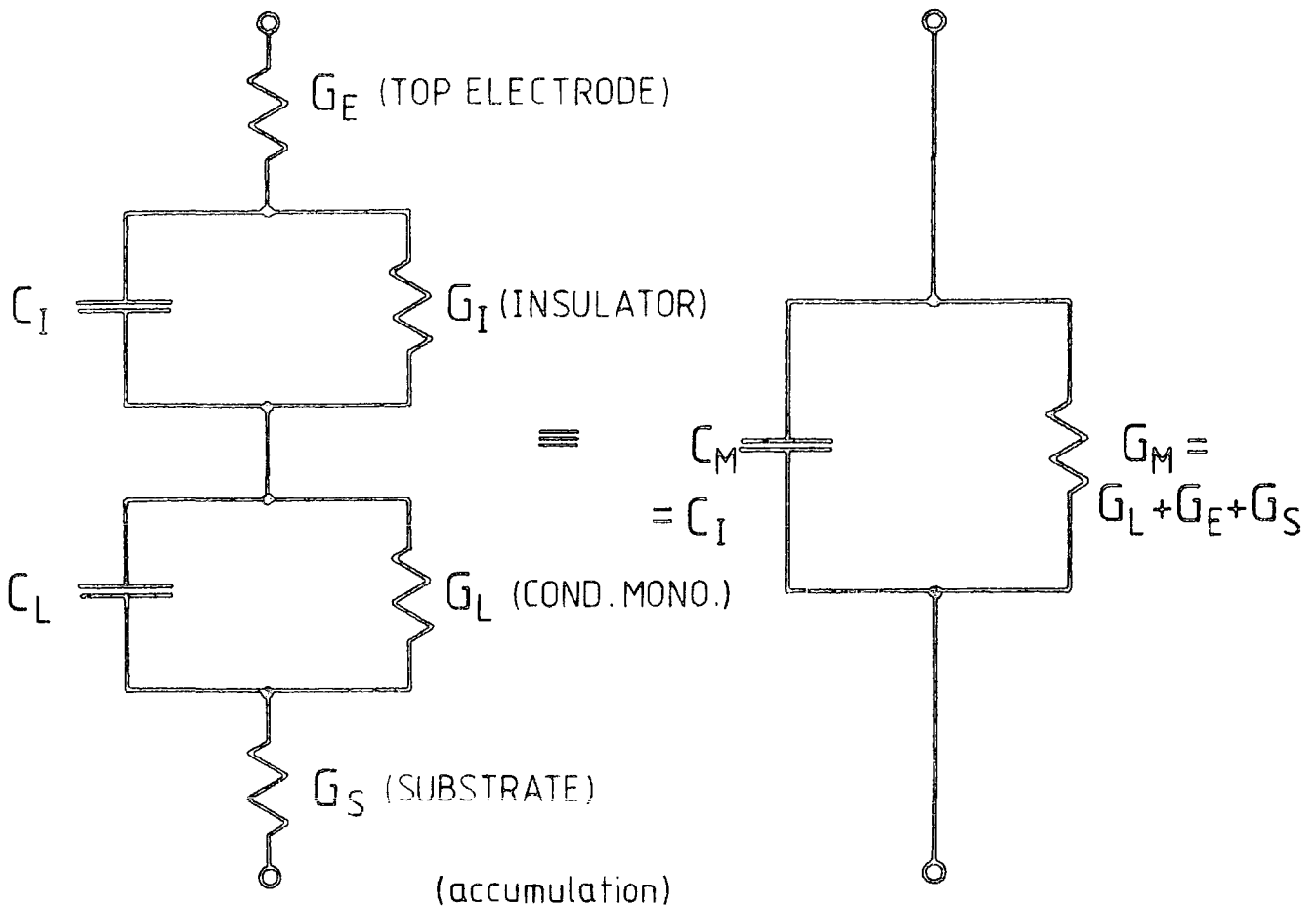


Figure 9.18 : Device equivalent circuit, incorporating conducting first monolayer.

It should of course be noted that as this interfacial effect only involves the first monolayer, the total capacitance ( $C_I$ ) will vary little from that initially calculated for the given film thickness, and thus will not significantly change any other characteristics of the device.

(b) Hysteresis and Charge Injection

From the results presented, it is clear that electron injection plays a very important role in many of the device effects observed. This injection is normally induced by the presence of an oxide layer, and it is apparent that the structure and thickness of the layers are important in defining the magnitude of the current. With a de-oxidised interface, the lack of oxide

appears to remove the injection problem, but also leads to a very abrupt interface and a high density of trapping sites. These states are responsible for the significant amounts of clockwise hysteresis noted. At the opposite extreme, the presence of an interfacial oxide passivates the surface states, but leads to considerable injection. In fact, this effect is also observed with the Si/SiO<sub>2</sub> system, where a layer of highly doped SiO<sub>2</sub> is used to aid current injection into the insulating area of an MIS or FET structure<sup>(7)</sup>. Between these two extremes of interface structure, the use of a thin oxide layer appears to lead to more satisfactory characteristics, and indeed under certain conditions weak inversion can be produced with n-type materials.

With the p-type substrates, the lack of large hysteresis or injection are merely further verification of the electron injection effects discussed earlier. Moreover, in the absence of the normally dominant trapping hysteresis, the effect of ion motion in the organic insulator (a phenomenon frequently observed by most workers using Langmuir films) is manifest in the presence of clockwise hysteresis, as described in Chapter 2.

#### (c) Device Reproducibility

In addition to the specific effects caused by various etches and other influences it was observed that a degree of irreproducibility existed from sample to sample, particularly for epitaxial grown RSRE samples. This was manifest in the device characteristics being generally closer to the optimum for certain older substrates. This effect has been observed by all workers using InP from RSRE for whatever purpose, particularly for microwave devices, and until now has remained unexplained. Recent exhaustive investigations<sup>(8)</sup> have however correlated this step change in material with the use of a new epitaxial growth reactor, and a change of material supplier. The extent of these effects is still under investigation but it is now thought that one of the major symptoms was the reduction in density of a bulk (impurity) level

located at  $\sim 0.1$  eV below the conduction band. The direct effect of this variation on MIS devices is equally not yet known, but it is likely that the movement of the Fermi level with  $V_g$  would be affected, and this in turn would directly influence the onset of accumulation and inversion. Indeed, certain very early n-type substrates have been observed to give a conductance peak<sup>(9)</sup>; a feature never observed during this work.

It is clear that further investigation of these effects is required in order to clarify this variability within epitaxial samples, and to this end RSRE are now attempting to reproduce the properties observed in these earlier samples. In addition, it should be noted that bulk samples of both n and p type, due to their origin from a single boule did not show any of these effects.

Before going on to discuss the location of the surface states in the InP band gap, it is important to explain the lack of surface state peak in the majority of the data presented here. In Chapter 2, the use of the conductance peak to obtain  $N_{ss}$  data was discussed at some length, and indeed this approach is quite valid. However, the lack of such a peak does not directly imply the absence of surface states, it merely reflects the inadequacies of the conductance technique, and in particular the limited range of the band gap over which it can measure ( $E_g \pm 0.3$  eV). Because of this, it is likely that the states responsible for the effects discussed are near the band edges, and are thus accessible only to a technique with a wider range of measurement, for example DLTS (see Chapter 2).

## 9.6 DISCUSSION OF FERMI LEVEL PINNING

In this section the MIS results obtained by the author are discussed in detail and compared to models proposed by other workers. From this comparison, it is clear that some modifications are required to explain the effects observed. N and p type materials are considered separately, but



the final section attempts to correlate the individual explanations and so present an unified model for the band gap of InP.

#### 9.6.1 N-Type Material

From the various MIS work carried out in recent years, using high temperature insulator deposition processes, the overall device behaviour has led to the proposition of two dominant trapping levels in the upper half of the band gap, as discussed previously in Chapter 8. The existence of these levels has been further verified by Spicer et al, by work on vacuum cleaned<sup>(110)</sup> surfaces. In these cases however the reference to two discrete levels is rather idealised, and it is likely that atmospheric exposure will broaden these levels into narrow bands 0.1 - 0.2 eV in depth.

From the "high temperature" characteristics, it can be seen that the lack of capacitance inversion under all conditions suggests the dominance of the upper (1.2 eV) band in restricting the downward movement of the Fermi level. Because of this, the lower level has no direct effect upon the characteristics. By contrast, although also showing accumulation and depletion, MIS devices using the low temperature Langmuir film also exhibit deep depletion, and under certain conditions, inversion, suggesting considerably greater freedom of movement at the Fermi level. In this situation, it is likely that the top level although undoubtedly still present, is much reduced in density, thereby allowing the Fermi level to move through to the lower level, and sometimes beyond.

It is generally agreed that the upper level or band is due to a phosphorus deficiency on the InP surface, the loss of which is enhanced by high temperature. Because of this, it is proposed that the majority of previous MIS work, most of which required substrate heating and sputter deposition, or some similar high energy process, inevitably led to surface damage, phosphorus loss, and thus the dominance of the 1.2 eV band. By

contrast, under carefully controlled conditions, the use of Langmuir films, (or indeed any other passive process) is proposed to virtually remove the upper level. Moreover, the occurrence of inversion, and the characteristics in general, because of their etch dependence, suggest that the lower level (which now controls the Fermi level freedom of movement), is not only rather broad, but is also controlled mainly by the surface chemistry. In consequence, it is very etch dependent.

The resultant model for the gap of n-type InP, based on these propositions is given in Fig. 9.19, along with the various corresponding C-V curves suggested to result from high and low energy deposition processes.

#### 9.6.2 P-Type Material

For p-type substrates, the contrast between the high temperature/energy deposition processes, and Langmuir films is even more significant. Once again, the model proposed by Spicer suggests two levels in virtually the same position as for n-type material, but now the extrinsic Fermi level is in the lower half of the band gap and the effect of these levels will be somewhat different.

The results obtained by the majority of workers show the surface normally inverted with little motion of the Fermi level available as a function of bias. This observation is consistent with the idea of surface damage and phosphorus loss as a high density of levels at the 1.2 eV band would produce this inversion pinning phenomenon. Here again, the lower level or indeed any other levels within the gap cannot be explored with devices prepared in this manner. By contrast, the results described previously for Langmuir film structures show no pinning in inversion, indeed the Fermi level appears free to move within the lower band gap region. The location and effect of the other level however seems less well defined and although it is somewhat etch dependent, the lack of inversion suggests that to date its density has not been reduced sufficiently. In addition, its influence must extend below

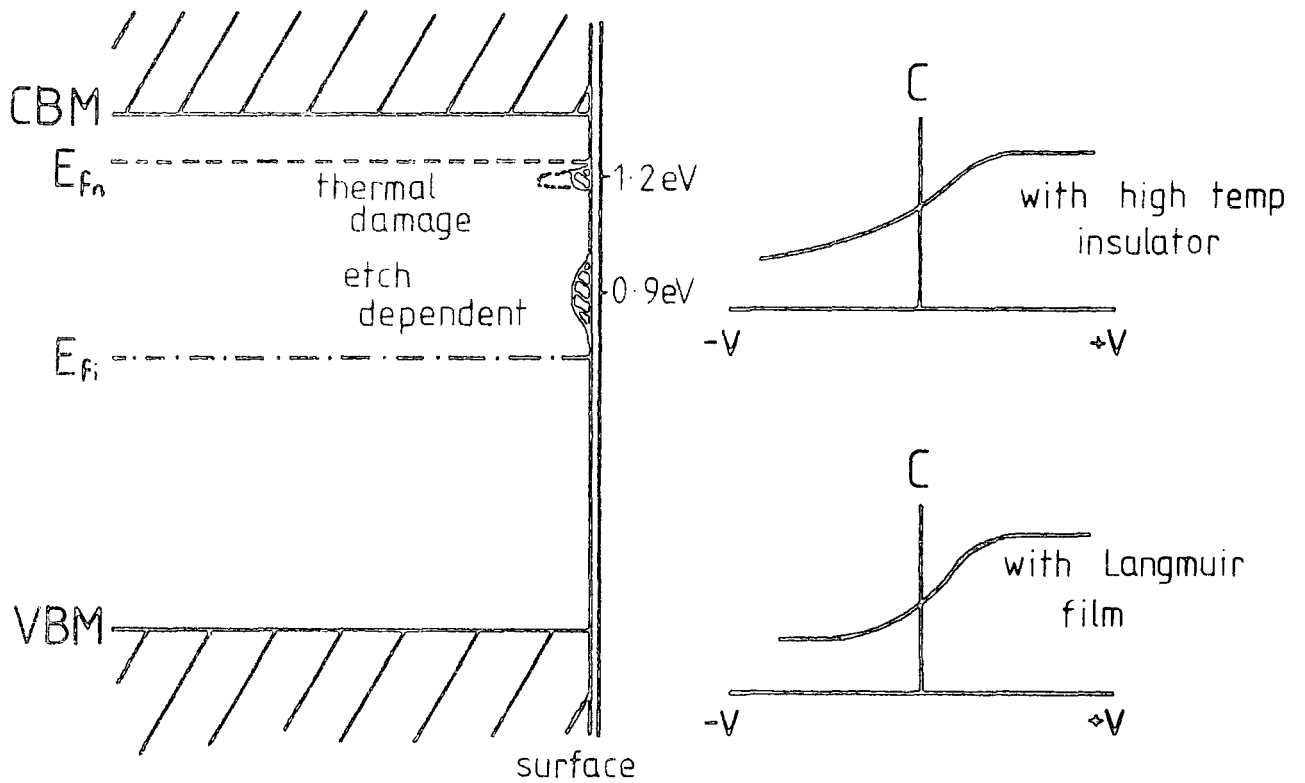


Figure 9.19 : Model for band gap of n-type InP.

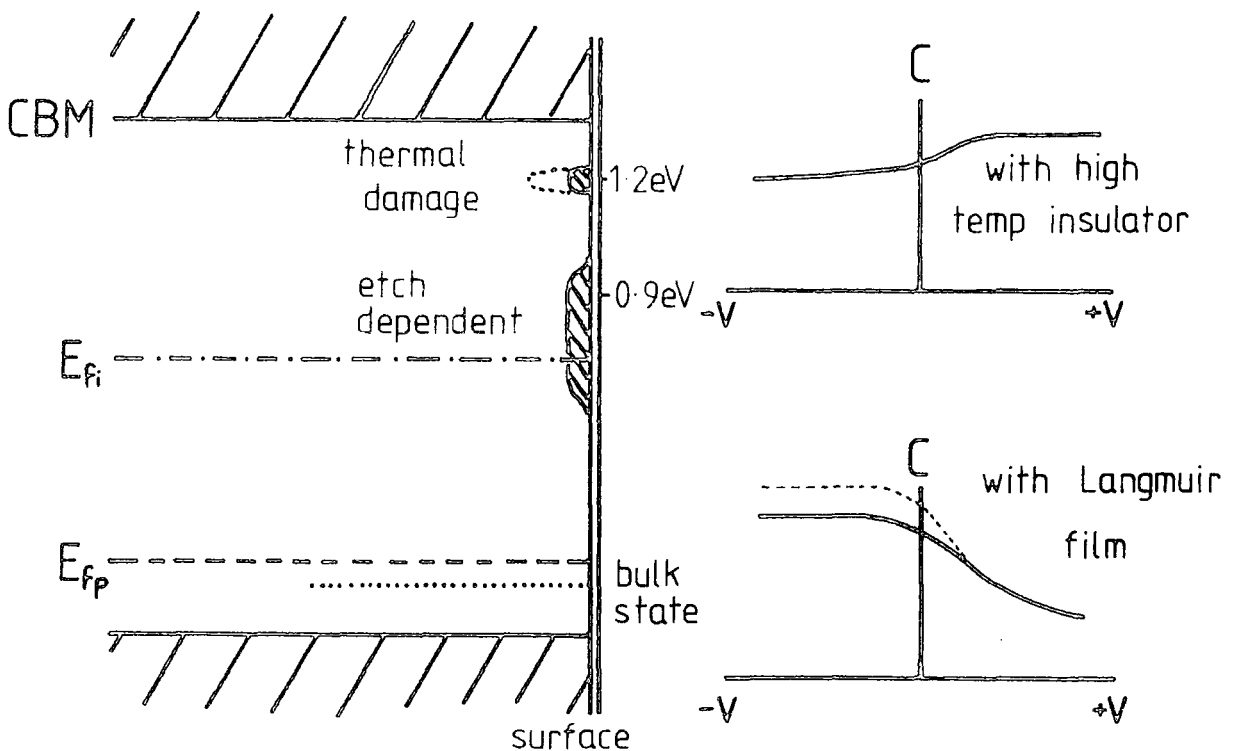


Figure 9.20 : Model for band gap of p-type InP.

the intrinsic Fermi level position in order to adequately explain the observed characteristics, and the optically excited  $G_m$  peak.

From the data presented, it is apparent that a further level (or band) exists slightly above the valence band, which generates Fermi level pinning below accumulation. The presence of this level is not totally surprising in view of the p-type nature of the material and the bulk levels normally produced by p-type dopants. It is however not possible to be more specific at this stage.

A summary diagram of these effects and the resultant band gap structure is given in Figure 9.20, together with schematic C-V curves demonstrating how the removal of certain of these levels will drastically affect the output data.

#### 9.6.3 Unified Band Gap Model: Summary

From the previous two sections, it can be seen that many of the arguments presented apply equally well to both p and n-type material. Because of this it is possible to propose a single model that will account for the majority of features observed.

The level slightly below the conduction band due mainly to surface damage and phosphorus loss is dominant for high energy temperature deposition approaches in both material types, its density is however considerably reduced by the use of a low temperature deposition process. The lower level is likely to be a broad band of states reaching below the intrinsic Fermi level, and of density dependent mainly upon surface preparation. In addition, with p-type samples, (and probably with n-type as well), there exists a narrow band of levels slightly above the valence band, likely to be associated with the extrinsic acceptor levels, and only observed in C-V measurements when the 1.2 eV level is not dominant. This proposed unified model is shown in Fig.9.21.

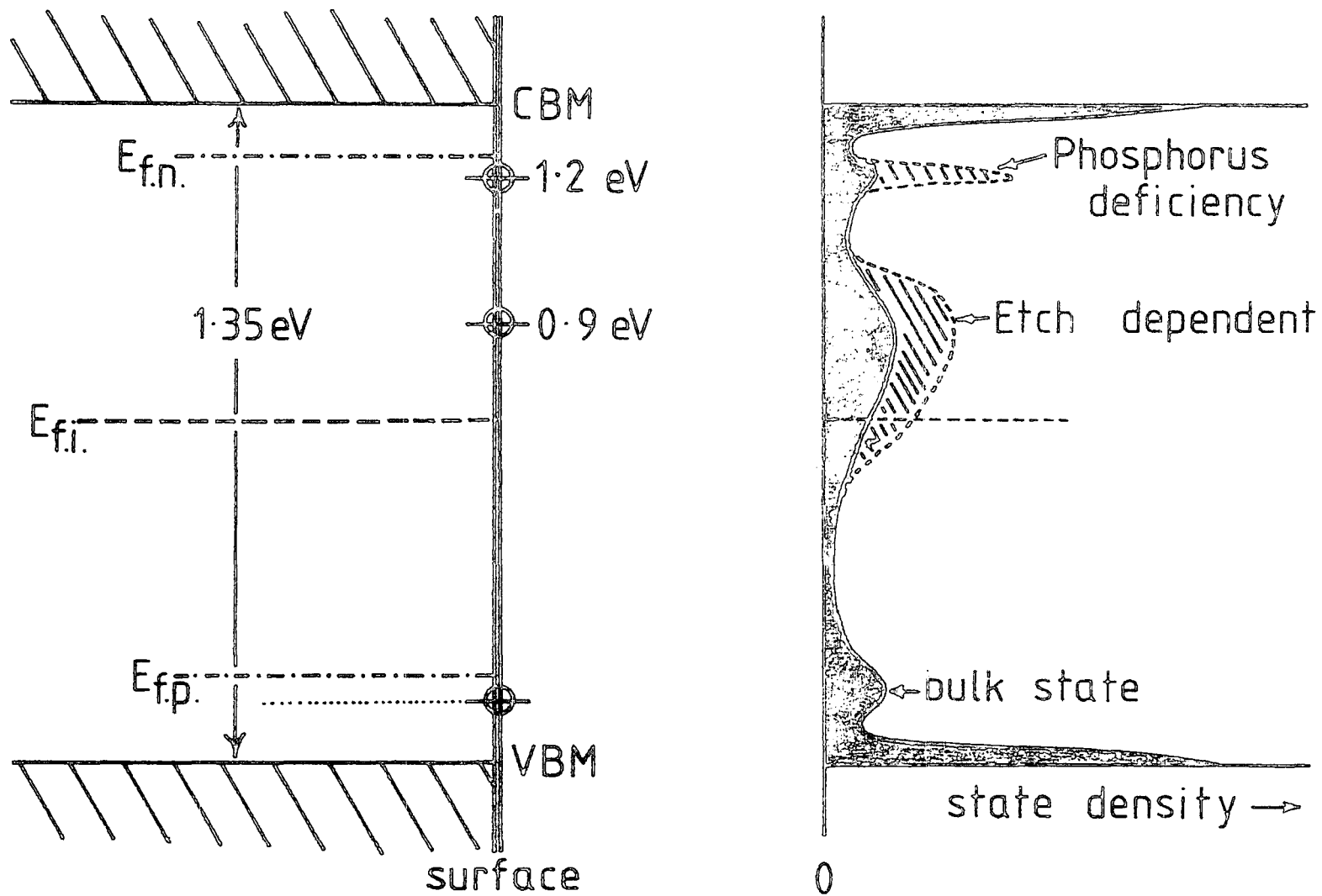


Figure 9.21 : Unified model for InP band gap.

In general, it is clear from both Schottky barrier and MIS work that the interface plays a crucial role in defining the characteristics of InP (and probably all other  $\text{III-V}$ ) devices. It is also apparent that damage of any kind, resulting from either insulator or metal deposition can lead to problems with Fermi level pinning.

From the results presented, it can be concluded that the use of a low temperature insulator deposition process avoids many of these effects. It is clear, therefore, that this type of approach together with further optimisation of the final surface preparation holds significant promise for improved device performance in the near future.

## CHAPTER 10

### GAS EFFECTS ON MIS DEVICES

The majority of this thesis has given details of the fabrication and characterisation of a novel MIS system. It is logical therefore to look at ways in which to capitalise upon the properties of this device.

In the field of gas detection, the majority of portable instrumentation is not only very bulky, but is rather empirical in design and operation. Because of this, any development of a compact, highly sensitive system cannot fail to be extremely useful. It is possible that the properties of the InP/Langmuir film system : its highly porous insulator, and its very sensitive interface region, may present an excellent vehicle for gas detection. In this application not only do the possibilities of top electrode and bulk insulator effects present themselves, but also the concept of contaminant gases inducing characteristic "fingerprint" changes upon the surface state spectrum, which would enable excellent selectivity to be achieved.

This chapter presents the results of a necessarily limited investigation into the effect of certain selected gases upon the characteristics of InP MIS devices.

#### 10.1 INTRODUCTION TO GAS DETECTION

##### (a) Possible areas of influence

When considering gas effects upon the MIS system it is possible to divide the device into three basic areas, the top electrode, the insulator, and the interface region. In each case the influence of a gas will result in a defined change in the device characteristics. Given that the electrode is thin enough to allow gas diffusion, let us first assume that the contaminant species only reaches the metal/insulator interface. In this case

additional charge will be introduced into the system and will result in a flat band voltage or work function shift of the device characteristics. The simple nature of this shift together with the rapid activation and recovery (due to the simple nature of the effect) enables its easy distinction from slower more complex bulk and interface effects.

If the gas enters the bulk of the insulator its dipole moment will change the dielectric constant of the material ( $\epsilon_r$ ). This will change the accumulation capacitance of the device ( $C_I$ ), thereby moving the experimental curve along the vertical axis. The effect here is largely dependent upon the chemical structure of the gas molecule, which defines its dipole moment and diffusion coefficient. In general however because of the relative thickness of the insulator, the effect may involve slightly longer response times.

The third area of influence, the semiconductor interface region, is by far the most complex, and indeed the most promising, if useful selectivity is to be achieved. From Chapter 2, it can be seen that the interface is composed of a variety of dangling bonds, trapping centres, surface charge etc., all contributing to extra levels in the band gap of the material. These surface states are normally modelled by additional components in the device equivalent circuit and are characterised most accurately by plotting the variation in the conductance peak ( $G_m$ ), or more precisely the parallel conductance peak ( $G_p$ ), with frequency and applied bias. Thus any effect upon these surface states caused by the introduction of a contaminant gas will be manifest not only in a change in the final surface state spectrum ( $N_{ss}$ ), but also in variation in the  $G_p$  peak. Moreover, although the  $G_p$  curve more accurately reflects the surface state density, the conversion from  $G_m$  to  $G_p$  is a simple rescaling process and therefore any variation of  $G_m$ , independent of capacitance, can be taken as originating at the interface.



Examples of each of these individual effects, together with other more complex interactions will be presented and discussed later in this chapter.

(b) Measurement techniques

Because of device hysteresis, continuous cycling (at 100 mV/sec) was used to establish a quasi-equilibrium and allow changes in device characteristics to be observed (see Chapter 3). In addition, because the p-type devices showed no accumulation, and the n-type devices no conductance peak, it was necessary to duplicate each gas exposure to enable both capacitance and conductance changes to be monitored.

At this stage of the investigation, selectivity rather than sensitivity was considered to be the most important criterion, as the latter could easily be greatly increased by the use of an FET type structure. Because of this, emphasis was placed upon looking for different effects by using a variety of gases, rather than employing smaller concentrations of only a few. The various vapours and gases used were as follows : 5% carbon monoxide, 40% hydrogen, dilute ammonia solution, and various organic vapours, all with nitrogen as a carrier. For these materials, a Dreschel bottle of calcium chloride was used as a desiccant prior to exposure, when required. During gas introduction, very small flow rates were used to avoid any cooling or damage effects, these rates were normally between 0.05 and 0.5 cm<sup>3</sup>/sec.

In general, although the majority of effects were quite rapid, cycling was continued over many days to repeat and identify the variety of changes occurring. These effects were recorded by continuous replotting of the admittance data.

10.2 TOP ELECTRODE EFFECTS

(a) The hydrogen-palladium effect

The simplest top electrode effect is peculiar to the hydrogen-palladium system, whereby molecular hydrogen, upon diffusing through the electrode is broken down into individual atoms which are thought to reside in a slightly

polarized manner at the metal-insulator interface. This additional positive charge produces a lateral (flat band) voltage shift in the capacitance curve.

The hydrogen effect has been the subject of considerable investigation upon the MOS (Si/SiO<sub>2</sub>/Pd) system, primarily by Lundstrom et al<sup>(1)</sup>, and the reproducible nature of the interaction forms the basis of a commercial hydrogen detector. There has been some dispute as to the precise location of the interaction, for while Lundstrom et al have maintained the idea of a flat band voltage electrode effect, work by Keramati and Zemel<sup>(2)</sup> led to the proposal of a surface state effect caused by the diffusion of the atomic hydrogen to the semiconductor interface. Recent detailed studies of the effect<sup>(3)</sup>, together with the now well established non-porous nature of SiO<sub>2</sub> seem to verify the electrode argument, although the possibility of a surface state effect as well cannot be totally dismissed.

In order to further investigate this effect, the porous nature of the Langmuir film was used incorporated in a Pd/Langmuir film/InP structure. The influence of hydrogen upon the device characteristics is illustrated in Fig. 10.1, where the expected lateral shift of the capacitance curve can be seen. It was found that the response time was rapid and the saturation displacement of ~ 600 mV (due to mutual repulsion between the disassociated atoms) was achieved in 20-30 seconds. No independent variation of the conductance peak was observed however, suggesting that either the hydrogen did not reach the interface (rather unlikely) or that its presence produced no significant disruption of the InP surface. Thus the existence of merely a capacitance displacement of 600 mV, virtually identical to that observed for the Si/SiO<sub>2</sub> system, can be concluded to reinforce the proposal of dipoles residing under the metal electrode.

#### (b) The effect of water vapour

For the majority of samples studied it was found that the presence of water vapour induced a lateral shift in both capacitance and conductance curves

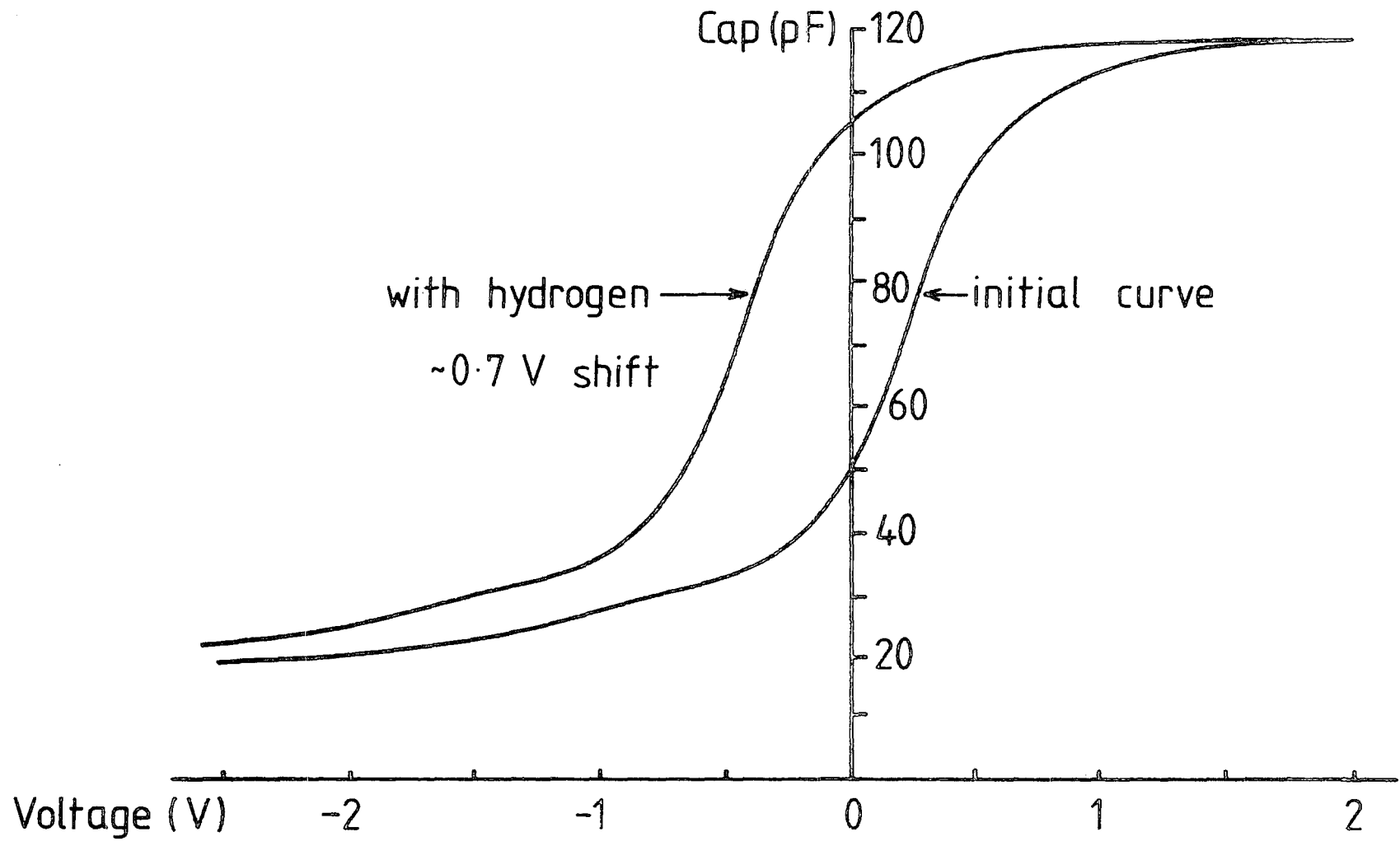


Figure 10.1 : The effect of hydrogen upon the Pd/Langmuir film/InP system.

as shown in Fig. 10.2. This shift, inevitably towards a positive voltage, was found to be symptomatic of the addition of an overall negative charge. The effect, when taken with the lack of any corresponding  $C_I$  variation, was concluded to indicate the interaction of water molecules with the insulator carboxyl(COOH) groups, resulting in an effective change of surface charge. This lateral shift was found to be quite reversible and was thus superimposed over any additional effect when wet gases were used. As with the hydrogen, there was found to exist a maximum displacement, in this case of about 1.0 V. In addition, the application of large amounts of water, for example by bubbling nitrogen through water before exposure, was found to result in surface condensation and the production of a lateral conduction channel. This caused marked changes in the device characteristics, drastically increasing the capacitance (due to effective area increase) and occasionally producing a lateral conduction  $G_m$  peak. These effects were also reversible, and in all cases it was found that the use of a purposely dried gas significantly increased the rate of recovery.

### 10.3 INSULATOR EFFECTS

In most cases, little or no variation in accumulation capacitance as a function of gas exposure was noticed. This lack of effect suggests that, in the quantities used, the gases could not significantly influence the already polar material. The one exception to this result was carbon monoxide, which, with prolonged exposure did result in a slight increase in capacitance ( $\sim 10\%$ ). Moreover, further investigation showed the process to be more complex, as initially a decrease was recorded over the first few minutes of exposure, and the increase only occurred after several minutes. Although not investigated in detail, it is apparent that the highly polar nature of carbon monoxide is the main reason for the overall effect, and that an early re-arrangement of the absorbed molecules takes place as diffusion progresses.

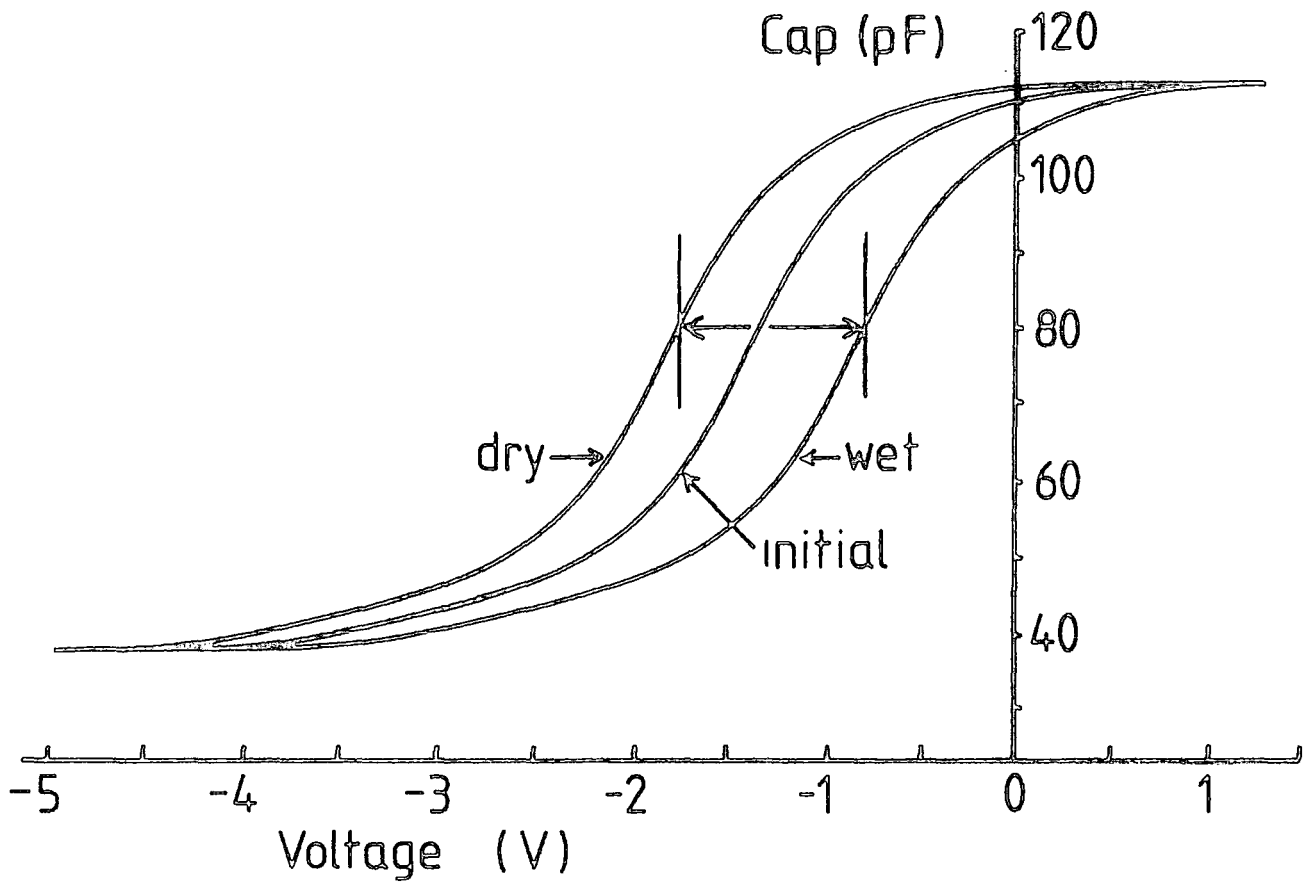


Figure 10.2 : The effect of water vapour.

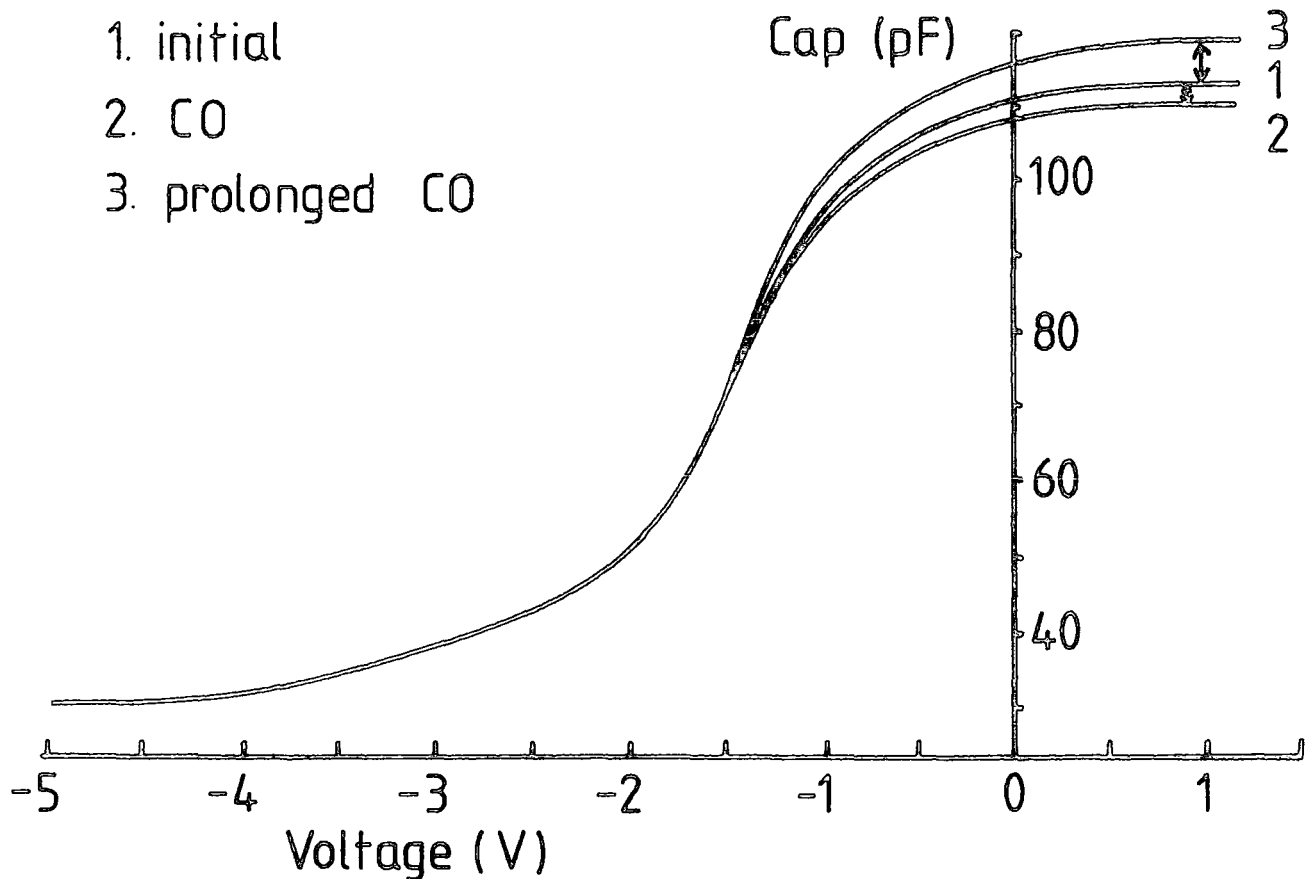


Figure 10.3 : The effect of carbon monoxide.

For the remaining gases, the lack of effect is not altogether surprising as the removal of water immediately after film deposition has earlier been shown to not significantly affect the bulk properties of the film. The effect of carbon monoxide exposure upon the capacitance curve of an MIS device is shown in Fig. 10.3.

#### 10.4 INTERFACE EFFECTS

As discussed earlier, although not quantitative, independent variation of the  $G_m$  peak as a function of gas exposure can be taken to indicate surface state effects. Of the various gases used, two significant interactions were observed.

##### (a) Ammonia

The effect of ammonia was by far the most promising, and is almost certainly due to an influence at the semiconductor interface. It was found that dried ammonia vapour produced a shift in the capacitance curve towards a positive voltage, up to a maximum of 750 mV before rapid degradation occurred. By contrast, the conductance peak was displaced in the opposite direction, and significantly decreased in magnitude, as shown in Fig. 10.4. In both cases the effect was reversible provided small concentrations were used. Thus by implication the  $G_p$  peak would be moved independently of the capacitance curve and an effect is likely to have occurred at the interface. In addition, the slow response of this process, especially the recovery, which could take many hours, is consistent with the idea of the formation of a chemical complex or some other interaction at the interface.

##### (b) Chloroform and other organic vapours

Because of their behaviour as solvents for stearic acid (but not Cd stearate), these materials were expected to result in quite drastic changes to the device and its characteristics. In practice, however, for small exposures, no visible structural or electrical degradation was produced, apart from some significant reversible gas effects.

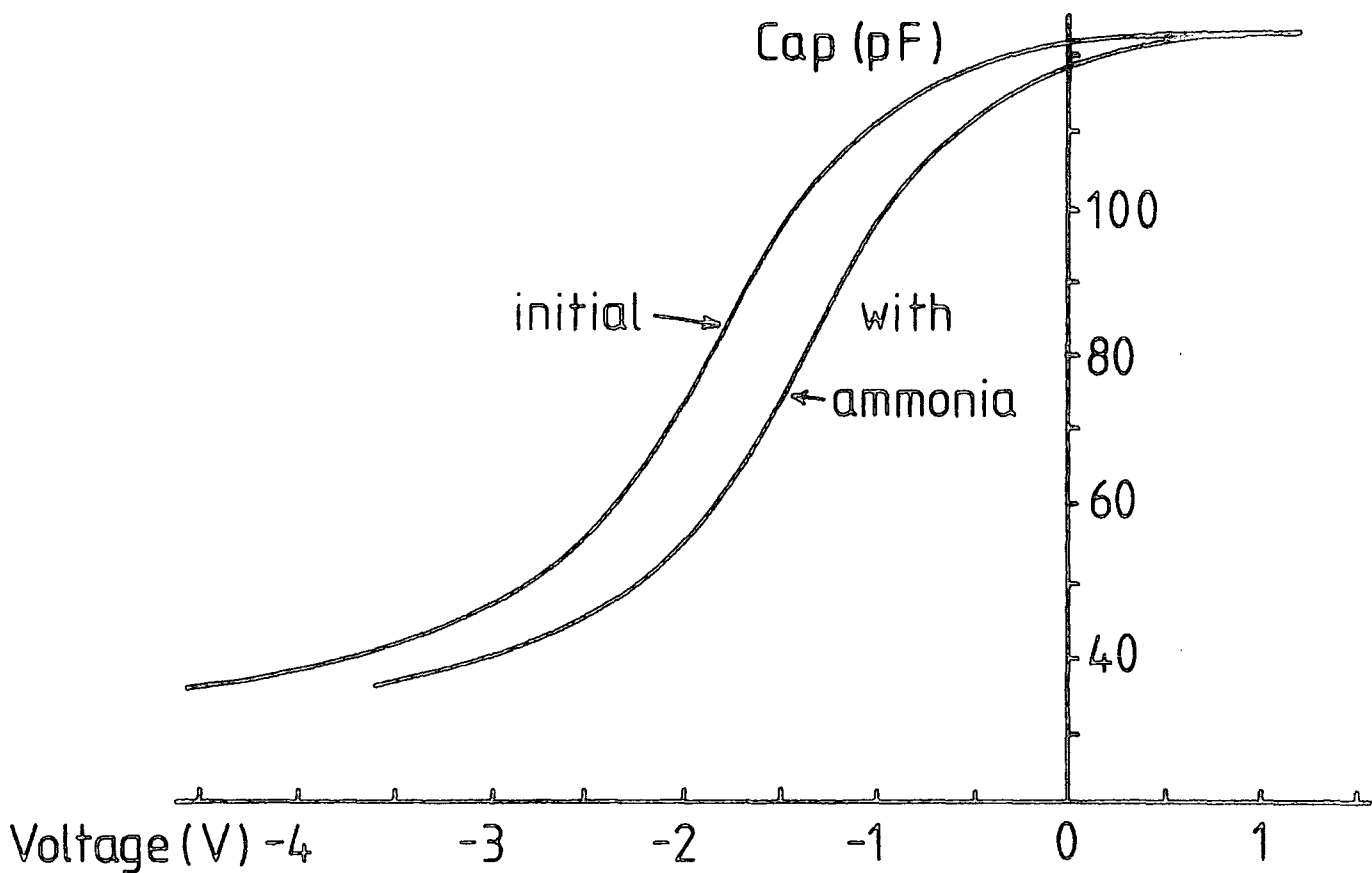
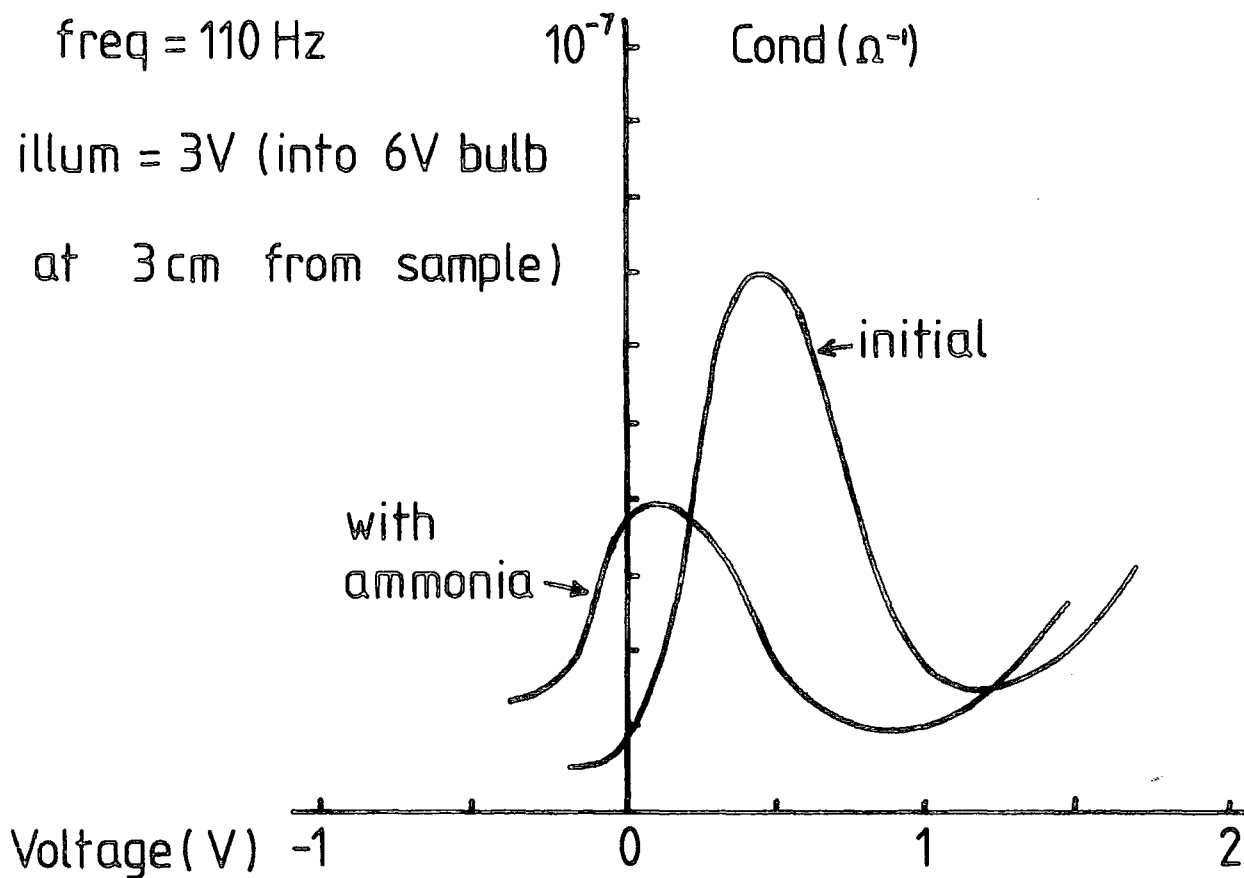


Figure 10.4 : The effect of dilute ammonia upon the capacitance and conductance curves.



For these materials, a rapid shift of both capacitance and conductance towards a positive bias were observed, together with the eventual disappearance of the  $G_m$  peak, as shown in Fig. 10.5. In addition, although the capacitance shift corresponded to a water vapour effect, the conductance variation suggested a considerably more complex interaction with the decrease in peak height implying an interface effect.

#### 10.5 SUMMARY OF EFFECTS

From the results presented in previous sections, it is possible to derive a more collective picture of the various interactions.

- (i) It is likely that water vapour interchange with the insulator is one of the major influences upon device characteristics ; considerable further investigation of this effect is thus required before more sensitive gas effects can be demonstrated.
- (ii) Carbon monoxide produces changes in the insulator dielectric constant due to its extremely high dipole moment.
- (iii) Ammonia vapour is likely to diffuse through the film and reside at the interface, thereby producing changes in the surface state spectrum.
- (iv) Chloroform and various other relatively large organic molecules also appear to give interface effects, however their behaviour as solvents for stearic acid casts doubt upon the precise origin of this effect.
- (v) The use of palladium top electrodes enables the production of lateral shifts in capacitance due to hydrogen. No corresponding surface state influence is observed however.

Although many interesting effects are present, it can be seen that only a limited number involve interface variations and surface state changes. This fact is initially surprising in view of the sensitive nature of InP. In practice, however, these results merely reflect the shortcomings of the conductance approach which can only examine a limited range of the band gap. Because



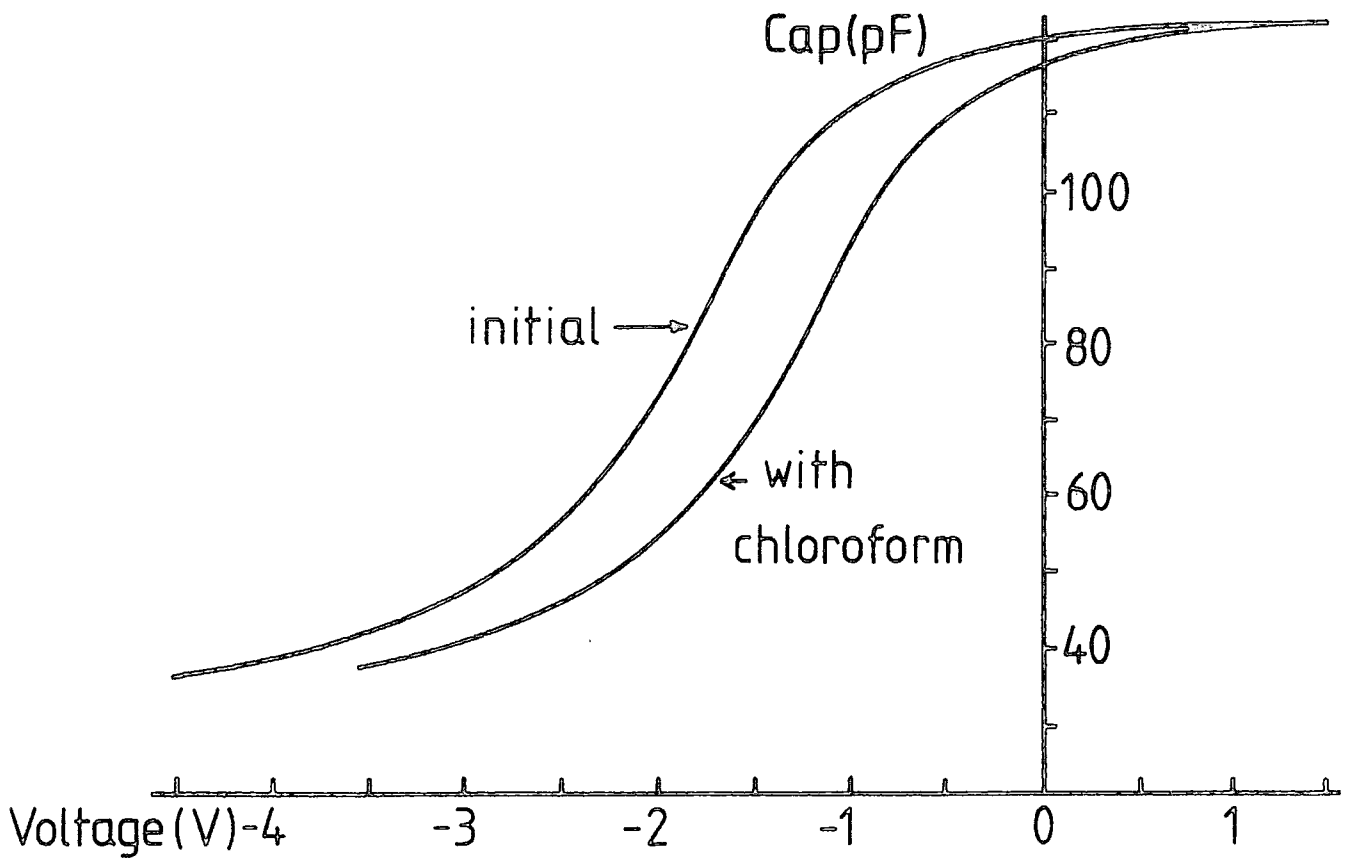
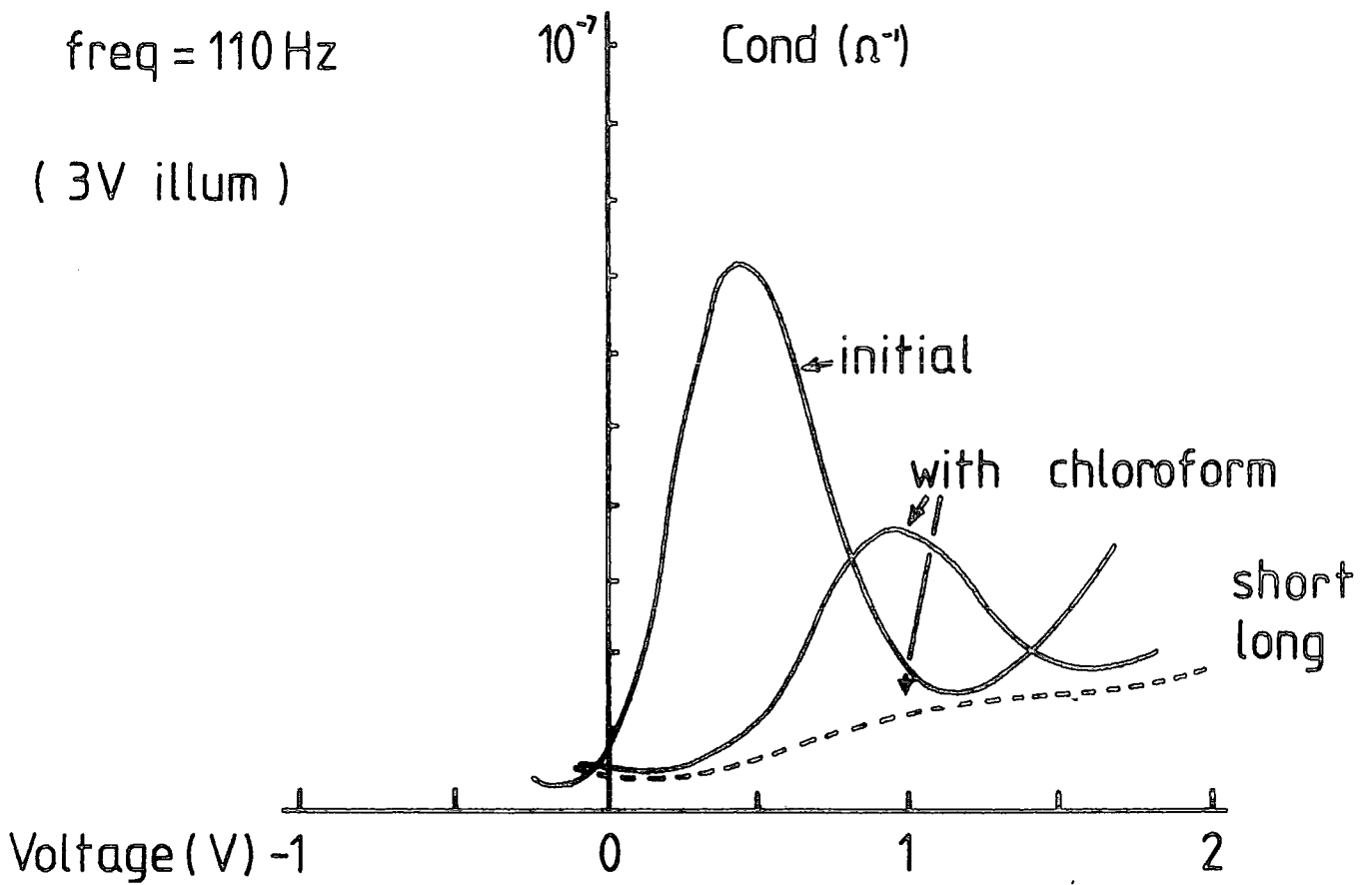


Figure 10.5 : The effect of organic solvent.



of this, many of the bulk effects may actually have associated interface effects, but upon surface states nearer the band edges. To clarify these points is rather difficult with the capacitance/conductance technique, and it is therefore necessary to use alternative means to totally scan the band gap (for example DLTS ; see Chapter 2).

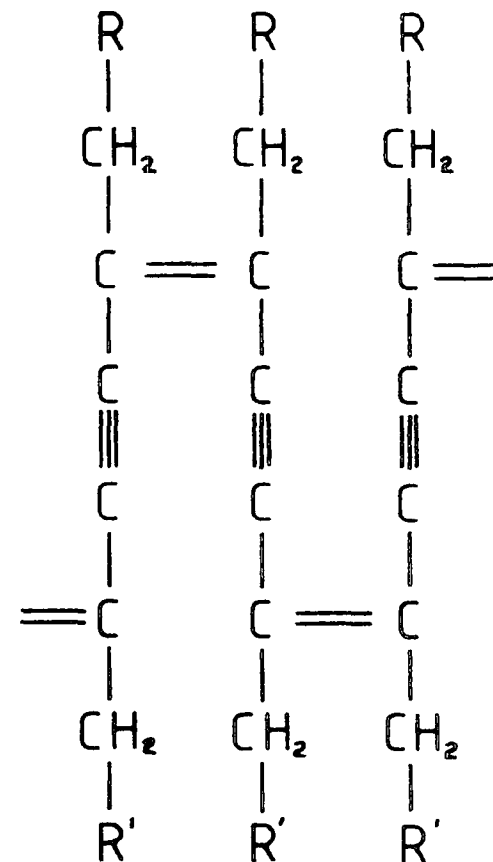
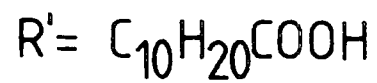
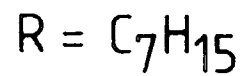
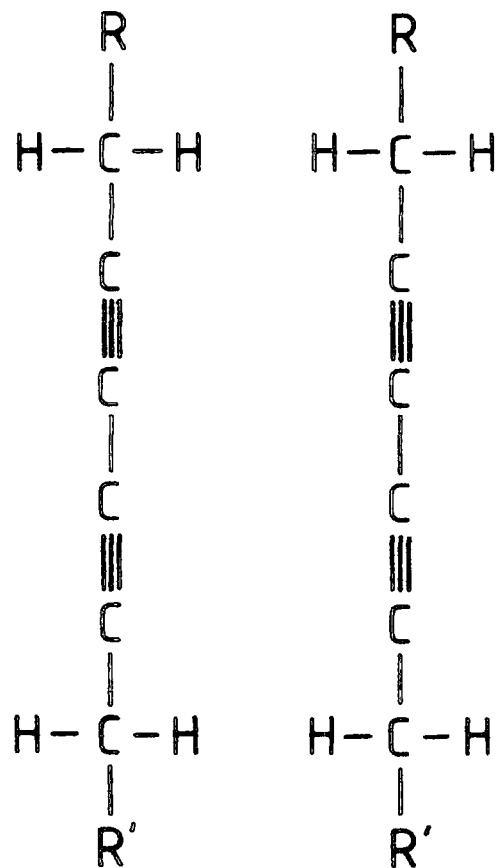
## 10.6 SUGGESTIONS FOR FURTHER DEVELOPMENT

Although it is apparent that a variety of interesting gas effects exist upon the InP/Cd stearate MIS system, there are certain shortcomings of the structure which obviously limit further development. To overcome these problems investigations have been carried out, and are currently continuing upon various improved MIS systems.

### 10.6.1 Polymeric Insulators

Stearic acid, although now well characterised, and ideal for Langmuir film deposition is relatively unstable, both thermally and structurally. In consequence, although usable under controlled conditions it is rather unsatisfactory for future development. Recent activity has therefore concentrated upon producing an improved material without sacrificing any of the advantages of this long chain open structure. One particularly promising material is diacetylene, a u.v. polymerizable organic compound, to which various long chain carbon hydrophobic and hydrophilic groups can be attached. The resulting amphipathic material can be deposited by the Langmuir-Blodgett process in a similar fashion to stearic acid (at a slightly higher pH) and once built up can be cross polymerized by u.v. exposure, as shown in Fig.10.6. The final film, considerably more stable than stearic acid, has been demonstrated to show MIS characteristics virtually identical to those for stearic acid<sup>(4)</sup>, as shown in Fig.10.7, and by contrast with most polymeric materials shows virtually no hysteresis.

Because of these encouraging results, further work is currently underway to produce and investigate derivatives of diacetylene with other long chain



MONOMER

POLYMER

**Figure 10.6 :** Diagrammatic representation of (12-8) diacetylene monomer, and after uv polymerisation.

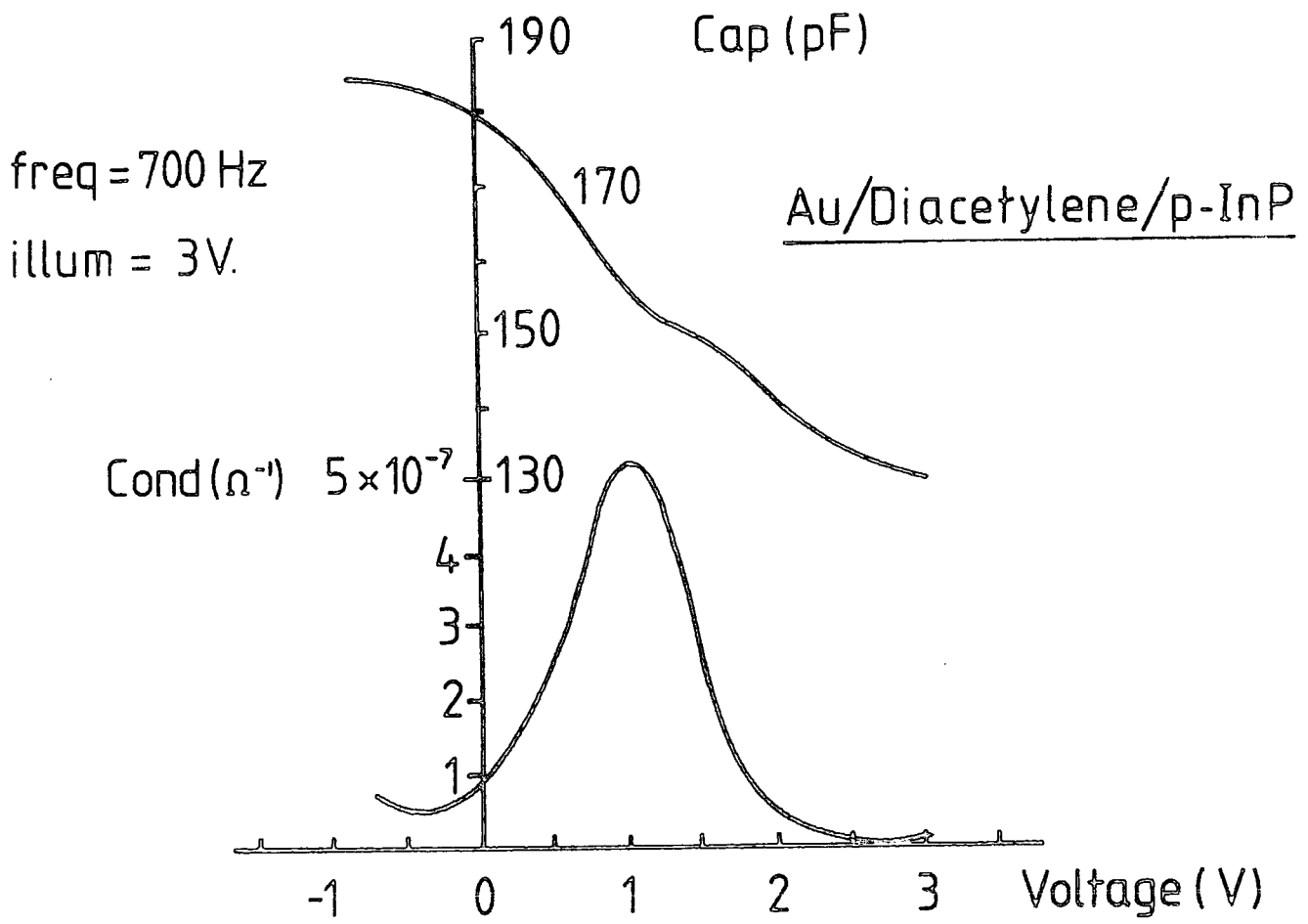


Figure 10.7 : Device characteristics for the diacetylene/InP system.

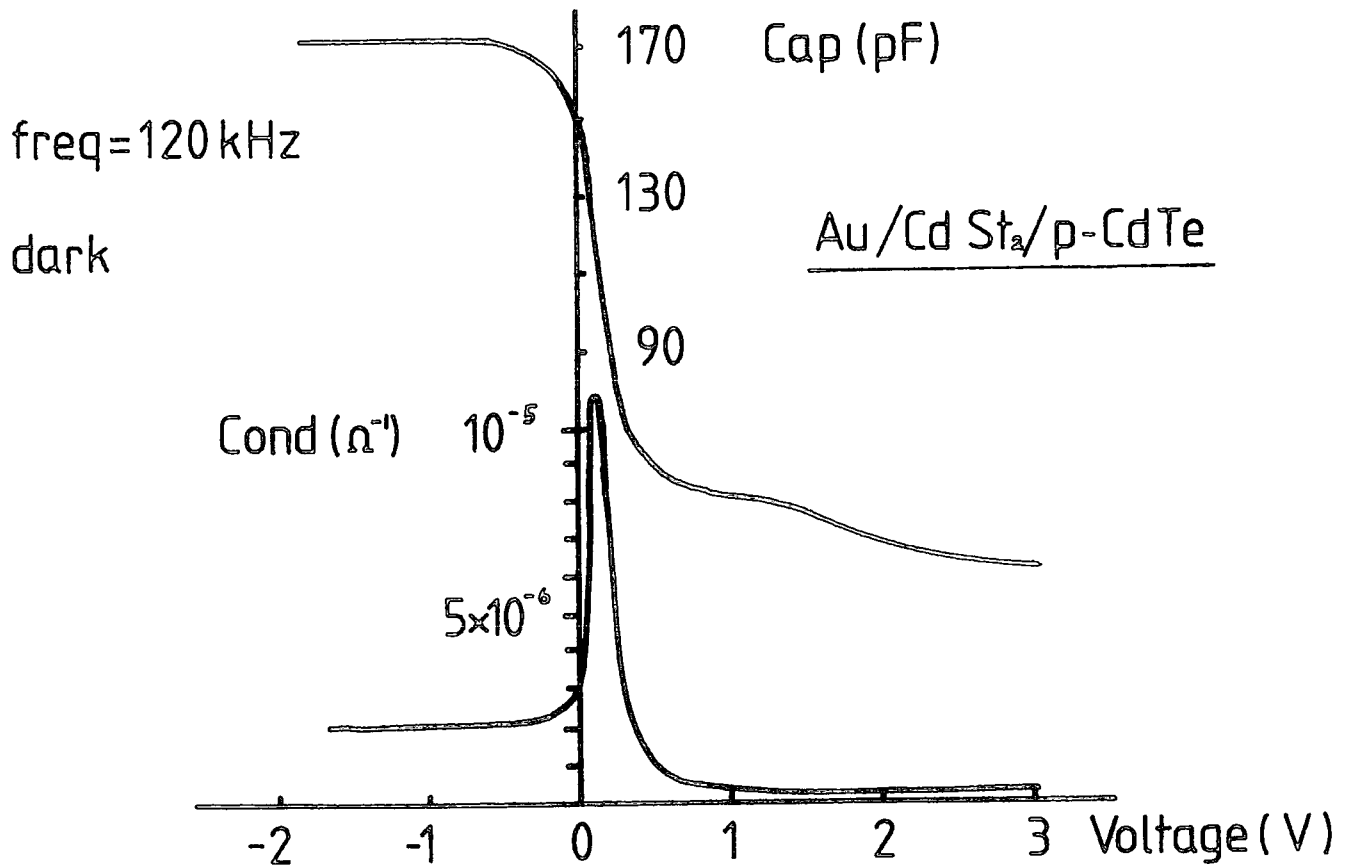


Figure 10.8 : Device characteristics for the CdSt<sub>2</sub>/CdTe system.

groups, which will exhibit even better stability, and melting points over 500 K.

#### 10.6.2 Other Semiconductor Substrates

Until more investigation has been carried out to overcome the interface preparation problems encountered with InP (as discussed in Chapter 9), the lack of an equilibrium conductance peak within the range of measurement available makes detailed analysis of the effect of a gas rather difficult. In view of this, it may well be advantageous to turn to other semiconductor substrates which have either states in the measurable band gap, or will allow the production of a surface state peak as a result of gas exposure. In practice, this latter possibility is potentially the most useful as it is likely that each gas would induce only characteristic states, and when used with specific insulators would allow a very sensitive and selective structure to be made.

Investigation is already underway into the former type of structures, and various studies of other systems are also being attempted in order to find the correct combination of semiconductor and insulator, that will allow this "induced state" type of device to be realised. For the former type of device two substrate materials have been considered, the preliminary results obtained will now be discussed.

##### (a) Silicon

Detailed studies of the Si/SiO<sub>2</sub> system<sup>(3)</sup> have largely concluded that the insulator is non-porous, thereby making it unsuitable for any application in gas detection. However, investigation is underway to utilise freshly etched (HF) silicon as a base for Langmuir films, and thus for more useful MIS structures. At present, difficulty is being encountered in depositing the insulator in a reproducible fashion; a problem thought to originate in the chemical structure of the silicon surface. It is likely however that a detailed characterisation of the effect of various etches upon this surface will produce sufficient variation to enable adequate deposition to be achieved.

Moreover, investigation is also underway to produce a double dielectric structure, which has an organic insulator deposited upon a thin porous layer of  $\text{SiO}_2$ . With this device, the oxide is used to passivate the silicon surface and define a low surface state density. In addition, however, if suitably thin, the oxide remains porous, and when used with a Langmuir film, will result in a device with low hysteresis and good behaviour (defined by the  $\text{Si}/\text{SiO}_2$  interface), but with considerably easier access to the interface for gases. It is also possible that this double dielectric structure will exhibit some memory effects similar to those seen with the  $\text{SiO}_2/\text{Si}_3\text{N}_4$  system, and may therefore be useful as an accumulative sensing system.

(b) Cadmium Telluride

Investigations of the cadmium telluride-Langmuir film MIS system have revealed the presence of near ideal characteristics<sup>(5)</sup>, as shown in Figure 10.8, with good accumulation, weak inversion, and the existence of a narrow surface state conductance peak. Moreover, the surface oxide, largely  $\text{TeO}_2$  appears well suited to the deposition of Langmuir films, yet adequately sensitive to variations in preparation. Preliminary studies of gas effects upon this system have shown certain similarities to the ones noted for InP, with respect to capacitance and conductance variation. Further work is required to enable analysis of the associated surface state spectrum variation and thus reveal the full potential of the system. It should be noted, however, that the growth of CdTe is presently in its infancy and thus not only is the material in very short supply, but considerable variation of properties from sample to sample largely prohibits the further investigation of this potentially very useful system. It is likely however, that the near future will see an easing of this situation.

10.6.3 Long Term Developments

As work upon the variety of novel Langmuir film materials progresses, it is anticipated that a wide range of FET type gas sensors will be produced. These devices will work by surface state effects, by insulator effects, or even

by a combination of the two. In the former case (as already discussed), the insulator material prefilters the gas in order to enhance the selectivity of the structure. This function will be achieved by the use of skeletonized films or by the use of hybrid mixtures of more than one monolayer material. The major selectivity will result from surface state interactions, whereby monitoring of the  $N_{ss}$  spectrum will allow the recognition of both contaminant type and quantity. Indeed, it is possible that the use of control electronics will allow the device to be programmed by changing the local cross-section of the spectrum examined or by using an electric field to remotely vary the prefilter pore size.

With the insulator based structure, the incorporation of sensitising molecules into the film will allow it to react to only one species. In this situation, the substrate interface will be less critical and the control electronics virtually non-existent. This will make the device considerably cheaper to produce, but will make it applicable to only one contaminant species. The use of piezo and pyro-electric polymeric materials (currently under development at Durham) within device structures can also be categorized into the second group of sensors. In this case however, selectivity will be produced by the gate electrode which will absorb only the desired species, and the film and semiconductor will be used merely to register its presence.

The areas of application of these various sensing structures in both industry and research are obviously many-fold, and as toxicity limits are reduced, and personal monitoring becomes mandatory the use of this type of small portable detector will become even more widespread.

It is also anticipated that these structures will be used with liquid ambients, to monitor solutes and various other dilute or undesirable material. In this area, model membranes and multilayer protein structures are already being used to simulate biological behaviour, and are being incorporated into FET devices to examine immunological and enzyme reactions (see Chapter 4).

Moreover, these membranes when used with organic rather than inorganic semiconductors could be implanted in the body with no rejection problems, and thus could be used to monitor indefinitely specific organ functions.

In general, it can be seen that the potential of this type of device is quite significant, and that given adequate development of both the specialised Langmuir film structures, and the semiconductor substrate materials, there is no fundamental reason why a wide range of Langmuir film-solid state sensors will not become available over the next few years.



CHAPTER 11

SUMMARY AND CONCLUSIONS

To facilitate the use of organic insulators within a variety of device structures, a sophisticated Langmuir trough system has been designed and built. After detailed commissioning, this apparatus has been applied to the characterisation of the indium phosphide-Langmuir film MIS structure.

In this work, the effects of various wet and dry etches upon both the chemical surface and the device electrical characteristics have been investigated. This is believed to be the first time such a detailed correlation of these two techniques has been undertaken for a semiconductor material. From this work, it has been found that the various wet etches can be divided into basically two groups ; resulting in either an oxidised or a de-oxidised surface. These interface types are characterised by MIS results which show dominant electron injection or the presence of considerable trapping hysteresis. It has however been shown that these effects can be virtually overcome by the combination of a de-oxidising etch followed by a brief oxidising etch. This operation appears to leave the surface covered with a thin native oxide layer.

The effect of dry etching in either hydrogen or oxygen plasmas, although giving significantly different surface chemistry, has so far only marginally improved the device results. The process has however been shown to be considerably cleaner and more controllable than wet etching, and it is likely that further investigation will prove its value in providing a means of accurately defining the sensitive interface region.

The use of a low temperature insulator deposition process, as well as allowing detailed investigation of the surface, has also enabled correlation of our device characteristics with those resulting from competing high temperature processes. This has led to our proposing a

modified model for the origin of the various trapping levels known to exist in the InP band gap, which now adequately explains the observed differences in device characteristics. Because of these detrimental effects induced by the high temperature process, it is clear that the utilisation of InP as a commercial device material must be accompanied by the application of a low temperature or low energy insulator deposition process. To this end the new and more stable Langmuir film materials currently under investigation may prove useful.

The preliminary investigation of gas effects upon these Langmuir film structures has shown many significant influences, particularly with carbon monoxide and ammonia. Although hindered by difficulties which preclude the application of surface state analysis, this study has developed useful techniques and proved the feasibility of this approach. It is clear therefore that given the investigation of other more suitable systems the use of organic/inorganic junctions as solid state sensors is an extremely practical concept.

REFERENCES

CHAPTER 2

1. H.K. Henisch, Rectifying Semiconductor Contacts, Oxford (1957).
2. E.H. Rhoderick, Metal-Semiconductor Contacts, Oxford (1978).
3. S.M. Sze, Physics of Semiconductor Devices, Wiley (1969).
4. H.C. Card and E.H. Rhoderick, J.Phys. D. 4 (1971) 1589.
5. A. Deneuveille, J.App.Phys, 45 (1974) 3079.
6. C. Barrett and A. Vapaille, Sol.St.Elect. 18 (1975) 25.
7. " " , Sol.St.Elect. 19 (1976) 73.
8. " " , Sol.St.Elect. 21 (1978) 1209.
9. " " , J.App.Phys. 50 (1979) 4217.
10. (For example:-) W.E.Spicer et al, Inst.Phys. Conf.Ser. 50, p 216. INFOS (1979).
11. T.Holstein, Ann.Phys. (NY) 8 (1959) 325, 343.
12. (For example:-)  
J.G.Simmons : DC Conduction in Thin Films (1971) Mills and Boon.  
D.R.Lamb : Electrical Conduction Mechanisms in Thin Insulating Films (1967) Methuen.
13. (For example:-)  
P.J.Harrop, Dielectrics (1972) Butterowrth & Co.  
J.C.Anderson, Dielectric (1964) Chapman & Hall.
14. M.A. Careem, A.K.Jonscher, Phil.Mag 35 (1977) 1503.
15. N.F. Mott, E.A.Davies, Electronic Processes in Non-Crystalline Materials, (1971) Clarendon Press, Oxford.
16. R.A.Street, G.Davies, A.D.Yoffe, J.Non-Cryst.Sol 5 (1971) 276.

17. (For example:-)  
A.S.Grove, B.E.Deal, E.H. Snow, C.T.Sah, Sol.St.Elect., 8 (1965) 145.
18. I.Tamm, Physik Z Sowjetunion 1 (1933) 733.
19. W.Shockley, Phys.Rev. 56 (1939) 317.
20. J.Koutecky, J.Phys.Chem.Sol 14 (1960) 233.
21. D.Pugh, Phys.Rev.Lett. 12 (1964) 390.
22. W.Shockley and G.L.Pearson, Phys.Rev.74 (1948) 232.
23. F.G.Allen, G.W.Gobeli, Phys.Rev. 127 (1962) 150.
24. K.Lehovec and A.Slobodskoy, Sol.St.Elect.7 (1964) 57.
25. E.H.Nicollian, A.Goetzberger, Bell Syst.Tech.Journ, 46, (1967)1055.
26. C.N.Berglund, IEEE Trans.Elect.Dev. 13 (1966) 701.
27. L.M.Terman, Sol.St.Elect. 5 (1962) 285.
28. P.V.Gray and D.M.Brown, App.Phys.Lett. 8 (1966) 31.
29. M.Kuhn, Sol.St.Elect. 13 (1970) 873.
30. R.Castagne, C.R.Acad. Sci. Paris, 267 (1968) 866.
31. D.V.Lang, J.App.Phys, 45 (1974) 3023.
32. E.H.Nicollian, A.Goetzberger, App.Phys.Lett. 10 (1967)60.
33. H. Preier, App.Phys. Lett. 7 (1967) 361.
34. J.Grosvalet and C.Jund, IEEE Trans.Elect.Dev. 14 (1967) 777.
35. M. Warashina and A. Ushirokawa, Jap.J.App.Phys.14 (1975) 1739.
36. E.H.Nicollian and A. Goetzberger, IEEE Trans.Elect.Dev.12 (1965) 108.

REFERENCES

CHAPTER 3

1. R.E.Honig, 'Surface and Thin Film Analysis of Semiconductor Materials', Thin Solid Films, 31 (1976) 89.
2. J.W.Coburn, E.Kay, 'Techniques for Elemental Composition Profiling in Thin Films', CRC Crit.Rev.Sol.St.Sci, 4 (1974) 561.
3. P.F.Kane and G.B.Larrabee, 'Characterisation of Solid Surfaces', (1974) Plenum.
4. H.Robinson, N.F.Rawlinson, Phil.Mag. 28 (1914) 277.
5. K. Siegbahn, E. Sokolowski, C.Nordling, Ark Physik, 13 (1958) 288.
6. K.Siegbahn, C.Nordling, A.Fahlamon, R. Nordberg, K.Hamrin, J. Hedman, G.Johansson, T.Bergmark, S. Karlsson, I. Lindgren, B.J.Lindberg, 'ESCA : Atomic, Molecular, and Solid State Structure Studies', Almquist and Wiksells, Uppsala (1967).
7. J.S.Levinger, Phys.Rev, 90 (1953) 11.
8. M.O.Krause, T.A.Carlson, Phys.Rev. 37 (1968) 170.
9. K. Siegbahn, C. Nordling, G.Johansson, J.Hedman, P.F.Hedan, K.Hamrin, U. Gelius, T.Bergmark, L.Werme, R.Manne, Y.Baer, 'ESCA Applied to Free Molecules', North Holland, Amsterdam (1969).
10. T.A.Koopmans, Physika, 1 (1933) 104.
11. D.T.Clark, Theoret Chim.Acta (Berl) 35 (1974) 341.
12. W.L.Jolly, D.N.Hendrickson, J.Amer.Chem.Soc, 92 (1970) 1963.
13. L.Holland, 'Vacuum Deposition of Thin Films', (Ch.3) Chapman & Hall (1966).
14. H.Abe, Circuit Manufacturing, 18 (1978) 22.
15. R.G.Poulsen, H.Nentwin, S.Ingreay, Proc.I.E.E.D.M. Washington (1976) 205.
16. 'Introduction to Lock-in Amplifiers', Technical Note 102, BrookdealElectronics Ltd,(Bracknell).
17. 'The Lock-in Amplifier'- Application Note,Princeton Applied Research Ltd.(1972).

18. B.E.Jones, 'Instrumentation, Measurement and Feedback',  
(Ch.7) McGraw Hill (1977).
19. 'The Automatic Measurement of Semiconductor Junction Capacitance'  
Application note No.5. Brookdeal Electronics Ltd.
20. M. Ruden, G. Spadini, Alta Frequenza, 34 (1974).
21. M. Freeman, R. Nottenburg, J. Duboir, J.Phys.E,13 (1980) 328.
22. C. Lawrence Anderson, R. Baron, Rev.Sci. Inst., 47 (1976) 1366.
23. BOC Special Gases (Deer Park Road, London).
24. Hamilton -Bondaduz AG, Switzerland.

REFERENCES

CHAPTER 4

1. For example : V.J.Bigelow "The complete works of Benjamin Franklin"  
Vol.5. p 253.
2. A. Pockels, Nature 43, (1891) 437.
3. Lord Rayleigh, Phil.Mag, 48 (1899) 321.
4. I. Langmuir, J.Am.Chem.Soc. 39 (1917) 1848.
5. K.B.Blodgett, J.Am.Chem.Soc. 56 (1934) 495.
6. K.B.Blodgett, J.Am.Chem.Soc. 57 (1935) 1007.
7. K.B.Blodgett and I.Langmuir, Phys.Rev. 51 (1937) 964.
8. H.H.Race and S.I.Reynolds, J.Am.Chem.Soc. 61 (1939) 1425.
9. G.L.Clark and R.R.Sterrett, J.Am.Chem.Soc. 57 (1935) 330.
10. N.K.Adam, "The Physics and Chemistry of Surfaces", Oxford Univ.Press  
(1941).
11. E.K.Rideal, "Surface Chemistry", Cam.Univ.Press (1930).
12. G.L.Gaines, Jnr, "Insoluble Monolayers at Liquid-Gas Interfaces",  
Wiley (1966).
13. J.Jaffe, G.Bricman and A.Gelbecke, J.de Chim. Phys. 64 (1967) 942.
14. H. Bucher, K.H.Drexhage, M.Fleck, H.Kuhn, D.Mobius, F.P.Schafer,  
J.Sondermann, W.Sperling, P.Tillmann, J.Wiegand, Mol.Cryst. 2, (1967) 199.
15. A.Finney, W.A.Barlow, P.S. Vincett and G.G.Roberts, J.Phys.E.  
  
(to be published).
16. H.Kuhn, Techniques of Chemistry, Vol.Pt.III B, Wiley (1972).
17. V.K.Agarwal, Electrical Behaviour of Langmuir Films, IAEA and UNESCO  
May (1974).
18. V.K. Srivastava, Physics of Thin Films, Vol.7 (1973) Academic Press.
19. V.K. Agarwal, Thin Solid Films, 50 (1978) 3.

20. P.S.Vincett and G.G.Roberts, *Thin Solid Films*, 68 (1980) 135.
21. G.L.Gaines, *Thin Solid Films*, 68 (1980) 1.
22. B.Mann and H.Kuhn, *J.App.Phys*, 42 (1971) 4398.
23. B.Mann, H.Kuhn and L.V.Szentpaly, *Chem.Phys.Lett*, 8 (1971) 82.
24. E.E.Polymeropoulos, *J.App.Phys*, 48 (1977) 2404.
25. M.A.Careem and R.M.Hill, *Thin Sol.Films*, 51 (1978) 363.
26. M.H.Nathoo, *Thin Solid Films*, 16 (1973) 215.
27. G.G.Roberts, P.S.Vincett and W.A.Barlow, *J.Phys.C*, 11 (1978) 2077.
28. P.S.Vincett and W.A.Barlow (to be published).
29. G.G.Roberts and K.P.Pande, *Electronics Lett*, 13 (1977) 581.
30. E.P.Honig, *Thin Sol.Films.*, 33 (1976) 231.
31. M.H.Nathoo and A.K. Jonscher, *J.Phys. C.*, 4 (1971) L301.
32. A.K.Jonscher and M.H.Nathoo, *Thin Sol.Films*, 12 (1972) S15.
33. M.A.Careem and A.K.Jonscher, *Phil.Mag.*, 35 (1977) 1489.
34. M.Sugi, K. Nembach, D.Mobius and H.Kuhn, *Sol.St.Comm*, 13 (1973) 603.
35. G.G.Roberts and T.M.McGinnity, *Thin Sol.Films*, 68 (1980) 223.
36. M.A.Careem and A.K.Jonscher, *Phil.Mag.*, 35 (1977) 1503.
37. V.K. Agarwal, *Electrocomp. Sci. & Tech.*, 2 (1975) 1,75.
38. A.Barraud & C.Rosilio, *Thin Sol.Films*, 68 (1980) 7.
39. A.Leger, J.Klein, M.Belin & D.Defourneau, *Thin.Sol.Films*, 8 (1971) R51.
40. S.K.Gupta, C.M.Singal, V.K.Srivastava, *J.App.Phys*, 48 (1977) 2583.
41. C.M.Singal, S.K.Gupta, A.K.Kapil, V.K.Srivastava, *J.Appl.Phys*, 49 (1978) 3402.
42. S.K.Gupta, A.K.Kapil, V.K.Srivastava, *J,Appl.Phys*, 50 (1979) 2852, 2856, 2896.
43. V.K.Agarwal, V.K.Srivastava, *Thin Sol.Films.*, 8 (1971) 377.
44. V.K.Agarwal, V.K.Srivastava, *Sol.St.Comm.*, 12 (1973) 829.
45. V.K.Agarwal, V.K.Srivastava, *J.App.Phys.*, 44 (1973) 2900.
46. V.K.Srivastava, *Electrocomp.Sci. & Tech.*, 3 (1976) 117.
47. V.K.Agarwal, *Thin Sol.Films*, 23 (1974) 53, 59.



48. V.K.Agarwal, *Thin Sol.Films.*, 33 (1976) L27.
49. A.Barraud and A. Rosilio, *Thin Sol.Films.*, 31 (1976) 243.
50. A. Barraud, J.Messier, A.Rosilio & J.Tanguy, *Colloque AVISEM, Versailles* (1971) 341.
51. J.Tanguy, *Thin Sol.Films*, 13 (1972) 33.
52. I.Lundstrom and D.McQueen, *Chem.Phys.Lipids*, 10 (1973) 181.
53. I.Lundstrom and M. Stenberg, *Chem.Phys.Lipids*, 12(1974) 287.
54. I.Lundstrom, *Phys.Scripta*, 18 (1978) 424.
55. G.G.Roberts, K.P.Pande, & W.A.Barlow, *Sol.St.and Electron Dev.*, 2 (1978) 169.
56. M.C.Petty and G.G.Roberts, *Electronics Lett*, 15 (1979) 375.
57. R.Singt and J.Sewchun, *App.Phys.Lett.*, 28 (1976) 512.
58. I.M.Dharmadasa, M.C.Petty, G.G.Roberts, *Elect.Lett.*, 16 (1980) 201.
59. G.G.Roberts, I.M.Dharmadasa, M.C.Petty, to be published (*Sol.St.Commun*).
60. C.W.Pitt and L.M.Walpitta, *Electronics Lett.*, 12 (1976) 479.
61. C.W.Pitt and L.M.Walpitta, *Thin Solid Films*, 68 (1980) 101.
62. L.M.Walpitta and C.W.Pitt, *Electronics Lett.*, 13 (1977) 210.
63. P.S.Vincett, W.A.Barlow, F.T.Boyle, J.A.Finney & G.G.Roberts, *Thin Sol.Films*, 60 (1979) 265.
64. J.Dresner, *RCA Review*, 30 (1969) 322.
65. G.G.Roberts, T.M.McGinnity, W.A.Barlow & P.S.Vincett, *Sol.State Comm.*, 32 (1979) 683.
66. A.Barraud, C.Rosilio & A.Ruauadel-Teixier, *Thin Sol.Films*, 68 (1980) 99.
67. A.Barraud, C.Rosilio & A.Ruauadel-Teixier, *Thin Solif Films*, 68 (1980) 101.
68. M.Sugi, K.Nembach and D.Mobius, *Thin Solid Films*, 27 (1975) 205.
69. R.Jones, & R.H.Tredgold, *Photochem & Photobio.*, 32 (1980) 223.
70. R.Pethig, *Dielectric and Electronic Properties of Biological Materials* (1979) Wiley.
71. N.L.Gershheld, *J.Phys.Chem.*, 66 (1962) 1923.
72. M.Montal and P.Mueller, *Proc.Nat.Acad.Sci.(U.S.A)*, 69 (1972) 3561.
73. M.Montal, A.Darszon & H.W.Trissl, *Nature*, 267 (1977) 221.
74. C.C.Johnson, S.D.Moss and J.A.Janata, U.S.Patent 4020830.

REFERENCES

CHAPTER 5

1. J. Jaffe, G. Bricman and A. Gelbecke, J.de Chim.Phys. 64 (1967)942.  
A. Finney, W.A.Barlow, P.S.Vincett and G.G.Roberts, J.Phys. E.  
(to be published).
2. I.Langmuir, J.Am.Chem.Soc., 39 (1917) 1848.
3. L. Wilhelmy, Ann. Physik, 119 (1863) 177.
4. H.B.Bull, 'Advances in Protein Chemistry' Vol.III, Academic Press,  
(1947).
5. W.D.Harkins and T.F.Anderson, J.Am. Chem.Soc., 59 (1937) 2189.

REFERENCES

CHAPTER 6

1. K.B.Blodgett, J.Am.Chem.Soc, 56 (1934) 495.  
    "                  "          57 (1935) 1007.
2. K.B.Blodgett & I.Langmuir, Phys.Rev. 51 (1937) 964.  
    G.L.Clark and R.R.Sterrett, J.Am.Chem.Soc. 57 (1935) 330.
3. G.L. Gaines(Jnr), 'Insoluble Monolayers at Liquid-Gas Interfaces'  
    Wiley (1966).
4. M.W.Charles, J.App.Phys, 42 (1971) 3329.
5. E.P. Honig, J.Colloid and Interface Sci, 43 (1973) 65.
6. H. Hasmoney, M.Vincent & M. Dupeyrat, Thin Solid Films, 68 (1980) 21.
7. H. E. Ries (Jnr) and W.A. Kimball, Proc.Second Int. Congress in  
    Surface Activity, Vol. I. (1957) 75.
8. C. Holley & S. Bernstein, Phys. Rev, 52 (1937) 525.
9. I. Fankuchen, Phys. Rev, 53 (1938) 909.

REFERENCES

CHAPTER 7

1. G.G.Roberts, P.S.Vincett, W.A.Barlow, J.Phys. C. 11 (1978) 2077.
2. G.G.Roberts, and K.P. Pande, J.Phys. D. 10 (1977) 1323.
3. T.M. Ginnai, D.P.Oxley and R.G.Pritchard, Thin Sol.Films, 68 (1980) 241.

REFERENCES

CHAPTER 8

1. H. Welker and H. Weiss, *Sol. St. Phys.*, 3 (1956) 1.
2. P. Blood and J. W. Orton, *J. Phys. C*, 7 (1974) 893.
3. J. B. Mullin, R. J. Heritage, C. H. Holliday, B. W. Straughan, *J. Cryst. Growth*, 3 (1968) 281.
4. O. Mizuno, *Japanese J. App. Phys.*, 14 (1975) 451.
5. K. J. Backmann and E. Buchler, *J. Electrochem. Soc.*, 123 (1976) 1509.
6. K. Hess, N. Stath and K. W. Benz, *J. Electrochem. Soc.*, 121 (1974) 1208.
7. C. Hilsum and H. D. Rees, *Elect. Lett.*, 6 (1970) 277.
8. C. Hilsum and J. B. Mullin, B. A. Prew, H. D. Rees and B. W. Straughan, *Elect. Lett.*, 6 (1970) 306.
9. R. J. Hamilton, R. D. Fairman, S. I. Long, M. Omari, F. B. Fank, *IEEE Trans*, MTT-24 (1976) 775.
10. D. J. Colliver, C. Hilsum, J. R. Morgan, H. D. Rees, B. C. Taylor, *Proc. Inst. Symp. GaAs*, (1970) 140.
11. P. M. White and G. Gibbons, *Elect. Lett.*, 8 (1972) 166.
12. J. S. Barrera and R. J. Archer, *IEEE Trans. ED* 22 (1975) 1023.
13. J. J. Loferski, *J. App. Phys.*, 27 (1956) 777.
14. P. Rappaport, *RCA Review*, 20 (1959) 373.
15. J. J. Loferski, *Proc. IEEE*, 51 (1963) 667.
16. K. Oe and K. Sugiyama, *Japanese J. App. Phys.*, 15 (1976) 2003.
17. C. C. Shen, J. J. Hsieh and T. A. Lind, *App. Phys. Lett.*, 30 (1977) 353.
18. C. R. Bayliss and D. L. Kirk, *Thin Solid Films*, 29 (1975) 97.
19. C. R. Bayliss and D. L. Kirk, *J. Phys. D* 9 (1976) 233.
20. D. L. Kirk and C. Jones, *J. Phys. D* 12 (1979) 651.
21. N. Keddar and D. L. Kirk, *J. Phys. D* 13 (1980) 53.
22. A. R. Clawson, W. Y. Lum, G. E. McWilliams & J. Monroe, *Nosc (California) Technical Note 506* (1978).
23. R. H. Williams and I. T. McGovern, *Surface Science* 51 (1975) 14  
(and refs. contained therein).
24. W. E. Spicer and I. Lindau, *Thin Solid Films*, 56 (1979) 1.

25. W.E.Spicer, P.W.Chye, P.R.Skeath, C.Y.Su & I.Lindau, INFOS(1979) IOP Conf. Ser. 50, 216, (IOP, London).
26. W.E.Spicer and P.W.Chye, C.Y.Su, I.Lindau, C.M.Garnier, P.Pianetta, Surface Science, 88 (1979) 439.
27. P. Skeath and W.E.Spicer, J.Vac.Sci.Tech. 15 (1978) 1219  
(and ref contained therein).
28. C.W.Wilmsen and R.W.Kee, J.Vac.Sci.Tech., 14 (1977) 953.
29. C.W.Wilmsen and R.W.Kee, J.Vac.Sci.Tech., 15 (1978) 1513.
30. C.W.Wilmsen, R.W.Kee, J.F.Wager, J.Stannard, & L.Messick, Thin Solid Films, 64 (1979) 49.
31. C.W.Wilmsen, J.F.Wager and J.Stannard, INFOS (1979) IOP. Conf. Ser.50, 251, (IOP, London).
32. C.W.Wilmsen, Crit.Rev.Sol.St. Sci., 5 (1975) 313.
33. C.W.Wilmsen and R.W.Kee, J.Vac.Sci.Tech., 15 (1978) 1513.
34. D.L.Lile and D.A.Collins, App.Phys.Lett., 28 (1976) 554.
35. H.L.Hartnagel, A.Colquhoun, Surf. Tech., 5 (1977) 291.
36. T. Ota and Y. Horikoshi, Japanese, J.Appl.Phys., 18 (1979) 989.
37. S. Hannah and B. Livingstone, INFOS (1979), IOP Conf.Ser.50, p271 (IOP, London).
38. P.N.Favennec, M.Le Contellec, H.L.Haridan, G.P.Pelcus, J.Richard, App.Phys.Lett., 34 (1979) 807.
39. K. Kamimura and Y. Sakai, Thin Solid Films, 56 (1979) 215.
40. L. Messick, J. App.Phys., 47 (1976) 4949.
41. D. Fritsche, Electronics Letters, 14 (1978) 52.
42. L.G. Meiners, Thin Solid Films, 56 (1979) 201.
43. A.J. Grant et al, INFOS (1979), IOP Conf.Ser. 50, p 266 (IOP, London).
44. L. G. Meiners, D.L.Lile, and D.A.Collins, J.Vac.Sci.Tech., 16  
Proc. 6th Conf. Phys. of Compound Semiconductors (1979).
45. K.P.Pande and G.G.Roberts, J.Vac.Sci.Tech., 16, Proc. 6th Conf. Phys. of Compound Semiconductors.
46. L.G.Meiners, J. Vac.Sci. Tech. 15 (1978) 1402.

REFERENCES

CHAPTER 9

1. K.S.Kim, W.E.Bartinger, J.W.Amy & N.Winograd, J.Electron.Spect.  
Rel.Phén.5 (1974) 351.
2. G.G.Roberts and K.P.Pande, J.Phys. D, 10 (1977) 1323.
3. L.D.Irving, RSRE (Malvern) : Private communication.
4. A.J.Grant, D.C.Cameron, L.D.Irving, C.E.Greenhalgh & P.R.Norton,  
INFOS 1979, Inst.Phys.Conf.Ser.50.
5. H.D.Rees, Metal-Semiconductor Contacts (1974) Inst.Phys.Conf . Ser.22.
6. B.L.Smith, J.Phys. D, 6 (1973) 1358.
7. D.J.Di Maria, Proc.Int.Conf. 'The Physics of MOS Insulators',  
North Carolina, U.S.A. (1980), (Pergamon Press).
8. D.Ashen, RSRE (Malvern): Private communication.
9. G.G.Roberts, K.P.Pande, W.A.Barlow, Sol.St. & Electron.Dev, 6 (1978) 169.

REFERENCES

CHAPTER 10

1. I. Lundstrom, *Physica Scripta*, 18 (1978) 424.  
(and refs. contained therein).
2. B. Keramati and J.N.Zemel, *Proc.Int.Conf.'The Physics of SiO<sub>2</sub> and its Interfaces'*, Yorktown Heights, U.S.A.(1978).
3. P.J.Martin, *Ph.D.Thesis*, University of Durham (1980).
4. K.K.Kan, M.C.Petty and G.G.Roberts, *Proc.Int.Conf. 'Physics of MOS Insulators'*, North Carolina, U.S.A. June (1980).
5. M.C.Petty and G.G.Roberts, *INFOS* (1979) *Inst.Phys. Conf. Ser.* 50, 186.



LIST OF LEGENDS

- 2.1 Simplified semiconductor band structure, showing (a) intrinsic, (b) n-type, (c) p-type.
- 2.2 Energy band diagrams for Ohmic and rectifying semiconductor contacts, (a,b) n-type, (c,d) p-type.
- 2.3 Schottky barrier contacts under various bias conditions.
- 2.4 Schematic representation of Schottky emission process.
- 2.5 Schematic representation of Poole-Frenkel emission process.
- Table 2.1 Summary of DC conduction mechanisms in thin films.
- 2.6 Representation of real capacitor, and accompanying vector diagram.
- 2.7 Ideal reciprocal capacitance against thickness plot.
- 2.8 Device equivalent circuit incorporating additional contact and series resistance components.
- 2.9 Zero bias energy band diagram for ideal MIS (n-type) device.
- 2.10 Energy band diagram for ideal MIS device under various bias conditions.
- 2.11 Idealized MIS capacitance-voltage curves (for p-type material).
- 2.12 Device equivalent circuits incorporating surface state components ( $R_s, C_s$ ).
- 2.13 Comparison of surface state effects on capacitance and conductance data (After Nicollian & Goetzberger, Ref.25).
- 2.14 High and low frequency capacitance curves illustrating additional effect of surface states.
- 2.15 Quasi-static equivalent circuit.
- 2.16 Sample device data showing  $G_m$  and  $G_p$  peaks as a function of applied bias (After Warashina and Ushirokawa, Ref.2.35).

- 2.17 The effect of electrode work function variation.
- 2.18 The effect of temperature variation.
- 2.19 Device equivalent circuit showing additional component for substrate resistance.
- 2.20 The effect of lateral conduction on capacitance and conductance curves, where  $G_g$  represents bias dependent conductance channel, and  $C_c, G_c$  represent lumped component network (After Nicollian and Goetzberger, Ref.2.36).
- 2.21 Device with mobile positive charge, under equilibrium, forward, and reverse bias.
- 2.22 The effect of (a) mobile positive ions, (b) mobile negative ions, and (c) hole and electron injection.
- Table 3.1 Survey of available methods for surface characterisation.
- Table 3.2 Summary of capabilities and limitations of various surface and thin film analysis techniques.
- 3.1 Energetics of electron binding energy measurement in solids, where  $E_D$  is the binding energy,  $T_s$  is the K.E. of the ejected electron, and  $T_{sp}$  the measured K.E.
- 3.2 Example of ESCA output data : for  $C_{1s}$  shell in ethyl-trifluoroacetate (After Siegbahn et al, Ref.3.6).
- 3.3 Schematic diagram of AEI ES200 X-Ray photoelectron spectrometer.
- 3.4 Schematic representation of electron take-off angle  $\theta$ , where  $d$  is the sampling depth and  $d'$  the transit distance.
- 3.5 Schematic diagram of glow discharge apparatus.
- Table 3.3 Summary of wet chemical etches used on InP.
- 3.6 Cooling attachment for evaporator.
- 3.7 Metal sample holder with lid removed : showing probe, moving table, electrical and gas leadthroughs.

- 3.8 Simplified representation of Brookdeal 9502 : Dual channel lock-in amplifier.
- 3.9 Simplified representation of sample biasing arrangement.
- 3.10 Circuit diagrams of low and high frequency input mixing circuits.
- 3.11 Block diagram of major components of electrical measurement system.
- 3.12 Schematic layout of gas handling and mixing system.
- 4.1 Representation of chemical structure of stearic acid, and its cadmium salt.
- 4.2 Idealised compression isotherm for stearic acid.
- 4.3 Schematic representation of X-type deposition.
- 4.4 " " Z-type deposition.
- 4.5 " " Y-type deposition.
- 4.6 Original Langmuir/Blodgett trough, showing (a) equilibrium, (b,c) after addition of fatty acid at X, (d) after addition of piston compression oil at Y, and (e) after removal of film onto substrate.
- 4.7 Early example of constant perimeter compression barrier, (After Jaffe et al, Ref.4.13).
- 5.1 Schematic representation of constant perimeter compression barrier, showing maximum and minimum areas.
- 5.2 Photograph of large trough.
- 5.3 Representation of surface pressure measurement.
- 5.4 Circuit diagram of barrier control instrumentation.
- 5.5 Circuit diagram of dipping mechanism control.
- 5.6 Photograph of Langmuir trough control instrumentation.
- 6.1 The effect of pH variation upon isotherm shape.
- 6.2 The effect of compressible, and incompressible surface contamination upon isotherm shape.

- 6.3 The use of recompression to remove certain contamination.
- 6.4 Area-time plot for good Y-type pick-up.
- 6.5 Area-time plot for Z-type pick-up.
- 6.6 Area-time plot showing apparent change from Y → Z type deposition.
- 7.1 Photograph showing typical good quality Langmuir film
- 7.2 Photograph showing slightly poor quality film, with significant density of pin holes.
- 7.3 Photograph showing bad quality film, with amorphous appearance, and large holes.
- 7.4 Photograph of good top electrode, deposited under correct conditions.
- 7.5 Photograph showing diffuse dark ring around contact, indicative of poor cooling procedure.
- 7.6 Photograph of cracked electrode, indicative of differential thermal expansion rates.
- 7.7 Typical reciprocal capacitance plot for thin stearic acid/Cd stearate film.
- 7.8 AC resistance plot for thin arachidic acid/Cd arachidate film along with ideal, and data of Sugi et al (Ref. 2.34).
- 7.9 Typical reciprocal capacitance plot for thick stearic acid/Cd stearate film.
- 7.10 Typical reciprocal capacitance plot for arachidic acid/Cd arachidate film.
- 7.11 DC current through a single monolayer of Ar Acid/Cd Ar<sub>2</sub>.
- 7.12 Log  $J-V^{\frac{1}{2}}$  plot for MIM structure, showing three different electrode materials.
- 7.13 Log  $J-V^{\frac{1}{2}}$  plot for n-InP/Langmuir film MIS structure.

- 7.14 Forward bias n-InP MIS data replotted on Log-Log axes.
- 7.15 Typical characteristics for poor quality n-InP MIS device.
- 7.16 Typical log  $J-V^{1/2}$  plot for p-InP MIS device.
- 7.17 Typical characteristics for poor quality p-InP MIS device.
- 7.18 Variation of AC conductance with frequency for good quality film.
  
- 8.1 Displacement of the Fermi level of (110) cleaved, n-type (o), and p-type ( ) InP as a function of oxygen exposure.  
(After Spicer et al, Ref.8.26 ).
  
- Table 9.1 Summary of model calibration materials.
- Table 9.2 Summary of ESCA data for as-received InP samples.
- Table 9.3 Summary of ESCA data for some etched InP substrates.
- Table 9.4 Summary of time dependent etching in 20% Br/HBr Soln.
- Table 9.5 Summary of time dependent etching in 5% Br/HBr soln.
  
- 9.1 Sample ESCA output data for  $In_{3d}$  and  $P_{2p}$  levels - after various wet etches.
- 9.2 Sample ESCA output data for time dependent 20% Br/HBr etch.
- 9.3 Output data for argon ion depth profile of wet (Br/HBr) etched oxide.
  
- 9.4 & 9.5 Schottky barrier data for p-type InP substrate.
  
- 9.6 & 9.7 Schottky barrier data for n-type InP substrate.
  
- 9.8 Typical output MIS data for oxidised InP interface.
- 9.9 Typical output MIS data for de-oxidised InP interface.
- 9.10 The effect of bias-stress upon an n-type MIS structure :  
Showing dominance of electron injection.
- 9.11 Example of optimum sample data obtained by using both oxidising and de-oxidising etches. Also shown for comparison is a typical curve obtained using a high temperature insulator deposition process.

- 9.12 Typical capacitance characteristics obtained using oxidised p-type interface. Also shown for comparison are typical GaAs and InP (high temp. insulator) curves.
- 9.13 Variation of p-type conductance peak with frequency.
- 9.14 Example of double conductance peak obtained with certain p-type samples.
- 9.15 The effect of different electrode materials upon the MIS capacitance curves.
- 9.16 The effect of insulator thickness.
- 9.17 The effect of low temperature annealing upon capacitance data.
- 9.18 Device equivalent circuit, incorporating conducting first monolayer.
- 9.19 Model for band gap of n-type InP.
- 9.20 Model for band gap of p-type InP.
- 9.21 Unified model for InP band gap.
- 10.1 The effect of hydrogen upon the Pd (Langmuir film/InP system).
- 10.2 The effect of water vapour.
- 10.3 The effect of carbon monoxide.
- 10.4 The effect of dilute ammonia upon the capacitance and conductance curves.
- 10.5 The effect of organic solvent.
- 10.6 Diagrammatic representation of (12.8) diacetylene monomer, and after uv polymerisation.
- 10.7 Device characteristics for the diacetylene/InP system.
- 10.8 Device characteristics for the CdSt<sub>2</sub>/CdTe system.

